Microfluidic magnetic fluidized bed for bioanalytical applications

Iago Pereiro

Université Pierre et Marie Curie

Ecole doctorale Physique en Ile-de-France (ED 564)

Institut Curie, Laboratoire Physico-Chimie

Microfluidic magnetic fluidized bed for bioanalytical applications

Présentée par :

Iago Pereiro

Pour obtenir le grade de :

DOCTEUR DE L'UNIVERSITE PIERRE ET MARIE CURIE

Dirigée par Jean-Louis Viovy et Stéphanie Descroix

Présentée et soutenue publiquement le 12 février 2016 devant un jury composé de :

Nicole Pamme	Rapporteuse
Anne-Marie Haghiri-Gosnet	Rapporteuse
Christine Ménager	Examinatrice
Myriam Taverna	Examinatrice
Pierre Sonigo	Examinateur
Jean-Louis Viovy	Directeur de thèse
Stéphanie Descroix	Co-directrice de thèse
Laurent Malaquin	Membre invité

Abstract

Fluidization is the process whereby a granular solid phase behaves like a fluid under the influence of an imposed upward fluid flow that counteracts gravitational forces. Fluidized bed reactors are nowadays routinely used in many chemical and biological engineering applications due to characteristics such as high surface to volume ratio, constant mixing, automation of operation and high heat transfer. We have developed a microfluidic magnetic fluidized bed system, in which gravity has been replaced with a magnetic field created by an external permanent magnet and the solid-phase by magnetic microbeads. These magnetic beads can be functionalized with different ligands in order to use the fluidized bed for biological target capture and preconcentration. The microfluidized bed system allows flow-through operations at low driving pressures with intimate liquid/solid contact and a continuous beads recirculation for enhanced target capture efficiencies. The physical system has been characterized, showing the importance of chamber angle of aperture and height confinement, as well as magnetic field distribution parameters, to obtain fluidization and further enhance mixing and maximize beads density. Moreover, the potential of the fluidized bed as a platform for analytical bioassays has been successfully explored with a series of biologically relevant applications:

(1) the preconcentration of rare Alzheimer's biomarkers together with their in situ fluorescence labeling for future enhanced detection with hyphenated detection techniques

(2) the label-free sensitive detection of bacteria in liquid food samples through the specific immunocapture and on-chip culture of these microorganisms and the subsequent physical changes induced in the fluidized support, displaying a quantitative dynamic range of 100 to 10^7 cfu/mL

(3) the gene-specific extraction of DNA and its subsequent enzymatic amplification on the surface of the beads, coupled to a microarray detection system for a multiplexed detection of cancer-inducing mutations, showing a limit of detection of 10 pM.

These results show that the applications of the magnetic fluidized bed go beyond its initial conception as a dynamical affinity-based concentrator, serving as an efficient platform for molecular biology protocols and even making use of its inherent auto-regulating properties as a detection mechanism.

Contents

Nomenclature

Latin characters

Variable	Meaning
A	Cross-sectional area
B	Magnetic flux density
D	Channel diameter
d	Spherical diameter
F_d	Drag force
F_g	Magnetic force
f_p	Friction factor
H	Magnetic field intensity
k	Intrinsic permeability of the medium
K	Kozeny constant
k_B	Boltzmann constant
M	Magnetization
m	Magnetic moment
P	Pressure
P_{ef}	Pressure of effective fluidization
P_{mf}	Pressure of minimum fluidization
S_v	Specific surface area
U_f	Superficial flow velocity
U_{mf}	Velocity of minimum fluidization
U_{p0}	Terminal settling velocity
U_t	Maximum fluidization velocity

Greek characters

Variable	Meaning
μ	Dynamic viscosity
ε	Porosity
ρ_f	Density of fluid
ρ_s	Density of solids
τ	Néel relaxation time

Acronyms and abbreviations

Shortcut	Meaning
AC	Alternating current
AD	Alzheimer's disease
APP	Amyloid precursor molecule
Aβ	Beta amyloid
BAM	Bacteriological Analytical Manual
BSA	Bovine serum albumin
C2CA	Circle to circle amplification
CE	Capillary electrophoresis
cfDNA	Circulating free DNA
CFU	Colony forming unit
COC	Cyclic olefin copolymer
CSF	Cerebrospinal fluid
CTC	Circulating tumor cell
ctDNA	Circulating tumor DNA
CZE	Capillary zone electrophoresis
DMP	2,2-Dimethoxypropane
DNA	Deoxyribonucleic acid
dPCR	Digital polymerase chain reaction
dsDNA	Double stranded DNA
ELISA	Enzyme-linked immunosorbent assay
FBS	Fetal bovine serum
FCC	Fluid catalytic cracking
FDA	Food and Drug Administration
FITC	Fluorescein isothiocyanate
GDP	Guanosine diphosphate
GFP	Green fluorescent protein
GTP	Guanosine triphosphate
HDA	Helicase-Dependent Amplification
HRCA	Hyper-branched rolling circle amplification
ID	Internal diameter
IgG	Immunoglobulin G
ITO	Indium tin oxide
KRAS	Kirsten rat sarcoma viral oncogene homolog
LAMP	Loop mediated AMPlification
LB	Lysogeny broth
LFA	Lateral flow assay
LIF	Laser-Induced Fluorescence Detection
LOD	Limit of detection
MSFB	Magnetically stabilized fluidized bed
NASBA	Nucleic-Acid Sequence-Based Amplification

PBS	Phosphate-buffered saline
PCR	Polymerase chain reaction
PDMA-AGE	Poly(dimethylacrylamide)-co)allyl glycidyl ether
PDMS	Polydimethylsiloxane
PEEK	Polyether ether ketone
Phi29	DNA polymerase from the bacteriophage Φ29
PIV	Particle image velocimetry
RCA	Rolling circle amplification
RCP	Rolling circle product
Re	Reynolds number
Re*	Modified Reynolds number
sAPPα	Soluble amyloid precursor protein-α
sAPPβ	Soluble amyloid precursor protein-β
SPR	Surface plasmon resonance
ssDNA	Single stranded DNA

Introduction

The detection of analytes present in liquid samples at low concentrations is of outmost importance, in particular for biomedical diagnosis and public and environmental safety. This desirable detection represents however in many cases a technical challenge, resulting in too long and/or expensive analyses, with the resulting risk for patients and consumers.

The field of microfluidics offers the possibility of automated and multiplexed analysis with low volumes of reagents, with the subsequent reduction in costs and enhanced portability. For enhanced sensitivity in order to detect rare analytes, the field has demonstrated the successful integration in microfluidic devices of many well-known preconcentration technologies such as electrokinetical separation or solid-phase extraction. In this latter case, membranes, porous monoliths and packed beds of beads have been shown to be efficient extractors of species. Nonetheless, their use has been limited by the need to use high pressures and their inherent proneness to clogging. Furthermore, an accurate fabrication control is still necessary to obtain the desired porous fraction and structural stability.

The microfluidic magnetic fluidized bed system object of this thesis represents an innovative step forward in the field of microfluidic preconcentration systems, because of its flow-through functioning at low back-pressure and resistance to clogging. Further, its constant particle recirculation serves as an additional enhancer of an otherwise high surface to volume ratio. Because it allows the fluidization of magnetic beads commonly employed for biological separation steps, the system can be used for the automation of bioanalytical protocols that usually require tedious manual handling. Finally, the system is simple, only requiring some general geometrical features and an external magnet, and necessitates a low amount of magnetic beads.

In this manuscript, besides the physical characterization of the system to reach a full comprehension of the requirements to obtain the fluidization of magnetic beads in microfluidic channels, the versatility of the system is demonstrated with a series of bioanalytical applications. While the use of the fluidized bed is demonstrated for very different targets (proteins, DNA, cells), the presented results show that the properties of the system can be used to go beyond simple preconcentrations. In particular, molecular enzymatic reactions and cell culture are shown to be possible in situ during the fluidization of the magnetic beads, this last case leading to physical expansion phenomena that can be used for the visual detection of bacteria.

This manuscript is divided into five chapters, each one giving a special focus to a different aspect of this technology:

In Chapter 1, the capacity of the magnetic fluidized bed as a preconcentration system is put into perspective with a review on the existing literature in microfluidic concentration methods, be them electrochemical, membrane or surface affinity-based. A particular focus will be given to these latter ones, in which the fluidized bed integrates itself. The end of the chapter will be dedicated to alternative magnetic bead-based systems reported for preconcentration applications.

In Chapter 2, the magnetic fluidized bed system will be presented after a first introduction on current fluidized bed technology and state of the art of fluidization integration in microfluidic systems. A full characterization of the physical properties of the system is then shown, with a special emphasis on critical parameters needed to obtain fluidization phenomena such as geometrical confinement and magnetic field distribution.

The remaining three chapters are dedicated to different bioanalytical applications developed with the fluidized bed system. Chapter 3 is dedicated to the preconcentration of proteins, first with a characterization with a model biomarker molecule and subsequently for the immunocapture and elution of Alzheimer's disease beta amyloids. This chapter is further completed with a scientific publication in appendix one, in which part of the presented results have been reported.

Chapter 4 presents a thorough study on bacteria concentration and detection. In this case, the physical properties of the fluidized bed are used for the immunocapture, culture and detection of Salmonella. This detection system can compete in time with current standard methods of detection and is much simpler than most alternative methods.

Finally, Chapter 5 presents the use of the fluidized bed system for the integration of long magnetic bead handling protocols for DNA amplification. This is the case of the circle to circle amplification (C2CA) composed of two amplification steps. While the fluidized bed will be used again as a preconcentration module, subsequent steps allow the in situ fluidized enzymatic amplification of the DNA target. The resulting product is then digested and sent to a downstream array for a second amplification and detection, everything integrated in a single microfluidic chamber.

Chapter 1

Preconcentration systems in microfluidics

1.1 Trace analysis

The analysis of molecules and cells at low and very low concentrations is growing in importance in fields as diverse as environmental protection, pharmaceutics, medical diagnosis or nanotechnology. The concentration at which a component can be considered to be present at trace levels can only be subjective and depends on the specific application, but an idea can be given by current definitions such as the one given by the IUPAC (International Union of Pure and Applied Chemistry) that considers the upper concentration limit for trace analysis to be 100 parts per million (ppm, Namieśnik 2002). However, as more and more methods are developed that are capable of performing analysis at these levels, the defined limit tends to be reduced. One can consider then than trace analysis is performed at the limit of current technologies, and hence is continually an area of active research.

This trace level analysis is particulary present in several key areas of science and technology:

- The production of high purity materials, where, as in the case of microelectronics, the concentration of impurities plays an essential role in device performance.

- Biotechnology, and in particular the biomedical field, where the detection of trace species can improve diagnostics or be fundamental in the preparation of drugs.

- Environmental protection and monitoring, for instance, the pollution of drinkable water being a particular source of concern in many areas of the globe.

Also, as can be inferred from this short but not exhaustive list, the trace components considered can come in a variety of forms, ranging from simple atoms, to more complex inorganic molecules, biomolecules such as proteins or DNA, all the way up to living organisms such as bacteria and eucariotic cells.

In the present work we will focus in the analysis of biological and biochemical species, with a particular consideration for biotechnological applications in which these biological entities need to be detected at very low concentrations, as this will be the final objective of all the research presented in this dissertation.

In particular, in this initial introductory chapter, an emphasis will be given to preconcentration methods that, as is the case of the fluidized bed system presented in the following chapters, are crucial steps to reach the limit of detection of common analytical detectors.

1.2 Biomarkers

Biomarkers are biological indicators that can be measured or assessed to confer information about some biological state or condition. They can be cellular, biochemical or molecular in nature and provide diagnostic, prognostic, or treatment-orienting information for patient care (Wagner et al. 2004). Further, to be considered as such, biomarkers need to be quantifiable with sensitivity enough detection system, be relatively easy to collect and provide valuable information for the benefit of the patient (Kohn et al. 2007).

Biomarker-containing samples can be both invasive, such as biopsies, or non invasive, such as body fluids (ex. urine, blood). Although the former ones may provide a more sensitive and specific information, they are limited to cases where such an intervention is necessary for lack of alternatives or part of an already planned surgery, as the procedure is complex and risk for the patient is involved. Body fluids on the other hand can be easily obtainable, making its use even possible for population screening, and in cases such as blood they may confer information of many processes, as they are exposed to different areas of the body. An overview of common clinical biomarkers, as well as their categorization and main sample sources, is illustrated in Fig. 1.1.

Although the term biomarker is usually reserved for biomedical diagnosis more particularly in the case of liquid biopsies, an analogy can be made with the analysis of biological entities in food or environmental samples, where, especially the presence of certain chemical compounds or pathogenic microorganisms is of utmost concern for public safety. Therefore, also in this case a need exists for the routine detection of entities at very low concentrations.

In spite of the high number of identified biomarkers, and the substantial economic investement employed for their development, so far only a limited amount of them are actually in use clinically. After discovery, the successful introduction of new biomarkers

requires proof of their consistent association with the disease of interest, verification of sufficient potential for investment, identification of most promising candidates due to the enormous associated costs, and finally validation with a sufficiently large pool of patients (Frangogiannis 2012). A bottleneck then exists that hinders biomarker development.

Besides the development of biomarkers themselves, there has been considerable investement in the development of devices for biomarker detection. In this respect, point of care devices, defined as medical testing that can be performed on the bedside of the patient, are a choice when enhanced accessiblity and a reduced time for answer are a priority. Two examples of successful applications so far for this kind of devices are pregnancy tets and glucose monitoring biosensors.

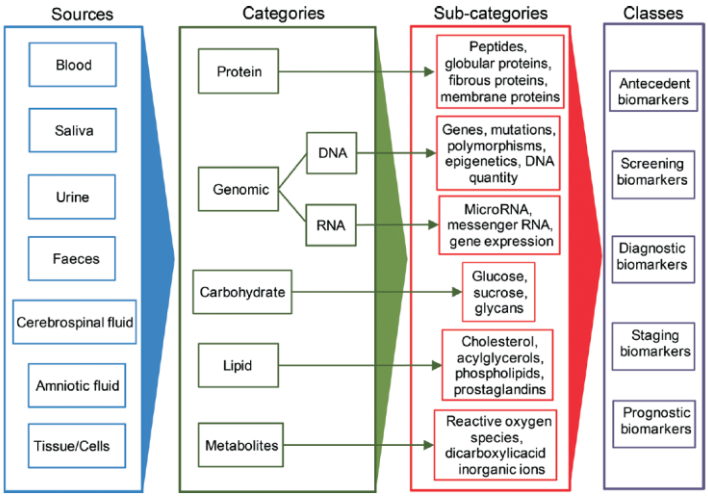

Figure 1.1. Overview of biomarkers (Nahavandi et al. 2014).

Because of the often liquid nature of the analyzed samples, the field of microfluidics, that allows the automation of liquid handling with high accuracy and low volume needs, has experienced an exponential development for this kind of applications (Nahavandi et al. 2014). One of its key features, the multiplexing of analysis, can offer a faster and multiple analysis both of candidate biomarkers in biomarker research and of a complete screening of panels of important biomarkers for patient or food samples. Further, the portability that it can offer should make this kind of analysis possible with point of care devices in low resource environments. A short overview of the field of microfluidics will be presented in the next section.

1.3 Microfluidics

Microfluidics is generally defined as the science and technology of manipulating and controlling fluids in the range of microliters to picoliters, with devices containing chambers and channels in the microscale. Having emerged in the 1990s, microfluidics is today a very multidisciplinary field, at the intersection of micro/nanotechnology, physics, chemistry, biology and material science.

A particularity of microfluidics is that the liquid phenomena that govern the behaviour of liquids at the macroscale is significantly different at the submilimiter length scale. For example, surface tension and capillary forces become more dominant at this scale, while the opposite occurs for gravitational forces. A characteristic difference between these two scales is given by flow regimes, as predicted by the Reynolds number:

$$Re = \frac{vl\rho}{\mu}$$

Where v represents the characteristic velocity, l a characteristic linear dimension, ρ the density of the fluid and μ the dynamic viscosity. High Reynolds numbers are characteristic of macroscopic pipes and channels, where the flow regime is turbulent, presenting chaotic velocity fluctuations. At low Reynolds numbers, typical of microfluidic systems where channel diameters are of the order of micrometers and flow velocities of 1 cm/s or below, viscosity effects predominate. This is associated with laminar regimes presenting an ordered and regular streamline pattern. This is a characteristic of microfluidic systems that on the one hand helps in the simulation and accurate control of fluid behavior, but at the same time complicates certain operations such as fluid mixing, something almost trivial at the macroscale where fluids mix convectively.

Nonetheless, the field of microfluidics has been very creative at adapting microscale phenomena for liquid handling. In this sense, many solutions have been presented for mixing, sorting, pumping and valve control, as illustrated in Fig. 1.2.

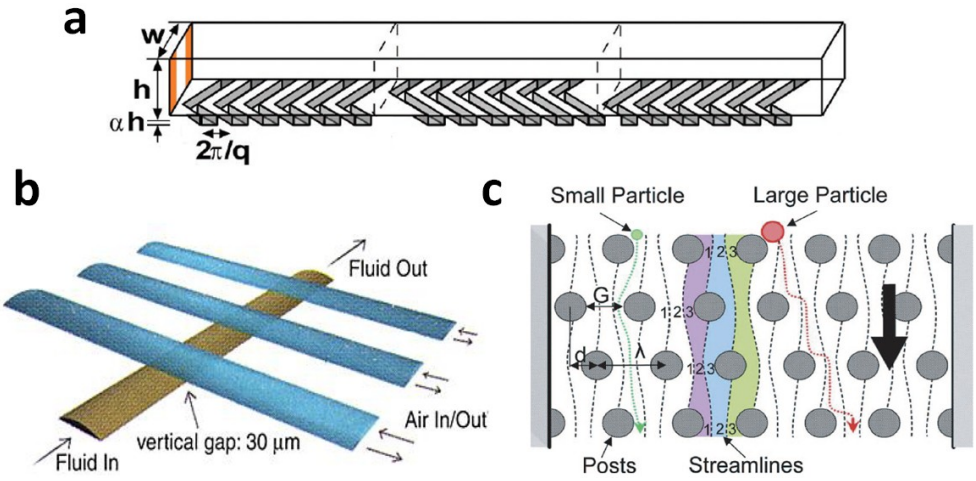

Figure 1.2. Different systems for microfluidic operations : (a) a passive chaotic micromixer based on a herringbone structure (Stroock et al. 2002), (b) micropump constituted of three valves obtained by multilayer soft litography of elastomeric material (Unger et al. 2000) and (c) size separation of particles by deterministic lateral displacement in a array of microposts (Davis et al. 2006).

By making use of these particular properties and modules, and combining them with a wide range of technologies, the field has attempted to address a myriad of problems in innovative ways, with a particular focus in chemical and biological applications. A simple

look at the most recent publications shows the dynamism and potential of this field, with reported applications as varied as cell pairing with droplet microfluidics (Hu et al. 2015), fabrication of collagen microparticles for 3D culture environments (Yamada et al. 2015) or the rapid detection of cell-free DNA in blood by integrated electrophoretic methods (Yang et al. 2015).

Of particular importance has been the constant adaptation of well known macroscale techniques into microfluidic chips. The interest of doing this often lies in the reduced volumes handled and the increased precision and reproducibility of operations with enhanced automation and integration. A further advantage is the possibility of coupling these integrated systems among themselves, either in series for the integration of protocols, or in parallel for multiplexing. These multi-function systems are commonly termed lab-on-a-chip (LOC). A particularly active area of microfluidic development has been the integration of preconcentration methods usually needed for the detection of rare species. This is sometimes a simple adaptation of a same mechanisms into a smaller scale, but more often than not this integration leads to new possibilities only available at the microscale, if not to altogether new preconcentration technologies.

1.4 Preconcentration methods based on microfluidics

The ability to increase the concentration of the analyte in a given sample volume offers the potentiality of lowering the limit of detection of biosensing techniques. It is therefore a key step for rare marker diagnosis, that must come hand in hand with the development of techniques for increased detector sensitivity.

These preconcentration steps can be done off-chif before sample analysis, but in this case contamination and loss of sample volume are common problems, besides these being often labor and time consuming procedures. This is especially true if the volumes handled are low. Microfluidics offers the advantage of integrating all necessary steps for preconcentration in a same module that can be directly coupled to the analysis or detection method, the manipulation of small volumes being particulary adapted.

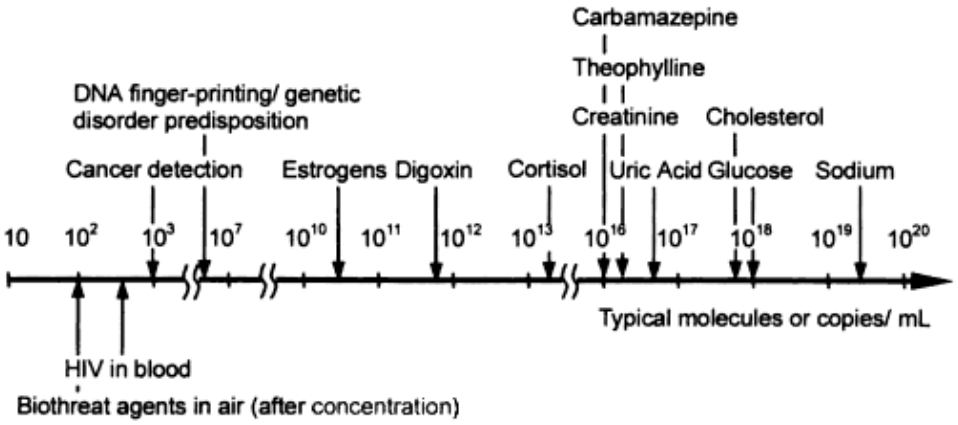

Figure 1.3. Presence of different molecules and ions in blood (Nguyen & Wereley 2002).

Besides the simple preconcentration of the desired species, an extraction of this one from a more complex matrix is usually desired to facilitate or even make possible the detection/analysis step. This is often a critical and complicating issue for biological samples, in which the sample matrix is often composed of a complex mix of species that can interfere with preconcentration by various mechanisms, such as non-specific adsorption on surfaces, clogging of extraction monoliths or channels, or reduction of binding capacity (Rogacs et al. 2014). This is further complicated by the rarity of the target. For example, the search for a protein biomarker must deal with the fact that more than 10000 proteins species are present in serum samples. Also, while most biomarker proteins are generally present at very low concentrations (<pg/mL), others such as albumin and immunoglobulins are present in very large amounts (>mg/mL, Fig. 2.3). As another example, for every circulating tumor cell originating in a primary tumor from the blood sample of a cancer patient, a few million white blood cells and a billion red blood cells are present. Low enough detection sensitivity and large enough dynamic range are thus needed for better sample preparation and sorting (Autebert et al. 2012).

Of fundamental importance is the fact that these preconcentration steps must take into account their compatibility with the downstream analysis/detection methods. For instance, the lysis of cells is often a fundamental step for DNA extraction and preconcentration, but the debris from this lysis can potentially interfere with the bioenzymatic reactions needed for downstream DNA amplification methods such as polymerase chain reaction (PCR) (Tichopad et al. 2004).

Finally, although useful for all kinds of rare biomarkers, preconcentration steps are of particular importance for the detection of proteins in low abundance as, in contrast to DNA amplificaton methods or culture methods for living cells, no equivalent exists for the amplification of a protein of interest.

Preconcentration techniques have been reported making use of a range of available mechanisms. For the sake of simplicity, in the following sections these techniques will be divided into electrokinetic and non-electrokinetic methods, the latter further divided into two groups: preconcentration methods based on the use of nanopores or membranes, and methods that make use of affinity-based separations with a solid phase. Although the most common techniques will be covered by this classification, its is by no means an exhaustive review and inevitably some reported alternative preconcentration methods (e.g. acoustic waves (Ravula et al. 2008) or on-chip evaporation (Walker & Beebe 2002)) will be left out.

1.5 Electrokinetic preconcentration

The microfluidic integration of electrokinetic techniques presents, in general, the advantage of not necessitating an external flow control as the preconcentration process is obtained through a generated electric field between two electrodes. For this reason, and because it was mostly based on well developed technologies, demonstrating the

integration of known macroscopic electrokinetic methods into microfluidic devices was particularly fruitful in the first years of microfluidic development. Electrokinetic techniques concentrate samples by bringing the transport of species to a local electrokinetic equilibrium state. Among all available techniques, isoelectric focusing, field amplified sample stacking and isotachophoresis are the most common for microfluidic integration, and hence they will be briefly explained and discussed next.

1.5.1 Isoelectric focusing (IEF)

Isoelectric focusing is an electrokinetic method that separates molecules as a function of their different isoelectric point (pI). Briefly, a channel is filled with a mixture of ampholytes and the analyte of interest, with one channel end immersed in acidic buffer and the other one in basic buffer. When an electric field is applied between the two ends, a gradient of pH is formed. Molecules present in a region of pH below their isoelectric point will be positively charged and hence attracted towards the cathode. This leads to a migration that results in progressively lower charge because of the linear increase in pH and a complete stop once the region reached contains a pH corresponding to the isoelectric point of the molecule (Fig. 1.4). The reverse is true for negatively charged molecules present in a too high pH region. Narrow zones of concentrated molecules according to their pI are then formed. IEF is usually used for the separation and preconcentration of proteins and peptides.

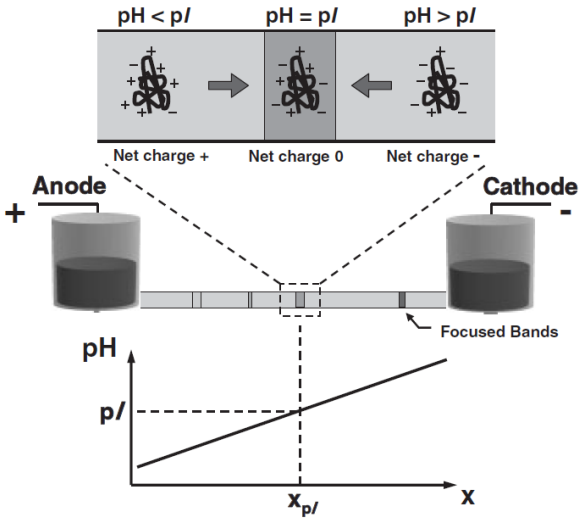

Figure 1.4. Schematic of IEF. A gradient of pH leads to the separation of molecules in narrow bands according to their isoelectric point (Sommer & Hatch 2009).

IEF was one of the first analytical techniques adapted for the microscale (Hofmann et al. 1999). Besides the aforementioned advantage of coupling with other modules in a single microfluidic device, the integration of IEF on chip allows faster assays speeds with reduced sample volumes without loss of resolution (Sommer & Hatch 2009).

One of the challenges of coupling this technique with other downstream analytical methods is the efficient separation of the obtained bands, as pressure-driven or

electroosmotic flow usually lead to dispersion and remixing. Some solutions to this problem have been reported in the litterature. (Zhao et al. 2014) showed the use of simple device containing a zig-zag channel formed by a sequence of wells distributed in the two halfs of a Slipchip (Fig. 1.5). After IEF separation sinde the channel, the wells are disconnected by chip slipping, leaving the analyte isolated in discrete compartments. These resulting droplets can then be pipetted for off-chip analysis or further mixed with the solution contained in other wells integrated in the same chip for in situ processing. Although small bands are difficult to separate with this method, a clear advantage is gained in terms of simplicity of operation and cost.

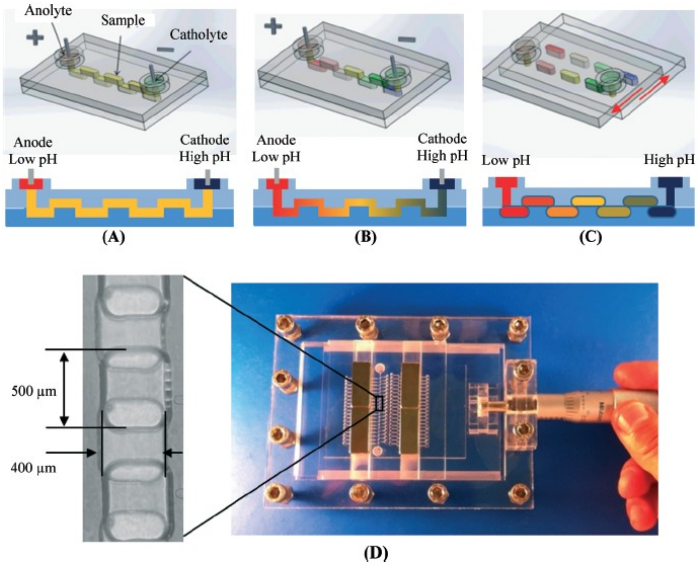

Figure 1.5. (a-c) Schematics of IEF separation and compartmentalisation using a zig-zag channels composed of wells that can be laterally slipped. (d) View of the PMMA chip (Zhao et al. 2014).

Coupling IEF separation to size separation is particularly interesting for proteomic analysis, as a simple separation based on pI is usually not enough to discriminate the very rich mixtures of proteins often studied. With this idea, chips have been reported based on the working principle of two-dimensional gel electrophoresis, commonly containing a channel for a first IEF separation, and a series of perpendicular channels for mass separation (based on electrophoretic migration) of the IEF-obtained bands (Das et al. 2007)(Lu et al. 2012). This allows a very accurate identification of species, but at the same time results in more complex protocols and an increase in fabrication costs.

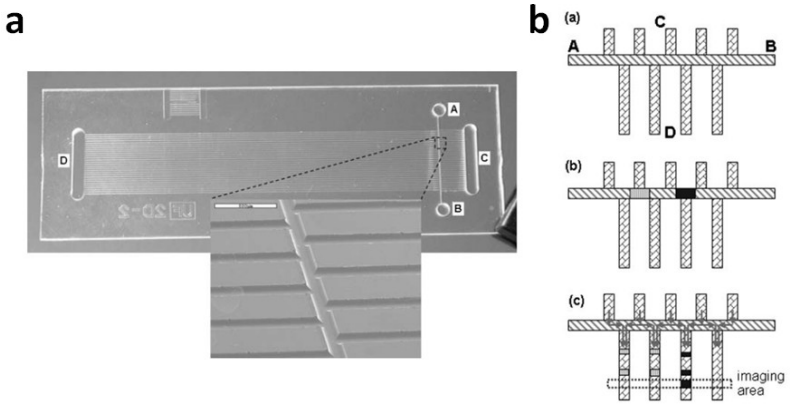

Figure 2.6. (a) Plastic chip for 2D protein separation, with AB being the channel for IEF separation and CD for polyacrylamide gel electrophoresis (PAGE). (b) Procedure: the sample is first separated in the AB channel by an pH gradient and the resulting bands are made migrate in the CD channels for size separation. The arrows indicate flow direction. Adapted from (Das et al. 2007).

Because of all the mention advantages IEF is a commonly used technique for microfluidic integration. It presents nontheless several disadvantages, in particular: (i) detection is usually done by a fluorescent tagging of sample proteins prior to their loading into the chip, meaning inconventient preparatory steps and possible shifts of the pI of molecules and (2) molecules with an accessible pI are needed, restricing the range of use of this technique to amphoteric compounds such as proteins (and even in this case many similar proteins share a same pI and cannot be resoluted).

1.5.2 Field-amplified sample stacking (FASS)

FASS is a relatively simple technique that makes use of a discontinous gradient in electrolyte conductivity to subject the ions of the sample to non-uniform local electric fields. More specifically, a sample containing the ionic species of interest is inserted between two regions with a higher conductivity (Fig. 1.7). When a voltage is applied between the two ends of the channel, the local electric field is highest in the low-conductivity sample region and lower in the high-conductivity buffer, in accordance with Ohm's law. As sample ions exit the high field region and enter the low velocity region, they undergo a sudden drop in electrophoretic velocity and hence locally accumulate in the interface and increase in concentration (stacking). The advantage of using microfluidics is that the resulting concentrated plug can then be transferred by fluid movement for further manipulation or detection.

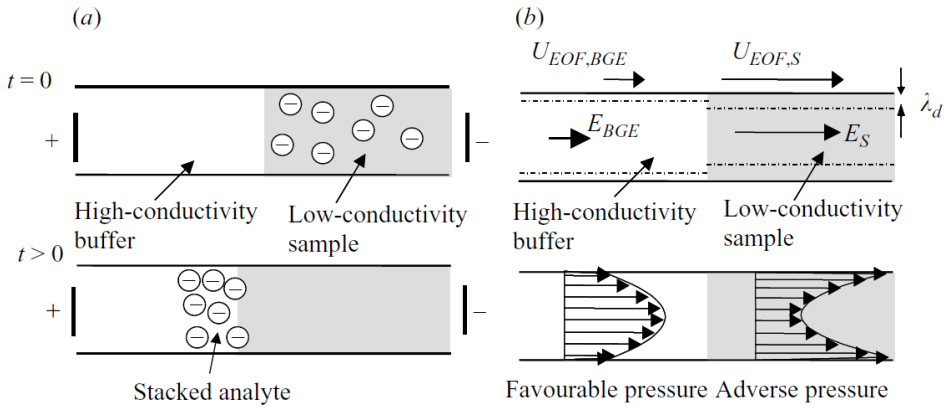

Figure 1.7. (a) Scheme showing FASS of ionic species in the idealised of a total absence of flow and (b) the more realistic case where the electric field resuls in an additional EOF generating a pressure gradient and lowering the efficiency of stacking. Adapted from (Bharadwaj & Santiago 2005)

Although a simple technique, it must be taken into account that the gradient in electrolyte concentration needed for stacking also results in an electroosmotic flow (EOF) that tends to disperse the concentration fields and lower the efficiency of the process, making it difficult to control the exact location of the stacked material. Also, to prevent the generation of back-pressure due to a mismatch of electroosmotic flows in different regions, the length and hence the volume of the injected sample is limited. Surface coatings are usually needed to limit EOF. In this sense, many surface treatments applied to microfluidic devices have been adapted from the vast litterature reported for the field of capillary electrophoresis (CE).

One of the challenges of integrating FASS in on-chip assays is creating the initial required boundaries of sample and buffer regions. (Jung et al. 2003) proposed a chip design containing a photoinitiated porous polymer structure that provides a high flow resistance in order to allow the pressure-injection of reagents but allows the internal electromigration of sample ions. The loading steps are described in Fig. 1.8.

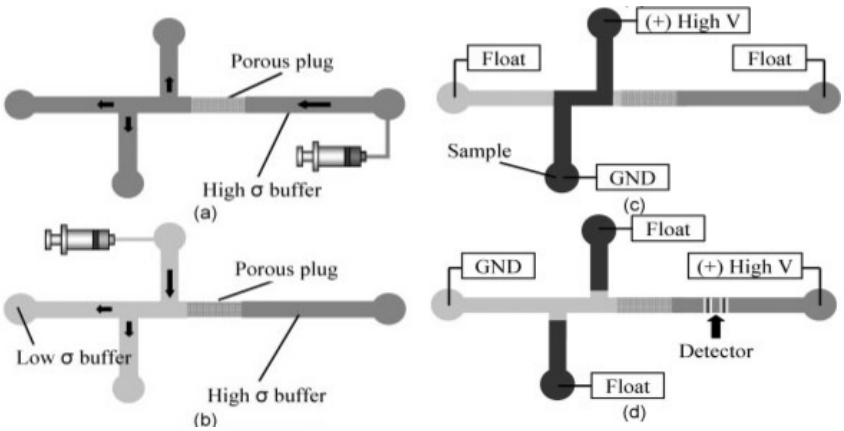

Figure 1.8. Loading steps of the porous plug FASS chip design: (a) high conductivity buffer is injected into all channels, (b) low conductivity buffer is introduced from the opposite inlet, the plug minimizing the mixing of the two buffers, (c) sample injection into the double-T and (d) stacking and detection of samples (Jung et al. 2003).

In more recent works, FASS separation processes are usually reported as complementary preconcentration step to enhance the limit of detection of integrated lab-on-chip assays. For example, (Giri & Dutta 2014) showed the increased sensitivity (60-fold smaller concentrations) of enzyme-linked immunosorbent assays (ELISA) performed on-chip when the enzyme reaction product obtained from the assay was preconcentrated before fluorescence measurement. In another example, (Shiddiky & Shim 2007) reported the integration of FASS and FASI (field-amplified sample injection) in the microfluidic channels of the chip as a first preconcentration step of double-stranded DNA (dsDNA) before sample separation by microchip gel electrophoresis and electrochemical detection. The authors report a ~5200-fold increase in preconcentration factors obtained with this system as compared with capillary electrophoresis analysis.

As seen, FASS is typically used as a preconcentration step before the electrophoretic separation of analyte ions. However, besides the difficult setup of sample and reagents and the limited volume of analysis, one disadvantage of this technique is the difficulty in its applicability to physiological samples containing a high concentration of salts, requiring complex sample preparation protocols before analysis (Zhu et al. 2001).

1.5.3 Isotachophoresis (ITP)

Isotachophoresis is a preconcentration and separation technique in which analytes are focused between a leading electrode (LE) of high effective ionic mobility and a terminating electrode (TE) of low effective ionic mobility. When an electric field is applied between the electrodes, analytes in the sample are arranged at the interface of the electrodes, and the electric field self-adjusts to maintain a constant velocity for all zones (electrodes and sample).

The ITP interface is self sharpening, meaning that if ions of the LE enter the TE zone, they will experience a restoring flux and will be returned to the leading zone, and vice versa. This makes the technique robust and insensitive to interferences such as pressure driven flows.

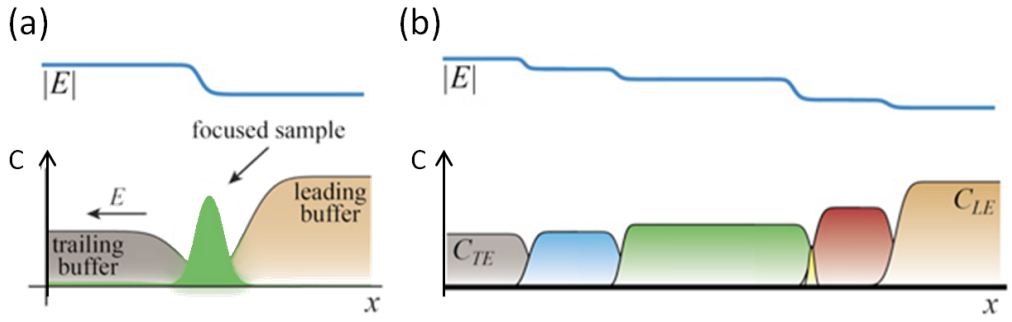

Figure 1.9. Principle of isotachophoresis, (a) the sample is focused in a peak when its concentration is not high enough to influence the local electric field, while (b) bands of different ion mobility form for higher concentrations, adapted from (Garcia-Schwarz et al. 2012).

Isotachophoresis exists in two modes. In “peak mode”, the concentration of sample ions is always significantly lower than the ion concentration in LE or TE. In this case, multiple sample ions stack together between both electrodes in essentially overlapping peaks. In “plateau mode” the concentration of the sample ions is sufficiently high to influence the local electric field and in this case the different ions arrange in discrete bands in order of mobility (Fig. 1.9).

Besides simple ionic molecules, isotachophoresis has been succesfully integrated on chip for the preconcentration of both DNA (Xu et al. 2009) and proteins (Cui et al. 2007). An example of microfluidics integration for increasing the sensitivity of signal obtained from DNA spots is presented in Fig. 1.10, where the focusing of DNA by ITP is then use to enhance the hybridization of DNA in downstream microarrays. The obtained narrow band of DNA in a 100 µm wide ITP zone, and its transport over the immobilized probes, speeds up the surface binding reaction, enabligh 30 fold shorter assay times, and increases the sensitivity by one order of magnitude (Han et al. 2014).

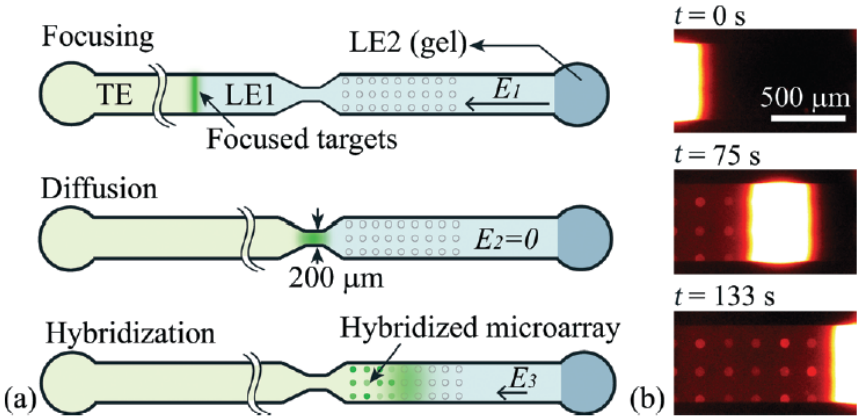

Figure 1.10. (a) illustration of ITP focusing, diffusion and hybridization of target ssDNA and (b) experimental demonstration of ITP microarray with fluorescently labeled ssDNA (Han et al. 2014).

All the electrokinetic techniques so far described present several important advantages such as short operation times and no need of fluid pumping or solid phase. Preconcentration factors in the order of 200-500 have been reported for ITP and 5.10^3-2.10^4 for FASS or other FASS-based techniques integrated in microfluidic devices (Lin et al. 2011). However, an efficient selectivity of the separation process requires an accurate control and understanding of the charge, pI and mobility and the target molecules. Other shortcomings of these techniques have already been mentioned, such as a need for a very accurate control of salt content or pH, difficult to obtain with biological samples and requiring an off-line sample pretreatment. Further, sample injection is usually laborious, the surface treatment of channels is usually indispensable and highly affects results, and the coupling with detection methods can be complicated without loss of concentration (due to sample mixing when a flow is applied). Also, in most cases these techniques cannot be employed with larger entities (ex. cells), although alternatives exist such as dielectrophoresis, that will not be discussed in this work.

In the following sections, techniques based on the use of a solid phase for either the mechanical trapping of the species of interest, or their capture by a specific or non-specific recognition, will be discussed.

1.6 Membrane concentration

Nowadays, membranes are used for a wide variety of applications in industry, including but not limited to waste water treatment, pervaporation, fuell cells and biomedical applications such as dialysis. Membranes are semi-permeable barriers, in which the transport of the species through the membrane can take place through the material, in which case single molecules permeate thanks to the solubility and diffusitity of the component, or through pores, in which case the morphology of the membrane (porosity, tortuosity and pore size distribution) governs transport and separation. Depending on the application, either the passing material (permeate) or the retained solution (retentate) can be the desired product (de Jong et al. 2006). The incorporation of membranes into microfluidic devices has been performed in the litterature by several means, which include the direct use of external often commercial membranes (Xiang et al. 1999), the preparation of the membranes as a part of the microfabrication of the chip (Metz et al. 2003), or the in situ preparation inside the closed device (Suzuki et al. 2006).

We will focus here in the case of porous membranes, in which case the separation can either be due to a simple size-filtering of the analytes, or to electrostatic effects.

Size filtering is a very straight-forward method, particularly useful as a sorting technique for microparticles of different size ranges by steric exclusion. As an example, Wei et al. 2011 fabricated PDMS porous membranes by simple molding of photoresist posts. The use of a series of membranes allows the capture of particles of different diameters, that can then be recovered with a side flow regulated by chip-integrated valves (Fig. 1.11a). The authors further demonstrate the possibility of controlling the pore size with the alignment of two overlapped membranes that can be sliped sideways (Fig. 1.11b). While the main application shown in this work was the separation of white and red blood cells, similar membrane-based devices have been shown effective for the preconcentration of more rare events, such as circulating tumor cells (CTC) (Fan et al. 2015).

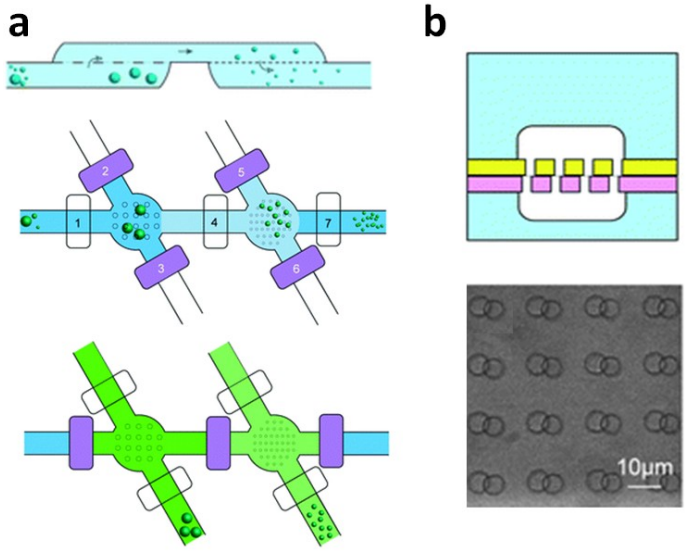

Fig. 1.11. (a) Double filtration of particles with porous membranes for particle sorting: clogging is avoided by frequent flushing and collection of filtered material. (b) An on-demand pore size can be obtained with overlapped PDMS membranes. Adapted from (Wei et al. 2011).

Although filtration by steric exclusion is relatively straightforward and the fabrication of membranes can be obtained with simple approaches, the concentration of molecules with this approach necessitates the use of nanofilters that can greatly reduce analysis throughput. Some solutions have nonetheless been proposed, such as a high speed nanofluidic protein accumulator reported by Wu & Steckl 2009. In this work, a commercial 10 nm polycarbonate membrane filter of high mechanical strength was sandwiched between two PDMS parts containing straight channels. With the use of an electrokinetic fluid flow, proteins (fluorescent human serum albumine) accumulated locally in the channel cross point with preconcentration factors of 1000 times within 200 s.

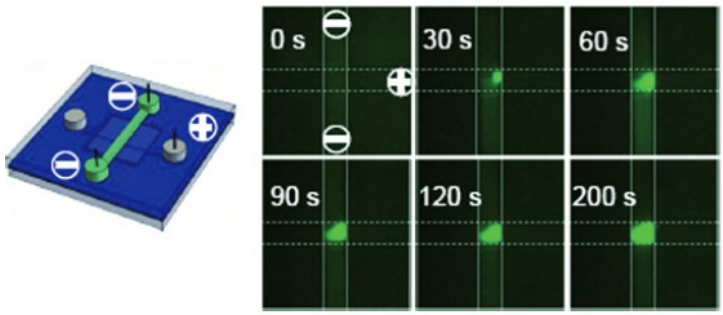

Fig. 1.12. Protein accumulation as a function of time in the crossing point of two straight channels of a PDMS chip where a nanopore membrane filter is positioned (Wu & Steckl 2009).

An alternative to these size exclusion methods is the filtration by exclusion-enrichment effects. In this case, the thickness of the electric double layer (EDL) is of the same order of magnitude as the pore diameter, leading to EDL overlap in the whole section of the pore. The result is that co-ions (having the same charge sign as the surface) are excluded from the pores, while counter-ions, are enriched to ensure overall electrical neutrality (Lin

et al. 2011). With the application of an electric field between both sides of the membrane, an ion depleted region is created on the anodic side while an ion enrichment region is created on the cathodic side. A very simplified but illustrative scheme of this phenomenon was reported by Pu et al. 2004 in the case of a negatively charged surface (Fig. 1.13). Very briefly, if the total current for a given section in the channel is carried by two cations and two anions, travelling to their respective electrodes (sectionx X1 and X2), because of the limited mobility of the anions in the nanogap, only one anion will contribute to the current in the pore, as compared to three cations (this ratio is naturally just an example, sections Y1 and Y2). On the anodic side the net change is a loss of one anion and one cation, thus leading to enrichment, while a net gain is experienced on the cathodic side. The situation is reversed if the surface charges are positive.

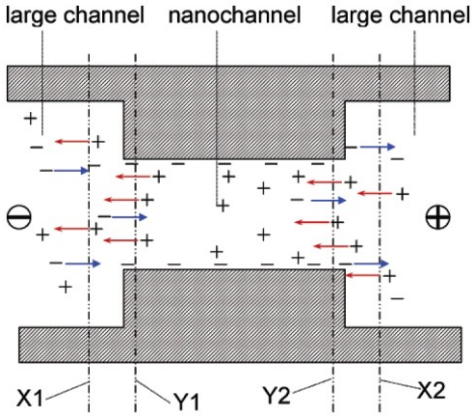

Figure 1.13. Schematic illustration of the exclusion-enrichment effect (Pu et al. 2004).

Most membranes reported for this kind of separation are made of nafion polymeric material, presenting ionomeric properties i.e. the polymer comprises repeat units of both electrically neutral and a low fraction of ionized units. In this way, and in a similar manner to the example shown before, Lee et al. 2008 assembled a nafion film between a glass substrate and a PDMS top for protein preconcentration (b-Phycoerythrin), obtaining factors of ~10^4 in operation times of 5 min.

Beyond porous membranes, the exclusion-enrichment effect can be used for other kinds of structures, such as nanochannels and nanogaps. Yu et al. 2008 reported the concentration of protein in nanofissures formed by the electric breakdown of the gap between two v-shaped channels (Fig. 1.14). In this way, besides a very low cost and simple fabrication (laser printing, voltage supply) preconcentration factors in the range of 10^3-10^5 could be achieved in 10 min.

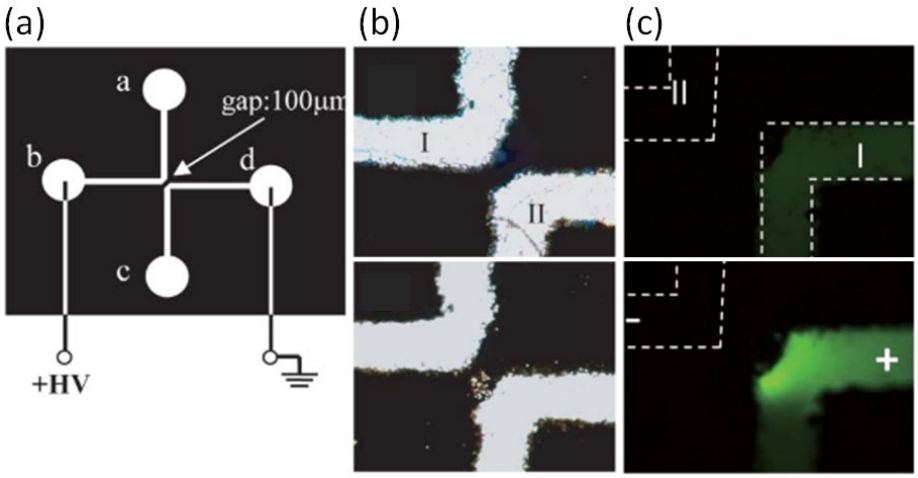

Figure 1.14. Protein concentrator by nanofissure: (a) design of printed chip, showing gap width between the two channels, (b) an image before and after nanofissure generation and (c) fluorescein concentration before and 1.5 min after voltage breakdown (Yu et al. 2008).

1.7 Affinity based concentration

An affinity-based concentration is a form of solid-phase extraction obtained by the specific or non-specific surface binding of the analyte of interest with either the walls of a microfluidic chamber, a monolith or the surface of beads. This binding can be both specific, such as those obtained with antibodes, lectins or aptamers, or non-specific, for example with hydrophobic or electrostatic interactions. Antibody-antigen interactions is a common choice for affinity extraction, with antibodies immobilized on the solid surface. In this case, in a typical preconcentration protocol the specific ligate is bound to the antibody during sample incubation, while the mobile phase is removed, thus separating the compound from the sample matrix. After a rinsing step, the bound analyte is finally eluted by either changing the pH or the ionic strength of the mobile phase.

Since the bounding occurs on surfaces, the essential difference between the following methods is their geometry and possible dynamic mixing for capture enhancing. Due to the nature of the project presented in this work, a more detailed review will be given to preconcentration methods based on magnetic beads.

1.7.1 Structured microchannel

Generating a stationary phase for the interaction of the analyte with the solid support means that the surface to volume ratio must be maximized for increased captured efficiency. One straightforward idea for this is the etching of pillar-shaped structures, or other pattern geometries, in a microfluidic chamber.

In this case, polymer embossing of microfabricated masters presents the advantage of reducing costs, allowing mass production and increasing the possibilities of its surface chemistry. As an example application, Witek et al. 2006 developed a microfluidic chip

with pillars obtained by the hot embossing of polycarbonate with a metal mold master (Fig. 1.15a). Prior to chip bonding the posts were exposed to UV radiation to induce a photo-oxidation reaction that creates surface-confined caboxylates. The result is an affinity bed that was used for the isolation of nucleic acids from bacterial (*Escherichia coli*) genomic DNA.

The surface to volume ratio of this kind of structures can be further optimized with the nanostructuring of the polymeric surface. An example is shown in Fig. 1.15b, where (Tsougeni et al. 2015) plasma treated a poly(methil methacrylate) (PMMA) array of pillars for enhanced surface rugosity, and demonstrated capture efficiencies in the range of 50-100% (depending on the initial concentration) of injected *Salmonella* cells by precoating the chip with specific antibodies.

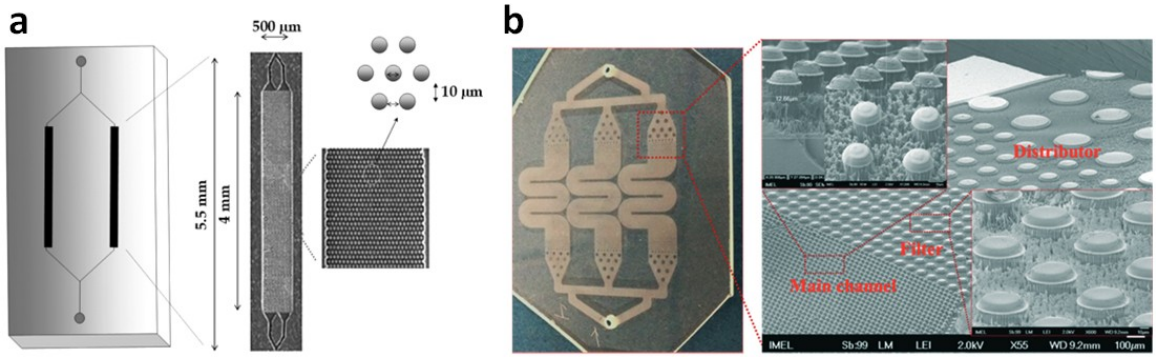

Fig. 1.15. (a) Schematic diagram of the polycarbonate chip used for DNA isolation with a pillar array with a high magnification view of the microposts (Witek et al. 2006) and (b) plasma nanotextured PMMA array for bacteria capture (Tsougeni et al. 2015).

Although the direct microstructuring of the microfluidic chamber presents the advantage of a highly controlled surface disposition, this is compensated at least for certain applications by disadvantages such limited surface area, relatively high fabrication costs, limited flow rate, especially for the efficient capture of smaller particles, and difficult grafting of specific ligands. The applicability of this technique has therefore remained relatively constrained.

1.7.2 Porous polymer monoliths

Monoliths are static structures presenting a very high surface to volume ratio for increased loading capacity, usually employed for chromatography separations. Most microfluidic monoliths are fabricated from polymeric materials by a very simple procedure, in which polymerization is photo-initiated inside a closed channel by exposing a mixture of monomers (cross-linker and initiator) and porogenic solvent to heat or UV light. The irradiation with UV light further presents the advantage of precisely controlling the size and location of the monolith by using a photolitography mask. After polymerisation, a solvent is flown into the microchannel to rinse the monolith. By varying the mixture composition and polymerisation conditions, properties such as pore size, surface charge and hydrophobicity can be accurately controlled. The result is a continuous unitary porous structure, as shown in Fig. 1.16.

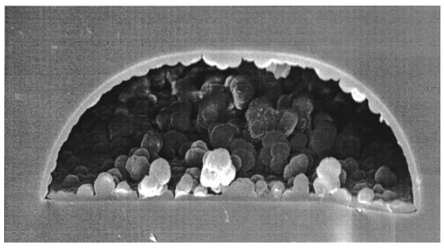

Figure 1.16. SEM image of a typical cross section of a microfluidic polymer monolith (adapted from (Yu et al. 2001))

For enhanced resistance to high pressures (needed due to the high resistance inherent to this kind of system), monoliths are covalently attached to the wall of the channels to avoid displacement and formation of voids. For this purpose, pretreatments with TMSPM (3-(trimethoxyslyl)propyl methacrylate) in glass chips and UV-initiated photo-grafting mediated by benzophene in polymeric chips are commonly used options (Vázquez & Paull 2010). The resulting high mechanical strength and relatively low flow resistance with appropriate porosity, mean that relatively high flow rates can be used.

Porous polymer monoliths have been used for the separation of species by ion exchange (Yu et al. 2001) or affinity chromatography (Kang et al. 2013). Although electrochromatography (Karenga & El Rassi 2010) has been the prefered method for microfluidic integration, micro-liquid chromatography (μLC) has been gaining popularity due to microfabrication improvements of chips for sustaining high back pressures (Vázquez & Paull 2010). With these porous polymer monoliths, enrichment factors of proteins of up to 1000 have been obtained (Yu et al. 2001), the main disadvantage of these systems being the high back pressures needed to attain significant flow rates, limited by the mechanical stability of the device. Monolith variation may also lead to difficulties in the reproducibility of operation (Kim & Herr 2013).

1.7.3 Packed beads

An alternative to these static monoliths can be found in the form of bead ensembles packed together, usually referred to as packed beds. This method presents the advantage of allowing the use of beads that are commercially available and which present well characterized properties, with surfaces that are often easily modifiable. Typically employed bead materials are silica and glass.

However, to obtain a packed bed of beads it is necessary to immobilize the solid phase, in order to obtain the desired porosity and avoid its flushing away with the mobile phase. As illustrated in Fig. 1.16, for this purpose several strategies have been shown so far in the litterature, such as the creation of frits (Thurmann et al. 2014), arrays of pillars fabricated in the chip (Andersson et al. 2000), dam structures (Sato et al. 2000) or by simple bead aggregation by geometry confinement (Ceriotti et al. 2002).

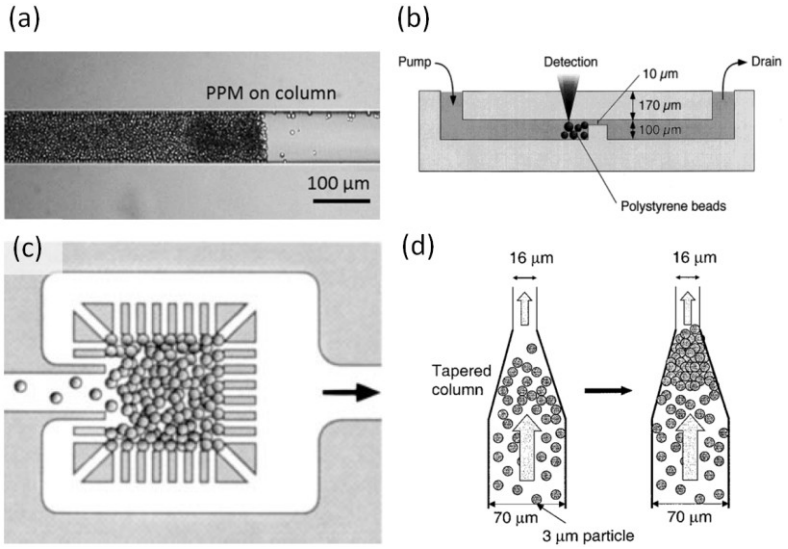

Figure 1.16. Examples of confinement strategies for packed beads: (a) frit obtained by laser photopolymerisation of a pre-polymeric solution of butyl acrylates (adapted from (Andersson et al. 2000)); (b) dam structure in a glass chip for trapping of polystyrene beads (adapted from (Sato et al. 2000)); (c) pillar structure defining a square reaction area and (d) fritless confinement by aggregation in a tapered column (adapted from (Ceriotti et al. 2002)).

An interesting recent development in this field is the possibility of controlling the packing of the beads during operation for enhanced flexibility, going beyond a simple stationary solid phase. In this sense, Hwang et al. 2012 have shown the extraction of bacterial DNA by packing 30-50 µm glass beads with a flexible PDMS membrane (Fig. 1.17). By pneumatically controlling the membrane shape, the surface to volume ratio could be altered to obtain either close or loose packed beds for different protocol steps. This allowed an enhanced capture efficiency by packing maximization (95% non-specific cell capture from swab samples at 200 µL/min, requiring 50 kPa of sample injection backpressure and 150 kPa of upward membrane pressure) and an improved DNA elution and recovery by the asynchronous vibration of the membrane and resulting mixing of the beads. Preconcentration factors of ~100 fold were obtained by concentrating the sample in 10 µL of eluate from 1 mL initial sample volumes.

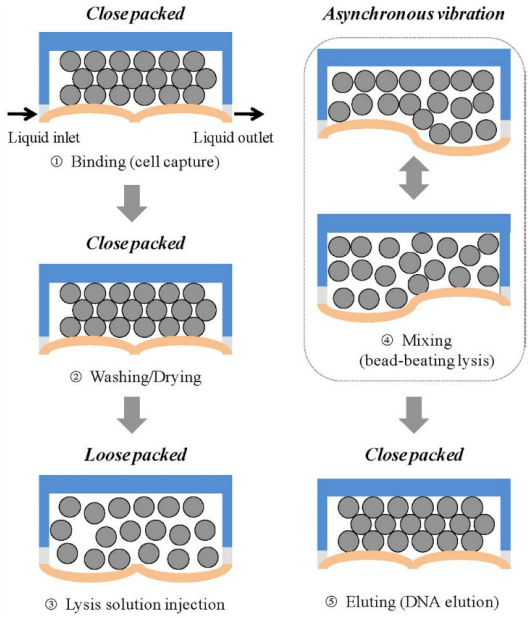

Figure 1.17. Extraction of DNA with preconcentration and elution steps enhanced by the use of a flexible PDMS membrane (yellow), that allows the rearrangement of beads in either a close or a loose pack, as well as mixing by vibration (adapted from (Hwang et al. 2012).

Although flexible in size and surface chemistry, the main disadvantage of the use of beads for bed preconcentration is still the need for particle retention strategies, as previously seen, increasing fabrication costs and complexity, as well as a laborious introduction of the beads into these retaining structures that can lead to anisotropic distributions. These problems are further increased when the diameter of the beads is reduced, limiting the obtained surface to volume ratios of these packed bed structures.

1.7.4 Magnetic bead-based concentrators

In comparison with the previous non-magnetic beads strategies, the use of magnetic beads presents the advantage of an easier distance manipulation (by a magnetic field gradient), while the advantage of being able to have access to a broad gallery of commercial products and surface chemistries is still available.

The structure of magnetic beads can be very varied, from a simple core of magnetic material, to a distribution of iron oxide particles in a polymer matrix, to a polymer sphere coated with the magnetic oxide. A commonly employed iron oxide is Fe_3O_4. In all cases, and as will be seen more in detail in the next chapter, the magnetic force acting on a magnetic moment **m** is written as (Boyer 1988):

$$\boldsymbol{F} = (\boldsymbol{m} \cdot \nabla)\boldsymbol{B}$$

Where **B** is the applied magnetic field. A force is then exerted on the bead as long as a magnetic field gradient is present, and is proportinal to this gradient. This allows the control of beads with an external permanent or electromagnet, as typically done for buffer exchange steps by pipetting handling. Furthermore, in the presence of a magnetic field,

superparamagnetic particles form chains and clusters due to the magnetic dipole interaction between the magnetic moments induced in the particles. This property is employed by some preconcentration methods, as it will be shown later.

The generation of magnetic fields for particle control can be obtained both with permanent magnets, that retain their magnetic properties after the removal of an external magnetising field (with materials such as iron, nickel or cobalt and especially rare earth metal alloys such as neodymium iron boron, NdFeB), or with electromagnetic fields generated around wires carrying a current. Both external and integrated magnets have been used depending on the application, the former presenting the advantage of lower fabrication costs and the latter allowing a closer proximity of the magnet to the microchannel and a more confined spatial control (Pamme 2006).

Integrated micro-electromagnets present the freedom of being able to play with the intensity of the magnetic field by adjusting the intesity of the injected electric current. In this way, turning the magnetic field on and off becomes possible, facilitating reagent separation steps. Furthermore, by optimizing microcoil design (Fig1.18) it is possible to obtain accurate magnetic field distributions (usually in the order of microteslas) in order to generate high magnetic field gradients (maximizing magnetic bead trapping) that would otherwise not be accessible with external magnets (Ramadan et al. 2004). Nonetheless, this kind of system requires the deposition of metal microlayers and lithography patterning, highly increasing device cost, and the intensity of the generated magnetic field is limited by the Joule heating resulting from injected currents.

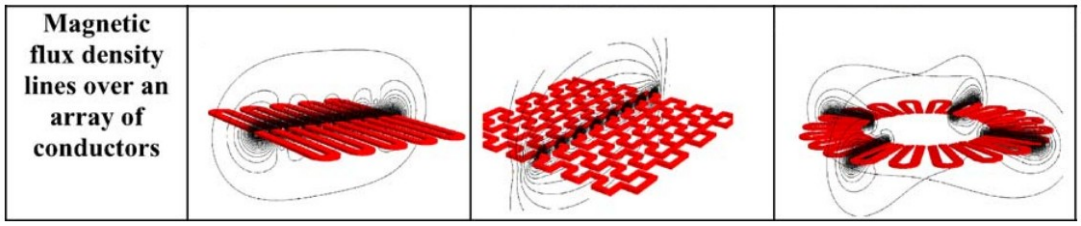

Figure 1.18. Magnetic flux density lines for micro-electromegnets of complex geometries (section 10x2 μm) (Ramadan et al. 2004).

An illustrative example is the work of Lien et al. 2007 (Fig. 1.19) where microcoil separators were integrated in the bottom of the chip chamber. After a first mixing of antibody-conjugated beads (Dynabeads) and target viruses inside a peristaltic rotary mixer, current was made pass through the coils for bead trapping, allowing a washing step with no bead loss. After enough rinsing, the magnetic field was switched back off, and magnetic beads pumped away for further detection steps.

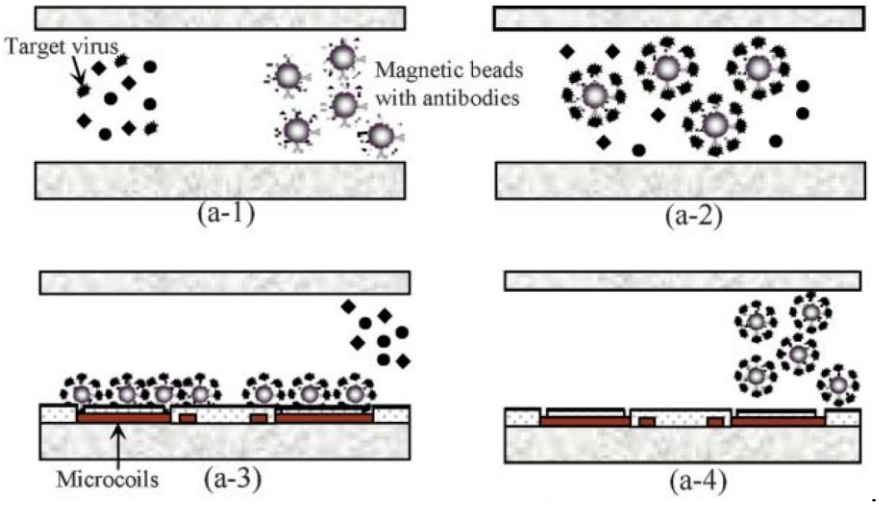

Figure 1.19. Operation principle of virus specific capturing and sample washing through integrated microcoils (Lien et al. 2007).

On the other hand, magnetic fields generated by permanent magnets can only be controlled by their geometrical displacement, but, in contrast to electromagnets, they are completely autonomous, requiring no power source and leading to no Joule heating. They have both been down-scaled and integrated in the microfluidic system, or used as external sources of magnetic fields. This is the case of the work of Hoshino et al. 2011 (Fig. 1.20) in which a chip containing a single large and thin chamber was placed above arrayed magnets for the separation of cancer cells from blood. The arrayed magnets with alternate polarities led to sharp magnetic field gradients, very effective at capturing the cancer cells labelled by magnetic nanoparticles. As the magnet is not attached to the chip, the bottom of the chip constituted by a glass cover slip can be used for direct visual detection after sample concentration.

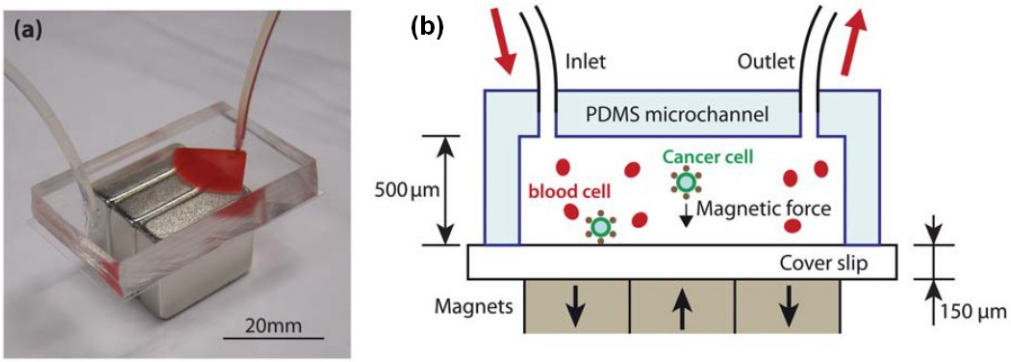

Figure 1.20. Cancer cell capture by an array of external permanent magnets (a) view of the chip during blood injection and (b) schematic showing the principle of operation (Hoshino et al. 2011).

Althouh convenient for the advantages just mentioned, obtaining high and localized magnetic gradients in a microfluidic device is difficult with external permanent magnets. A solution for this problem is found in the form of ferromagnetic lines and dots that can be included in the fabrication of the microfluidic device. When combinations of these elements are placed in the presence of magnetic fields, their induced magnetization results in the generation of local flux-density maxima. Further, the direction of

magnetization can be set with the position of the external magnet, enabling precise magnetic field distributions that can be modified during experimental time (Fig. 1.21a). By using magnetically soft materials the magnetic field can be turned off when the permanent magnet is removed, allowing particle release (Deng et al. 2002). Hard materials on the other hand retain their magnetization after the removal of the external magnetic field. (Dempsey et al. 2014) showed the imprinting of hard magnetic powder structures in PDMS using micro-patterned magnetic films as master structures, a simple and low-cost fabrication procedure, something especially important for lab-on-chip applications. More especifically, magnetic particles concentrated magnetophoretically at the interfaces between neighboring micromagnets, and a layer of liquid PDMS was then poured and let cure in order to obtain the composite by peeling it off the master surface (Fig. 1.21b). A biological application was shown in the same work in which fibroblast cells functionalized with superparamagnetic beads were trapped by these structures.

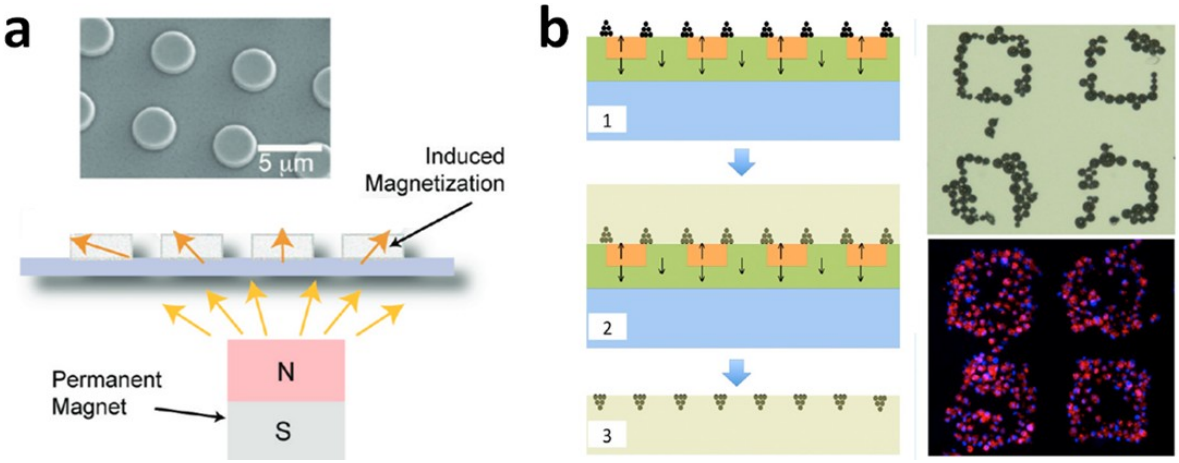

Figure 1.21. (a) Ferromagnetic array of 2 µm dots in a PDMS chip and diagram of induced magnetizations in an array of ferromagnetic spots created by an external permanent magnet situated under the substrate (Tseng et al. 2009), and (b) schematic diagram of imprinting process of hard magnetic particles in PDMS by magnetophoretic concentration at the interface between micromagnets and liquid PDMS pouring: fibroblasts functionalized with magnetic particles were captured following the geometry of the patterns (Dempsey et al. 2014).

A further option in order to obtain highly localized magnetic field gradients is the use of low coercivity magnets ending in a microtip that can be placed inside the device closed to the microfluidic channel, its core body placed inside an external electromagnet (Fig. 1.22a). This soft magnet concentrates the magnetic field lines and leads to very high field gradients in the vicinity of the microtip, effective for fast bead capture. (Afshar et al. 2011) showed the use of a pair of tips on each side of a microfluidic channel to attract beads in suspension resulting in the formation of a plug of beads (Fig. 1.22b). Demagnetization of the tips results in plug release and the formation of a narrow stream of beads moving downstream under a constant flow. Under the influence of a second pair of magnetic poles formed by a broad tip and a double tip on either side, magnetic gradients favorable for separation are generated, with particle trajectories that deviate more strongly with larger bead diameters or bead clusters (authors used 1.0 and 2.8 µm

superparamegnetic beads). This kind of device is particularly interesting for the on-chip intregration of magnetic agglutination assays.

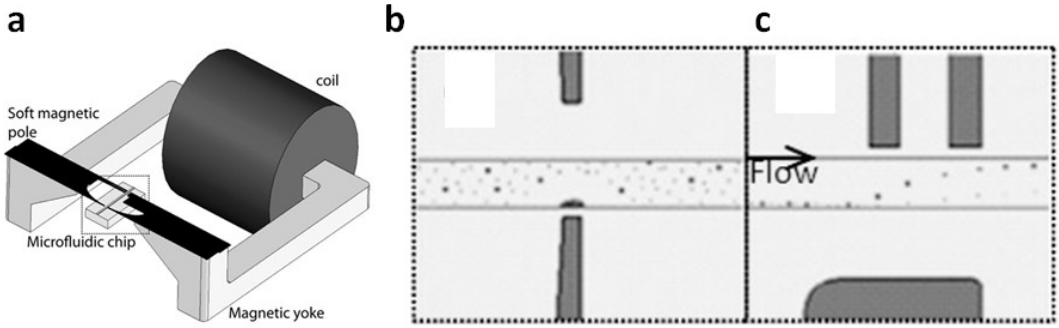

Figure 1.22. (a) Magnetic actuation system with soft magnet microtips integrated in a microfluidic chip and connected to a magnetic yoke and electromagnet. (b) magnetic plug formation with two opposite tips and (c) magnetic bead separation with a broad and a double tip (Afshar et al. 2011).

So far, all the magnetic preconcentration applications shown have focused on the first labeling of the target with magnetic beads and their concentration in an area where the magnetic field was particularly strong. Although effective for certain applications, this requires a good mixing between beads and target, often performed off chip, and is less of a good option for molecular targets, where surface contact must be particularly high for efficient capture. Furthermore, if the mixing step is performed on-chip, it is usually performed in a limited space and hence in a limited volume, preventing the extraction of biomarkers from larger sample volumes than typical microfluidic chamber sizes. This is particularly a problem for rare biomarkers, as relatively large sample volumes must be processed to extract significant detectable quantities of analyte.

A solution to this problem is the capture of the analyte of interest with magnetic beads inside the microfluidic chip. Ideally, the physical arrangement of magnetic beads should lead to a maximum surface to volume ratio, allowing a high capture rate at a constant fluid flow, in analogy with other solid-phase preconcentration systems previously described. For this purpose, several possibilities have been reported:

Lacharme et al. 2008 made use of periodically enlarged cross sections of a microfluidic channel to retain self-assembled magnetic bead chains (Fig. 1.23). A complete on-chip sandwich immunoassay (as described in chapter 3) was able to detect concentrations of up to 1 ng/mL of fluorescent monoclonal antibodies for small sample volumes (several nL). This method is conceptually very interesting, but requires the microfabrication of a relatively complex structure and is limited to very thin channels, reducing throughput.

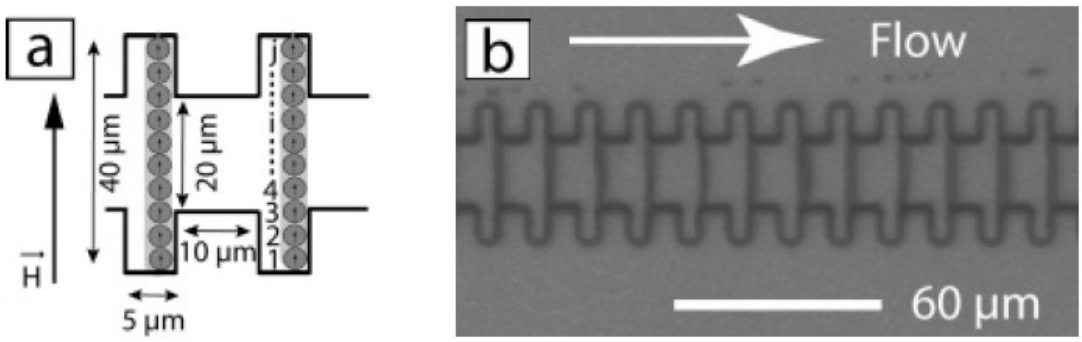

Figure 1.23. (a) Microchannel with periodically varying channel width for retention of self-assembled magnetic particle columns and (b) optical image of the microchannel (Lacharme et al. 2008).

Playing on a similar idea, Saliba et al. 2010 presented self-assembled magnetic columns formed by the application of a vertical magnetic field, their position determined by a hexagonal array of magnetic ink, patterned at the bottom of a microfluidic chamber (Fig. 1.24). This allows the use of much higher flow rates before columns destruction (as compared with the previous case) with a low backpressure, but the minimum separation of the columns is limited by their tendency to cluster together. Therefore, they were able to use this system for the highly efficient capture of circulating tumor cells, but the capture of smaller species would lead to low efficacies. This system is the equivalent of the structured microchannels described in section 1.7.1, with the advantage that the pillars can be disassembled by the removal of the magnetic field and rebuilt with new beads when switching on the magnetic field. This technique further avoids complex fabrication and chamber grafting protocols, and allows the reuse of chips.

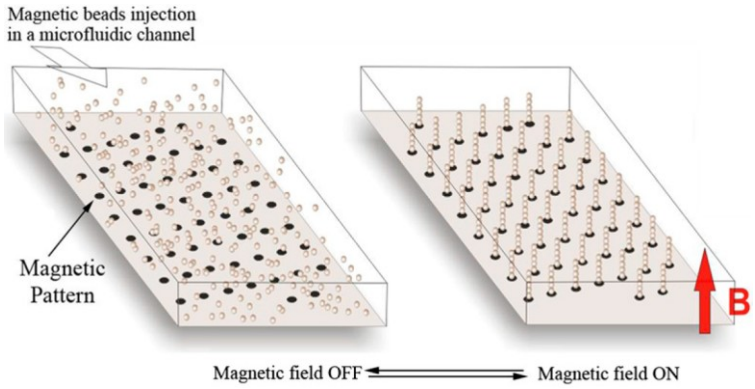

Figure 1.24. Formation of magnetic bead columns under the application of a vertical magnetic field. Columns are positioned on magnetic ink dots (Saliba et al. 2010).

The regular patterning of magnetic particles is hence limiting for the preconcentration of biomolecules at high-throughput. An alternative to this is the random distribution of particles in an ensemble (magnetic plug) kept together by the presence of a magnetic field while the sample flow percolates through it. Bronzeau & Pamme 2008 showed the possibility of using a series of plugs of magnetic particles with different magnetic chemistries, for the capturing of several components simultaneously (Fig. 1.25). In this case, silica capillaries (ID 100 µm) were positioned in the gap between two NdFeB permanent magnets with opposite poles facing each other. As a result of the generated

magnetic field gradients, magnetic particles (2.8 μm Dynabeads) aggregated in the center of this gap when loaded in the capillary with a constant flow, with trapping efficiencies of 100%. By forming a series of particle plugs of different surface functionalization with the use magnet pairs along the capillary, the authors demonstrate the capture on each plug of a specific protein target. The chemical elution of target is also shown, although channel networks would probably be needed in this case for specific recovery. This study shows that the multiplexing of target preconcentration is possible with magnetic beads in a microfluidic device, although the authors do not provide information on capture and elution efficiencies.

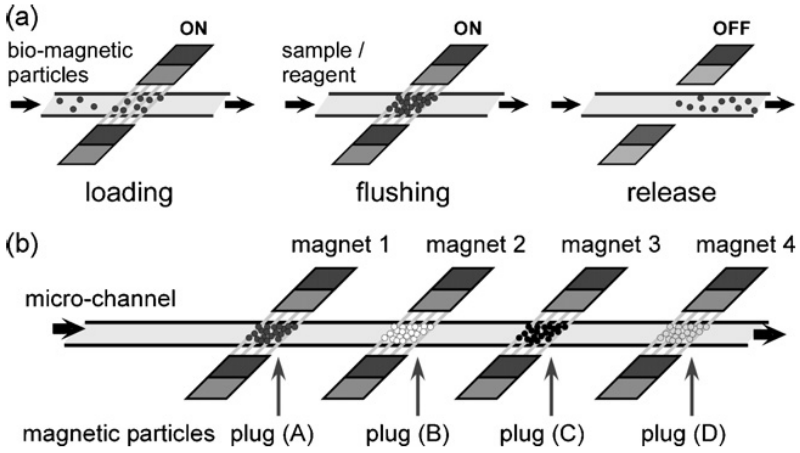

Figure 1.25. (a) prinicple of particle loading for the formation, sample capture, and release of magnetic plugs and (b) example of system formed by a series of plugs of different surface characteristis (Bronzeau & Pamme 2008).

Easy in their principle, static magnetic plugs require high backpressures for inner flow percolation, and usually present suboptimal capture rates due to clustering and agglomeration. Furthermore, in very compact magnetic plugs a preferential flow path is usually formed, meaning that a majority of liquid will go through this lower resistance zone, reducing the contact surface with the liquid phase (Le Nel et al. 2008). A step towards a more efficient system is the development of dynamically actuated magnetic plugs. Moser et al. 2009 have shown that by using two magnetic microtips on each side of a microfluidic channel, the alternating displacement of magnetic particles from and to the opposite channel walls could be controlled by applying sinusoidal AC field frequencies to the electromagnet (Fig. 1.26). This dynamically actuated plug should present higher capture efficiencies than its static equivalent, as this latter one did not fill the entire section of the channel. However, since the plug oscillates in a nearly horizontal plane, the authors estimate a maximum achievable capture efficiency of 10%. A further detection step was performed by the generation of a static magnetic field, leading to the subsequent swelling of the plug when the field was switched off. Different swelling velocities as a function of the amount of capture analyte allowed the detection of protein captured by streptavidin/biotin interaction, with a limit of detection of 3 pM.

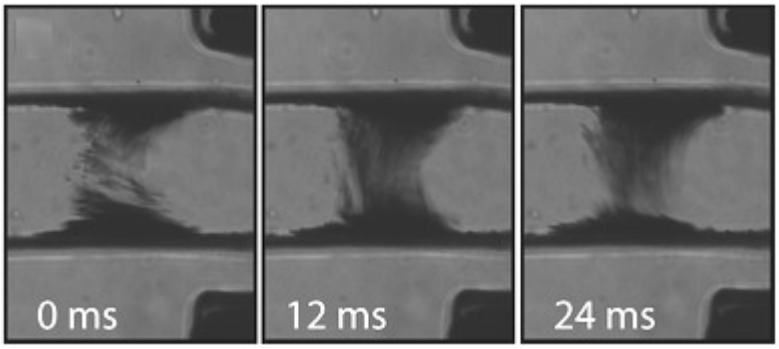

Figure 1.26. Dynamically actuated magnetic plug with a continuous motion of beads resulting in a relatively uniform plug distribution obtained with a sinusoidal field frequency between two magnetic microtips (Moser et al. 2009).

In her thesis work, Sanae Tabnaoui (Tabnaoui 2012) presented a microfluidic fluidized bed based on the equilibrium of forces obtained by using magnetic beads (2.8 µm Dynabeads) attracted by an external permanent magnet in the presence of an opposing constant flow. In comparison with previous reported works on the development of capture systems based on the magnetic confinement of functionalized particles, the obtained bed was seen to present a rather homogeneous fluidization, stability in a relatively large range of flow rates and both packed and fluidization working modes. A perspective on previous attempts at creating a similar system showed the importance of a v-shaped chamber geometry and a relatively small chamber height. A protein capture protocol further showed the applicability of this system to biological extraction procedures. This promising initial proof of concept will be the starting point for the present thesis, in which the potentialities of the microfluidic fluidized bed will be explored for: (i) a series of biologically relevant applications and (ii) a more in depth physical characterization of the system.

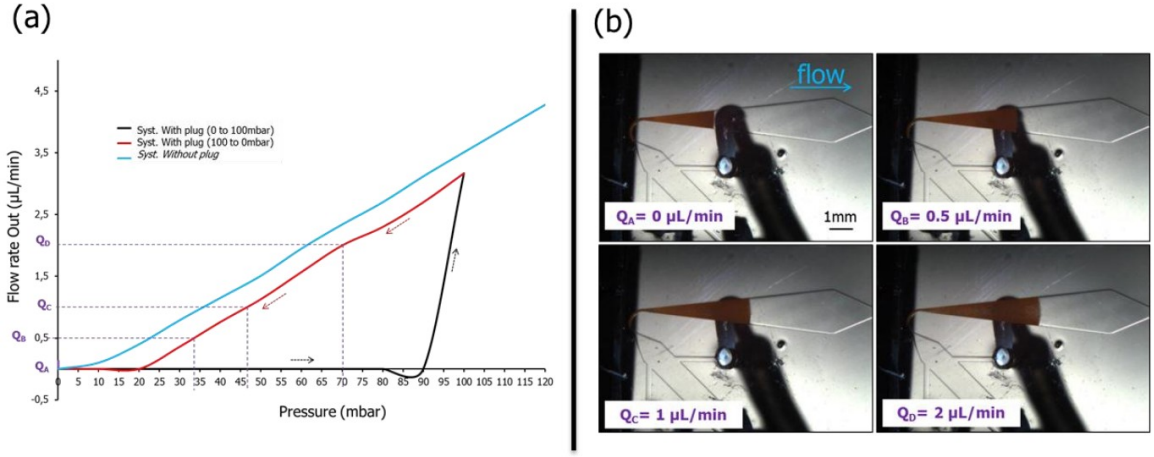

Figure 1.27. (a) Variation of the flow rate versus pressure for a fluidized bed formed by 50 µg of 2.8µm magnetic particles and (b) pictures of the fluidized bed at different flow rates (Tabnaoui 2012).

1.8. Conclusions

As shown so far, the literature on analyte preconcentration methods integrated in microfluidic devices is particularly rich. The choice of a particular method over another depends on molecule/cell or sample matrix properties and on whether this preconcentration process allows the coupling with other possible downstream analytical steps. The integration of different preconcentration methods in a given device is also possible for enhanced sensitivity. An illustrative example is the work of (Mohamadi et al. 2015), in which a single microfluidic chip integrates a plug of magnetic beads for protein immunocapture, a nano-porous membrane for further target preconcentration and an electrophoresis channel for protein discrimination and detection. However, the complexity of this kind of systems usually results in long protocols and high fabrication costs, with lower robustness of operation than simpler system designs.

An added difficulty in the choice of the most suitable method for a given application lies in the fact that the reported limits of detection (or preconcentration factors) are usually difficult to compare between methods due to their important differences both in experimental conditions and the nature of the analytes evaluated. In the case of solid-phase extraction methods it is nonetheless clear that the use of dynamic systems could offer enhanced performance in terms of target capture efficiency and elution, going beyond a simple diffusion-based process. Due to their ease of manipulation, magnetic beads are seen as an attractive support, as applications based on them have shown advantageous features such as multiplexing, flexibility, lower fabrication costs and dynamical control. Further, the surface functionalization of magnetic beads is versatile and relatively easily obtained, with many commercially existing particles available.

In the next chapters, the micro-fluidized bed system, based on the constant recirculation of magnetic beads, will be presented. In chapter 2 a full physical characterization of the system will provide a better understanding of the physical properties needed to obtain fluidization of magnetic particles in a microfluidic device, and how this fluidization compares with conventional macro-fluidized bed systems. In the following chapters, the particular properties of this fluidized bed will be employed, not only as a preconcentration system, but for the further integration of biomolecular protocols or the specific culture of cells and subsequent detection.

1.9. References

Afshar, R. et al., 2011. Magnetic particle dosing and size separation in a microfluidic channel. *Sensors and Actuators, B: Chemical*, 154(1), pp.73–80.

Andersson, H. et al., 2000. Micromachined flow-through filter-chamber for chemical reactions on beads. *Sensors and Actuators, B: Chemical*, 67(1), pp.203–208.

Autebert, J. et al., 2012. Microfluidic: An innovative tool for efficient cell sorting. *Methods*, 57(3), pp.297–307.

Bharadwaj, R. & Santiago, J.G., 2005. Dynamics of field-amplified sample stacking. *Journal of Fluid Mechanics*, 543(-1), p.57.

Boyer, T.H., 1988. The force on a magnetic dipole. *American Journal of Physics*, 56(8), p.688.

Bronzeau, S. & Pamme, N., 2008. Simultaneous bioassays in a microfluidic channel on plugs of different magnetic particles. *Analytica Chimica Acta*, 609(1), pp.105–112.

Ceriotti, L., De Rooij, N.F. & Verpoorte, E., 2002. An integrated fritless column for on-chip capillary electrochromatography with conventional stationary phases. *Analytical Chemistry*, 74(3), pp.639–647.

Cui, H., Dutta, P. & Ivory, C.F., 2007. Isotachophoresis of proteins in a networked microfluidic chip: Experiment and 2-D simulation. *Electrophoresis*, 28(7), pp.1138–1145.

Das, C. et al., 2007. Integration of isoelectric focusing with multi-channel gel electrophoresis by using microfluidic pseudo-valves. *Lab on a chip*, 7(12), pp.1806–1812.

Davis, J.A. et al., 2006. Deterministic hydrodynamics: taking blood apart. *Proceedings of the National Academy of Sciences of the United States of America*, 103(40), pp.14779–14784.

Dempsey, N.M. et al., 2014. Micro-magnetic imprinting of high field gradient magnetic flux sources. *Applied Physics Letters*, 104(26).

Deng, T., Prentiss, M. & Whitesides, G.M., 2002. Fabrication of magnetic microfiltration systems using soft lithography. *Applied Physics Letters*, 80(3), pp.461–463.

Fan, X. et al., 2015. A microfluidic chip integrated with a high-density PDMS-based microfiltration membrane for rapid isolation and detection of circulating tumor cells. *Biosensors & bioelectronics*, 71, pp.380–6.

Frangogiannis, N.G., 2012. BIOMARKERS: HOPES AND CHALLENGES IN THE PATH FROM DISCOVERY TO CLINICAL PRACTICE. *Translational research : the journal of laboratory and clinical medicine*, 159(4), pp.197–204.

Garcia-Schwarz, G. et al., 2012. On-chip Isotachophoresis for Separation of Ions and Purification of Nucleic Acids. *Journal of Visualized Experiments*, (61).

Giri, B. & Dutta, D., 2014. Improvement in the sensitivity of microfluidic ELISA through field amplified stacking of the enzyme reaction product. *Analytica chimica acta*, 810, pp.32–38.

Han, C.M., Katilius, E. & Santiago, J.G., 2014. Increasing hybridization rate and sensitivity of DNA microarrays using isotachophoresis. *Lab on a chip*, 14(16), pp.2958–67.

Hofmann, O. et al., 1999. Adaptation of capillary isoelectric focusing to microchannels on a glass chip. *Analytical Chemistry*, 71(3), pp.678–686.

Hoshino, K. et al., 2011. Microchip-based immunomagnetic detection of circulating tumor cells. *Lab on a Chip*, 11(20), p.3449.

Hu, H., Eustace, D. & Merten, C.A., 2015. Efficient cell pairing in droplets using dual-color sorting. *Lab Chip*, p.-.

Hwang, K.Y. et al., 2012. Solid phase DNA extraction with a flexible bead-packed microfluidic device to detect methicillin-resistant staphylococcus aureus in nasal swabs. *Analytical Chemistry*, 84(18), pp.7912–7918.

De Jong, J., Lammertink, R.G.H. & Wessling, M., 2006. Membranes and microfluidics: a review. *Lab on a chip*, 6(9), pp.1125–1139.

Jung, B., Bharadwaj, R. & Santiago, J.G., 2003. Thousandfold signal increase using field-amplified sample stacking for on-chip electrophoresis. *Electrophoresis*, 24(19-20), pp.3476–83.

Kang, Q.-S. et al., 2013. A 3D porous polymer monolith-based platform integrated in poly(dimethylsiloxane) microchips for immunoassay. *The Analyst*, 138(9), pp.2613–9.

Karenga, S. & El Rassi, Z., 2010. A novel, neutral hydroxylated octadecyl acrylate monolith with fast electroosmotic flow velocity and its application to the separation of various solutes including peptides and proteins in the absence of electrostatic interactions. *Electrophoresis*, 31(19), pp.3192–3199.

Kim, D. & Herr, A.E., 2013. Protein immobilization techniques for microfluidic assays. *Biomicrofluidics*, 7(4), pp.1–47.

Kohn, E.C. et al., 2007. Proteomics as a tool for biomarker discovery. *Disease markers*, 23(5-6), pp.411–417.

Lacharme, F., Vandevyver, C. & Gijs, M.A.M., 2008. Full on-chip nanoliter immunoassay by geometrical magnetic trapping of nanoparticle chains. *Analytical Chemistry*, 80(8), pp.2905–2910.

Lee, J.H., Song, Y.-A. & Han, J., 2008. Multiplexed proteomic sample preconcentration device using surface-patterned ion-selective membrane. *Lab on a chip*, 8(4), pp.596–601.

Lien, K.-Y. et al., 2007. Purification and enrichment of virus samples utilizing magnetic beads on a microfluidic system. *Lab on a chip*, 7(7), pp.868–875.

Lin, C.C., Hsu, J.L. & Lee, G.B., 2011. Sample preconcentration in microfluidic devices. *Microfluidics and Nanofluidics*, 10(3), pp.481–511.

Lu, J.J. et al., 2012. Chip-capillary hybrid device for automated transfer of sample preseparated by capillary isoelectric focusing to parallel capillary gel electrophoresis for two-dimensional protein separation. *Analytical chemistry*, 84(16), pp.7001–7.

Metz, S. et al., 2003. Polyimide microfluidic devices with integrated nanoporous filtration areas manufactured by micromachining and ion track technology. *Journal of Micromechanics and Microengineering*, 14(3), pp.324–331.

Mohamadi, R.M. et al., 2015. An integrated microfluidic chip for immunocapture, preconcentration and separation of β-amyloid peptides. *Biomicrofluidics*, 9(5), p.054117.

Moser, Y., Lehnert, T. & Gijs, M.A.M., 2009. On-chip immuno-agglutination assay with analyte capture by dynamic manipulation of superparamagnetic beads. *Lab on a chip*, 9(22), pp.3261–3267.

Nahavandi, S. et al., 2014. Microfluidic platforms for biomarker analysis. *Lab on a chip*, 14(9), pp.1496–514. Available at: http://www.ncbi.nlm.nih.gov/pubmed/24663505.

Namieśnik, J., 2002. Trace Analysis — Challenges and Problems. *Critical Reviews in Analytical Chemistry*, 32(4), pp.271–300.

Le Nel, A. et al., 2008. Controlled proteolysis of normal and pathological prion protein in a microfluidic chip. *Lab on a chip*, 8(2), pp.294–301.

Nguyen, N.-T. & Wereley, S.T., 2002. *Fundamentals and applications of microfluidics*, Artech House.

Pamme, N., 2006. Magnetism and microfluidics. *Lab on a chip*, 6(1), pp.24–38.

Pu, Q. et al., 2004. Ion-enrichment and ion-depletion effect of nanochannel structures. *Nano Letters*, 4(6), pp.1099–1103.

Ramadan, Q. et al., 2004. On-chip micro-electromagnets for magnetic-based bio-molecules separation. *Journal of Magnetism and Magnetic Materials*, 281(2-3), pp.150–172.

Ravula, S.K. et al., 2008. A microfluidic system combining acoustic and dielectrophoretic particle preconcentration and focusing. *Sensors and Actuators, B: Chemical*, 130, pp.645–652.

Rogacs, A., Marshall, L.A. & Santiago, J.G., 2014. Purification of nucleic acids using isotachophoresis. *Journal of Chromatography A*, 1335, pp.105–120.

Saliba, A.-E. et al., 2010. Microfluidic sorting and multimodal typing of cancer cells in self-assembled magnetic arrays. *Proceedings of the National Academy of Sciences of the United States of America*, 107(33), pp.14524–14529.

Sato, K. et al., 2000. Integration of an immunosorbent assay system: Analysis of secretory human immunoglobulin A on polystyrene beads in a microchip. *Analytical Chemistry*, 72(6), pp.1144–1147.

Shiddiky, M.J. a & Shim, Y.-B., 2007. Trace analysis of DNA: preconcentration, separation, and electrochemical detection in microchip electrophoresis using Au nanoparticles. *Analytical chemistry*, 79(10), pp.3724–3733.

Sommer, G.J. & Hatch, A. V., 2009. IEF in microfluidic devices. *Electrophoresis*, 30(5), pp.742–757.

Stroock, A.D. et al., 2002. Chaotic mixer for microchannels. *Science (New York, N.Y.)*, 295(5555), pp.647–651.

Suzuki, H. et al., 2006. Highly reproducible method of planar lipid bilayer reconstitution in polymethyl methacrylate microfluidic chip. *Langmuir*, 22(4), pp.1937–1942.

Tabnaoui, S., 2012. *Magnetic fluidized bed for sample preconcentration and immunoextraction in microfluidic systems*. Available at: http://www.theses.fr/2012PAO66470.

Thurmann, S. et al., 2014. High-performance liquid chromatography on glass chips using precisely defined porous polymer monoliths as particle retaining elements. *Journal of chromatography. A*, 1370, pp.33–9.

Tichopad, A., Didier, A. & Pfaffl, M.W., 2004. Inhibition of real-time RT-PCR quantification due to tissue-specific contaminants. *Molecular and Cellular Probes*, 18, pp.45–50.

Tseng, P., Carlo, D. Di & Judy, J.W., 2009. Rapid and Dynamic Intracellular Patterning of Cell-Internalized Magnetic Fluorescent Nanoparticles. *Nano Letters*, 9(8), pp.3053–3059.

Tsougeni, K. et al., 2015. Plasma nanotextured polymeric lab-on-a-chip for highly efficient bacteria capture and lysis. *Lab Chip*, p.-.

Unger, M.A. et al., 2000. Monolithic microfabricated valves and pumps by multilayer soft lithography. *Science (New York, N.Y.)*, 288(5463), pp.113–116.

Vázquez, M. & Paull, B., 2010. Review on recent and advanced applications of monoliths and related porous polymer gels in micro-fluidic devices. *Analytica Chimica Acta*, 668(2), pp.100–113.

Wagner, P.D., Verma, M. & Srivastava, S., 2004. Challenges for biomarkers in cancer detection. In *Annals of the New York Academy of Sciences*. pp. 9–16.

Walker, G.M. & Beebe, D.J., 2002. An evaporation-based microfluidic sample concentration method. *Lab on a chip*, 2(2), pp.57–61.

Wei, H. et al., 2011. Particle sorting using a porous membrane in a microfluidic device. *Lab on a chip*, 11(2), pp.238–245.

Witek, M.A. et al., 2006. Purification and preconcentration of genomic DNA from whole cell lysates using photoactivated polycarbonate (PPC) microfluidic chips. *Nucleic acids research*, 34(10), p.e74.

Wu, D. & Steckl, A.J., 2009. High speed nanofluidic protein accumulator. *Lab on a chip*, 9(13), pp.1890–1896.

Xiang, F. et al., 1999. An integrated microfabricated device for dual microdialysis and on-line ESI-ion trap mass spectrometry for analysis of complex biological samples. *Analytical Chemistry*, 71(8), pp.1485–1490.

Xu, Z. et al., 2009. High-sensitive analysis of DNA fragments by capillary gel electrophoresis using transient isotachophoresis preconcentration and fluorescence detection. *Journal of Chromatography A*, 1216(17), pp.3602–3605.

Yamada, M. et al., 2015. Cell-sized condensed collagen microparticles for preparing microengineered composite spheroids of primary hepatocytes. *Lab Chip*, p.-.

Yang, J. et al., 2015. A microfluidic device for rapid quantification of cell-free DNA in patients with severe sepsis. *Lab Chip*, p.-. Available at: http://dx.doi.org/10.1039/C5LC00681C.

Yu, C. et al., 2001. Monolithic Porous Polymer for On-Chip Solid-Phase Extraction and Preconcentration Prepared by Photoinitiated in Situ Polymerization within a Microfluidic Device. *Analytical Chemistry*, 73(21), pp.5088–5096.

Yu, H. et al., 2008. A simple, disposable microfluidic device for rapid protein concentration and purification via direct-printing. *Lab on a chip*, 8(9), pp.1496–1501.

Zhao, Y. et al., 2014. Droplet-based in situ compartmentalization of chemically separated components after isoelectric focusing in a Slipchip. *Lab on a chip*, 14(3), pp.555–61.

Zhu, L., Tu, C. & Lee, H.K., 2001. Liquid-phase microextraction of phenolic compounds combined with on-line preconcentration by field-amplified sample injection at low pH in micellar electrokinetic chromatography. *Analytical chemistry*, 73(23), pp.5655–60.

Chapter 2

Microfluidic magnetic fluidized bed

2.1 Introduction

Fluidization is a process whereby a granular solid material transitions into a dynamic fluid-like state when an upward-flowing fluid imposes a high enough drag force to overcome the downward gravitational forces. The resulting high stirring, surface to volume ratio, low backpressures and high heat transfer properties have resulted in fluidized bed reactors being widely used in the chemical industry.

With the advent of microfluidic technology, existing macroscopic affinity solid-phase extraction systems such as membranes, chromatography columns or packed beds have been adapted into lab-on-chip devices for integrated preconcentration and separation steps. However, several reported attempts at the microfluidic integration of fluidization processes have so far been hampered by the reduced gravitational forces at the micro-scale. Nonetheless, as seen in the previous chapter, an interest and need exists for more dynamic systems that go beyond simple static porous structures, in order to enhance capture efficiency, facilitate mixing and increase throughput.

The microfluidic magnetic fluidized bed system developed in our lab (Tabnaoui 2012) has demonstrated the feasibility of obtaining fluidization with the use of magnetic beads and an external permanent magnet. This system presents the further advantage of being able to use commercial beads that are routinely used in laboratory environments for biological separation and biomolecular protocols. However, the physical mechanisms implicated in the obtained fluidization phenomena had not been studied and therefore the optimization of the device (magnetic field, microfluidic design, operational protocol…) was still pending.

In the present chapter, a deeper characterization of this magnetic fluidized bed is presented, and an attempt is made to offer a more complete understanding of the physical mechanisms and main parameters leading to this kind of fluidization. More specifically, a study is presented on the influence of chamber geometry, magnetic field distribution and particle loading, on fluidized parameters such as porosity and recirculation. This recirculation phenomenon is further characterized through particle tracking, and attempts at explaining its origin are discussed.

For a better comprehension, the general physics, characteristics and most common types of conventional fluidized beds are presented first. The system is also put into context with the current state of the art in fluidized bed miniaturization.

2.2. Fluidized bed reactors in industry

The unique charateristics of fluidized beds provide certain features advantageous for certain industrial applications. Some examples are a rapid mixing, leading to almost isothermal conditions for the whole bed, very high heat transfer, easy solid phase handling and automation and suitability for large scale operations. Some characteristics that can result in low performance must however be taken into account when this kind of reactors are employed, namely bubbling effects in gas phase fluidized beds, the loss of solid phase if pulverization occurs or the abrasion of reaction walls. The overall advantage of fluidized beds has nonetheless lead to a wide range of applications in industry starting from the 1940s. A brief non-exhaustive summary of main applications ispresented in this section.

First, due to their high heat transfer and isothermal properties, fluidized bed reactors are often used as heat exchangers between a gas and a solid phase. The use of fluidized bed driers is particularly common, allowing a high drying throughput available for any wet solid as long as its fluidization with gas is possible. A typical example is the drying of coal before coke oven feeding in the steel industry. Besides hot gas, heat can be supplied with heat exchange tubes, reducing the volume of fluidizing gas needed (Fig. 2.1a). A further application of these drying operations is the coating of particles or their growth from an initial seed with cycles of solid-phase wetting through liquid spraying and subsequent drying (Fig. 2.1b).

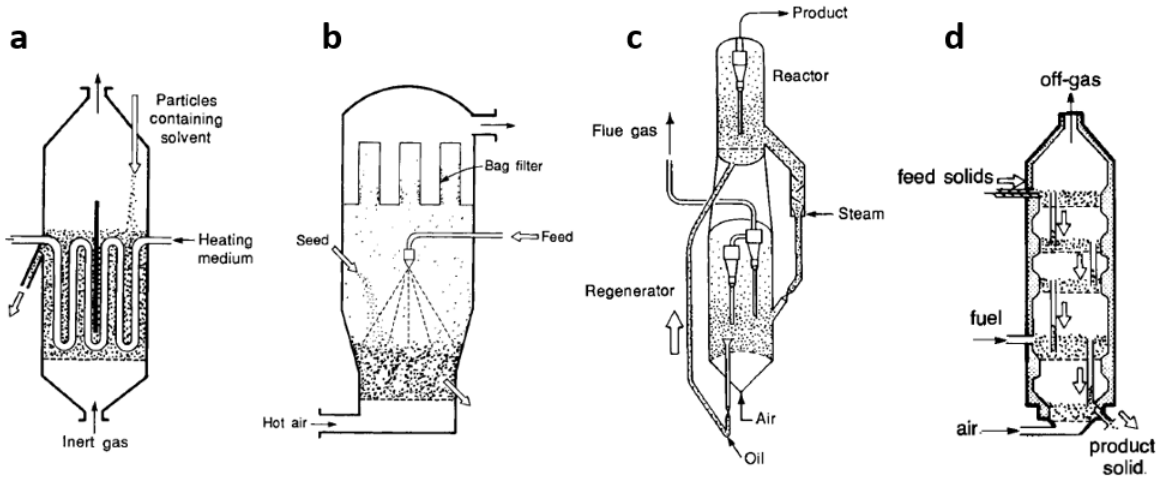

Figure 2.1. Examples of industrail fluidized bed reactors: (a) particle growth from initial seed, (b) drier, (c) Kunii-Kunugi for thermal cracking and olefin production and (d) multistage reactor for the calcination of limestone. Adapted from (Kunii et al. 1991a).

The adsorption of chemical components (typically solvants or air pollutants) from a gas stream is another application where fluidized beds can present higher throuhput than simple fixed beds, in particular when this operation is performed in multiple stages. Efficent protein purifications with this technology are achieved even from cell-rich feedstocks (Chase et al. 1992).

Another application is the use of fluidized bed reactors for efficient synthetis of chemical products, the solid phase typically being used as a catalyzer of a gas-phase reaction. As compared with packed beds, fluidized bed reactors present the added advantage of presenting very homogeneous thermal distributions, with constant mixing reducing hot spots, necessary for accurate temperature control. This makes the technology suitable for very exothermal reactions, for which a loss of control can represent an important danger. Examples of chemical products obtained this way are polyethylene, polypropylene, acrylonitrile or hydrocarbons through the Fischer-Tropsch process (Kang et al. 2011).

It is, however, the cracking of long chain hydrocarbon molecules into lighter hydrocarbons that has mostly propelled the development of fluidized bed reactors technology. In the most commonly used cracking process in petroleum refineries, the fluid catalytic cracking (FCC) process, a combination of two fluidization units is used (Fig. 2.1c). In a first vessel (reactor), vaporized petroleum is cracked in contact with hot catalyst particles. This endothermic process results in carbon deposition on the surface of the particles. Therefore, after a certain resident time, these particles are sent to the second unit at higher temperature to reduce their carbon content by burning in air, and subsequently returned to the initial reactor. The heat produced by this burning step is used to feed the cracking reactor increase the overall energy efficiency of the system (Kunii et al. 1991a). As solids need to be constantly recirculated, particle fluidization is imperative, making fluidized bed reactors a key technology in most petroleum refineries today.

Due to the inherent mixing of gas and solid phases, the combustion of low-grade coal, (which cannot be efficiently burned in conventional furnaces) by fluidization processes has also raised interest, particularly in times of energy crisis. Further, as the burning of fuel takes places at lower temperatures than other conventional methods, pollutant emission (such as sulfur and nitrogen oxides) can be reduced (Johnsson 1994).

Further common applications of fluidized bed reactors are calcination processes, such as the decomposition of carbonate materials (ex. limestone) to drive off carbon oxide (Fig. 2.1d), or gasification of coal or solid waste to produce fuel gas (Belgiorno et al. 2003).

A relatively more recent development are bioengineering applications such as the cultivation of microorganisms in these reactors due to fluidization characteristics such as large effective surface, efficient oxygen transfer, constant removal of waste products or accurate control of medium conditions. A particularly interesting application for wastewater treatment is the use of fluidized bed biofilm reactors (FBBR) in which microorganisms fixated on the surface of the fluidized particles consume the biodegradable waste contaminants of the fluidizing liquid. As a result of fluidization of the solid phase, the available area for microorganism growth is maximized, and higher flow rates and lower backpressures can be used as compared with fixed bed equivalent systems (Nicolella 2000).

2.2 Theoretical background

Fluidization is obtained by passing a fluid phase (gas or liquid) through a packed bed of particles at a sufficient velocity to compensate gravitational forces. While in a packed bed particles are in close contact, in a fluidized bed the interparticle distance increases resulting in an increase in porosity but also of the fluid/solid contact. These two regimes (packed bed and fluidized bed) are then complementary to each other and an understanding of their physical properties is necessary for a complete comprehension of the system. A description of their main characteristics and most commonly followed theoretical expressions is described next.

2.2.1 Packed bed

A typical packed bed is composed of a cylindrical column filled with a suitable packing material. Flow passes through the interstitial porosity of this material enabling a very high surface to volume contact. Many applications are then based on packed bed systems (some of them already described in the preceding chapter), the main drawback being their high resistance to flow, requiring high input pressures and significantly limiting throughput.

The **Hagen-Poiseuille equation** defines the pressure drop accros an empty circular channel under laminar flow as:

$$\frac{\Delta P}{L} = \frac{32\mu}{D^2}\frac{dU}{dt} \quad (1)$$

With *dU/dt* being the flow velocity, μ the viscosity of the fluid and *L* and *D* the length and diameter of the channel.

For the most general case of a porous medium of any distribution, the pressure drop of a Newtonian fluid passing trough the column can be obtained through **Darcy's law**:

$$\frac{\Delta P}{L} = \frac{\mu}{kA}\frac{dU}{dt} \quad (2)$$

With *k* being the intrinsic permeability of the medium and *A* the cross-sectional area. The law is only valid for laminar flow (see section 1.2).

This expression was derived by Henri Darcy from experimental observations and published in 1856 (Darcy 1856). It has since then become an essential tool in the study of granular media and soils, and a basic relationship from which more sophisticated derivations have been devised.

The permeability (*k*) of Darcy's law is an empirical constant, that depends on the structure of the solid phase, being a function of parameters such as porosity, grain shape and pore interconnectivity. This is the most limiting term in Darcy's law, as simulating flow through a porous medium requires the determination of this permeability.

Kozeny proposed a solution to this problem by considering the medium as a bundle of parallel capillary channels with the same radius. By making use of Hagen-Poiseuille (Eq. 1) and the concept of characteristic linear dimension (volume of void fraction divided by the surface area in contact with flow), Kozeny obtained an expression for permeability:

$$k = \frac{\varepsilon^3}{K(1-\varepsilon)^2 S_v^2} \quad (3)$$

Where S_v is the specific surface area (surface area by unit volume) and K is the Kozeny constant, that includes the concept of tortuosity (τ) defined as the ratio of the length of flow path through the porous medium to the length of flow path in the absence of solid medium. The value of this constant is 5 in many cases, although this is by no means a general rule. The Kozeny-Carman equation defines the pressure drop by making use of this permeability, and is a subset of Darcy's law (Eq. 2):

$$\frac{\Delta P}{L} = \frac{\mu}{A}\frac{K(1-\varepsilon)^2 S_v^2}{\varepsilon^3}\frac{dU}{dt} \quad (4)$$

This expression is widely used and can be found in many alternative forms. In the case of a packed bed of spherical particles, the specific surface area can be calculated as the surface of a sphere divided by its volume, resulting in the following expression:

$$\frac{\Delta P}{L} = \frac{\mu}{A}\frac{36K(1-\varepsilon)^2}{\varepsilon^3 d^2}\frac{dU}{dt} \quad (5)$$

d being the spherical diameter.

Ergun studied the friction forces that act on the solid particles due to the fluid flow, this forces being the primary cause of the observed pressure drop. This frictional force can be estimated for mono-sized spherical particles through the **Ergun equation**:

$$f_p = \frac{150}{Re^*} + 1.75 \quad (6)$$

With f_p being the friction factor and Re* a modified Reynolds number that identifies the flow regime flowing through a packed bed. These two terms are themselves defined as

$$f_p = \frac{\Delta p}{L}\frac{D_p}{\rho U_s^2}\frac{\varepsilon^3}{1-\varepsilon} \quad \text{and} \quad Re^* = \frac{\rho v_s d}{1-\varepsilon\ \mu} \quad (7)$$

With ρ being the density of the fluid, U_s the superficial velocity (defined as the volumetric flow rate of the fluid divided by the cross sectional area of the bed) and *d* the equivalent spherical diameter of the particle, as previously described.

From this equation, a rearrangement can be obtained to calculate the pressure drop of the bed:

$$\frac{\Delta p}{L} = \frac{150\mu}{d^2}\frac{(1-\varepsilon)^2}{\varepsilon^3}\frac{dV}{dt} + \frac{1.75\rho}{d}\frac{(1-\varepsilon)}{\varepsilon^3}\frac{dU}{dt}^2 \quad (8)$$

This resulting equation is a combination of a first component that dominates under laminar flow (Re*<10), reducing the equation to the Kozeny-Carman equation (Eq. 4), while for a turbulent flow (Re*>2000) the second component dominates, the pressure drop increasing with the square of the superficial velocity.

2.2.2 Minimum fluidization velocity

If the superficial velocity of the fluid through the packed bed increases sufficiently, the upward drag forces generated by this flow can end up equalizing the apparent weight of the particles. This is the velocity that determines the moment of incipient fluidization, which in general is referred to as velocity of minimum fluidization (U_{mf}). Fluidization will then take place for any velocity value above this limit ($U>U_{mf}$).

From a general pressure-weight balance, taking buoyance into consideration, the pressure-drop of the solid phase of the bed can be written as:

$$\frac{\Delta P}{L} = \ 1 - \varepsilon \ g(\rho_p - \rho_f) \qquad (9)$$

This equation can be considered for the case of incipient fluidization ($L = L_{mf,}$ and $\varepsilon = \varepsilon_{mf,}$ although both terms are generally considered constant and equal to the packed bed state) and then be combined with Darcy's law (Eq. 2) to calculate the velocity of incipient fluidization or minimum fluidization velocity:

$$U_{mf} = \frac{k}{\mu} \ \rho_s - \rho \ g(1 - \varepsilon) \qquad (10)$$

Another frequently employed possibility to determine U_{mf} is combining the pressure-weight balance just seen with the laminar component of Ergun's equation (Eq. 8):

$$U_{mf} = \frac{D_p^2(\rho_p - \rho_f)g}{150\mu} \frac{\varepsilon^3}{(1 - \varepsilon)} \qquad (11)$$

The choice of neglecting the turbulent term is often employed for fine particles fluidized by a gas, which is the usual case for industrial reactors, and because of the microscale is inevitably the case in miniaturized fluidized beds (see Chapter 1).

2.2.3 Fluidized bed

Fig. 2.2 shows the pressure drop as a function of the superficial velocity for the situations described so far. For a packed bed the system behaves as a fluid resistance, with a linear relationship between pressure and fluid flow. Once fluidized, however, the pressure drop is constant for all imposed velocities due to the newly formed equilibrium of forces, this pressure drop being described by Equation 9. An increase in flow rate will nonetheless result in an increase in the porosity of the system and hence an expansion process will take place.

Notice that a ΔP peak can occur close to the point of incipient fluidization for increasing flow rates, but this is generally absent for decreasing flow rates. This phenomenon is more common for gas fluidized beds, especially for small or low density particles for which interparticle cohesion forces due to surface rugosity might become significant. It is generally absent in liquid fluidized beds, with exceptions such as very heavy particles or tapered beds (Peng et al. 1997).

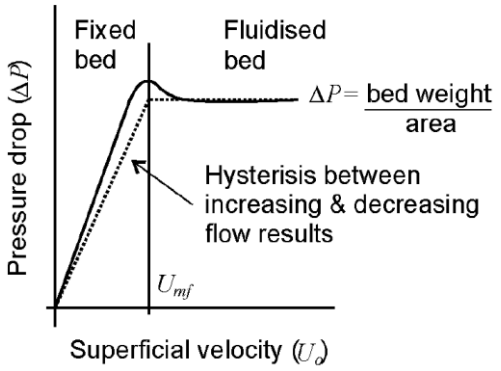

Figure 2.2. Fluidization/compaction cycle showing the resistant behavior of the packed bed and the constant pressure drop once fluidization is established. Hysteresis is a common phenomenon (Yates 1983).

A liquid fluidized bed, where particles are kept in suspension by an upward flow of liquid, is essentially the same process as liquid suspensions where particles fall under the influence of gravity in a stationary liquid, only viewed from a different frame of reference. It is therefore possible to study the expansion of liquid-fluidized beds, except for very dense particles, with the Richardson-Zaki (RZ) empirical equation:

$$U_f = U_t \varepsilon^n \tag{12}$$

Where U_f is the superficial fluid velocity (instead of the settling velocity of liquid suspensions), U_t is the terminal settling velocity of individual particles and n is the RZ exponent (that depends on the particle Reynolds number if wall effects are negligible). This exponent depends on Reynolds numbers when wall effects are negligible.

If the fluid velocity is sufficiently increased, it can occur that the drag force acting on the particles will surpass their gravitational force. This situation arises when the velocity of the fluid exceeds the free fall velocity of the particles, U_t. Particles will then be entrained by the fluid and carried out of the bed. The velocity at which this occurs is called the maximum fluidization velocity. For very low Reynolds numbers (Re<0.4), (Kunii et al. 1991b) give the following expression:

$$U_t = \frac{g(\rho_s - \rho)d_p^2}{18\mu} \tag{13}$$

Hence, the working superficial velocity to obtain fluidization is limited by U_{mf} and U_t ($U_{mf}<U<U_t$).

2.3 Fluidization regimes

The behavior of macroscopic fluidized beds is highly dependent upon fluidization parameters such as velocity, fluid and solid properties, and the dimensions of the cylinder. All of these lead to a variety of possible fluidization regimes. For example, in the case of

fluidization with a gas phase, a series of regimes exist depending on the imposed velocity of the gas: beyond the U_{mf}, the packed bed (Fig. 2.3a) gives rise to a fluidization regime with a maximum of homogeneity (Fig. 2.3b). However, with increasing fluid velocities the formation of bubbles sets in, these bubbles increasing in size with an increase in flow velocity due to their coalescence (Fig. 2.3c). If these bubbles become large enough to have a diameter comparable to that of the fluidized bed, slugging will start taking place, with the bed continually disrupted by pulsed pockets of rising gas (Fig. 2.3d). Higher velocities will eventually result in a completely turbulent regime, exceeding the terminal velocity of the particles (Fig. 2.3e).

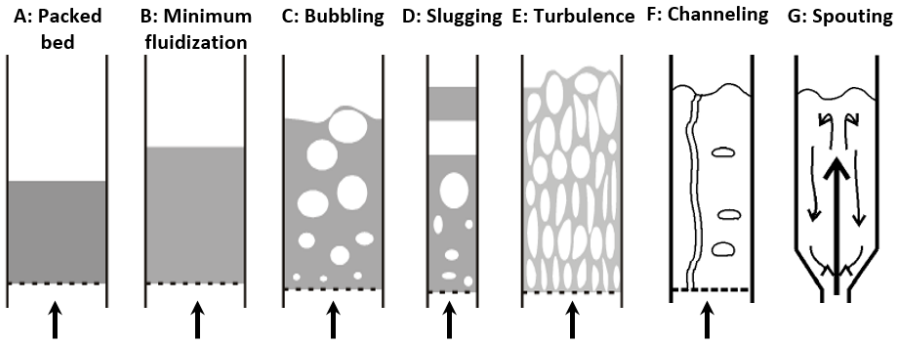

Figure 2.3. Schematic representation of fluidized bed regimes. Adapted from [ref] and (Yates 1983).

Other regimes are possible, more dependent on chamber geometry or axial motion. Channeling can occur as a result of poor fluid/solid phase mixing (Fig. 2.2f), especially in cases where the bed material does not present a uniform size or if interparticle or particle-wall interactions are strong. A preferential path of lower particle concentration is formed and, because of its lower resistance, the fluid tends to flow preferentially in this region.

Spouting occurs when the fluid is introduced in the chamber through a single nozzle at the entrance of a conical shape (Fig. 2.2g). This regime provides a good mixing and constant recirculation of particles. This allows the fluidization of particles coarser than 1 mm, having found many industrial applications such as drying of granular material, coating of tables or granulation of fertilizers (Mathur et al. 1974).

2.4 Magnetism and fluidized beds

While a homogeneous fluidized bed is generally obtained close to the point of incipient fluidization, increased flow-rates generally result in bubbling and slugging phenomena. This means that the fluid passes through the bed bypassing the solid phase, and thus lowering surface contact efficiencies. This problem led to the development of magnetically stabilized fluidized bed (MSFB) systems, where an additional magnetic field is employed for additional bed stability. In these systems, a magnetizable material (or a mix of magnetizable and non-magnetizable particles) is used as the solid phase, and an electromagnetic coil or permanent magnets are configured to create a homogeneous and steady magnetic field inside the cylinder of the bed. In most cases the magnetic field

is generated parallel to the direction of flow (Fig. 2.4a). This results is a bubble-free stable fluidization for a larger range of working fluid velocities than non-magnetic fluidized beds (Fig. 2.4b), and has even proven effective in the fluidization of small particles that are otherwise difficult to fluidize due to the formation of channeling (Zhu et al. 1996). The obtained stability is thought to be due to the formation of particle chains inside the bed due to interparticle magnetic attraction, these chains aligned with the magnetic streamlines. This stabilization due to chain formation seems to occur even when the magnetic field is oriented in a cross-flow configuration, although in this case the chains form an angle (~60°C) with respect to the applied field due to the perpendicular direction of flow (Valverde et al. 2010).

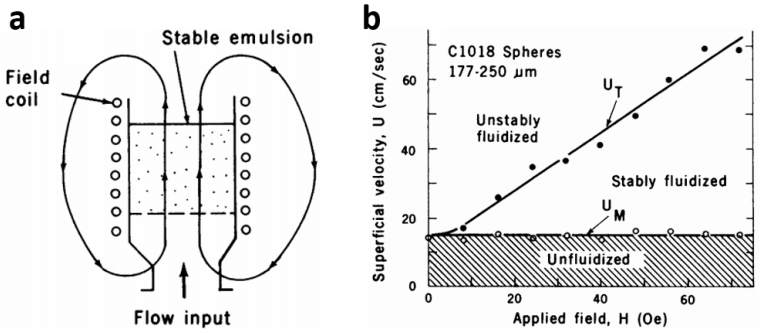

Figure 2.4. Sketch of magnetically stabilized fluidization, with a field parallel to the direction of flow (a) and unfluidized-stable fluidized-unstable transition regimes as a function of flow velocity and strength of applied magnetic field for steel spheres (b). Adapted from (Rosensweig 1979).

With this system, mixing is usually reduced due to the resulting interaction of the magnetized particles, and therefore heat transfer is considerably low as compared to conventional fluidized beds. However, for certain applications, a need exists for plug-like systems (no recirculation) that can overcome the limiting fluid resistance of packed beds preserving their characteristic low shear stress. MSFBs have thus been successfully used for chromatographic and adsorptive separation (Siegell et al. 1984), bioseparations (Putnam et al. 2003) or dry solid-solid separations (Rosensweig et al. 1987).

In MSFBs, magnetic fields are used exclusevily for stability purposes and, as indicated, no net magnetic force is applied on the solid phase. Since generally no need to substitute gravitational forces exists, the literature on magnetic force-controlled beds is scarce. NASA has shown some interest in fluidized bed technology adapted for zero gravity or microgravity environments. In a reported study, Helmholtz rings were used to create a magnetic field gradient inside a tappered 2D fluidization column (Sornchamni et al. 2004). The experimental apparatus was installed on board in a NASA aircraft to conduct microgravity experiments in parabolic flights. (Fig. 2.5) This unique study proved the possibility of replacing gravitational forces with magnetic forces to obtain fluidization phenomena. To our knowledge, this is so far the only published study concerning this kind of system.

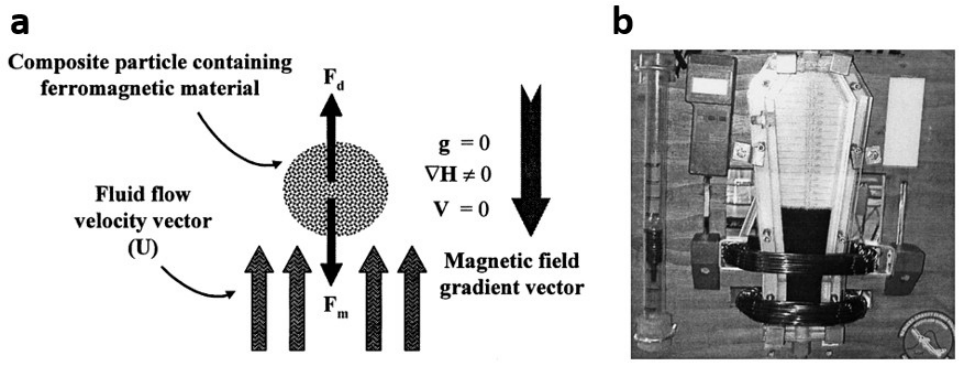

Figure 2.5. (a) Balance of forces in thre presence of a magnetic field gradient and absence of gravity for a fluidized bed containing ferromagnetic material and (b) experimental apparatus for microgravity fluidization experiments. Adapted from (Sornchamni et al. 2004)

2.5 Attempts at creating a microfluidic fluidized bed

The high mixing and resulting higher heat and mass transfer characteristic of fluidized bed systems are particularly interesting in the field of microfluidics, where laminar flows predominate and phase interactions are governed by slow molecular diffusion.

Although the literature on the microfluidic integration of fluidized beds is scarce, some attempts previously reported will be described in this section. As it will be seen, however, while many of these attempts are successful in the miniaturization of fluidization under certain conditions, in most cases particle and chamber dimensions are not sufficiently small to be able to consider these works as truly microfluidic (particle diameters close to or greater than 100 μm being particularly limiting).

The group of Andreas Manz reported a first example of integration of fluidized bed in microfluidic devices in 2005 (Vilkner et al. 2005). In their approach, the authors used a nitrogen flow to generate fluidization of a dry powder in a vertical cone of 4 mL (inner diameter 8.5 mm, mean particle size 113 ± 2.7 mm) whose base was connected to a microfluidic T-shaped channel (Fig. 2.6a). After a short cycle of fluidization, the gas flow was halted and part of the solid particles entered the main channel due to their downward movement when the bed collapsed (Fig. 2.6b). With a new gas injection, fluidization started again and the particles in the channel were forced to the outlet. This paper showed for the first time the application of chip technology for dry powder handling as a way to automatize time-consuming weighting processes. Nevertheless, the application was limited to the injection and transport of small amounts of dry, non-cohesive powder and was thus restricted to the use of a gas phase as a fluid carrier. Further, although connected to a microfluidic device, fluidization takes place in an external macroscopic vessel.

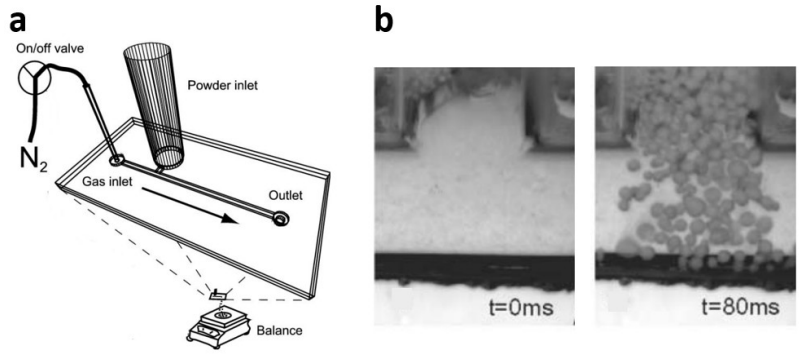

Figure 2.6. (a) Schematic of experimental design for fluidized bed injection of a dry powder and (b) T-junction of the microfluidic chip before and after fluidized bed collapse and subsequent particle flow towards the channel (Vilkner et al. 2005).

(Potic et al. 2005) also published a miniaturized device for biomass gasification in hot compressed water. A cylindrical quartz reactor with an internal diameter of 1 mm was used, and as a distributor a quartz ball (diameter 0.9 mm) was placed just fitting the section of the capillary. As bed material, sand with 2450 Kg/m^3 of density and four different particle sizes (60-70 µm, 80-90 µm, 100-150 µm and 150-250 µm) were used. Under these conditions, the authors observed the formation of homogeneous, slugging and turbulent regimes, with an expansion of the fluidized bed in the homogeneous regime similar to larger beds (Fig. 2.7). A discrete particle model proposed by the authors was able to simulate some behavior. This study demonstrates the possibility for the fluidized bed to be operated in rather harsh operating conditions (P> 200 bars, T >500°C, supercritical water), but the experiments also involve large sand particles in still too large reactors to be considered microfluidics.

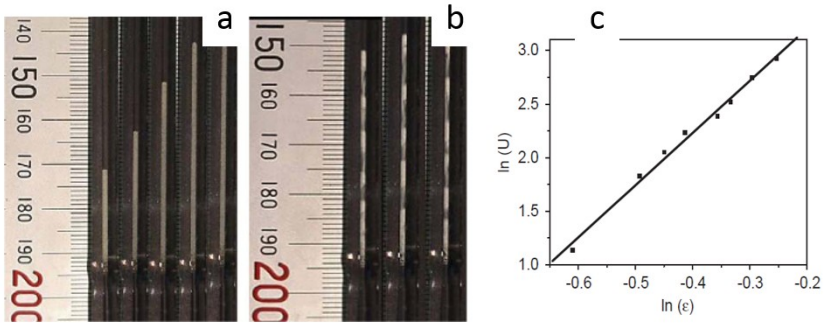

Figure 2.7. Photographs of (a) a homogeneous fluidization at different flow rates (300°C, 160 bar) and (b) slugging regime for the same rates (370°C, 160 bar). (c) linear relationship between velocity and porosity. Particle diameter was 80-90 µm (Potic et al. 2005),.

Doroodchi et al. (Doroodchi et al. 2012) have shown the fluidization of large 225 µm glass particles (density 2492 Kg/m3) inside capillaries with inner diameters of 0.8 mm and above. The fluidization medium was water. Fig. 2.8 shows the pressure drop of the bed as a function of the imposed fluid velocity for three different diameters of the capillary. For the larger diameter (17.1 mm) the behavior of the bed is typical of macroscopic fluid-solid fluidized bed, that is, before fluidization a linear relationship exists between pressure and fluid velocity and once the minimum fluidization velocity is

reached (U_{mf}) fluidization occurs and the pressure drop stays constant for increasing velocities (section 2.2). For smaller diameters (1.2 and 0.8 mm) a hysteresis effect becomes visible, with a pressure drop overshoot before reaching fluidization for increasing flow rates. The authors argue that since a reduction in tube increases the particle diameter to surface wall ratio, this in turn results in more dominant frictional forces of the beads against the walls, having the drag force to compensate for both bed weight and these forces. They further show how Ergun's equation, which does not take into account wall friction forces, differs from experimental results for smaller capillaries. Thus, this paper provides intriguing insights about the hydrodynamic behavior of fluidized beds at smaller scales. It is, however, still restricted to the use of large particles.

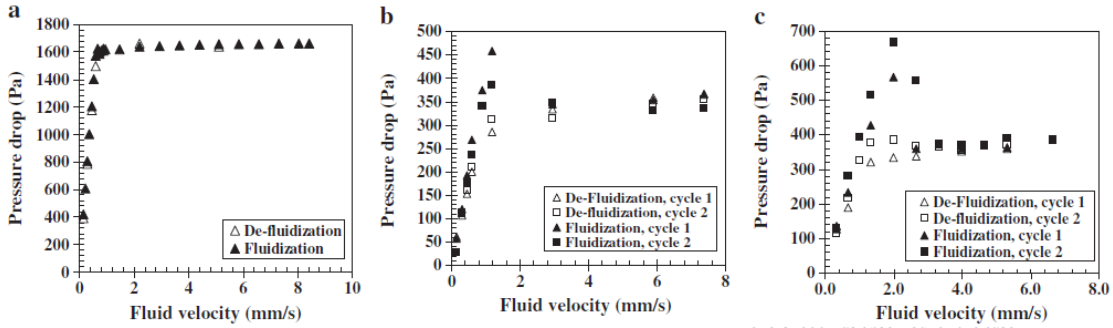

Figure 2.8. Pressure drop versus fluid superficial velocity for three different capillary diameters (a) 17.1 mm, (b) 1.2 mm and (c) 0.8 mm (Doroodchi et al. 2012).

A recent work was reported by Alwahabi et al. (Zivkovic et al. 2013) in what the authors consider to be the first truly microfluidic fluidized bed. The authors reported the liquid fluidization of 30 µm glass micro-particles in rectangular microfluidic channel (PDMS) with a cross-section of 400 um x 175 um. A distributor of 40 µm-wide pillars ensured particle retention at the base of the bed. This work has shown the failure to fluidize the glass micro-particles with water even in the presence of surfactants, due to the importance of adhesive forces. By using ethanol the authors obtained a fluidization process whose minimum fluidization velocity U_{mf} and porosity during expansion could be closely predicted by the Ergun equation and the Richardson and Zaki correlation respectively (Fig. 2.9). Despite its integration in a microfluidic device, this approach was limited to the use of relatively large and dense particles, in combination with ethanol as a fluidizing medium to ensure the particle suspension stability and limit particle-surface interactions.

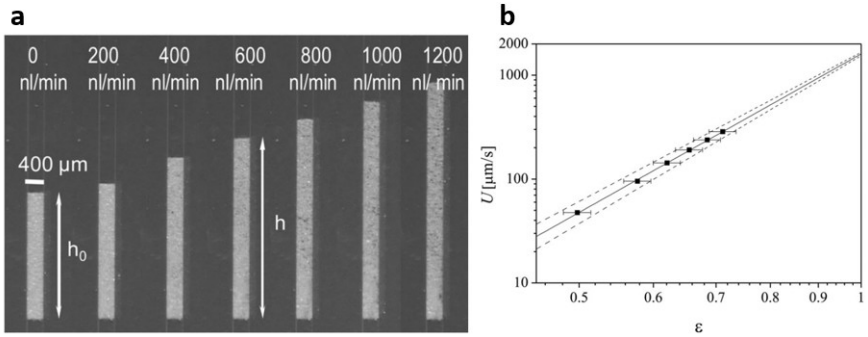

Figure 2.9. (a) Optical micrographs of a fluidized bed of 30 µm glass particles with ethanol as fluidization medium and (b) fit to Richardson-Zaki model of experimental results on porosity-flow velocity.

The approaches described above typically consist in a scaling down of the concepts used in more conventional macroscopic fluidization devices, where the implementation and stability of fluidized bed relies on the balance between gravity forces on one side and the combination of buoyancy and hydrodynamic forces induced by the liquid flow on the other side.

However, when scaling down the dimensions of a fluidized bed device below the millimeter length scale, and/or the dimensions of the particles down to a few micrometers, gravity is no longer sufficient to ensure bed stability. Indeed, the hydrodynamic drag force scales with the diameter d of particles whereas the gravity force scales with d^3. This causes a significant dependence of gravity driven fluidized beds on particle volume. As a numerical illustration, the gravity force experienced by a 2.8 µm magnetic particle (e.g. Dynal©) is $F_g = 9{,}7.10^{-15}$ N whereas the expected drag force obtained from the Stockes equation gives $F_d = 4\ {,}24.10^{-11}$ N for a liquid flow of mean velocity of 1 mm/s. This clearly shows that gravity forces are not sufficient (three decades lower) to compensate for the fluid drag and that, for most inorganic particles, material density is too low to compensate the low particle volume.

In order to compensate for these limitations, the use of magnetic forces has been proposed to mimic the influence of gravitational forces. The use of magnetic microparticles in combination with permanent magnets gives the opportunity to access higher handling forces, typically $\sim 10^{-11}$ N (for Dynabeads and conventional Neodymium-Iron-Boron permanent magnets) that are sufficient to ensure particles confinement in a microfluidic device and to mimic the role of gravity forces involved in macroscopic devices.

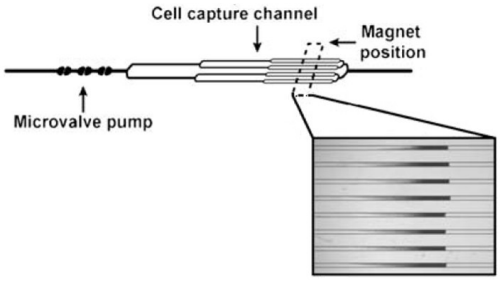

Figure 2.10. Schematic of microchip consisting of microvalves for pump actuation, bifurcated channel and an external permanent magnet on top. Zoom image shows plugs of beads in the parallel channels.

Besides the microfluidic magnetic fluidized bed that is the object of this work, to our knowledge the only other work that claims to make use of magnetic forces for microscale fluidization has been reported by (Beyor et al. 2008). In this work, bifurcated channels are used to obtain plugs in channel branches containing the same amount of magnetic beads (2.8 µm, Dynabeads©), these plugs retained by an external permanent magnet situated on top of the chip (Fig. 2.10). A series of valves are then used to pulsate the injected fluid, resulting in the immediate downstream flow of beads. After each pulse, flow stops and the beads flow back attracted by the magnet, reestablishing the plug. The authors studied the capture of bacteria (Escherichia coli K12) with surface grafted antibodies, and

observed that capture efficiency increased with the number of bifurcations and with smaller sections. This is indeed an interesting study to show the possibility of automation of entity capture with magnetic beads in a microfluidic device. However, although the authors refer to this system as a fluidized bed, we believe that this is an inappropriate terminology, as no stationary fluidized behavior is obtained.

In the following section, a brief description of the magnetic forces acting on these microbeads precedes the presentation and characterization of the magnetic fluidized bed for its better comprehension.

2.6 Magnetic forces acting on superparamagnetic particles

Superparamagnetism is a form of magnetism that appears in small enough ferromagnetic or ferrimagnetic nanoparticles that present a single magnetic domain. Induced by thermal energy, the direction of this magnetization randomly flips, at an average time given by the Néel relaxation time:

$$\tau = \tau_0 exp \frac{\Delta E}{k_B T} \quad (14)$$

Where τ_0 is a length of time characteristic of the material, ΔE the energy barrier, k_B the Boltzmann constant and T the temperature.

Without an external magnetic field, the magnetic moments of the different superparamagnetic particles are randomly oriented and the global net magnetization is zero. However, the presence of a magnetic field leads to an alignment of these moments, giving rise to a net magnetization. A representation of this magnetization (M) as a function of the applied field (H) results in a sigmoidal shape without any hysteresis cycles (in contrast to ferromagnetic materials) (Fig. 2.11).

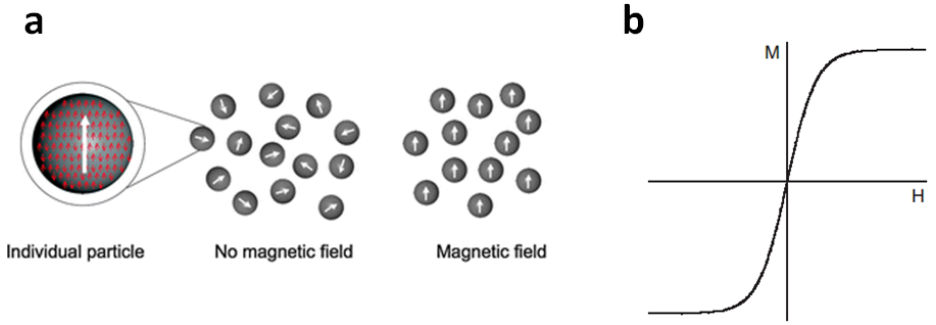

Figure 2.11. (a) Schematic of superparamagnetic particle and alignment of magnetic moments in the presence of a magnetic field (Colombo et al. 2012) and (b) superparamagnetic net magnetization as a function of applied magnetic field.

This magnetization can follow two different equations depending on temperature:

If $T_B < T < \Delta E/(10k_B)$: $$M\ H\ = nm\ tanh\ \frac{\mu_0 Hm}{K_B T} \quad (15)$$

If $\Delta E/(k_B) > T$: $$M\ H\ = nm\ L\ \frac{\mu_0 Hm}{K_B T} \quad (16)$$

Where n is the density of nanoparticles, m is the magnetic moment of the particle, μ_0 the magnetic permeability in vacuum, L the Langevin function ($L\ x\ = \coth\ x\ - \frac{1}{x}$) and T_B is the blocking temperature that defines the minimum temperature for the superparamagnetic state to occur. Importantly, in the absence of magnetic fields superparamagnetic particles present no remanent magnetization, an advantage for protocols requiring their redispersion in solution.

Homogeneous magnetic fields result in a torque that tends to align this net magnetization with the magnetic field lines. Further, as a result of dipole-dipole interactions superparamagnetic beads tend to form columns, which align in parallel to these field lines. However, these homogeneous fields do not result in translational forces. For this to occur a magnetic gradient is required. The magnetic force acting on a point-like magnetic dipole moment **m** is given by (Pankhurst et al. 2003):

$$\boldsymbol{F_m} = (\boldsymbol{m} \cdot \nabla)\boldsymbol{B} \quad (17)$$

Since the nanoparticles will be used in some water-based fluid, it is reasonable to follow some simplifications:

$\mathbf{m} = V_m\mathbf{M}$ (V_m, volume of the particle, M volumetric magnetization)

$\mathbf{M} = \Delta\chi\mathbf{H}$ ($\Delta\chi$ effective susceptibility of particle relative to water)

$\mathbf{B} = \mu_0\mathbf{H}$ (valid for vacuum and water-based media)

$\nabla \times \mathbf{B} = 0$ (Maxwell equation if magnetic field is stationary)

Resulting in the following expressions:

$$\boldsymbol{F_m} = V_m \Delta\chi\ \frac{B^2}{2\mu_0} \quad \text{or} \quad \boldsymbol{F_m} = V_m \Delta\chi\ \frac{1}{2}\boldsymbol{B} \cdot \boldsymbol{H} \quad (18)$$

Showing a relationship between magnetic forces and the differential of the magnetostatic field energy density, $\frac{1}{2}B\ \cdot$.

As seen from Fig. 2.11b, the curve representing the magnetization of superparamagnetic particles as a function of the magnetic field is composed of a linear region for low values of the field, a nonlinear variation for higher values and a saturation region presenting a constant value of M for the upper range. For the present work, all experiments were performed with 2.8 μm Dynabeads®: commercial magnetic beads fabricated by incorporation of iron oxides in porous polymer beads, further coated with a polymer

layer. The magnetization curve for these particles saturates at magnetic field values of ~150 mT (Fonnum et al. 2005), which is superior to the field present in the microfluidic chamber of our device for most bed expansion lengths, as will be seen later (see Fig. 2.19).

2.7 The microfluidic magnetic fluidized bed

The magnetic fluidized bed system is shown in Fig. 2.12 and a more detailed description of chip and setup can be found in the materials and methods section at the end of this chapter. As shown, a v-shaped microfluidic chamber contains the ensemble of magnetic beads, retained by an external permanent magnet positioned in alignment with the central axis of the chamber. The main dimensions of the chamber were an angle of 13° and a height of 50 µm. A bent 100 µm wide input channel avoids the return of beads towards the inlet when flow is stopped: the combination of magnetic force and geometric confinement induces a compaction effect that turns the beads ensemble into a closely packed arrangement associated with a low bead mobility.

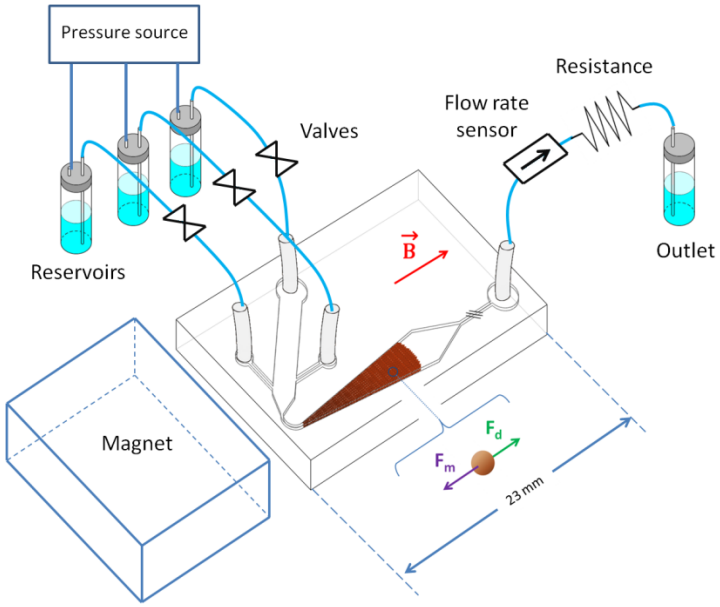

Figure 2.12. Diagram of experimental setup.

Two working regimes exist depending on the input pressure. If the pressure is low, more exactly if it is insufficient to compensate for the magnetic forces applied on the beads due to the magnetic field gradient, a static packed bed regime exists (Fig. 2.13a) with a very low flow-rate percolating through the bed. When the input pressure increases beyond a certain minimum fluidization pressure, compensation forces are possible and fluidization occurs, with a constant recirculation of particles moving downstream in the chamber axis region and coming back following the walls of the chamber (Fig. 2.13b). Bed size and hence porosity also increases with increasing imposed flow-rates. These first results show that the behavior of the magnetically stabilized fluidized bed is quite similar to those of more conventional gravity driven devices.

This system was optimized for the fluidization of superparamagnetic particles in the range of 1 to 5 µm. We investigated the influence of channel geometry, magnet position and pressure/flow-rate conditions in order to i) optimize the bed capacity and stability over a large range of flow rates ii) ensure a uniform sample flow across the device and iii) favor the recirculation and mobility of the particles in the device to maximize sample/particle interaction. Characterization results will be shown next.

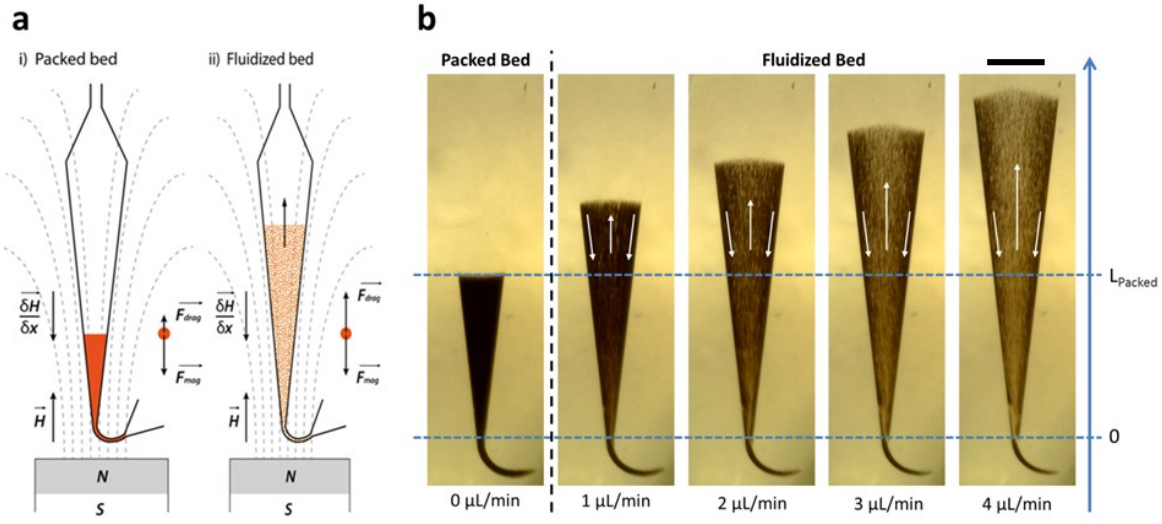

Figure 2.13. (a) Schematic illustrations of the microfluidic fluidized bed for two working regimes: packed bed when the imposed pressure is not sufficient for fluidization, and fluidized bed where an equilibrium between drag and magnetic forces is reached. (b) Images of the fluidized bed in the packed regime and fluidized for a series of flow rates (scale bar = 1 cm).

2.7.1 Chamber geometry

It is interesting to notice that conical micro-fluid beds are considered to suppress slugging and to favor particle mixing in regards to simple cylindrical beds. This geometry is interesting in particular when the particle tend to interact and agglomerate (Potic et al. 2005). Previous work performed by our team suggested some limitations arising from the channel geometry and magnetic field distribution on the particle mixing and recirculation (Le Nel et al. 2008). Channeling mechanisms were indeed observed in straight microchannels with magnets placed on both sides of the device. One of the main objectives was to generate a homogeneous magnetic field distribution in the device. As we suggested before, a single magnet aligned along the main channel axis provides an efficient solution to generate a uniform magnetic field parallel to the channel midline axis thus avoiding the drawbacks that were encountered with two magnets. We believe that both the homogeneity of the magnetic field orientation and the v- shape of the channel are essential to enhance the fluidization regime and favor particle recirculation through a spouting-like mechanism (Holdich 2003).

The vertical confinement imposed by the channel geometry (50 µm high) is also important as it favors favor the homogeneity of the fluid flow distribution across the

channel (perpendicular to the channel axis). Whereas Poiseuille flow may arise in a square channel geometry, hydrodynamic simulations clearly show a rather uniform flow distribution across the v-shaped chamber along the y axis (Fig. 2.14). This means that the balance between magnetic and drag forces is homogeneous across the channel and is mostly affected by the distance to the magnet. We believe that this feature is essential to maintain the homogeneity of the fluidization. Also importantly, the downstream reduction of flow velocity due to the channel v-shape is expected to compensate for the downstream reduction of the magnetic force.

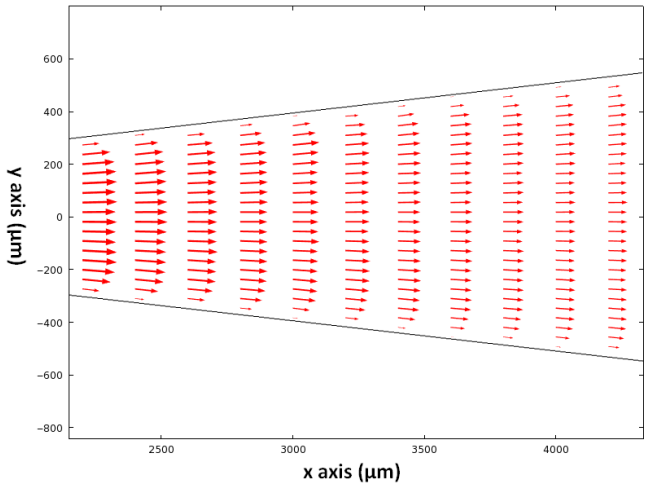

Fig. 2.14. Typical flow intensity distribution inside the microfluidic v-shaped chamber for a 3 µL/min flow rate. The profile of velocities is relatively flat across the width of the channel. Velocities decrease towards the output (right side) from 2 mm/s on left to 1 mm/s right.

In line with our experience, simple constant-width channels loaded with magnetic beads resulted in the formation of preferential ways (channeling) that only managed to disturb the cohesion of a narrow central region (Fig. 2.15a). On the other hand, V-shaped chamber were succesfully used to obtain fluidization, the results on fluidization distribution of a series of chamber angles shown in Fig 2.15a. Although fluidization is seen to be possible even with large angles, the expansion capacity of the bed is in this case severely limited as magnetic beads tend to flow preferentially in the central region, losing mobility on either side. A chamber angle of 13° was on the other hand seen to show a more homogeneous particle distribution and more efficient expansions, almost linear as a function of imposed flow-rate (Fig. 2.15b). This particular angle was initally chosen because of its similarity to the natural angle formed by preferential fluidization paths in confined channels (such as seen for 0° in Fig. 2.15a). Due to its response to imposed flow rate (in line with gravity-based beds), highest porosity homogeneity and fraction of fluidized beads, this was the selected option for further studies.

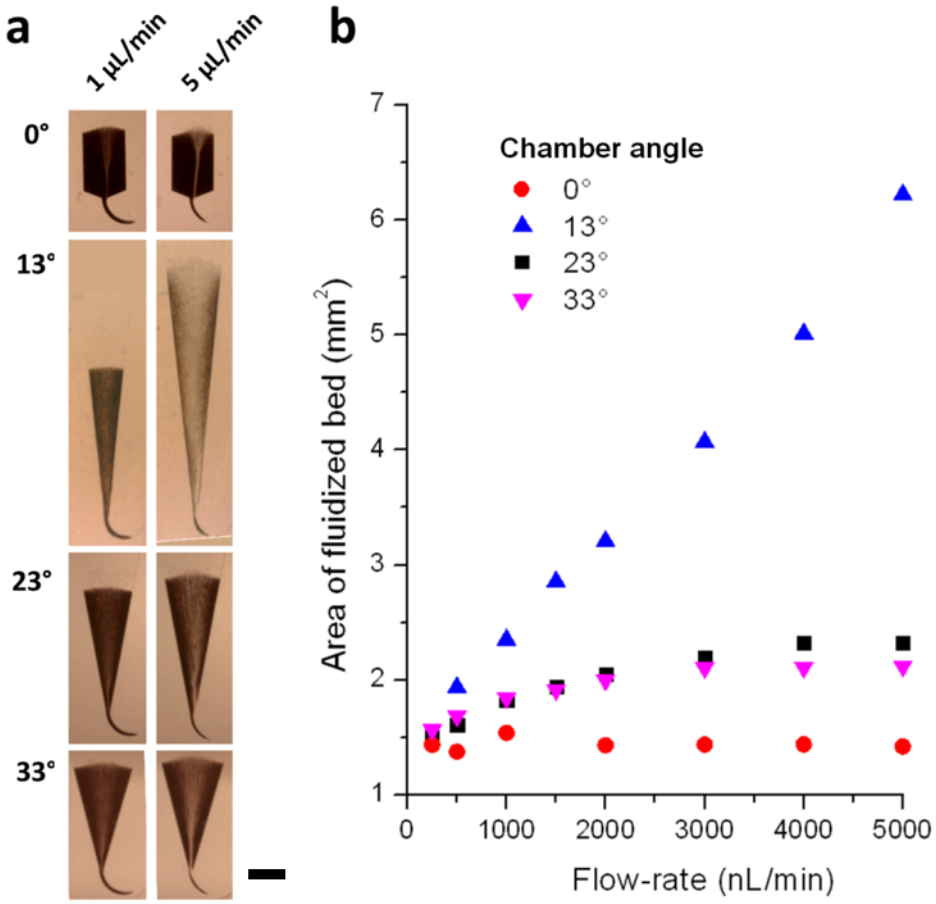

Figure 2.15. (a) Influence of chamber angle on fluidization behavior and (b) expansion as a function of imposed flow-rate. A chamber angle of 13° was seen to be optimal for the fluidization of a maximum of solid phase fraction (scale bar = 1 cm).

2.7.2 Influence of magnetic field distribution

An optimal distribution of the magnetic field was also seen to be necessary in order to make fluidization possible and further adjust the geometry of the solid phase. Superparamagnetic beads are known to self-assemble in the form of chains and clusters in the presence of magnetic fields due to the magnetic pole interaction between the magnetic moments induced on the particles (Hayes et al. 2001). The resulting clusters tend to align parallel to the streamlines of the magnetic field. This behavior was reproduced in our system, where bead clusters formed and further aligned with the magnetic field independently of fluid flow (Fig. 2.16).

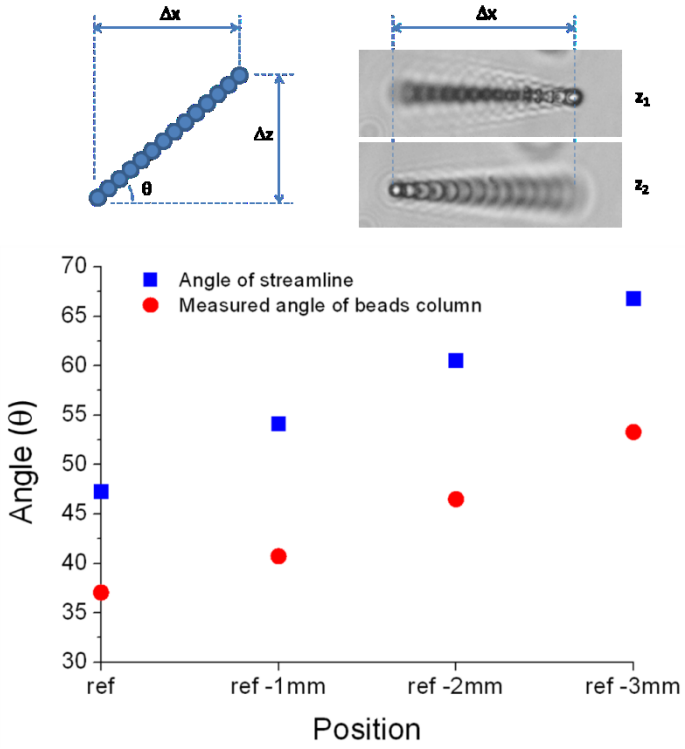

Figure 2.16. Measured angle for an independent and straight 13-beads column inside the microfluidic chamber. Angle measurements were obtained by focusing on each terminal bead of the column. The angle of the column is compared with the angle of the magnetic field streamlines obtained from finite elements simulation, showing a strong correlation.

Fig. 2.17 shows the effect on bead distribution in the fluidized bed as a function of the position of the magnet in the z axis (perpendicular to the plane of the chamber). All the results seen in the previous section were obtained with a chamber z position at the level of the bottom face of the magnet, a position considered the reference in the figure.

The results show that a chamber closer to the axis of magnetization of the external permanent magnet leads to more compact and hence less porous bed. This is partly due to the resulting increase in magnetic forces in the x direction, but also importantly due to the formation of longer clusters allowed by reduced inclination angles (the length of the cluster being limited in the z dimension by the height of the chamber). For a chamber z position close to the axis, the clusters become long enough to increase particle cohesion to the point of impeding recirculation even at high flowrates (Fig. 2.17a). In these conditions, a preferential channeling tends to appear in an otherwise compact bed (Fig. 2.17b). A minimum cluster angle is hence essential for fluidization.

On the other hand, an increased z distance between magnet and chamber axes results in more vertical magnetic streamlines, the resulting tilted clusters being shorter (Fig. 2.17a). This is accompanied by an increase in bed length and thus porosity (Fig. 2.17b). The reference position previously described (resulting in cluster angles of ~35-45° and thus ~70-85 µm in length) was found to be a good compromise between low void fraction and even porosity distribution for the purposes of the present work, although other

configurations could be more suitable depending on the application. Fluidization was also seen to be possible with an increased chamber thickness (data not shown), although in this case the larger clusters present a reduced surface to volume surface, less interesting for bioanalytical applications. Other changes in magnet position only lead to an increased void fraction (if magnet-chamber distance increased following the x axis), or uneven distribution and side compaction (y axis).

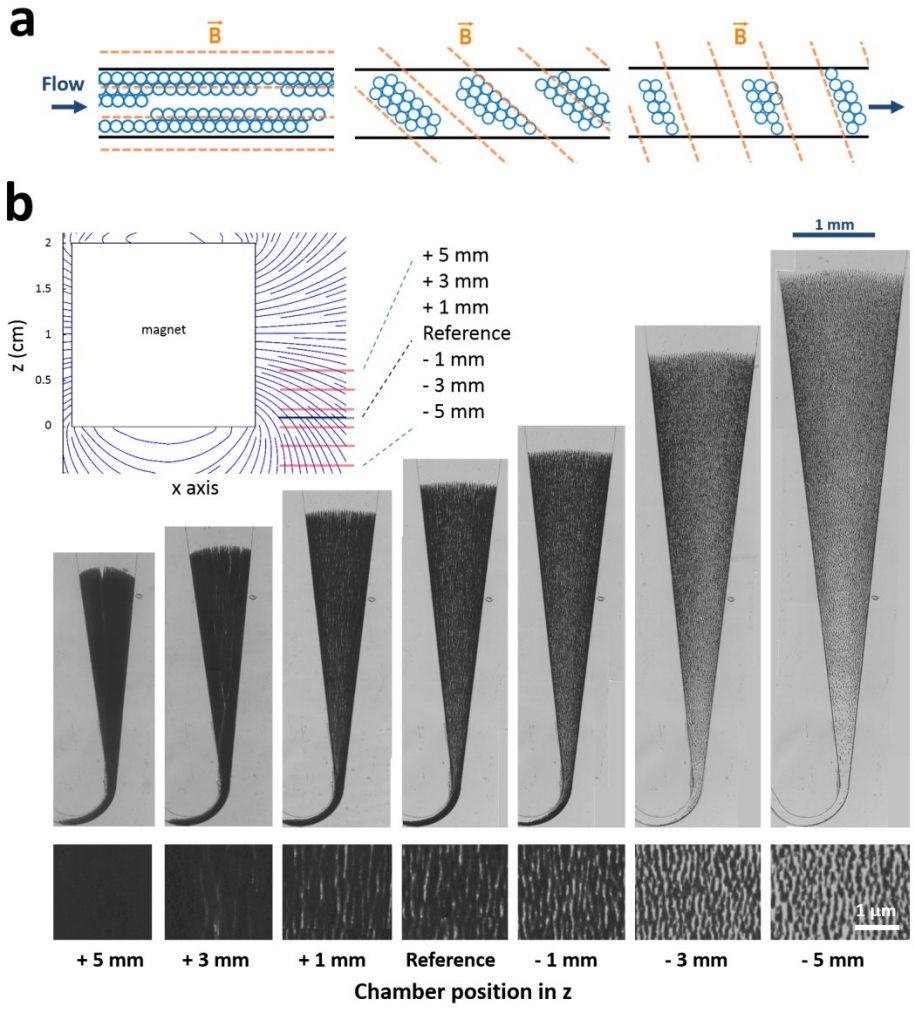

Figure 2.17. Effect of magnetic streamline angle and field gradients in the fluidization of the magnetic beads. Higher angles lead to smaller clusters and higher porosity. Small angles result in channeling effects and no fluidization (1 µL/min flow rate for all images).

2.7.3 Hydrodynamic regimes

With the resulting angle and magnetic field parameters, investigations were devoted to the hydrodynamic behavior of the fluidized bed and the operating conditions giving rise to a change in the bed regime. The inlet pressure in the device was imposed in the system and the corresponding flow rate was measured downstream. The black curve in Fig. 2.18a shows the evolution of the flow rate in an empty device i.e. where no particles were introduced. As expected, a linear dependence of the flow with pressure is observed thus showing that the device behaves as a simple fluidic resistance. The other three curves

were obtained after introducing three different quantities of microparticles in the system (25, 50 and 75 µg). The pressure vs. flow dependence of the corresponding bed was monitored in the 0-70 mbar range.

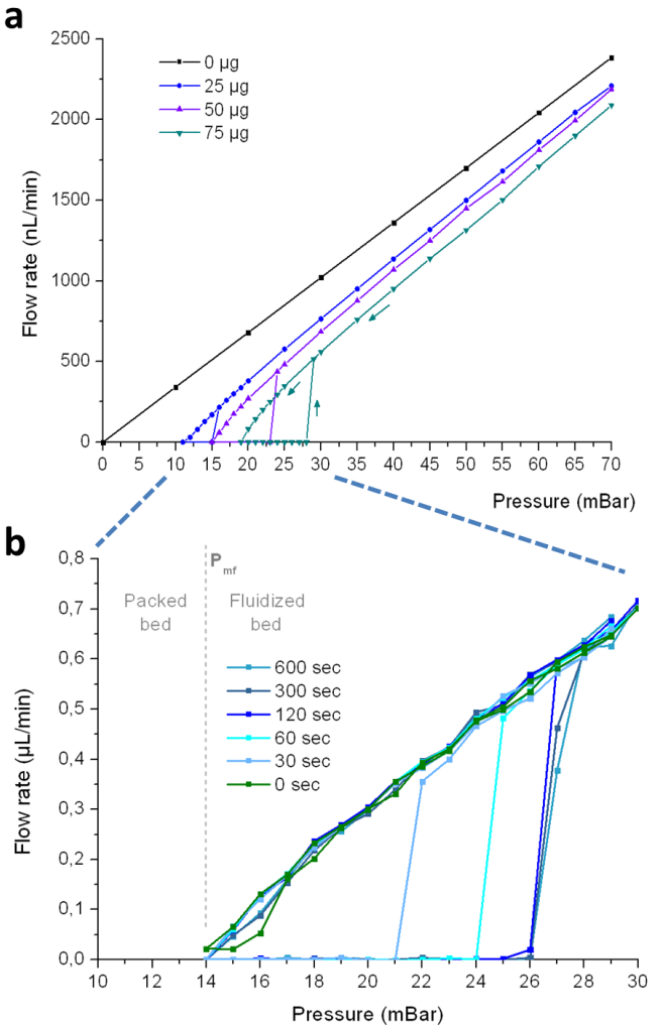

Figure 2.18. (a) Hydrodynamic pressure-flow-rate behavior of microfluidic magnetic fluidized bed for three different amounts of beads and for an empty chip. (b) Hysteresis observed for the effective fluidization pressure after different packing times.

Starting from a packed bed at 0 pressure, the pressure was increased at a constant semi-stationary rate of 1 mBar/min. During this phase the flow-rate value remains below the sensitivity of the sensor (<10 nL/min) meaning that the packed bed exhibits a very high hydrodynamic resistance. As shown by optical observations, the bed is in a packed state all along the pressure increase meaning that in this regime, the drag force induced by the liquid flowing in the bed is not sufficient to compensate for magnetic forces and to destabilize the particle assembly.

When reaching a certain pressure (15, 23 and 28 mBar for the mass of beads given before), the bed suddenly expands causing an abrupt increase of the flow rate. We will refer to this point as the pressure of effective fluidization (P_{ef}). At this point, the

hydrodynamic drag force overcomes the magnetic force plus interparticle interactions, preventing compaction of the particles.

As the pressure further increases, the bed expands and the flow rate in the fluidized bed follows a linear increase, with a slope comparable to the one obtained in the empty device (fig. 18a). This intriguing result suggests that the particle bed, in its fluidized regime induces an almost constant pressure drop which varies slightly with flow rate. This observation is consistent with the hypothesis that this pressure drop is directly related to the total magnetic force applied on the particle ensemble that maintains the bed stability and compensates for viscous forces. In the case of gravity based beds, this force can be considered as constant, and also gives rise to a constant pressure drop across the bed independently of flowrate (Fig. 2.2). In our case, however, the magnetic field gradient is not constant all over the device. In particular, it decreases in the x direction (Fig. 2.19), meaning that the total force applied on the bed is slightly reduced with the expansion of the bed, with an accompanying small reduction in its resistance. As another confirmation, the pressure drop increases with the amount of particles introduced in the bed i.e. with the total magnetic force exerted on the bed (Fig 2.18a). As a consequence, taking into account the whole microfluidic system, the hydrodynamic behavior of the device can be described as the sum of i) the contributions of the empty microfluidics channels and ii) the pressure drop induced by the magnetic force exerted on the whole bed.

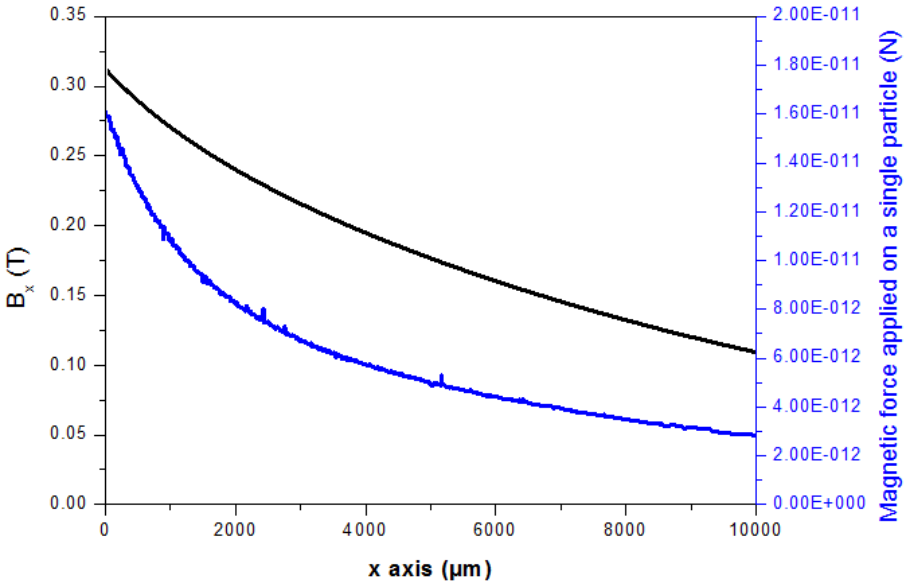

Figure 2.19. x component of the magnetic field along the main axis of the chamber, and the magnetic force applied on the magnetic beads as a result of the gradient of this field.

According to this, a very simple expression can be written for the pressure drop across the bed, if we further make the simplification that the porosity is constant for the whole volume of the bed :

$$\Delta P_{mf} = \frac{(1-\varepsilon)}{V_p} \int_0^L F_{mag/part} dx \qquad (19)$$

Where ε represents the porosity of the bed (considered homogeneous), V_p is the volume of a magnetic particle, and $F_{mag/part}$ is the magnetic force applied on each particle (force considered constant for each transversal section of the bed but varying in x). The x-component of the magnetic force on the particles was obtained from the magnetic field gradient in the chamber (finite elements simulations of the magnetic field distribution (COMSOL), Fig 2.19) and magnetization curves of Dynal particles (Fonnum et al. 2005), through the expression $F = (m \cdot \nabla)B$ (Eq. 17). By applying this force in Equation 19, as well as the information of bed length and porosity extracted from experimental data, ΔP-flow curves were obtained (Fig. 2.20). In this case, experimental and calculated values agree for low flow-rate values, when the homogeneity of the bed is maximal. For higher flow-rates the assumption of constant porosity for the entire section and length of the bed becomes less true, resulting in slight deviations. In any case, the overall good agreement between experimental and calculated results confirms the hypothesis that the bed properties are mainly driven by the balance between hydrodynamic and magnetic forces.

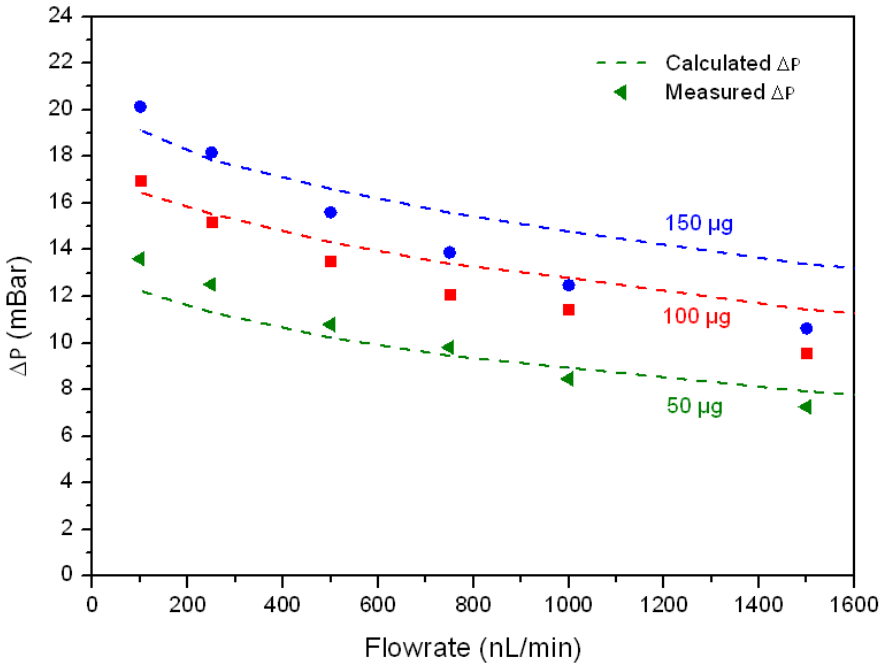

Figure 2.20. Experimentally measured pressured drop and values obtained with expression 20 as a function of the imposed flow-rate for three different loadings of beads.

Further, for zero flow-rate we can consider that this pressure drop is equivalent to the pressure of minimum fluidization P_{mf} in analogy to gravitational systems. The small values of P_{mf} also indicate the easy implementation of this fluidization, with a large range of accessible working pressures.

In order to validate the applicability of the fluidized bed in microfluidic devices, and better characterize the operating parameter for its further integration, more detailed investigations of the fluidization mechanism were performed through repeated

fluidization and compaction steps (Fig. 2.18b). Hysteresis is indeed an important feature in the characterization of fluidized bed devices, in particular in the case of interacting particles. Aggregation processes may cause variation in the incipient fluidization parameters and hinder bed efficiency (Potic et al. 2005). The experimental pressures observed for the actual fluidization can hence be higher than the calculated values of P_{mf} and will from now on be referred to as pressure of effective fluidization P_{ef}. The figure shows the evolution of the hydrodynamic characteristics of a fluidized bed during opening and closing cycles that were performed for a 50 µg bed by increasing the pressure from 0 up to 100 mBar at a 1 mBar/min rate and decreasing down to 0 at the same rate. Delayed times varying from 0 to 600 s were added before each new cycle.

The experimental analysis suggests a clear dependence of the incipient fluidization parameters on the packing process. The longer the bed remains in the packed state the higher the pressure has to be exerted in order to reach the incipient fluidization. Variation of the P_{ef} value from 21 up to 26 mBars were observed in our experiments (for a 50 µg bed). As previously stated, when switching from an already established fluidized regime to a packed one, the pressure threshold giving rise to the transition from fluidized to packed regime is constant (P_{mf} = 14 mBar for 50 µg of beads) and independent from bed history. A simple hypothesis to explain these results can be given on the base of the establishment of particle-particle interactions in the packed state. While the bed is maintained in the packed state, both rearrangement of the particle assembly and the establishment of interparticle cohesive and magnetic forces increase the bed compaction and stability. When switching to the fluidized regime, the force applied to the bed has to compensate for the magnetic pulling forces and these additional interparticle forces, thus giving rise to an increase of the effective fluidization pressure value. When integrating the fluidized bed in an analytical workflow, this behavior has to be taken into account in order to provide a robust and repeatable set of parameters to initiate fluidization. Once open, the behavior of the bed is, however, independent of its history.

2.7.4 Bed porosity

Fig. 2.21a shows measurements of the 2D area of the chamber filled by the fluidized particles at different flow rates for three loading amounts of magnetic beads. Although apparently trivial, the fact that the length of the fluidized bed proportionally increases with the amount of beads indicates that the total length of the fluidized bed cannot be predicted from an equilibrium of forces that would take place at the single particle. The total volume of the bed was then used to calculate its total porosity (ε), the total amount of particles and their individual volume being known (Fig. 2.21b). The void fraction of the packed bed was found to be around 40 %. When switching to the fluidized bed regime the mean porosity immediately increases to a minimum of 60% and further increases according to a non-linear curve up to 85% for 2µL/min. For the three bead loadings studied, remarkably similar and almost overlapping ε-flowrate curves were found. This seems to suggest that, even if a slight deviation can be observed at high velocities, the porosity is relatively independent of the bead loading, and of its total length. The

compensating effect that the v-shape of the chamber has in the equilibrium of forces along the x axis might be the reason behind this feature.

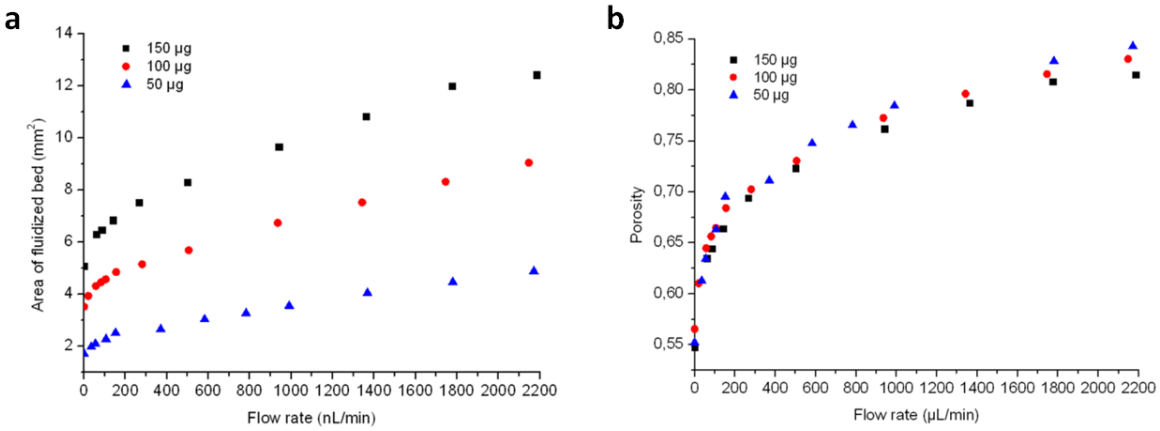

Figure 2.21. (a) Total area filled by the fluidized bed for three different amounts of beads as a function of flow-rate and (b) calculated void fraction of the fluidized bed as a function of flow rate for the three different amounts of beads.

2.7.5 Particle recirculation inside the bed

Previous calculations were made with the assumption that porosity was homogeneously distributed within the bed. This is an approximation at best, as the constant recirculation of particles leads to a complex particle distribution that also depends on flowrate. In order to characterize the motion of particles, image sequences of the particle bed were acquired in the fluidized regime and used for particle tracking followed by correlation analysis (Figure 2.22a). Both the flow distribution and particle motion in the fluidized bed were investigated for a fluidized bed containing 50 µg of 2.8 µm magnetic particles for a given flow rate of 1.5 µL/min.

The results revealed a particle trajectory pattern that is comparable to the spouting regimes sometimes employed in macroscopic fluidized beds (Holdich, 2003, see section 2.3). A flow of particles takes place in the center of the channel bringing the particles downstream. In this central region the particle velocity ranges from 8 µm/s close to the channel entrance down to 0 when reaching the terminal part of the fluidized bed. In this latter region, the particles are dragged away from the channel center towards the channel walls, according to an axisymmetric pattern (approximate velocity 1 µm/s). A backward flow following the walls moves then the particles back towards the entrance of the chamber (approximate velocity 3-7 µm/s). At the interface between the central and sidewall regions dead zones are observed: in these regions, the particle velocity along the chamber axis is almost null (Fig. 2.22b).

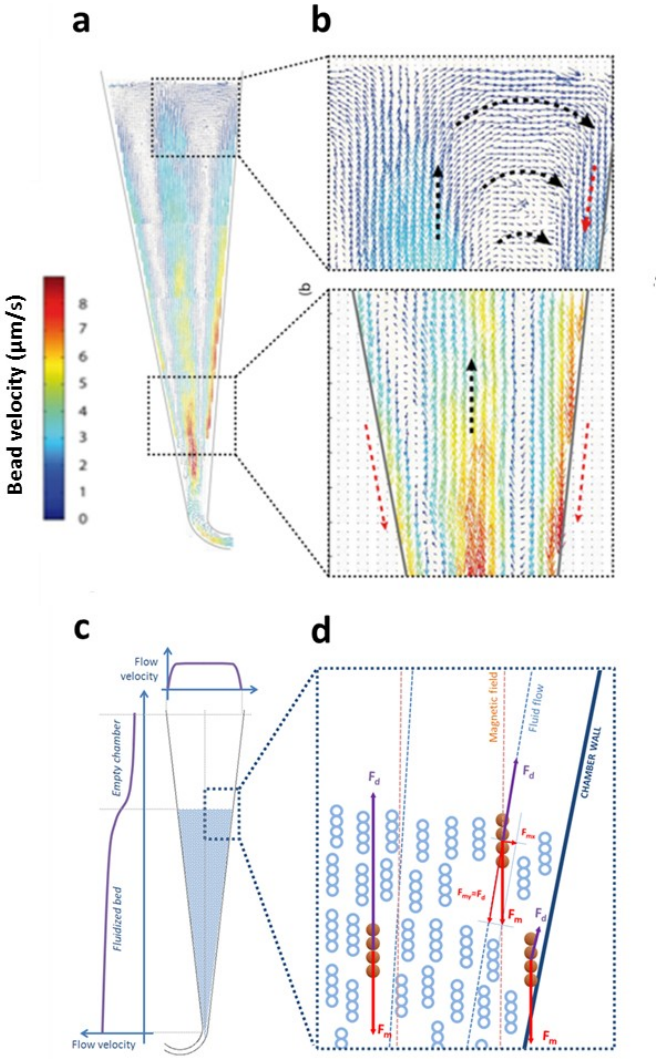

Figure 2.22. (a) Particle tracking cartography of the fluidized bed for a flow rate of 1.5 µL/min; (b) detail of the sideward recirculation in the downstream limit of the bed, and of the opposite flow regions near the entrance; (c) flow velocity distribution in the longitudinal and transversal axis of the system and (d) scheme of equilibrium of forces for the three main steps in bead recirculation.

The origin of this intriguing recirculation phenomenon can be explained, at least qualitatively, as illustrated in Fig. 2.22c and d. We hypothesize that in the central part, drag forces are dominant over magnetic forces. Particles are then dragged downstream. However, when reaching the limit front of the fluidized bed a sudden drop in flow velocity, due to the end of the solid fraction, leads to the equilibrium of forces in the x direction. The lateral displacement of particles could then be explained partly as the combined consequences of the particle inflow, that maintains the mass transfer balance, and partly the result of the no slip boundary condition near the walls: in this region, the fluid velocity decreases significantly (Fig. 2.14) such that the upstream magnetic forces become dominant. As a result, a flow of particles is formed back to the channel entrance. Moreover, simulations suggest a sideward increase in angle difference between flow and magnetic streamlines, which results in an increasing lateral force close to the walls (Fig. 2.22d).

This mechanism ensures a mass transport balance and is thus essential to provide a stable and continuous recirculation of particles within the fluidized bed. It is particularly interesting in the context of biomarker capture and extraction as it provides a continuous and homogeneous recirculation of particles and enhances their interaction with the fluid.

We have shown that investigation of the magnetic field distribution in the device could be advantageously used to predict the minimum fluidization pressure P_{mf}. Coupling these results to hydrodynamic simulations would also provide an interesting approach to predict the fluidization parameters, in particular, the bed porosity (void fraction **ε)** and expansion length. Nevertheless, investigating the balance between magnetic force and hydrodynamic drag turned out to be difficult for several reasons. Detailed observations of the particle distribution in the fluidized regime first revealed a rather non-homogenous particle spatial density and subsequently a relatively non-uniform porosity in the bed, particularly so for flow rates over 1 μL/min. Areas of maximum density are found close to the vicinity of the chamber sidewalls, where the particles are dragged back towards the channel entrance. On the contrary, the porosity increases in the regions of high flow velocity, in particular in the center of the device, where the hydrodynamic drag forces and flow velocity are maximal. This first observation is consistent with the principle of mass conservation: as the velocity of particles increases in the center, the porosity decreases in order to maintain the mass transport balance. As a result of this non-uniformity, it is rather difficult to estimate the hydrodynamic flow field distribution in the device and consequently to estimate the spatial distribution of drag forces acting on the particles. Moreover, experimental observations also revealed a fluidization regime far from the idealistic image of a fluidized bed with mobile particles independent from each other. Because of their magnetization, particles interact with each other and tend to form aggregates. These aggregates behave themselves as dynamic structures that interact with other aggregates, dissociate close to the chamber inlet because of shear stress and eventually rearrange while they are dragged along the fluidized bed. This mechanism makes the understanding and quantitative investigation of the fluidized bed parameters even more complex.

2.8. Conclusion

Fluidized bed reactors present interesting features such as constant mixing and high surface to volume ratio, that make them particularly suitable when intimate liquid-solid interaction is needed. This has resulted in the development of a myriad of industrial applications in the 20^{th} century making fluidized bed technology indispensable in chemical engineering, and particularly so in petroleum refineries.

The use of solid supports in the form of magnetic beads is also essential in many biological applications, but so far an easy and automatable method for easy bead handling is still missing. The microfluidic fluidized bed system shows clear advantages in terms of high porosity, constant mixing and relatively large range of working flow-rates. With a straightforward chip design, its implementation is particularly convenient, as the

movement is obtained simply by a time steady magnetic field obtained by an external permanent magnet, coupled to an imposed fluid flow in a microfluidic chamber that only needs to respond to certain characteristics in terms of height and tapered angle. The magnetic forces needed for its operation are also compatible with the use of commercial magnetic beads of a size typically employed in biological applications. Porosity and cluster size can be further adjusted on demand.

As is the case with its macroscopic counterparts, the microfluidic fluidized bed presents features interesting for many applications, particularly in the field of biology. This potential was investigated for three very different applications based on three different types of initial target (proteins, DNA or cells), the results presented in the following chapters.

2.9. Materials and methods

Fabrication of microfluidic device

Devices were fabricated by pouring polydimethylsiloxane (PDMS, Sylgard 184, Dow Corning) on PCB/copper molds containing positive-relief channels patterned in dry film resist (SY355, Microchem). The masters were prepared according to the process described in our previous work (Miserere et al. 2012). Briefly, a 55um thick photoresist dry film resist was laminated on a 50mm copper PCB wafer. The chip patterns were then exposed through a mask (SELBA) to UV light by conventional photolithography and finally developed. The masters were directly used for the replication of structures by PDMS casting. The resulting 3 mm thick PDMS replica was then bonded to a 100um thick PDMS layer that was previously spin coated on a 180um thick glass slide. The bonding was performed by activation of both sample surfaces through oxygen-plasma treatment.

A surface treatment with PDMA-AGE 0.5% (Chiari et al. 2000) was finally performed by incubating the polymer solution inside the chip for one hour followed by water rinsing and drying.

The design of the chip, as illustrated in Fig. 2.12, consisted of three inlets composed of two 200 μm wide channels joining a larger middle channel of 1000 μm at 45ºC. This main channel then narrows to connect the main chamber of the chip to a curved channel (100 μm wide) that will serve as the constraint for the retention of magnetic beads. The main chamber presents a linearly varying width from the starting 100 μm at the entrance to a maximum of 1.8 mm and a total length of 9.5 mm. This chamber finally leads to the output of the chip by an 11.5 mm long and 100 μm thick channel that will serve as an internal resistance of the chip.

Microfluidic setup

As shown in Fig. 1 SI the three inlets are connected to independent reservoirs, all of them controlled by a solenoid valve (Burkert 6604) used in a switch-on/switch-off configuration. The fluid flow coming from the starting reservoirs is pressure-regulated with the use of a pressure controller with three independent pressure exits (MFCS^{TM}, Fluigent) and further feedback-regulated with the flow rate measurements taken at the exit of the chip by a flow rate sensor (Flowell^{TM}, Fluigent). The material chosen for all tubings was PEEK. A 80 mm long and 50 μm

in internal diameter PEEK tube was placed at the end of the system to impose the desired global resistance.

Analysis workflow

Prior to the injection of magnetic beads in the chip the whole system was filled with buffer (PBS + 1% BSA) and 50 µg of magnetic beads (Dynabeads© M-270 Carboxylic Acid) were washed three times in batch with the same buffer. The injection of beads was then performed by disconnecting the PEEK tube of one of the entrances. A pipette cone was then inserted in the flexible PDMS chip entrance half-filled with buffer. The magnetic beads were then loaded inside the cone by pipetting them in a volume of around 30 µL. A small placed below the chip was used to bring the beads inside the chip and into the main chamber. Finally, a NdFeB12 permanent magnet (N50, Chen yang Technologies) was placed close to the channel. Permanent magnets are advantageous as they offer high magnetic field intensity value (around 1.47 Tesla). The dimensions of the magnet (30x20x20 mm) were chosen to provide a magnetic field mainly oriented along the channel axis and to minimize the lateral component of the magnetic forces is minimized. A separation of 2 mm was left between the outermost limit of the curved channel of the chip and the border of the magnet. Once both beads and magnet were in place a fluid flow could be set to pass through the system.

Particle tracking

A bed with 1% of the total number of magnetic particles Cy5-labelled was used for fluorescence imaging with a flowrate of 1.5 µL/min. Fluorescence images were taken with an interval of 100 ms and analyzed with the software PIVLab.

2.10. References

Belgiorno, V. et al., 2003. Energy from gasification of solid wastes. *Waste Management*, 23(1), pp.1–15.

Beyor, N. et al., 2008. Immunomagnetic bead-based cell concentration microdevice for dilute pathogen detection. *Biomedical Microdevices*, 10(6), pp.909–917.

Chase, H.A. & Draeger, N.M., 1992. Affinity purification of proteins using expanded beds. *Journal of Chromatography A*, 597(1-2), pp.129–145.

Chiari, M. et al., 2000. New adsorbed coatings for capillary electrophoresis. *Electrophoresis*, 21(5), pp.909–916.

Colombo, M. et al., 2012. Biological applications of magnetic nanoparticles. *Chemical Society Reviews*, 41(11), p.4306.

Darcy, H., 1856. Les fontaines publiques de la ville de Dijon : exposition et application des principes à suivre et des formules à employer dans les questions de distribution d'eau. *Recherche*, p.647.

Doroodchi, E. et al., 2012. Fluidisation and packed bed behaviour in capillary tubes. *Powder Technology*, 223, pp.131–136.

Fonnum, G. et al., 2005. Characterisation of Dynabeads® by magnetization measurements and Mössbauer spectroscopy. *Journal of Magnetism and Magnetic Materials*, 293(1), pp.41–47.

Hayes, M. a, Polson, N. a & Garcia, A. a, 2001. Active control of dynamic supraparticle structures in microchannels. *Langmuir*, 17(16), pp.2866–2871.

Holdich, R.G., 2003. Fundamentals of particle technology. *online book at http://www. particles. org. uk/particle_technology_book/particle_ book. htm, Loughborough UniversityAcknowledgment*.

Johnsson, 1994. Formation and reduction of nitrogen oxides in fluidized-bed combustion. *Fuel*, 73(9), pp.1398–1415.

Kang, S.H. et al., 2011. Catalytic performance on iron-based Fischer-Tropsch catalyst in fixed-bed and bubbling fluidized-bed reactor. *Applied Catalysis B: Environmental*, 103(1-2), pp.169–180.

Kunii, D. & Levenspiel, O., 1991a. CHAPTER 2 - Industrial Applications of Fluidized Beds. In D. K. B. T.-F. E. (Second E. Levenspiel, ed. Boston: Butterworth-Heinemann, pp. 15–59.

Kunii, D. & Levenspiel, O., 1991b. CHAPTER 8 - High-Velocity Fluidization. In D. K. B. T.-F. E. (Second E. Levenspiel, ed. Boston: Butterworth-Heinemann, pp. 193–210.

Mathur, K.B. & Epstein, N., 1974. *Spouted beds*, Academic Press New York.

Miserere, S. et al., 2012. Fabrication of thermoplastics chips through lamination based techniques. *Lab on a chip*, 12(10), pp.1849–56.

Le Nel, A. et al., 2008. Controlled proteolysis of normal and pathological prion protein in a microfluidic chip. *Lab on a chip*, 8(2), pp.294–301.

Nicolella, C., 2000. Wastewater treatment with particulate biofilm reactors. *Journal of Biotechnology*, 80(1), pp.1–33.

Pankhurst, Q.A. et al., 2003. Applications of magnetic nanoparticles in biomedicine. *Journal of Physics D: Applied Physics*, 36(13), pp.R167–R181.

Peng, Y. & Fan, L.T., 1997. Hydrodynamic characteristics of fluidization in liquid-solid tapered beds. *Chemical Engineering Science*, 52(14), pp.2277–2290.

Potic, B. et al., 2005. Fluidization with hot compressed water in micro-reactors. In *Chemical Engineering Science*. pp. 5982–5990.

Putnam, D.D., Namasivayam, V. & Burns, M. a, 2003. Cell affinity separations using magnetically stabilized fluidized beds: erythrocyte subpopulation fractionation utilizing a lectin-magnetite support. *Biotechnology and bioengineering*, 81(6), pp.650–65.

Rosensweig, R.E., 1979. Fluidization: hydrodynamic stabilization with a magnetic field. *Science*, 204(4388), pp.57–60.

Rosensweig, R.E., Lee, W.K. & Siegell, J.H., 1987. Magnetically Stabilized Fluidized Beds for Solids Separation by Density. *Separation Science and Technology*, 22(1), pp.25–45.

Siegell, J.H., JR, J.C.P. & Dupre, G.D., 1984. Crossflow Magnetically Stabilized Bed Chromatography. *Separation Science and Technology*, 19(13-15), pp.977–993.

Sornchamni, T. et al., 2004. Operation of magnetically assisted fluidized beds in microgravity and variable gravity: experiment and theory. *Advances in space research : the official journal of the Committee on Space Research (COSPAR)*, 34(7), pp.1494–8.

Tabnaoui, S., 2012. *Magnetic fluidized bed for sample preconcentration and immunoextraction in microfluidic systems*.

Valverde, J.M. et al., 2010. Fluid to solid transition in magnetofluidized beds of fine powders. *Journal of Applied Physics*, 108(5), p.54903.

Vilkner, T., Shivji, A. & Manz, A., 2005. Dry powder injection on chip. *Lab on a chip*, 5(2), pp.140–145.

Yates, J.G., 1983. Preface. In J. G. Yates, ed. *Fundamentals of Fluidized Bed Chemical Processes*. Butterworths Monographs in Chemical Engineering. Butterworth-Heinemann, pp. v – vi.

Zhu, Q. & Li, H., 1996. Study on magnetic fluidization of group C powders. *Powder Technology*, 86(2), pp.179–185.

Zivkovic, V., Biggs, M.J. & Alwahabi, Z.T., 2013. Experimental study of a liquid fluidization in a microfluidic channel. *AIChE Journal*, 59(2), pp.361–364.

Chapter 3

Protein extraction and detection applied to beta amyloids

3.1 Introduction

The global prevalence of dementia has been estimated at 6% of the population of those aged 60 and more (Prince et al. 2013). This means that an estimated 35.6 million people worlwide live with dementia, and this figure is expected to double every 20 years due to a global aging population. Alzheimer's disease (AD) is the most common form of dementia (60 to 80% of cases (Fargo & Bleiler 2014)), causing problems with memory, thinking and behavior. Its risk increases with age and symptoms usually develop slowly, getting worse overtime, eventually becoming severe enough to interfere with daily tasks.

Currently, no treatment exists for the treatment of AD. Although several FDA-approved drugs exist in the market (*Acetylholinesterase inhibitors, Memantine*) they can only help with a modest cognitive function improvement in moderate to severe patients (Winblad et al. 2007)(Howard et al. 2007), without any effect on disease progression. Research efforts are thus intense, and while so far clear slowing of disease symptoms has only been confirmed by cognitive stimulation (Woods et al. 2012), breakthroughs might be starting to appear in drug development (*solanezumab*). This is important, as an early diagnosis could potentially offer the patient the opportunity to live with the disease for as long as possible with a better quality of life. Current diagnosis relies mainly on symptoms on mental decline, a moment when severe brain damage has already taken place. A definite diagnosis can, however, only be established postmortem through the histological examination of brain tissue. Recently though, both neuroimaging (Varghese et al. 2013) and molecular biomarker detection (in the form of proteins, hormones (Doecke et al. 2012) or lipids (Mapstone et al. 2014)) are areas of research that have shown potential as indicators of early stages of AD. Among a range of studied biomarkers, levels of tau and

beta-amyloid proteins, found in the cerebrospinal fluid (CSF), have shown a strong correlation with AD (Frankfort et al. 2008). However, since no individual biomarker has been shown to fully discriminate AD from other neurodegenerative illnesses, current research on AD diagnosis is particularly focused on the finding of biomarker signatures ie. sets of relevant biomarkers with a maximum predictive potential.

Beta-amyloid peptides (Aβ) are mainly produced in the CSF by the proteolysis of a larger protein known as amyloid precursor protein (APP). This protein is a transmembrane protein consisting of 695-770 amino acids expressed in many tissues and particularly concentrated in the synapses of neurons. Evidence suggests that APP is involved in cell growth and proliferation, with possible tissue-repair functions in the brain (Dawkins & Small 2014). APP proteolysis can happen following two pathways (Fig. 3.1). In the predominant one (non-amyloidogenic), the enzyme α-secretase cleavages APP resulting in the release of two fragments (sAAPα and C83). Since this cleavage takes place in the Aβ domain of the APP, this pathway completely hinders the generation of Aβ peptides. The non-cleaved APP in this preferential pathway becomes a substrate for the β-secretase enzyme in the amyloidogenic pathway, releasing sAPPβ. The remaining peptide is cut by the γ-secretase complex in a variable sequence position, resulting in the release of Aβ peptides with a size range of 37 to 43 amino acids. Most resulting peptides are Aβ 1-40, with a proportion of 10:1 over Aβ 1-42 (LaFerla et al. 2007).

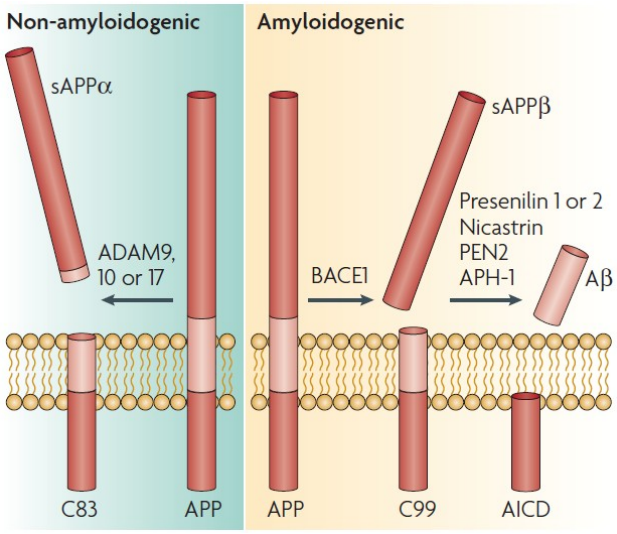

Figure 3.1. APP proteolysis pathways (LaFerla et al. 2007).

The function of Aβ peptides in the organism is to this day not completely understood, although it is known that its absence does not lead to apparent physiological changes in mice (Luo et al. 2003). Aβ overproduction is on the other hand known to lead to neurotoxicity, the formation of neural tangles, synapse damage and eventually neuron loss (Shankar & Walsh 2009). They accumulate as densely packed fibrils forming extracellular structures known as amyloid plaques. Although these plaques were for a long time thought to be the main cause of cognitive decline, research has more recently

shown that soluble Aβ oligomers are the central source of neurotoxicity (Mucke & Selkoe 2012).

Tau protein on the other hand has a clear role in the assembly and stability of neuronal microtubules. In AD patients, tau is hyperphosphorylated, leading to its dissociation from microtubules and self-polymerization. The resulting neurofibrillary tangles (NFTs) are thought to lead to neuron death through intracellular space occupancy.

The mechanism of this disease is to this day not completely understood, with opposing major hypothesis suggesting that either tau or Aβ are the main causative factor for AD. Independently of the primary AD cause, both tau and Aβ have been extensively studied as possible indicators of the illness (Frankfort et al. 2008). In particular, signature baseline levels of T-tau, P-tau, Aβ 1-42 and Aβ 1-42 to Aβ 1-40 ratio have been correlated in longitudinal studies with decrease cognitive function and AD (Humpel 2011).

We will focus here on Aβ research, as this will be the object of the present chapter. Aβ 1-42 levels have been shown to be lower in the CSF of AD patients (<500 pg/mL) than in the normal population (about 800 pg/mL) as a result of their clearance from the brain to CSF and/or blood, and their aggregation in the form of senile plaques (Humpel 2011). However, these lower levels have also been correlated with other neurodegenerative diseases such as Lewy body (Schade & Mollenhauer 2014), Parkinson's disease (Parnetti et al. 2013) or Creutzfeld-Jacob disease (Wiltfang et al. 2003). Discrimination is thus needed with a panel of biomarkers, including other beta amyloids such as Aβ 1-40, Aβ 1-38 or Aβ 2-42 (Bibl et al. 2006).

Diagnosis through CSF analysis presents a series of drawbacks, requiring for their extraction a lumbar puncture, an invasive procedure that carries non-negligible risk of nerve damage. This further hinders the possibility of using CSF for the screening of AD in the population at risk. It is for this reason that blood has been proposed as a convenient alternative to CSF. The detection of Aβ peptides in blood is however a particular challenge, as their concentration is much lower (10 to 100 times lower than CSF) due to the presence of the blood-brain barrier, their dilution in the large plasma volume and their possible degradation. While many studies have tried to find a correlation between Aβ 1-42 and Aβ 1-40 levels in blood and incipient AD, so far this possibility has not been well established, with studies showing even contradictory results (van Oijen et al. 2006)(Mayeux et al. 2003)(Gabelle et al. 2013). One reason for the difficulty in establishing strong correlations is the difficulty in accurately quantifying Aβ at trace concentrations.

While several analytical approaches based on immunoassays (Xia et al. 2010), mass spectrometry (Grasso 2011) and western blot (Wiltfang et al. 2002) have been reported for Aβ analysis, the Enzyme-linked Immunosorbent Assay (ELISA) is by far the most established technique (Schmidt et al. 2005) with a quantification performance for 1-42 peptides of 125 pg/mL (Kang et al. 2013).

Aβ are usually detected through a sandwich ELISA (Fig. 3.2). In this case the initial surface attaching is obtained through a specific antibody capture (Fig. 3.2.1) making unnecessary any previous sample purification. This initial capture is usually specific for the N-terminus of the peptide common to all Aβ isoforms. A primary antibody is then used to capture the C-terminus specific of each isoform (Fig. 3.2.2). Having a secondary enzyme-linked antibody attach to the primary one (Fig. 3.2.3) avoids the expensive preparation of enzyme-linked primary antibodies for each target of interest. Detection by substrate reaction is then obtained either by colorimetry or fluorescence detection (Fig. 3.2.4).

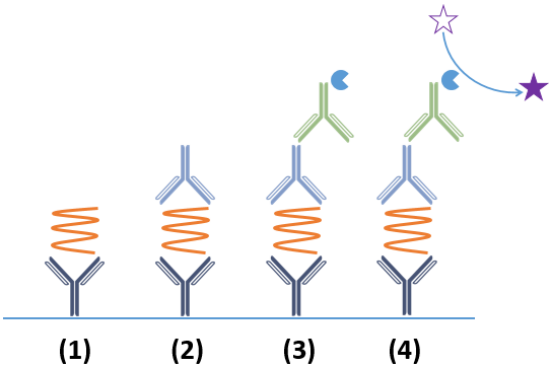

Figure 3.2. Sandwich ELISA.

These techniques, particularly ELISA, are today considered as very promissing, but they still present some limitations regarding Aβ analysis in blood. In particular, this detection is particularly difficult because of the trace concentrations of these biomarkers and detection variabilities induced by the different assessment platforms and methods of analysis, with varying degrees in terms of precision and analytical accuracy (Snyder et al. 2014). However, while research on ELISA development focuses on reducing shortcomings such as relatively large sample volumes and processing times (Oh et al. 2010), a global standarization of immuno assays is still needed for reliable comparison of reported studies (Carrillo et al. 2013). Further, the analytical workflow of ELISA techniques also presents disadvantages such as being labor intensive, with operator manipulation affecting the reproducibility of results.

On the other hand, the development of microfluidic chips, where the different operation units can be integrated, presents the potential of requiring less sample and reagent volumes, allowing automation and eventually lower cost per test. Microfluidic systems for neurodegenerative biomarker analysis have been reported for CSF (Mohamadi et al. 2010), blood and urine (Devadhasan et al. 2011). Due to the low concentrations of Aβ peptides in these sample media, preconcentration solutions have been proposed based on either electrokinetic or solid surface separation. In the first case, electrophoretic separations have been shown to lead to good separation of different Aβ peptides but too low sensitivity (200 nM, (Mesbah et al. 2014)), while methods based on isoelectric focusing are unable to separate c-truncated peptides presenting the same isoelectric point (Haußmann et al. 2013),as is the case for common Aβ peptides such as 1-39, 1-40 and 1-

42. A first preconcentratoin/enrichment step based on bead immunocapture has been proposed as a solution to increase the sensitivity of the electrokinetic techniques (Verpillot et al. 2011). As discussed previously, the use of magnetic particles offers the advantage of easier off-chip antibody grafting and on-chip bead manipulation with magnetic fields. Following on this idea, our group has already reported protein immunocapture strategies based on the percolation of samples through a self-assembled magnetic plug (Slovakova et al. 2005)(Le Nel et al. 2008). This plug made of micrometric superparamagnetic particles was obtained thanks to a magnetic field distribution generated by two external permanent magnets placed on either side of a microfluidic channel at an angle of 20° (Fig. 3.3a). With the use of enzyme-grafted beads, and due to the thin diffusion layers inside the plug, reaction kinetics could be accelerated a hundred-fold as compared with conventional batch reactions. With the use of antibody-grafted beads this system allowed high capture efficiencies. Plug stability was also shown until relatively high flow rates (~4 µL/min), although fracture phenomena were possibly already present at lower flow rates. Further, the system has also been used as a preconcentrator with the use of antibody-grafted beads, with its integration in a more complex lab-on-chip including electrophoretic steps to separate A□ peptides (Fig. 3.3b) (Mohamadi et al. 2015). Nonetheless, the low permeability (and hence low surface/volume ratio) of the plug meant that the use of complementary concentration strategies such as porous membranes made of hydrogel, was necessary (and even in this case was not able to reach the sensitivities required for Aβ detection in CSF, LOD = 25 ng).

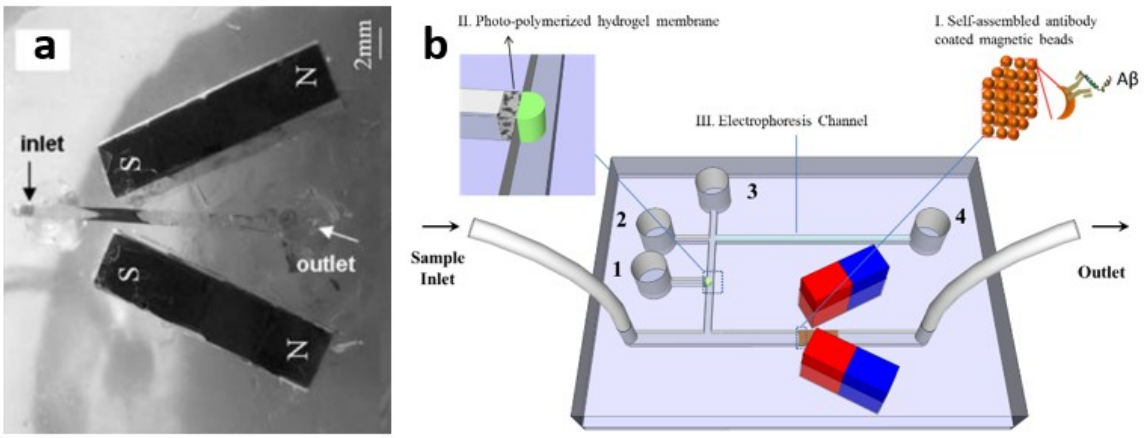

Figure 3.3. (a) Magnetic plug obtained by the injection of magnetic beads in a channel with two neodynium magnets placed on either side. (b) Integration of this system in a lab-on-chip platform for Aβ preconcentration and electrophoretic separation.

The magnetic fluidized bed described in the previous chapter seems to present interesting features such as high internal porosity and constant particle recirculation, that could lead to better performance in terms of sample extraction and preconcentration. Indeed, the development of this fluidized bed was initially an effort to obtain more efficient magnetic bead plugs as part of the EU FP7 Nadine project. For this ambitious 5-year project (2010-2015) focused on early AD detection, a preconcentration module was needed that could

benefit from the partner's expertise in antibody and bead/nanoparticle development. The objective being to couple this preconcentration module to one of the several highly sensitive detection strategies (microarray, electrophoresis, mass spectroscopy) developed by the NADINE partners.

In the following section, we will investigate the potential of our microfluidic fluidized to extract and preconcentrate AD biomarkers This characterization will be done first with a model protein, and with beta amyloids in a later time.

3.2 Preconcentration of model biomolecule

Preliminary results on the use of the fluidized to extract and preconcentrate a model biomarker were first reported in the thesis of Sanae Tabnaoui (Tabnaoui 2012). Briefly, commercial antibody-grafted magnetic beads (anti-rabbit M-270 Dynabeads©) were used to form fluidized beds to perform the immunocapture of a model fluorescent biomolecule (Rabbit Anti-Sheep IgG Alexa© fluor 488). The protocol has been optimized so that the capture and washing steps are performed in the fluidized bed regime, to take benefit of the fluidized bed properties previously reported. The elution is then performed by the introduction of an eluent solution (citric acid 0.05%, pH = 2). This resulted in target release by disrupting the antibody-antigen interactions, and the flow of this fluorescent target through a downstream channel was optically detected (Fig 3.4a). At the time, it was observed that performing the elution in a continuous fluidized bed regime led to dispersion resulting in a large eluting peak with low signal to noise ratio. Sanae Tabnaoui thus showed that stopping the flow of eluting buffer by closing the fluidized bed and letting it incubate for a given time (stop-flow mode) resulted in enhanced fluorescent peaks (Fig. 3.4b). In preliminary results she was able to reach limits of detection of 10 ng/mL (70 pM) by analysing 20 µL IgG samples in PBS medium, with this stop-flow configuration.

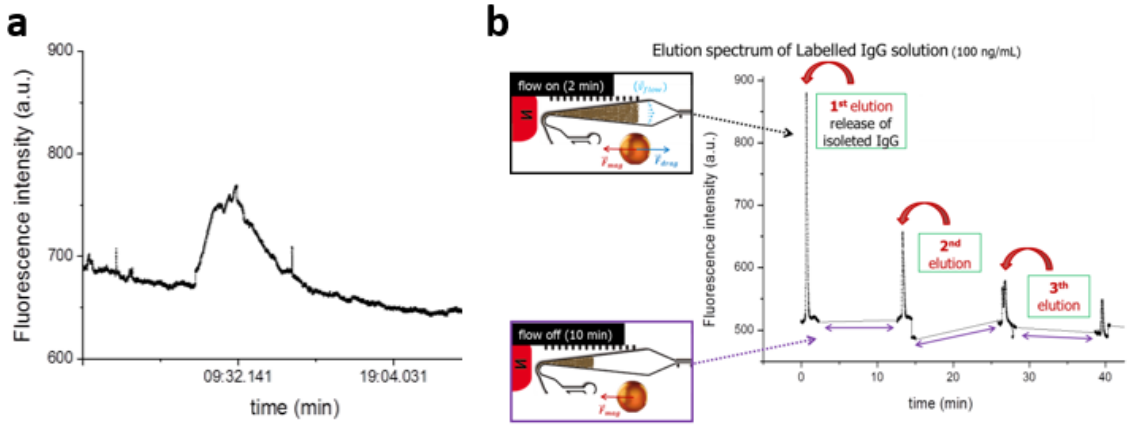

Fig. 3.4. Initial proof-of-concept of immunocapture and elution with the fluidized bed in constant flow (a) and stop-flow (b) elution modes.

These were very encouraging results, although the existence of improvement potential is already observable in Fig. 3.4b. Indeed a series of stop-flow elutions led to peaks of comparable height, a clear sign of low elution performance. Furthermore, during the elution step, the eluent is flown trough the bed till fluorescent signal was detected. This means that a fraction of target had already been eluted before incubation, resulting in lower and sometimes double peaks. Based on these observations, I have first optimized protocol parameters for both capture and elution steps to increase the system reliability and to achieve lower detection limits. Therefore, all the work presented from this point onwards are new results obtained for this aim.

The system was first characterized in regards to its capture efficiency starting with a fluorescent model protein (ALexa IgG). To evaluate this capture efficiency, the fluorescence was recorded before and after the sample flow through the fluidized bed (Fig. 3.5a). The difference between the two signals was considered to be the captured fraction, and the capture rate was evaluated with the expression$(I_0\text{-}I_C)/I_0$, where I_0 is the initial fluorescent intensity of the non-treated sample and I_C the fluorescence intensity after capture. As described in Chapter 2, the magnetic field created by the external magnet has a direct influence in the size and distribution of the magnetic bead bundles forming the fluidized bed. On the other hand, the imposed flow rate directly determines the expansion and hence the porosity of the fluidized bed. Porosity and flow rate are parameters that are expected to directly affect the residence time of analytes in the bed and hence influence their capture efficiency. The capture rate was therefore tested for a range of flow rates between 0.2 and 2 µL/min with the position of the magnet in two different positions (two separate distances of the main chamber, 2 or 5 mm in the x axis) to evaluate the influence of these parameters and determine the optimal compromise between analysis time and performance.

The results (Fig. 3.5b) show a maximum capture rate plateau of ~87% for both magnet positions and up to 0.5 µL/min. The rate then drops for higher flow rates, the decrease being particularly important for the 5 mm magnet configuration (in the order of 77% for 2 mm and 60% for 5 mm at 2 µL/min). This decrease in efficiency was expected, a result of the reduced residence times between analyte and immunosorbents for high fluid velocities. Furthermore, as seen in the preceding chapter, higher flow rates result in higher void fractions of the bed, increasing diffusion times and thus further reducing capture efficiency. This is especially the case for the 5 mm configuration, with lower magnetic forces acting on the particles to balance drag forces (for 2 µg/mL magnet positions at 2 and 5 mm result in porosity values of 0.83 and 0.9 respectively). As both high capture efficiencies and flow rates are important for the performance of the system, a compromise of 1 µL/min and 2 mm magnet distance was chosen for further testing.

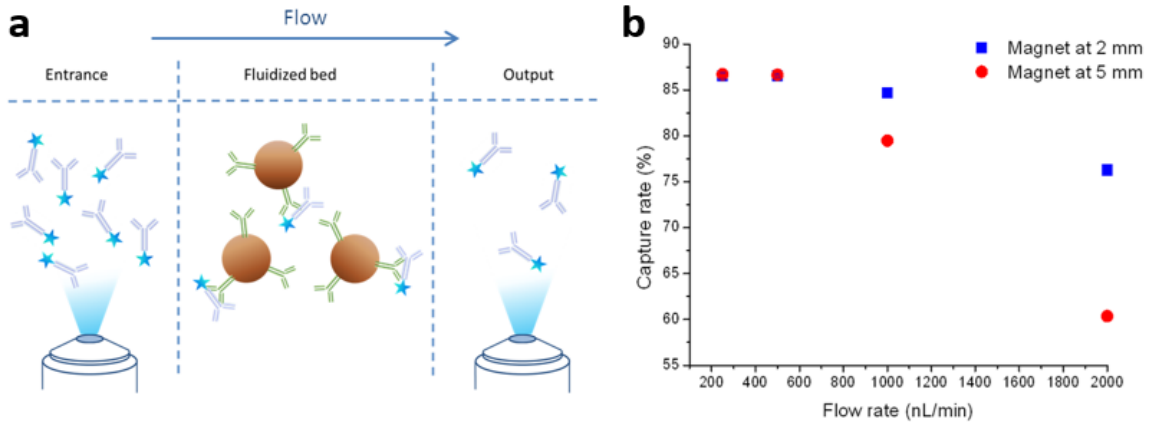

Figure 3.5. Evaluation of capture efficiency by measuring the intensity of our biomarker before and after fluidized bed and comparing fluorescent intensity (a). Results for different flow-rates and magnet distance (b).

As compared with the negatively charged (carboxylic acid functionalized particles) magnetic particles of the previous chapter, antibody-grafted beads present more interparticle interaction. This has some consequences, nominally an increased fluidization hysteresis (increased effective pressure of minimum fluidization, P_{eff}) and reduced particle recirculation. The former is particularly unhelpful when the bed needs to be fluidized at low flow rates (such as for elution step) since higher P_{eff} values mean an aperture of the bed at higher flow rates. This problem was nonetheless easy to solve with a higher global resistance of the system obtained by adding an additional tubing to the chip outlet (PEEK tube, 50 µm ID, 40 cm in length). On the other hand, the reduction in particle recirculation is largely dependent on surface grafting, but was not seen to significantly affect the capture or elution efficiencies.

Fig. 3.6 shows the capture/elution protocol as optimized for the results presented in this chapter. In particular, the elution step was optimized for a "stop and go" configuration that maximized the height and sharpness of eluent fluorescent peak signals. This was obtained with an accurate control of injected eluent volumes and closing/opening flow rates for homogeneous fluidization during eluent incubation steps. Surface treatment and bead insertion were performed as previously described (Chapter 2). A PDMS chip with three entrances contains the v-shaped chamber already described in chapter 2 and this chamber is followed by a narrow (110 µm) channel for fluorescence acquisition. Entrances are opened/closed with magnetically actuated valves (Burkert© 2/2 solenoid valve 6604, approx internal volume 45 µL), the permanent magnet (NdFeB12 N50, 2x2x3 cm, Chen yang Technologies) is positioned at a distance of 2 mm and pressure control is performed as described for other applications. For the protocol of IgG fluorescent detection the reservoirs of the three inlets are loaded in this order: entrance 1 will be used for sample, entrance 2 for washinig buffer and entrance 3 for eluent. The protocol is as follows: a given volume of sample (either 20 or 200 µL) is passed through the fluidized bed from entrance 1 at a flow rate of 1 µL/min. After this stage, entrance 1 is closed and entrance 2 is opened, and 20 µL of buffer (PBS + 0.1% BSA) are used to remove any

non-captured target at 1.5 µL/min. The bed is then let to close and compact for one minute. After this time, both entrance 1 and 3 are opened and citric acid 0.1% is flown from 3 to 1 at a sufficiently small pressure (around 20 mBar) to allow flow without leading to fluidization. This has the objective of placing the eluent in direct contact with the entrance of the fluidized bed at the right concentration and without limited dilution due to front diffusion. Measurements taken from the collected liquid from inlet 1 show that two minutes are usally enough to ensure the right pH inside the chip. At this time, entrance 1 is closed forcing fluidization, ideally at 0.1 µL/min.

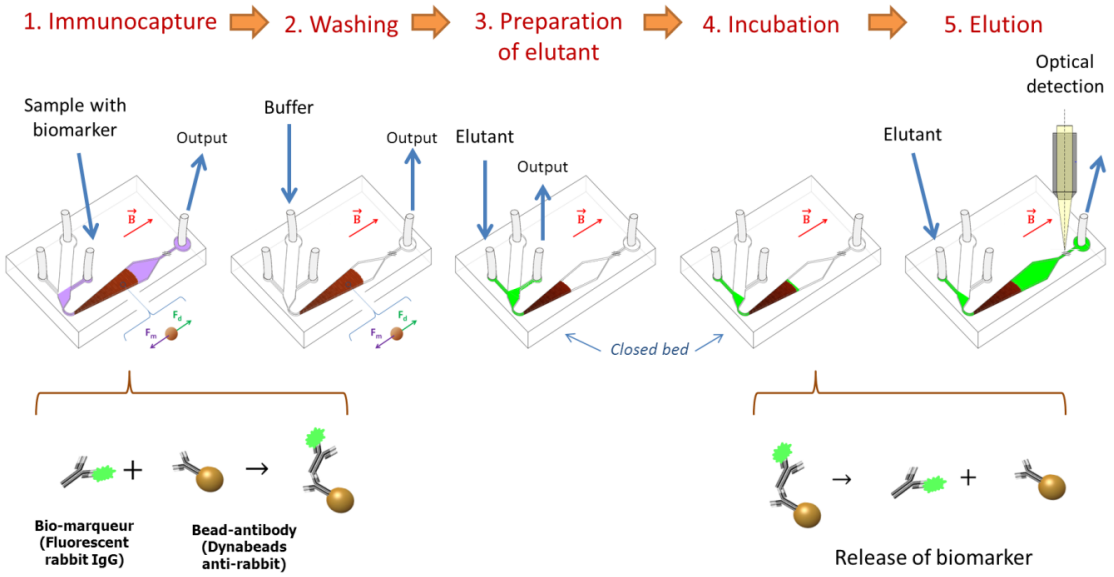

Figure 3.6. Protocol for extraction and detection of fluorescent rabbit IgG captured with anti-rabbit dynabeads©.

Opening the bed at low flowrates results in a more homogeneous initial fluidization (avoiding the formation of temporary channeling effects) and therefore allows a better percolation of small injected volumes. As previoulsy explained, the flow is thus stopped after 1 µL of injected eluent volume to limit the band dispersion while leting time for the reaction to take place. Ten minutes of incubation have been seen to be sufficient for an almost complete elution under this protocol. After this time, pressure is again increased for fluidization (0.1 µL/min), with the subsequent target release, detected in the downstream channel by fluorescence microscopy (inverted Nikon Ti-E microscope, FITC filter, 40x magnification). After 4 minutes of elution the flow is again stopped to repeat the incubation/detection cycle. The height of the resulting second elution peak is an indication of the efficiency of the initial elution. Fig. 3.7 shows the results obtained for typical experiment (200 µL IgG PBS sample at 10 ng/mL). The preconcentration factor was determined as previoulsy described: the fluorescence of the initial sample is measured before the beads injection (Fig. 3.7a) and this fluorescence signal is then compared to the height of the elution peak (Fig. 3.7b). For the stated conditions, the concentration factor obtained was 485x. By following the described protocol, the height of the second elution peak (Fig. 3.7c) was invariably below 10% of the first one,

indicating high elution efficiency. This shows a marked improvement as compared with results from the proof-of-concept phase (Fig. 3.4), when subsequent elutions still led up to 50% of the initial peak height.

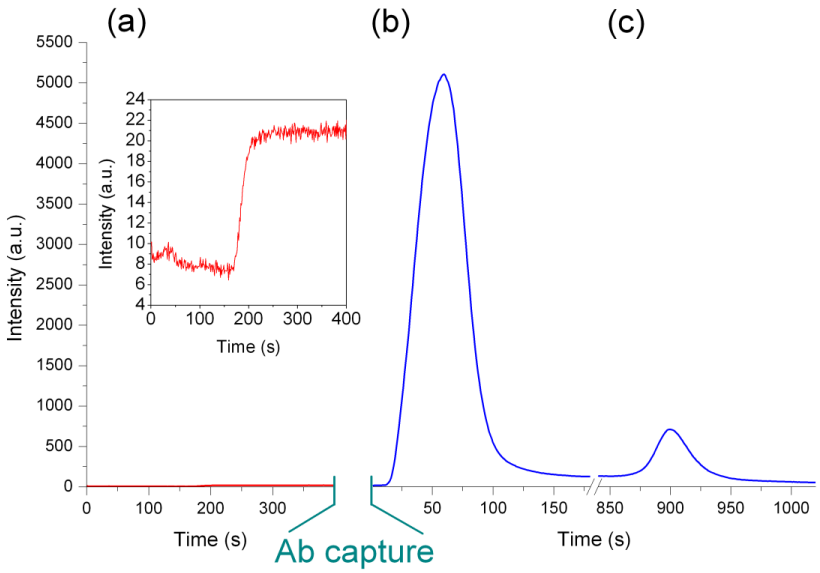

Figure 3.7. Fluorescent signal obtained for our initial sample before the introduction of the beads in the chip (a) and after the first (b) and second elution (c).

To evaluate the dynamic range, a calibration curve was obtained for concentrations of IgG in PBS (20 µL sample volumes) ranging from 1 to 110 ng/mL (Fig. 3.8a). As shown, the fluorescent signal obtained linearly follows the concentration of the biomarker flown through the chip. No saturation was observed, meaning that the immunocapture capacity of our support was not reached, and the data could be well correlated with a linear fit (ρ=0.98). The limit of detection found for these conditions (three times the noise) was 0.2 ng/mL (0.7 pM), 50 times smaller than the preliminary LOD found in the proof of concept phase. Since the initial sample volume analyzed in the immunocapture step determines the total amount of extracted analyte, higher volumes result in lower LODs. For 200 µL of sample this LOD would then be 10 times lower, that is 20 pg/mL. This is reflected by the mean concentration factors obtained for the two sample volumes (Fig. 3.8b): 39x for 20 µL and 485x for 200 µL. The error bar of the latter is more important simply because 10 times lower concentrations were analyzed, resulting in weaker calibration signals.

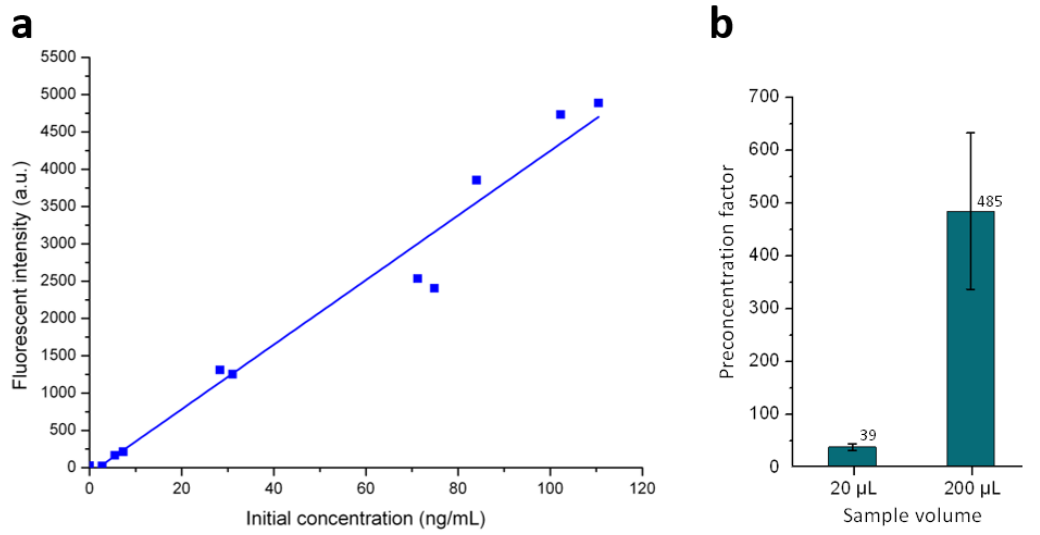

Figure 3.8. Calibration curve obtained after extraction and detection of model biomarker for analyzed sample volumes of 20 µL (a) and concentration factors obtained for two sample volumes (b).

The robustness of the system was then tested with a more complex matrix than PBS. For this purpose, fetal bovine serum (FBS) was chosen as a test medium, since the extraction of biomarkers from blood would probably require an initial separation step into either serum or plasma. Furthermore, serum is an interesting matrix because of its rich content in a variety of complex proteins (with normal serum protein levels of 6-8 g/dl (Lichstein. 1990), mostly albumin and globulin) and other lower molecular weight components (carbohydrates, nucleotides, lipids…), with possible detrimental effects on the efficiency of our immunocapture step. Rabbit IgG was thus spiked either in diluted FBS (1:10 PBS:FBS) or pure FBS, and analyzed following the same protocol previously described. The results were encouraging: as shown in Fig. 3.9 the fluorescent intensity obtained for these two conditions was equivalent, and similar to what would be expected with a PBS sample (note however that a change in the mercury lamp led to a 3x increase in intensity units as compared with Fig. 3.8). This indicates that the efficiency of our immunocapture is relatively independent of the protein content of our sample, and shows the potential of our system for analyte extraction in complex media.

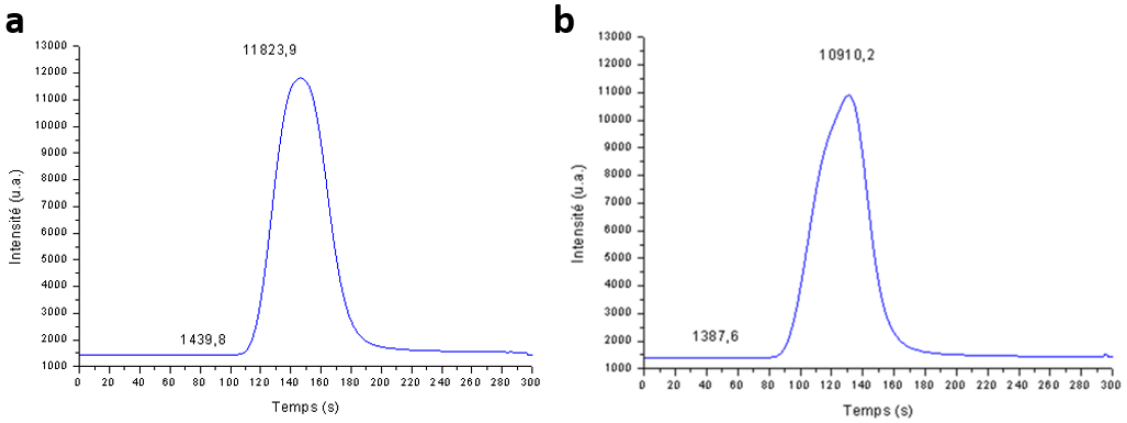

Figure 3.9. Elution peaks obtained for analyzed samples of model biomarker spiked in 10% (a) and 100% (b) fetal bovin serum. Peak height is equivalent to the expected result for PBS.

3.3 Capture of labeled Beta-Amyloid

Having validated the extraction and fluorescent quantification capacity of our system with a model biomarker, we have thus investigated the potential of our device regarding Aβ peptide analysis.

As previously mentioned, the magnetic fluidized bed system is seen as a good candidate for analyte preconcentration steps that can be coupled to a second detection system for sensitivity enhancement. In the context of the Nadine project, the fluidized bed was envisioned as a module that would be couple to one of our partner's microarray technology to achieve the limits of detection necessary for Aβ detection in blood. Indeed, the group of Marcella Chiari in the Istituto di Chimica del Riconoscimento Molecolare (ICRM, Milan, Italy) showed that by enhancing the fluorescence intensity of immunoassays with constructive interface in a Si/SiO2 substrate, they could reach sensitivities as low as 73 pg/mL for Aβ 1-42, sufficient for CSF analysis. The levels of this beta amyloid have been seen to vary in blood in a range between 5-100 pg/mL depending on whether free or cell bound amyloids are considered and whether a patient cognitive impairment is present or not (Pesini et al. 2012). Therefore, an initial preconcentration step of at least 20 times would be needed for reliable blood analysis with the indicated technology. Since the sample transfer between the microfluidic modules might induce a risk of sample dispersion due to channel migration or its dilution in the larger chamber volumes of the microarray, even higher preconcentration factors would be desirable.

Commercially labeled Aβs (HiLyte^{TM} Beta-Amyloid, fluorescent at 488 nM) were first tested. As opposed to the previous tests, no commercial beads are available presenting specific antibodies for the immunocapture of Aβs. Therefore, a grafting protocol was proposed with an antibody known for its robustness and specificity: 6E10 Monoclonal antibody (mouse IgG1, Covance®). This antibody is reactive to amino acid residues 1-16 of Aβ and hence to their N-terminal region, common to all beta-amyloid types. Further, to increase the density of this antibody on the beads surface, M-280 sheep anti-mouse IgG Dynabeads, (same size and magnetization as those used in the previous section) were selected. The antibodies already present on the beads have the capacity to capture one or more mouse 6E10 antibodies by their heavy chain, forming a double layer of antibodies that is denser than the one that could be obtained by directly grafting the 6E10 Ab on the beads surface (Fig. 3.10a). The protocol used was provided by our partners in the Clinic for Psychiatry and Psychotherapy of the Universitätsklinikum Essen (UKES) in Germany, described in detail in the materials and methods section (section 3.7). Very briefly, the 6E10 antibodies are incubated in the presence of magnetic beads for their immunocapture and this interaction is then fixated by a reaction with 2,2-Dimethoxypropane (DMP), an imidoester that covalently binds to primary amines in the antibodies. This ensures the storage stability of the immunosorbents and makes it more resistant to changes in pH and temperature.

For elution purposes, solutions of citric (0.05%, pH = 2) and formic acid (0.5%, pH = 2) were tested in order to reduce the antigen-antibody equilibrium constant through low pH values. Citric acid was tested due to its verified eluent efficiency for the model biomarker previously described. On the other hand, formic acid has already been reported as an efficient eluent of beta amyloids after magnetic immunocapture (Portelius et al. 2006)(Portelius et al. 2007). This acid is also widely used for the dissolution of Aβ from brain homogenates, as these peptides are otherwise highly insoluble (Klunk & Pettegrew 1990), and could therefore not only lead to its elution but also to its efficient dissolution in the eluent solution, necessary for subsequent analysis performance.

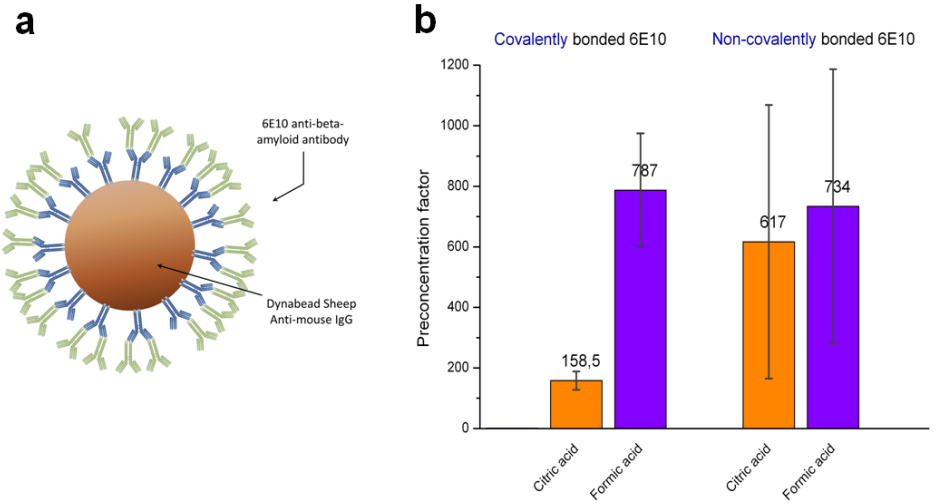

Figure 3.10. (a) Diagram of the resulting double layer of antibodies obtained with our grafting protocol and (b) preconcentration factors obtained for hilyte beta amyloid 1-40 with the same beads for two different grafting protocols and different eluents.

Fig.3.10b shows preconcentration results obtained for 200 µL sample volumes containing 5 ng/mL of 1-40 HiLyte beta-amyloids. Citric acid resulted in higher preconcentration factors when no covalent antibody fixation was used. The reproducibility of these results were low (617±420, n=3), however, when the 6E10 antibodies were not covalently fixated. This most probably indicates that non-covalently bonded beads are not stable enough either in stock or during the experiment, leading to varying results. Also, the fact that citric acid is a good eluent without Ab fixation is probably due to a break of Ab-Ab interactions rather than Ab-Aβ. This explains the low preconcentration factors when fixated antibodies are used. These results prove in any case that similar preconcentration factors (if not better) can be obtained with Aβ 1-40 as compared to our model IgG. Formic acid, appears as the best eluting buffer candidate as results were very similar for both fixation and no fixation cases with formic acid, with preconcentration factors of 787±190 (n=3, covalent bonding). A covalent Ab-grafting protocol coupled with formic acid elution seems to offer the best results in terms of elution efficiency and reproducibility for Aβ 1-40 extraction and preconcentration.

The eluent obtained from formic acid elution steps was collected at the outlet of the chip in 10 µL collecting tubes (Tygon® ID = 500 µm) for further analysis by capillary-zone

electrophoresis/laser-induced fluorescence detection (CZE/LIF). The results (Fig. 3.11) revealed that the non-covalent bonding of the antibodies resulted in several electrophoretic peaks, probably due to the presence of eluted antibodies together with the fluorescent amyloids (Fig. 3.11a). A peak due to Aβ 1-40 was nonetheless positively identified. However, the use of DMP bonded 6E10 antibodies gave rise to single peak electropherograms, a peak that we believe was due to Aβ 1-40 and that would indicate a high purity of our eluent product. This was confirmed with negative controls in which beads grafted with a non-specific antibody (anti-CD44 mouse antibody), following the same covalent functionalization protocol, were used to capture the same concentration of Aβ 1-40. In this case no peak signals were observed with capillary electrophoresis analysis, indicating a high specificity of our immunoassay.

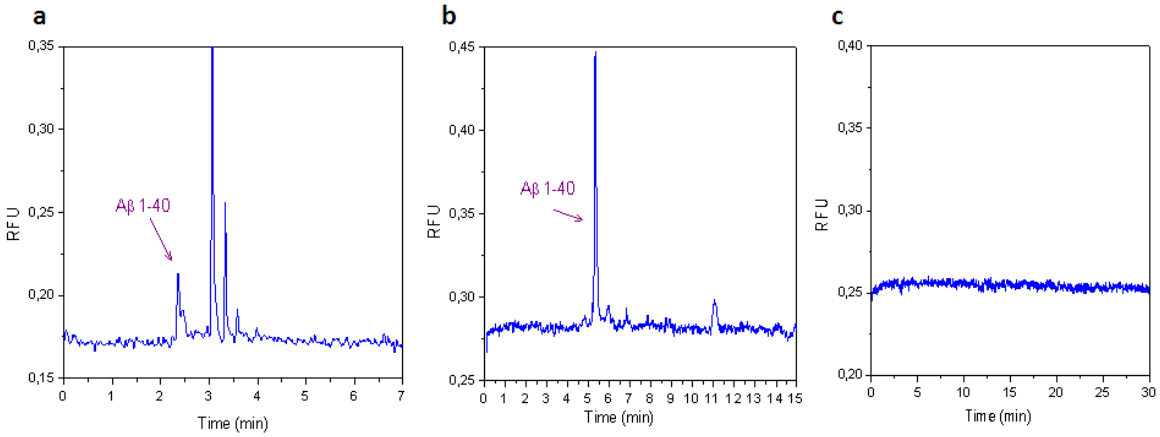

Figure 3.11. Electropherograms obtained for the recovered eluent after Aβ 1-40 immunoconcentration on-chip for (a) non-covalently bonded 6E10 antibody, (b) covalently bonded 6E10 and (c) covalently bonded anti-CD44 antibodies. Peak signals identified as Aβ 1-40 are indicated. RFU = relative fluorescence units.

As Aβ 1-42 is known to be more clinically relevant than Aβ 1-41 (Shaw et al. 2009), and to evaluate the potential of our approach to be used for biomarkers signature, the same study was performed for this peptide with these optimized conditions. As the fluorescence for the labeled Aβ 1-42 was lower (around 5 times lower) than for its 1-40 counterpart, higher initial concentrations were used, as indicated in Fig. 3.12. In this figure the elution profiles obtained for Aβ 1-40 and 1-42 peptides are compared. The results indicate that the elution step is less efficient in the latter case: preconcentration factors are seen to be ~1/4 of those obtained for 1-40 and, more importantly, the second elution peak is only half the height of the first one, an indication of an incomplete first elution. The difference in elution efficiency between the two peptides might be due to their structural differences, 1-42 beta amyloids presenting conformational states that confer it with a strong tendency to aggregate and form AD plaques. Bundles of aggregated Aβ on the immunosorbents could be more resistant to elution conditions. Although this same phenomenon could also result in different immunoaffinities, the total area of all elution peaks seems to be similar for the two peptides, suggesting that our initial capture rates are comparable.

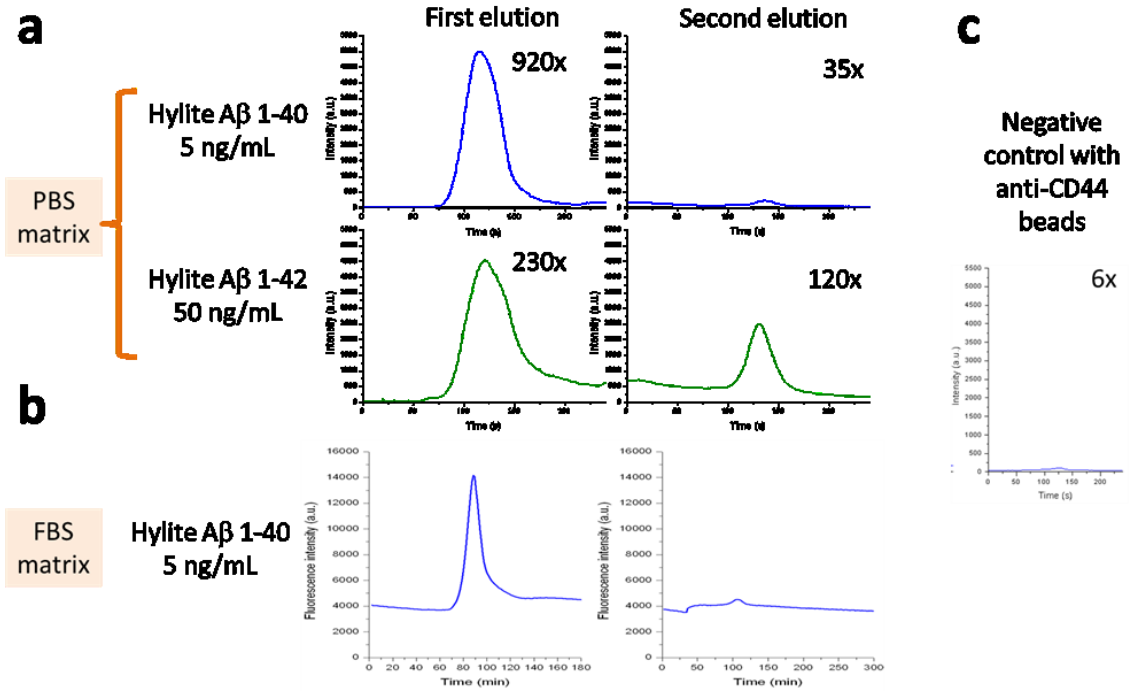

Figure 3.12. (a) First and second elution peaks obtained after extraction from 200 µL of sample and elution with formic acid of 1-40 and 1-42 fluorescent abetas. (b) Same procedure performed for 1-40 abetas in FBS matrix and (c) negative control with 1-40 abetas but non-specific capturing antibodies.

As previously, the experiments were reproduced with Aβ 1-40 in an FBS medium (Fig. 3.12b). This resulted in efficient elution peaks (with Aβ 1-40). In this case though, it was not possible to determine the preconcentration factors, as the initial FBS solution is intrinsically fluorescent at 488 nm even in the absence of Aβ. For this quantitative evaluation, the same procedure should be repeated with Aβ labelled by a different fluorophore.

Finally, to evaluate the selectivity for our approach, negative controls were performed by replacing the 6E10 antibody with a different mouse antibody (anti-CD44) following the same grafting protocol. Repeating the same protocol of capture/elution with Aβ HiLytes 1-40 concentration factors more than 100 times lower (~6x) were obtained. This not only indicated that our positive results are due to a highly specific immunocapture, but also that the peak signal obtained does not present a significant contribution of free fluorophores from the HiLyte^{TM} solution, that could be adsorbed on the surface of the beads and released during elution.

3.4 In situ fluorescent labeling of beta amyloids

The results from the previous section show the potentiality of our system as an extraction and preconcentration module for Aβ peptides, the final goal being to combine this module with a detection module for protein identification developed by our Nadine partners.

For the detection/analysis of real patient samples, however, the derivatization of the peptides is a necessary step to allow their downstream detection with most methods developed in the EU project, particularly so for capillary electrophoresis, a promising candidate for chip integration.

While previous systems based on an on-chip immunocapture of Aβ peptides with magnetic beads relied on an off-line derivatization of the peptides prior to on-chip operation (Mohamadi et al. 2010)(Mohamadi et al. 2015), this labeling-capture-elution sequence is hardly adaptable for complete chip integration. This is the case due to two main limitations: (i) it would be necessary to add a microfluidic chamber containing no beads for fluorescent labeling before immunocapture and (ii) it would be particularly inconvenient to mix the sample and fluorophore solutions due to the prevailing laminar flows in microchannels. Initiated by our partners in the Faculty of Pharmacy (University of Paris-Sud), we have proposed a capture-labeling-elution sequence that would allow a full integration, with all the steps taking place on the surface of the beads under fluidization conditions. The labeling protocols were first developed off-chip by our colleagues in order to, in a second step, perform an on-chip Aβ labeling after the immunocapture step of untagged peptides, followed by elution.

The conditions for the capture of Aβ peptides were kept identical to the previous section i.e. magnetic beads functionalized with the 6E10 antibody following the covalent grafting procedure described in section 3.3 and in the materials and methods, were employed. For this part, since the labeling step is not specific for the different peptides isomorphs, three different Aβ peptides (1-38, 1-40 and 1-42) have been used for the capture-labeling-elution in order to compare the performance of the protocol with a capillary electrophoresis analysis after on-chip procedure.

FP488 was the fluorescent dye of choice for the labeling of the immunocaptured proteins. This fluorophore binds covalently to the amino groups of the peptides, each Aβ presenting three conjugable amino groups: one primary amine in the N terminus and lysines 16 and 28. Borate buffer (pH = 10.5) was employed as the medium for FP488 fluorophore. A basic medium is known to lead to the formation of ditagged labeling that then result in higher intensities and better resolution than monotagged species when analyzed by CE-LIF. However, due to the immunocapture of the N terminus with the 6E10 antibody, there is a risk of less availability of the primary amine for fluorescent labeling. Also, the basic medium employed might accelerate the hydrolysis of FP488 resulting in a reduced labeling efficiency. Therefore, the concentration of FP488 was increased (0.6 mg/mL) as compared with previous reported work (0.2 mg/mL) ((Mesbah et al. 2014)(Verpillot et al. 2011) and batch labeling steps were performed for longer times (30 min instead of 5 min) to compensate for the loss of fluorophore and ensure stable conjugate formation.

Preliminary batch results indicated that chemical elution at room temperature with formic acid (0.5%), citric acid 100 mM or ammonium hydroxide 1% led to no beta amyloid

signal in subsequent capillary electrophoresis analysis. This was in contradiction with reported successful elutions of bead-immunocaptured Aβs using these chemicals (Verpillot et al. 2011)(Portelius et al. 2006)(Svobodova et al. 2012). In these cases, however, a labeling-capture-elution approach was employed, meaning that our on bead labeling process may result in more difficult Aβ peptide elutions due to the hindrance of FP488 dyes non-specifically adsorbed on the surface of the beads. An alternative reported elution method is the use of high temperatures to break the interaction between antibodies and Aβ peptides (Haußmann et al. 2013). This possibility was successfully tested in batch for a range of temperatures and, while 95°C was seen to be optimal, temperatures as low as 60°C resulted in significant CE signals, offering encouragement for on-chip thermal elution integration. Further, borate buffer (pH 10.5) was used successfully as the medium for these elutions, simplifying the protocol by using the same buffer for labeling, washing and elution steps and being this medium highly compatible with subsequent CE analysis.

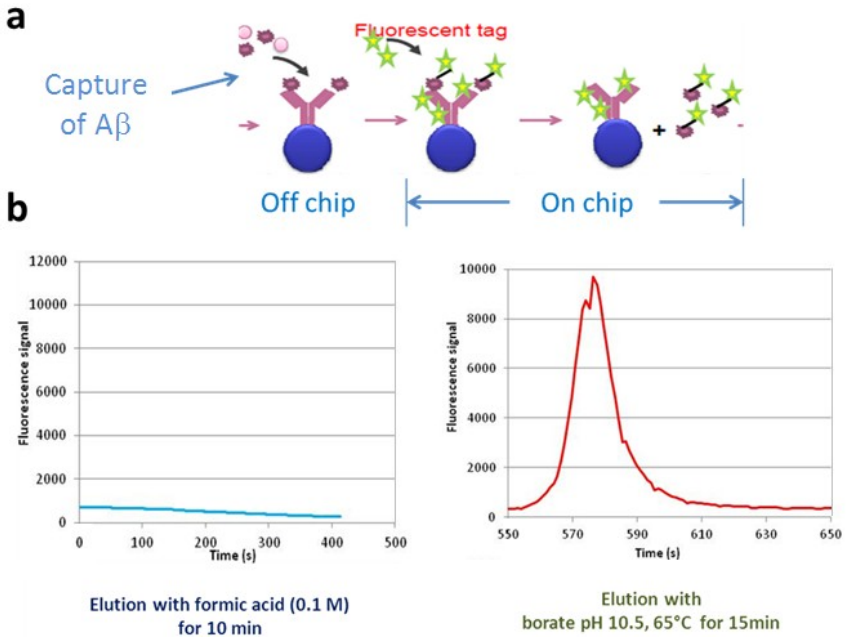

Figure 3.13. (a) Diagram of the protocol used for off-chip immunocapture followed by on chip labeling and elution. (b) Elution results obtained with either a formic acid elution at ambient temperature or a thermal elution at 65 °C in the presence of basic pH.

After this preliminary off-chip study, the protocol was adapted to the characteristics of the magnetic fluidized bed. For simplicity reasons, in a first time the immunocapture step was performed off chip and the beads (50 µg) inserted in the chip once Aβ capture was established (Fig. 3.13a). This immunocapture was performed with overnight incubations at 4°C with a highly concentrated solution of 1-39, 1-40 and 1-42 Aβ peptides in equal proportion, the presence of several peptides allowing the comparison of their capture/elution efficiency in the final eluent by capillary electrophoresis analysis. By doing this overnight and high concentration off-chip capture, it is ensured that the amount of captured Aβ is maximum, also maximizing the possible signal and eluted peptides for a first proof of concept.

The on-chip labeling was then performed by passing borate buffer (pH 10.5, 15 µL) containing Fluoprobe-488 NHS (0.6 mg/mL) through the fluidized bed at a flow rate of 0.5 µL/min. After this labeling step, the extra and unreacted fluorophore was washed away by flowing borate buffer (2 µL/min for 20 min). In a first time, the possibility of a chemical elution was tested following the same procedure with formic acid that had been successfully applied to the elution of Hylite Aβ peptides. However, as was the case in preliminary batch experiments, this resulted in no elution peak, as shown in Fig. 3.13b.

Alternative thermal elution steps were thus considered, following the encouraging results from batch tests. This presents the added advantage of simplifying the protocol, as no extra eluent is needed and hence also no precise prefilling of the fluidized bed for incubation. However, high heating in a microfluidic chip, and more precisely in a PDMS chip, can lead to the formation of air bubbles in the channels due to PDMS gas permeability. On-chip thermal elution tests were therefore performed with borate buffer at high pH (pH = 10.5) and a temperature of 65°C. These conditions resulted in fluorescent elution peaks, as shown in Fig. 3.13b.

To characterize the contribution of this fluorescent peak from either the tagged beta amyloids or free flowing fluorophores, the eluted solution was pushed and collected into a PEEK tubing (length of 30 cm, internal diameter of 250 µm) connected at the output of the microfluidic chip. The solution was subsequently analyzed by capillary electrophoresis coupled to Laser Induced Fluorescence (CE-LIF). Unfortunately, these conditions did not lead to the appearance of peaks due to beta amyloids, the electropherogram only showing peaks identified as free fluorophore. This suggests that our peak in Fig. 3.12c is essentially due to the elution of fluorophore non-specifically adsorbed to the surface of the beads or microfluidic channels and later eluted by the temperature increase. A reason for the absence of peptide related signals might be the insufficient elution temperature, but the fact that the eluted product is diluted in the outlet collecting tube could also contribute to a loss of peptide signal.

To maximize the efficiency of the thermal elution and verify its validity after an on-chip labeling step, similar tests were performed following the capture-labeling-elution sequence but with the elution performed off-chip at 95°C. This time however, the capture step was implemented inside the chip, extracting 1-38, 1-40 and 1-42 at 60 nM (248, 260 and 271 ng/mL respectively) from a sample of 100 µL at 1 µL/min (Fig. 3.14a). A fluidized bed with 100 µg of beads instead of 50 was used to maximize the amount of captured peptides. After the washing step with borate buffer, a labeling step was performed (same protocol as previous case). Another washing step followed, after which the magnetic beads were extracted from the chip by removing the magnet and collecting the output solution in an external tube. The tube containing the beads was then heated at 95 °C and the resulting supernatant analyzed by CE-LIF. In this case, the resulting electropherograms (Fig. 3.14b) showed observable peaks attributed to the three beta amyloids and, even if the intensity of the peaks was relatively small, the peptides were well separated by the electrophoresis technique and easily identifiable.

These results show that the unlabeled Aβ peptides can be extracted and preconcentrated thanks to the fluidized bed and that a subsequent on chip labeling can be directly implemented on chip. To our knowledge, this is the first time that bead immunocaptured beta amyloids are directly labeled on-chip. The operation times were also considerably shortened, from 15 hours in batch mode to around 3 hours with the fluidized bed. Furthermore, while an undesirable preferential capture of 1-42 over other peptides was reported for bead immunocaptured beta amyloids after an off-chip labeling (Svobodova et al. 2012), this was not observed in our case. These are therefore very encouraging results, as they show the feasibility and advantages of the integrated capture-labeling-elution approach. To overcome the limitations in terms applicable temperature, that hinder the efficiency of our on-chip elution step, further tests are still needed. In particular, chips fabricated with thermostable materials, such as cyclic olefin copolymer (COC), should allow the increase of on-chip elution temperatures while avoiding the appearance of gas bubbles. Finally, a future coupling of the electrophoretic separation together with the fluidized bed in a single microfluidic device should lead to much improved limits of detection, due to the elimination of volume loss, resulting in much enhanced enrichment gains and reduced variability.

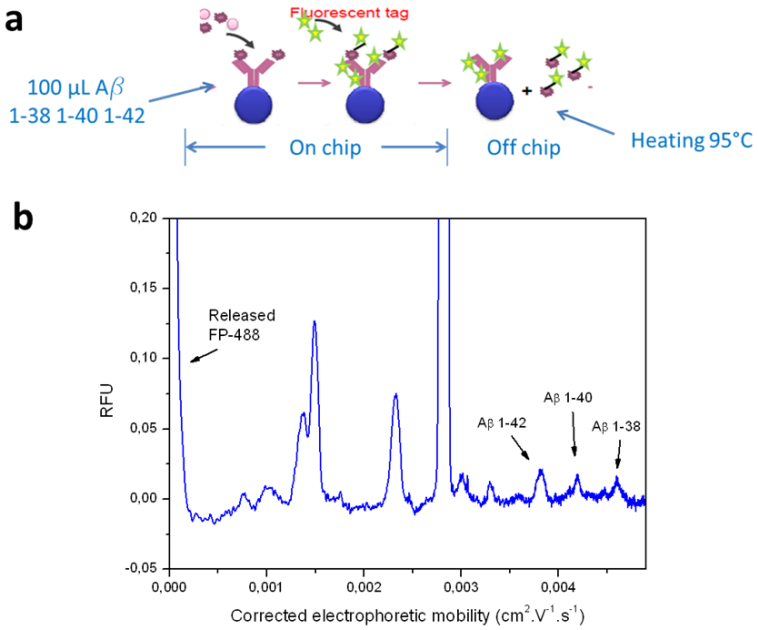

Figure 3.14. (a) Diagram of the procedure followed for maximizing the elution temperature, including on chip capture and labeling steps, and off-chip heating at 95 °C. (b) Electropherogram obtained by CE-LIF showing the presence of the three beta amyloids.

3.5 Perspectives for on chip detection

Efforts so far were focused on the non-specific labeling of Aβ peptides. This is certainly interesting in the case of integration of electrophoresis or other peptide discriminating methods in a lab-on-chip system. However, if the elution step is to be used for an in situ fluorescent detection without downstream separation, this labeling can at most indicate

the presence of Aβ peptides (although in this case non-specific fluorophores need to be effectively removed to avoid their masking effect).

Based on the promising results of ELISA techniques for Aβ detection reported in the literature, its integration in our system was envisioned. Indeed, ELISA is a surface binding technique, and thus adaptable to magnetic bead separation methods. We would like to take benefit of the solid supports use in the fluidized bed, as well as to the ability of our device to work through two regimes: packed or fluidized regimes to perform the enzymatic amplification step of an on chip ELISA. As our magnetic beads coupled with 6E10 antibody do not discriminate between Aβ isomorphs, this could be used to capture a variety Aβ peptides from a given sample and then add a solution containing an enzyme-grafted primary antibody specific for the C-terminus of one of the peptides (Fig. 3.15a). A substrate would then be added inside the microfluidic chamber and, if the primary antibody was specifically bound to any beta amyloid, a constant detection signal would appear at the chamber output in a constant flow-through configuration (Fig. 3.15b), or a signal peak if incubation steps were used.

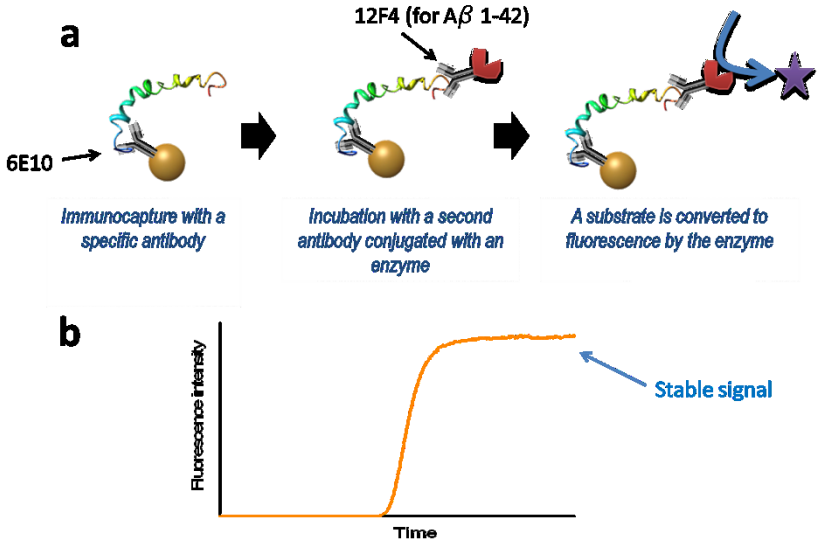

Figure 3.15. (a) Concept of on-chip ELISA test consisting of a first capture of the peptide with our magnetic beads, followed by the binding of a second antibody on the C-terminus of the molecule, associated to an enzyme. A substrate would then lead to a signal produced by the enzyme. (b) Expected constant signal at the output of the chip during substrate flow through the fluidized bed.

The antibody chosen for the C-terminus was 12F4 (Covance©) known for its reliability and specificity to 1-42 Aβ peptides, and used successfully in pair with 6E10 in reported microfluidic assays (Gagni et al. 2013). An ELISA kit was employed (QuantaRed^{TM}, LifeTechnologies) making use of the Horseradish Peroxidase (HRP) enzyme, the enzymatic product presenting excitation/emission maxima of ~570/585 nm. The enzyme was coupled to the referred primary antibody via a biotin-streptavidin interaction.

Preliminary results were, however, not as encouraging as expected. Indeed, very high signals were obtained even for negative controls (no beta amyloid introduced). Issues

related with the non-specific adsorption of the enzyme-antibody couple led to a complete masking of the contribution of the specifically captured Aβs. Many protocol changes were tested to reduce this non-specific signal (different primary antibody, stronger and longer washing steps, different 6E10 grafting procedures, alternative enzyme…) without results that could lead to a low enough non-specific signal to allow the detection of Aβ peptides at any relevant concentration. Further work is thus needed in order to establish the conditions that minimize non-specific signal and maximize peptide-specific substrate reactions. A more systematic in-batch study, with a battery of different immunosorbent and washing conditions, should *a priori* offer light in terms of the most feasible parameters for efficient on-chip ELISA integration.

In spite of these initial problems, an integrated ELISA protocol presents many advantages, not only in terms of possible detection multiplexing with the use of Aβ specific secondary antibodies in a single fluidized bed device, but also in terms of its relative simplicity of integration, as incubation steps should in principle be unnecessary.

3.6 Conclusions

The potential of the magnetic fluidized bed for the integration of a bioanalytical application for the capture of proteins was shown in this chapter. Characterization efforts indicate that particle distribution and hydrodynamic parameters are to be taken into account for optimal immunocapture efficiencies. Furthermore, fluidization was achieved even with antibody-grafted particles, and the stability of the bed was confirmed in both acidic and basic media. The two working regimes (packed/fluidized) of the bed further increase its versatility, with the packed state verified as an efficient incubator.

The robustness of the system for immunocapture/elution protocols was proved with a model protein. This protocol was subsequently applied to a real biomarker (Aβ peptides) with successful preconcentration proved with commercially-labeled peptides. A peptide labeling was also obtained on-chip, and an innovative capture-labeling-elution approach was used successfully, showing promising potential in terms of microintegration with downstream separation systems. These results were part of a journal publication (Mai et al. 2015) (see appendix A)

Further tests are required for the optimization of labeling protocols. In the case of direct on-chip detection, although so far the use of the fluidized bed as a specific detection system for proteins (beyond its preconcentration capabilities) has been elusive, there is no strong reason to think that this should not be feasible.

3.7 Additional materials and methods

Magnetic bead coating: 10 mg of Dynabeads Sheep-Anti Mouse IgG were washed with PBS and let incubate with 40 µg of 6E10 antibody (Covance) in 1 mL of PBS with 0.1% BSA overnight at 4°C. This was followed by a washinig of the beads with 0.2 M TEA

(3% v/v, pH 10.8) and 1 mL of 0.2 M TEA solution containing 5 mg of DMP were added and let incubate for 1 h under shaking. The reaction was stopped by adding Tris-HCl pH 7.5 up to 50 mL and shaked for 5 min, followed by washing and storing in PBS 0.1% BSA.

Peptide preparation and storage: amyloid peptides were dissolved in ammonium hydroxide 1% and immediately diluted in PBS at a concentration of 1 mg/mL, for further aliquoting and storage at -20°C until use.

CE-LIF conditions: details can be found in (Verpillot et al. 2011). The peak of non-specifically adsorbed FP-488 was employed as a reference for profile correlation.

On-chip ELISA protocol: the fluidized bed was formed with 50 µg of the same 6E10-grafted beads so far used, followed by a solution of 1-42 beta amyloids (50 µL in PBS medium, 1µL/min). A short washing with buffer (PBS + 1% BSA) ensued, with the subsequent introduction of the conjugated 12F4-HRP (20 µL 1µL/min), thorough washing with PBS (1.5 µL/min 40 µL), and a final injection of substrate at 1 µL/min.

3.8 References

Bibl, M. et al., 2006. CSF amyloid-beta-peptides in Alzheimer's disease, dementia with Lewy bodies and Parkinson's disease dementia. *Brain : a journal of neurology*, 129, pp.1177–1187.

Carrillo, M.C. et al., 2013. Global standardization measurement of cerebral spinal fluid for Alzheimer's disease: An update from the Alzheimer's Association Global Biomarkers Consortium. *Alzheimer's and Dementia*, 9(2), pp.137–140.

Dawkins, E. & Small, D.H., 2014. Insights into the physiological function of the β-amyloid precursor protein: Beyond Alzheimer's disease. *Journal of Neurochemistry*, 129(5), pp.756–769.

Devadhasan, J.P., Kim, S. & An, J., 2011. Fish-on-a-chip: a sensitive detection microfluidic system for Alzheimer's disease. *Journal of biomedical science*, 18(1), p.33.

Doecke, J.D. et al., 2012. Blood-based protein biomarkers for diagnosis of Alzheimer disease. *Archives of neurology*, 69(10), pp.1318–25.

Fargo, K. & Bleiler, L., 2014. Alzheimer's Association report. *Alzheimers Dement*, 10(2), pp.e47–92.

Frankfort, S. V et al., 2008. Amyloid beta protein and tau in cerebrospinal fluid and plasma as biomarkers for dementia: a review of recent literature. *Curr Clin Pharmacol*, 3(2), pp.123–131.

Gabelle, A. et al., 2013. Plasma amyloid-β levels and prognosis in incident dementia cases of the 3-City Study. *Journal of Alzheimer's disease : JAD*, 33(2), pp.381–91.

Gagni, P. et al., 2013. Development of a high-sensitivity immunoassay for amyloid-beta 1-42 using a silicon microarray platform. *Biosensors and Bioelectronics*, 47, pp.490–495.

Grasso, G., 2011. The use of mass spectrometry to study amyloid-β peptides. *Mass spectrometry reviews*, 30(3), pp.347–65.

Haußmann, U. et al., 2013. Analysis of amino-terminal variants of amyloid-β peptides by capillary isoelectric focusing immunoassay. *Analytical Chemistry*, 85(17), pp.8142–8149.

Howard, R.J. et al., 2007. Donepezil for the treatment of agitation in Alzheimer's disease. *The New England journal of medicine*, 357(14), pp.1382–1392.

Humpel, C., 2011. Identifying and validating biomarkers for Alzheimer's disease. *Trends in Biotechnology*, 29(1), pp.26–32.

Kang, J.H. et al., 2013. Clinical utility and analytical challenges in measurement of cerebrospinal fluid amyloid-β1-42 and τ proteins as alzheimer disease biomarkers. *Clinical Chemistry*, 59, pp.903–916.

Klunk, W.E. & Pettegrew, J.W., 1990. Alzheimer's beta-amyloid protein is covalently modified when dissolved in formic acid. *Journal of neurochemistry*, 54(6), pp.2050–6.

LaFerla, F.M., Green, K.N. & Oddo, S., 2007. Intracellular amyloid-beta in Alzheimer's disease. *Nature reviews. Neuroscience*, 8(7), pp.499–509.

Lichstein., P.R., 1990. *Clinical Methods: The History, Physical, and Laboratory Examinations.*,

Luo, Y. et al., 2003. BACE1 (β-secretase) knockout mice do not acquire compensatory gene expression changes or develop neural lesions over time. *Neurobiology of Disease*, 14(1), pp.81–88.

Mai, T.D. et al., 2015. Magneto-immunocapture with on-bead fluorescent labeling of amyloid-β peptides: towards a microfluidized-bed-based operation. *The Analyst*.

Mapstone, M. et al., 2014. Plasma phospholipids identify antecedent memory impairment in older adults. *Nature medicine*, 20(4), pp.415–8.

Mayeux, R. et al., 2003. Plasma A[beta]40 and A[beta]42 and Alzheimer's disease: relation to age, mortality, and risk. *Neurology*, 61(9), pp.1185–90.

Mesbah, K. et al., 2014. Neutral polymers as coatings for high resolution electrophoretic separation of Aβ peptides on glass microchips. *The Analyst*, 00, pp.1–9.

Mohamadi, M.R. et al., 2010. Microchip electrophoresis profiling of Aβ peptides in the cerebrospinal fluid of patients with Alzheimer's disease. *Analytical Chemistry*, 82(18), pp.7611–7617.

Mohamadi, R.M. et al., 2015. An integrated microfluidic chip for immunocapture, preconcentration and separation of β-amyloid peptides. *Biomicrofluidics*, 9(5), p.054117.

Mucke, L. & Selkoe, D.J., 2012. Neurotoxicity of amyloid β-protein: Synaptic and network dysfunction. *Cold Spring Harbor Perspectives in Medicine*, 2(7).

Le Nel, A. et al., 2008. Controlled proteolysis of normal and pathological prion protein in a microfluidic chip. *Lab on a chip*, 8(2), pp.294–301.

Oh, E.S. et al., 2010. Comparison of conventional ELISA with electrochemiluminescence technology for detection of amyloid-β in plasma. *Journal of Alzheimer's disease (JAD)*, 21(3), pp.769–773.

Van Oijen, M. et al., 2006. Plasma Abeta1-40 and Abeta1-42 and the risk of dementia: a prospective case-cohort study. *Lancet Neurology*, 5(8), pp.655–660.

Parnetti, L. et al., 2013. Cerebrospinal fluid biomarkers in Parkinson disease. *Nature reviews. Neurology*, 9(3), pp.131–40.

Pesini, P. et al., 2012. Reliable Measurements of the β-Amyloid Pool in Blood Could Help in the Early Diagnosis of AD. *International journal of Alzheimer's disease*, 2012, p.604141.

Portelius, E. et al., 2007. Characterization of amyloid peptides in cerebrospinal fluid by an automated immunoprecipitation procedure followed by mass spectrometry. *Journal of Proteome Research*, 6(11), pp.4433–4439.

Portelius, E. et al., 2006. Determination of beta-amyloid peptide signatures in cerebrospinal fluid using immunoprecipitation-mass spectrometry. *J Proteome Res*, 5(4), pp.1010–1016.

Prince, M. et al., 2013. The global prevalence of dementia: a systematic review and metaanalysis. *Alzheimer's & dementia : the journal of the Alzheimer's Association*, 9(1), pp.63–75.e2.

Schade, S. & Mollenhauer, B., 2014. Biomarkers in biological fluids for dementia with Lewy bodies. *Alzheimer's research & therapy*, 6(5-8), p.72.

Schmidt, S., Nixon, R. & Matthews, P., 2005. ELISA method for measurement of amyloid-beta levels. *Methods in Molecular Biology*, 299, pp.279–297.

Shankar, G.M. & Walsh, D.M., 2009. Alzheimer's disease: synaptic dysfunction and Abeta. *Molecular neurodegeneration*, 4, p.48.

Shaw, L.M. et al., 2009. Cerebrospinal fluid biomarker signature in alzheimer's disease neuroimaging initiative subjects. *Annals of Neurology*, 65(4), pp.403–413.

Slovakova, M. et al., 2005. Use of self assembled magnetic beads for on-chip protein digestion. *Lab on a chip*, 5(9), p.935.

Snyder, H.M. et al., 2014. Developing novel blood-based biomarkers for Alzheimer's disease. *Alzheimer's and Dementia*, 10(1), pp.109–114.

Svobodova, Z. et al., 2012. Development of a magnetic immunosorbent for on-chip preconcentration of amyloid β isoforms: Representatives of Alzheimer's disease biomarkers. *Biomicrofluidics*, 6(2), pp.24126–2412612.

Tabnaoui, S., 2012. *Magnetic fluidized bed for sample preconcentration and immunoextraction in microfluidic systems*.

Varghese, T. et al., 2013. A review of neuroimaging biomarkers of Alzheimer's disease. *Neurology Asia*, 18(3), pp.239–248.

Verpillot, R. et al., 2011. Analysis of amyloid-β peptides in cerebrospinal fluid samples by capillary electrophoresis coupled with LIF detection. *Analytical Chemistry*, 83(5), pp.1696–1703.

Wiltfang, J. et al., 2003. Beta-amyloid peptides in cerebrospinal fluid of patients with Creutzfeldt-Jakob disease. *Annals of neurology*, 54(2), pp.263–267.

Wiltfang, J. et al., 2002. Highly conserved and disease-specific patterns of carboxyterminally truncated Abeta peptides 1-37/38/39 in addition to 1-40/42 in Alzheimer's disease and in patients with chronic neuroinflammation. *Journal of neurochemistry*, 81(3), pp.481–96.

Winblad, B. et al., 2007. Memantine in moderate to severe alzheimer's disease: A meta-analysis of randomised clinical trials. *Dementia and Geriatric Cognitive Disorders*, 24(1), pp.20–27.

Woods, B. et al., 2012. Cognitive stimulation to improve cognitive functioning in people with dementia. *The Cochrane database of systematic reviews*, 2, p.CD005562.

Xia, N. et al., 2010. Regenerable and simultaneous surface plasmon resonance detection of aβ(1-40) and aβ(1-42) peptides in cerebrospinal fluids with signal amplification by streptavidin conjugated to an N-terminus-specific antibody. *Analytical chemistry*, 82(24), pp.10151–7.

Chapter 4

Bacteria Analysis

4.1 Introduction

The detection of pathogenic microorganisms is crucial in various fields such as food industry, environmental and water monitoring and clinical diagnosis. In the first case, detection methods are essential to protect the public from disease-causing threats, while in the latter case pathogen identification is essential for the effective treatment of infected patients. Current detection methods rely on microorganism culture and/or immunological/genetical testing. Although highly accurate and specific, these are long and labor-intensive procedures. A need then exists for faster more automated analysis and/ord detection methods that can significantly lower detection times without loss of identification specificity.

In this chapter, we show how the microfluidic fluidized we developed presents specific features that could be of interest regarding bacteria extraction and detection. To put this work in the context of the current state of the art, a brief overview of current standard identification methods will be first presented, followed by a short review on the many reported microfluidic alternatives. A particular focus will be given to foodborne pathogen detection, as this will be the object of the presented work. The results obtained with the fluidized bed will then be shown in a publication format, as submitted for peer review.

4.2 Conventional identification methods

The culture and quantification of bacteria on medium-rich plates is nowadays the gold standard to ensure accurate bacteria identifications. Conventional procedures for the detection of foodborne bacterial pathogens are based on a complete or partial series of the following steps: pre-enrichment, selective enrichment, plating on selective agar medium and biochemical/serological identification. For the identification of specific microorganisms, standard protocols are enforced by standardization or public safety

agencies. As an illustrative example, Fig. 4.1 shows a scheme of a standard protocol for *Salmonella* identification from the Bacteriological Analytical Manual (BAM) of the Food and Drug Administration (FDA). In a typical protocol, a first pre-enrichment step recovers injured or stressed bacterial cells with the use of non-selective nutritious medium. This 24hours enrichment step also serves to reduce false-negative tests. An enrichment phase follows, in which the pre-enrichment medium is inoculated in selective media containing inhibitors of other propagating bacteria. When a concentration of 10^4 cells/mL is reached, the enrichment medium is spread on agar plates. Plating procedures assume that from every single microorganism (colony forming unit, CFU), a single separate colony will form. Since too many colonies in a single plate can lead to colony overlap, typical ranges of valid CFU per plate are 25-30 CFU to 250-300 CFU (Goldman et al. 2015). Agar containing coliforms are often used, allowing the distinction by color of colonies of different serotypes. However, some serotypes are not distinctive or even colored by this method, needing additional supplements in the plating medium. Colonies presumed to be salmonella are then isolated for further screening with specific agar preparations. Positive cultures are finally submitted to biochemical or serological identification tests.

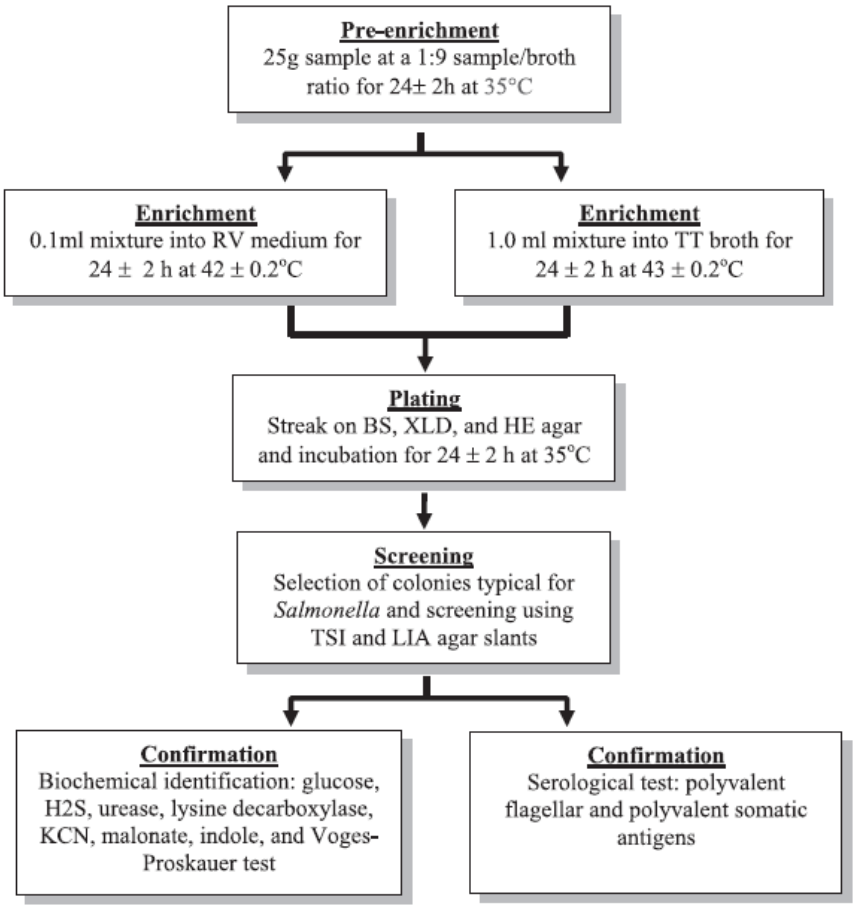

Figure 4.1. Standard Salmonella identification protocol from the FDA. RV: Rappaport-Vassiliadis; BS: bismuth sulfite; HE: Hektoen enteric; XLD: xylose lysine desoxycholate; TT: tetrathionate; TSI: triple sugar iron; LIA: lysine iron agar (Lee et al. 2015).

These methods are highly specific and sensitive, reliable, relatively inexpensive and easy to use. They are therefore widely used in public health laboratories and food industry. However, the procedure is laborious, difficult to implement for high-throughput screening and a full identification can take more than 5 days, with the subsequent delayed illness diagnosis or the risk for the consumer in case of contamination of marketed food.

In this context, many molecular biology-based technologies have emerged, some of which have been validated and can already be found on the market. These methods can be essentially categorized into two groups: immunology-based assays and nucleic-acid based assays.

4.3 Molecular-based methods

The most commonly employed immunology assay is the Enzyme-linked immunoabsorbent assay (ELISA). ELISA kits can be found commercially for a series of bacterial strains, with specificity and sensitivity similar to conventional plating methods (10^4-10^5 CFU/mL (Lee et al. 2015)) but in most cases providing no real gain in time. Another example of immunology-based assays are agglutination assays, in which latex beads grafted with specific antibodies are mixed with a bacterial sample. The capture of bacteria from more than one bead leads to the formation of bead aggregates that are readily visible with the naked eye. This procedure is uncomplicated, rapid and specific, although high bacteria concentrations are needed for detection.

On the other hand, nucleic-acid assays are DNA sequence specific, leading to the best results in terms of strain recognition. Polymerase chain reaction (PCR) is by far the preferred technique, with an exponential amplification of specific sequences resulting in very good sensitivities (ideally able to detect a single DNA strand) (Fig. 4.2). Very briefly, PCR amplification is obtained with a first denaturation of the double stranded DNA into single strands at high temperature (94-96°C), followed by the annealing (hybridization) of primers at a lower temperature (50-65°C). A replication enzyme (typically Taq polymerase) then completes the sequence (extension) with nucleotides present in the surrounding medium to obtain double stranded products (at 75-80°C for Taq polymerase). After each 3-step cycle the number of DNA strands, specific of the primer-defined sequence, is doubled. An exponential amplification is then obtained with a sequence of cycles, the only limitation being the available nucleotides in the medium and the life of the polymerase. The resulting PCR products are often analyzed through an electrophoresis separation in agarose gel. Due to the success of the technique, many variants have been developed along the years. For example, quantitative PCR (qPCR) allows the quantification (in real time) of the exponential amplification products through fluorescence dyes or fluorophore-labeled DNA probes. This has the advantage of avoiding any post-PCR step, reducing turn-around time and contamination risks.

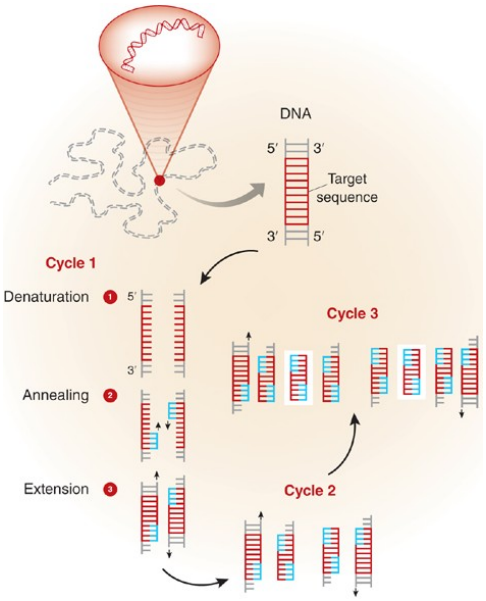

Figure 4.2. Schematic of the polymerase chain reaction principle (Garibyan et al. 2013).

Bacteria detection and identification with PCR (and especially qPCR) has become common in clinical laboratories with the amplification and sequencing of the gene encoding 16S ribosomal RNA. This gene is 1500 nucleotides long, highly conserved component of the 30S subunit of prokaryotic ribosomes, present in all bacteria. Signatures in this gene allow the identification of microorganisms at the genus and species level. PCR amplification is nonetheless performed with universal pan-bacterial primers, and subsequent strain identification requires sequencing techniques that are not yet available in most laboratories (Sontakke et al. 2009). Therefore the technique is most useful when a single bacterium strain is present or when a negative presence of bacteria is evaluated.

In order to obtain strain-specific amplifications and allow serotype identification, it is necessary to perform primer-specific PCRs. Multiplex identifications have been shown possible for given bacteria strains. For example, (Kim et al. 2006) developed a PCR-based method for the identification and discrimination of up to 19 serotypes of *Salmonella enterica* subsp. Enterica. This method is based on sets of primers for the amplification of specific genes. A post-PCR gel electrophoresis migration allows the visualization of fluorescent bands that serve as serotype-specific signatures, with 97% correct serotype assignment. Multiplex real-time PCR methods have shown limits of detection of for example of *Salmonella* or *Shigella* in the order of 10^4 CFU/mL in stool samples (Barletta et al. 2013) or 10-100 CFU/mL in food samples (Radhika et al. 2014). However, enrichment steps during several hours are usually required before PCR amplification. Increased sensitivities are found when coupling PCR to mass spectrometry techniques. By combining PCR and electrospray ionization mass spectrometry (PCR/ESI-MS) (Bacconi et al. 2014) could detect *Candida* bacteria from blood samples with a limit of detection of 16 CFU/mL without the need for a pre-enrichment step in an approximate total time of 6 hours.

Although PCR is a very powerful technique, several limitations still hinder its applicability. In the case of bacteria serotyping, misidentification can lead to false positives of rare serotypes that create the same amplicon patterns than more common ones (Kim et al. 2006). Additionally, sample preparation is usually not simple, as the DNA needs to be extracted by cell lysis and further purified to remove PCR inhibitors typically present in clinical specimens (such as hemin, that binds to Taq polymerase inhibiting its activity (Byrnes et al. 1975)). Furthermore, due to the amplification nature of PCR, false positives due to carryover or cross contamination are relatively common (Longo et al. 1990) and sample preparation must be performed in an environment isolated from the reaction space. As seen, pre-enrichment steps are still largely necessary to reach the limits of detection required for example for the detection of clinically relevant bacteria in blood (1-30 CFU/mL (Bacconi et al. 2014)) . This can be avoided if powerful detection techniques, such as mass spectrometry, are used for post-PCR processing, but this comes in detriment of procedure simplicity and cost. Moreover, this enrichment phase is still required if only viable bacteria are to be detected.

Finally, PCR presents the disadvantage of employing fast cycling requiring the use of thermocycling apparatus. This is especially fastidious for miniaturized portable devices. Alternatives isothermal amplification techniques have thus been developed. These will be briefly discussed in the following section and described in more detail in the next chapter.

4.4 Microfluidic-based systems

The preceding methods have been validated for bacteria detection and all of them present standard protocols and are available on the market. Nonetheless, even though molecular-based techniques are faster than conventional methods, they are still not as discriminative as conventional methods (immunology-based assays) or require laborious preparation steps (DNA-based assays). The reliability of both methods can also be affected by the sample matrix. Therefore, conventional plating is still the standard in most laboratories, both public and industrial. However, when fast detection responses are needed, these culture methods are not convenient, and in most cases, molecular-based alternatives cannot give responses in less than 24h, in many cases requiring a further confirmation by culture.

In the last decade, a variety of biosensor methods have been proposed for efficient microorganism detection. In these sensor methods a signal is obtained through antibody-antigen or nucleic acid recognition, enzymatic reaction or mechanical changes of micro/nano-structures. These biosensors are usually integrated in microfluidic platforms to couple detection capabilities with the automation, low-cost and multiplexing characteristic of these systems. The development of this field has especially been empowered by the need of portability in cases of point-of-care diagnosis or food/water safety analysis in remote locations. Furthermore, since the concentration of microorganisms in real life is usually low (both in sepsis injected patients and initial contamination of food products) an isolation/enrichment step is usually required. Lab-on-

chips have been the object of an enormous development in the past two decades in terms of separation, mixing operations and detection methods. Therefore, they present nowadays the possibility of being able to integrate different technologies in a single chip, although they are so far limited in terms of sample throughput. Original ideas have then to be envisioned to overtake these limitations.

In the following sections, a brief review of reported isolation and detection techniques for microfluidic devices is presented. The literature on this kind of systems being particularly rich, this review is aimed at providing the reader with a perspective on existing systems and has no ambition of being exhaustive. Also, many of the presented detection methods integrate in the same platform an initial sample preparation step, most often consisting in an enrichment and sample extraction of the microorganism of interest. As this has been the object of Chapter 1, these preconcentration techniques will only be mentioned here.

4.3.1 Immunoassay techniques

Immunoassays are, as previously explained, a common alternative to conventional plating methods. It is therefore not surprising that they represent a preferred method for microfluidic integration.

ELISA represents the assay of choice for many bacteria detection systems. In many reported works, ELISA is simply adapted to the surface of a microfluidic channel with light emission and detection taking place on opposite channel sides (Fig. 4.3a). For example, by this method (LI et al. 2006) showed limits of detection of 10-100 CFU/mL for *E. Coli* in 1 mL spiked PBS samples and a total procedure time of 2 h without enrichment. This shows a marked improvement as compared with conventional batch ELISA results due to improved immunoassay kinetics at the microscale, with an accompanying reduction in reagent volumes. This microfluidic integration is also particularly well suited to facilitate automation (rinsing and change of medium steps). However, the long channels used in the device (from 10 to 60 cm in length, 100 µm in depth), needed to ensure the residence times required for the obtained sensitivity, are prone to clogging if real clinical or food samples are to be used. While in this case a conventional ELISA method was directly transferred to a microfluidic device, other works have focused on using the microscale properties for alternative ELISA-based methods. Some examples include: the replacement of enzymatic or fluorescent probes with nanoparticle light scattering mechanisms (Lin et al. 2005), allowing result storage for several hours after analysis without loss of signal (although in this case no sensitivity improvement is gained); or immuno-sandwiches formed by antibody-grafted magnetic nanoparticles and quantum dots (QD) for multiplexed pathogen detection (Agrawal et al. 2012).

These types of immunoassays usually display the best limits of detection, better than non-microfluidic ELISA, but present the inconvenient of requiring a labeled probe. Surface Plasmon Resonance (SPR) is an alternative label-free detection method based on the total internal reflection of light when hitting a metal-liquid interface (due to a difference of

refractive index between the two media) (Fig. 4.3b). Polarized light is used and, when hitting the metal surface (usually a gold thin film), electric charges will oscillate in a single direction, this oscillation propagating in the form of an evanescent wave. For certain angles the incident light and the evanescent wave are matched, and the intensity of the reflected light is largely reduced. Since this wave depends on the refraction properties of both the metal and the liquid, the adsorption of molecules on the interface will lead to refractive index changes and thus to different resonance angles. In SPR microfluidic immunosensors, antibodies are grafted on the thin film surface in a microfluidic channel, and a sample containing the antigen is made flow for immunorecognition, thus changing refraction properties when target is present (with the subsequent angle shift). This technique presents the advantage of being faster and more straightforward than ELISA systems. Portability is an issue but some portable systems have been described, although with low sensitivity (~10^5 CFU/mL of E. Coli spiked in peritoneal dialysis fluid, Tokel et al. 2015). Indeed relatively low sensitivities are one of the main drawback of this system, with most reported limits of detection in the order of 10^4 CFU/mL (Yoon et al. 2012). It is also a technique that requires the use and calibration of relatively complex optics.

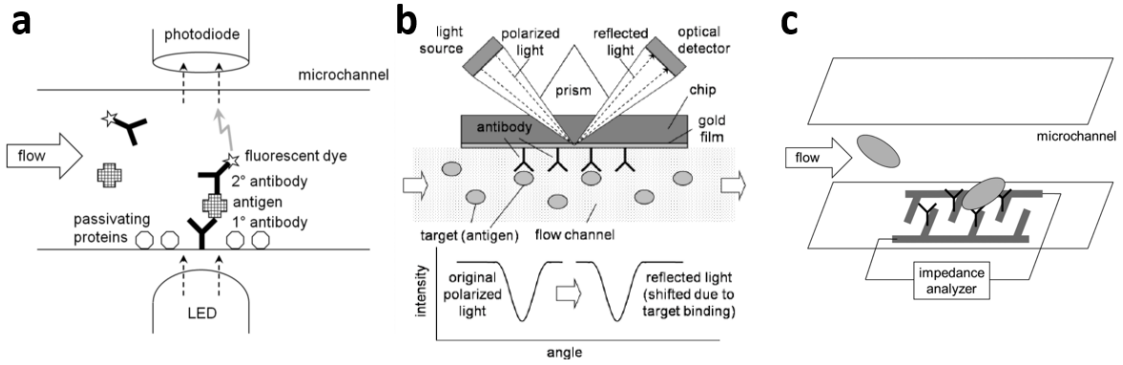

Figure 4.3. Microfluidic immunoassays based on ELISA (a), Surface Plasmon Resonance (b) and impedance (c) detection (Yoon et al. 2012).

Other alternative label-free detection methods can be obtained with an electrochemical detection, such as with impedance measurements. In this case, two electrodes patterned in an inderdigitated microelectrode (IME) configuration are grafted with anti-pathogen antibodies (Fig. 4.3c). During the capture step, some surface-captured target will get in contact simultaneously with both electrodes, lowering the inter-electrode electrical resistance. Since alternating current (AC) is usually employed to avoid oxidation/reduction processes and the damage of the antibody grafting, complex impedance measurements are used instead of the direct electrical resistance. Alternative impedance measurements without surface antibody-grafting have also been reported, for example by concentrating bacteria with a magnetic nanoparticle capture and optimizing the geometrical configuration (Varshney et al. 2007). Reported limits of detection with these techniques range between 10^2 and 10^4 CFU/mL (Yoon et al. 2012), with longer assay times than ELISA-based microfluidic systems.

The literature on reported alternative immunodetection is large and goes beyond the scope of this short review. Alternative methods include Lateral Flow Assays (LFA), Latex Immunoagglutination Assays (LIA) and carbon nanotube-based immunoassays. While all of these techniques present advantages that make them especially suitable for some applications, they have so far not been able to overtake ELISA-based detection limits or suffer from specificity issues.

4.3.2 Nucleic acid techniques

Although antibody-antigen interactions are highly specific, non-specific interaction can take place, in particular between similar strains (Ex. *E. Coli* and *Salmonella*). DNA identification is on the other hand extremely specific, allowing the identification of species and subspecies.

As indicated before, a drawback of DNA analysis is that it requires the preceding lysis of cells and purification of their genomic material. This is sometimes integrated into lab-on-chip systems, with an unavoidable increase in complexity. Further, due to the low concentration of the resulting DNA, for most applications an exponential amplification is required, commonly through PCR, before an optical or electrochemical detection. Because of the need for thermal cycling, several solutions have been adopted for microfluidic integration.

A simple idea is the use of stationary chambers coupled with a fast temperature control. This is a direct adaptation of conventional PCR systems, helped by the microscale due to its more efficient heat transfer. Examples abound in the literature, presenting different DNA extraction strategies: (Lee et al. 2006) developed a system for the rapid lysis of bacteria by heating in-solution magnetic beads with laser irradiation. They further showed the possibility of performing PCR in the same microfluidic chamber, although no sensitivity study is shown and the sample size is restricted to the volume of the chamber (4 μL). A similar approach has been shown with the lysis of bacteria by heat transfer from laser-irradiated gold nanoparticles (Cheong et al. 2008). However, while in these cases PCR is performed without a preceding DNA extraction step (direct PCR), this is most often not possible with real samples, which generally contain PCR inhibitors. This extraction need typically results in an increased device complexity, and examples have been reported that made use of integrated pumps, valves and magnetic control for immunomagnetic bead separation (Liu et al. 2004). More recently, (Oblath et al. 2013) reported a microfluidic chip that overcomes these problems by integrating DNA extraction, amplification and detection in seven parallel reaction wells (Fig. 4.4) containing a nanoporous aluminum oxide membrane. Bacteria-spiked saliva (off-chip lysed by heating) is then pipetted in the wells and aspired through a common waste outlet to force the solution through the membrane. This is followed by pipetting a PCR mix containing the primers, and an oil droplet is placed on top to avoid evaporation. This kind of simple systems allow a multiplex analysis in relatively short times (~2 hours), and while the volume used was limited (10 μL) this could be increased by aspirating more

sample volume through the membrane. However, the authors did not study their sensitivity, which could be affected by the known inhibiting properties of the aluminum oxide used.

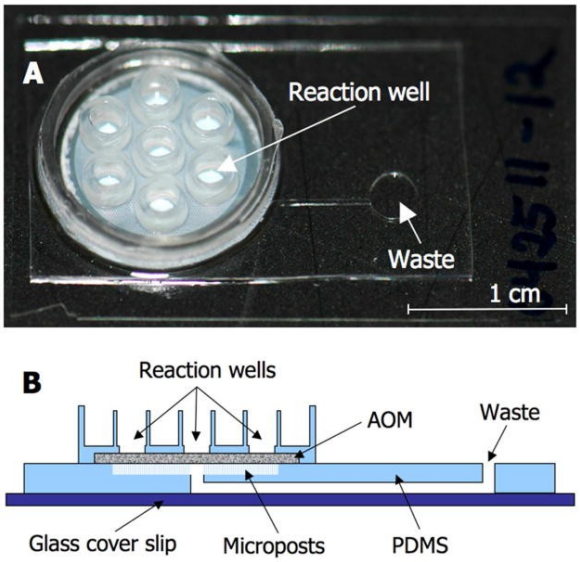

Figure 4.4. (A) Image of chip for multiple-chamber PCR analysis of bacteria and (B) cross section diagram showing the fluidics for sample aspiration through the oxide membrane (grey).

An alternative solution, that makes more use of the flow control possibilities offered by microfluidics and obtains higher throughputs, is the use of continuous-flow serpentine channels passing through areas of the chip at different temperatures. In general, these devices present three discrete isothermal zones (for denaturing, annealing and extension) although this configuration results in heat isolation challenges. Therefore, simpler systems based on two isothermal zones (Sun et al. 2002) or temperature gradients (Zhang et al. 2010) have been developed. Based on the former, (Jiang et al. 2014) reported a chip for the PCR amplification of six air-collected bacteria species (Fig. 4.5). The chip consists of six valve-controlled s-shaped channel entrances for multiplexed analysis. Once filled with samples, the PCR mix pushes the liquid into the serpentine channel (eventually resulting in a mix of sample and reagents) for a continuous-flow PCR reaction of 31 cycles between two temperature zones (95 and 55 °C). The on-chip procedure lasted ~1 hour, but in this case the detection step was not integrated and the readout was performed through gel electrophoresis. Further, the limit of detection obtained (~120 CFU) was limited by the very small injected volumes (0.13 μL), although the authors state that a continuous sample injection should be feasible.

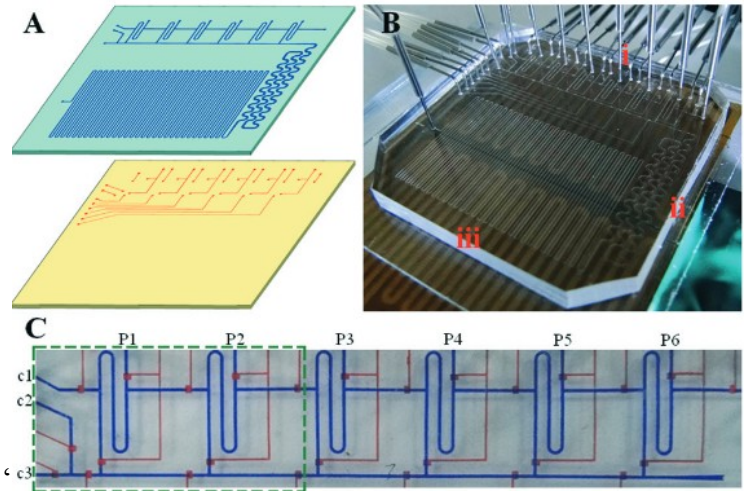

Figure 4.5. Microfluidic device for continuous-flow PCR analysis of bacteria. (A) Fabrication from two layers of PDMS for microchannels and micro valves, (B) Photograph of the system, showing the thermal resistors below the chip two create the isothermal zones and (C) the six entrances controlles with the microvalves.

The first commercial device for PCR detection of bacteria (GeneXpert MTB/RIF) is currently marketed by Cepheid. In this system, cartridges consisting of multiple chambers are employed to contain all the sample, lysis and PCR reagents, and these cartridges are thermo-cycled through heating/cooling plates when inserted in the device. Optical blocks are used for real-time fluorescence detection of the amplification products (Raja et al. 2005). This system has been successfully used for the detection of tuberculosis (rpoB gene) as well as antibiotic (rifampicin) resistance from sputum samples with ~90% accuracy in one hour running times. It has also shown its adequate applicability to resource-scarce settings (Boehme et al. 2011). Further, this technology replaced sputum smear microscopy as the first-line test for tuberculous diagnosis in the national laboraty service of South Africa (a country with the third largest number of tuberculosis cases in the world). This, however, did not result in mortality decrease, suggesting that in this case health system weaknesses need to be taken care of first to maximize the effect of more accurate diagnoses (Theron et al. 2013).

Due to the complexity of PCR systems in terms of precise thermal control, isothermal amplification techniques have been particularly investigated in the case of micro-device integration. A common example is the Loop mediated AMPlification (LAMP), requiring a single enzyme with strand displacement activity and in general 4 different primers (for a detailed description of the LAMP principles the reader is referred to (Notomi et al. 2000)). This technique has been successfully used for the detection of pathogens such as *Salmonella* (Jenkins et al. 2011) or *Listeria* (Wang et al. 2011) in handheld devices. Other isothermal methods such as Helicase-Dependent Amplification (HDA) (Mahalanabis et al. 2011), Nucleic-Acid Sequence-Based Amplification (NASBA) (Zhao et al. 2012) or Rolling-Circle Amplification (RCA) (Mahmoudian et al. 2008) have also been used successfully for microfluidic pathogen detection. The choice of the method depends mostly on the target (double stranded DNA, mRNA, genomic RNA…), sequence length

or work temperature. Their reported limit of detection is very variable ranging from 20 to 10^5 CFU/mL (Zanoli et al. 2013), mostly limited by the capacity of the system to extract pathogen oligonucleotides from sufficiently large sample volumes. Also, in these reported works the lysis and extraction steps were performed off-chip before sample injection. Due to their complexity, the principle of these techniques is not shown here, but RCA-based techniques will be more thoroughly treated in Chapter 5.

4.3.3 Mechanical techniques

Most reported mechanical devices for microorganism detection rely on the use of cantilevers. The presence of particles on the surface of micro-beams leads to flexion due to material elasticity, and the resulting deformation can be measured by optical or piezoelectric resistance changes. Changes in the resonant frequency of the cantilever have also been used to quantify the mass of bacteria adhered to the surface of the beam. These structures are usually fabricated in silicon through clean room procedures. (Campbell et al. 2005) showed that they could detect antibody-immobilized E. Coli on the surface of a glass cantilever when immersed in liquid containing the pathogen. The reductions of resonant frequency led to a limit of detection of 700 CFU/mL. In a more recent publication (Fig. 4.5, McKendry & Kappeler, 2013) bacteria (*E. Coli* and *Staphylococcus aureus*) were immobilized on both sides of an cantilever by APTES linker (Fig. 4.6). By flushing sequentially PBS, ampicillin-containing nutritious medium or simple nutritious medium, the fluctuation frequency of the bacteria-loaded cantilevers was seen to be an indicator of antibiotic-resistance (lower mechanical fluctuations for antibiotic-resistant bacteria in the presence of antibiotics-rich medium). Therefore, this method, while requiring a precise and costly fabrication/setup, can add more information than simple detections, such as the dynamic effects that different media have on a given population.

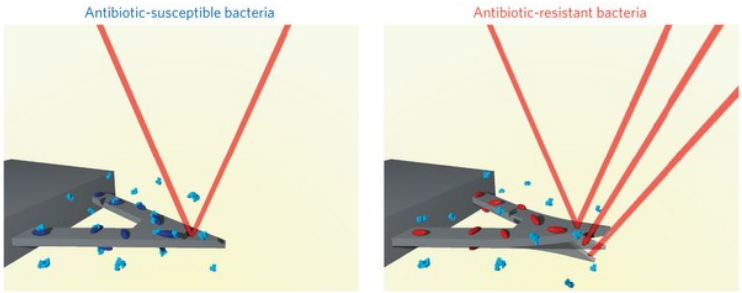

Figure 4.6. Mechanical fluctuations of cantilevers can be measured with laser beams as an indicator of the antibiotic resistance of surface-adhered bacteria (McKendry et al. 2013).

4.3.4 Droplet microfluidics

In droplet microfluidics, monodisperse picoliter-sized liquid droplets are generated in an immiscible carrier oil fluid. This droplets act as isolated reactors of small length scale and high surface to volume ratio, significantly increasing reaction kinetics and further allowing massively parallel studies with batteries of droplets at different compositions. This technique has shown great promise in terms of sensitive and selectivity. For

example, digital PCR for bacteria detection has been shown to offer highly multiplexed and multigene analysis (Ottesen et al. 2006). However, the technology has been limited by the required sample volumes and throughput (and PCR is still limited by the aforementioned need to extract and purify DNA). Recently, (Lien et al. 2007) have shown the potential of droplet microfluidics as a way to rapidly encapsulate bacteria-spiked blood samples mixed with a lysis agent and DNAzymes, a synthetic ssDNA with catalytic activities that generates a fluorescent signal in the presence of strain-specific lysate (Fig. 4.7a). The resulting droplets are recovered in an external vial preserving their structure (no merging) and then digitally analyzed by a 3D particle counter that can detect fluorescent particles at high throughput in a tube rotating in a spiral motion (1 mL of tube analyzed in 100 s, Fig. 4.7b). The system is hence selective and quantitative, and in principle able to detect single-digit bacteria under 4 hours. The authors show the very specific detection of E. Coli, but, while the reading is extremely efficient, the system is still limited by the encapsulation throughput of 25 µm droplets (2000 Hz droplet generation frequency, leading to a flow rate of 10 µL/min of 20% blood by using 8 parallel channels) that would require hundreds of parallel droplet-generating channels to reach clinically relevant mL volumes in the reported times. A multiplexed analysis would also require different laser sources and detectors, complicating an otherwise relatively cost-efficient method. In any case, if faster encapsulation rates were achieved, this technology could certainly make an impact for rapid bacteria diagnosis.

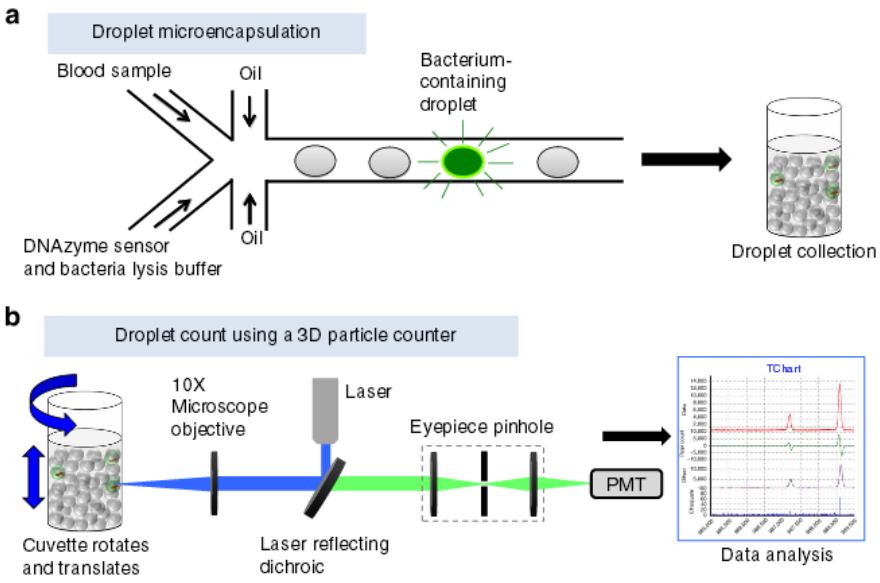

Figure 4.7. Schematic description of (a) microdroplet encapsulation of blood, DNAzyme and lysis buffer in a microfluidic device followed by droplet recovery in an external vial and (b) detection of fluorescent droplets by using a high-throughput 3D particle counter.

4.3.5 Culture

The literature on on-chip detection of pathogens by an *in situ* culture step is scarce. As previously indicated, a culture step is usually required in conventional methods in order to increase the population of analysis and favor the growth of the microorganism population

of interest. Since culture can only be obtained with viable bacteria, the enrichment of inactive organisms is not possible. However, most detection needs are only concerned with living bacteria, and especially in treated samples, dead bacteria can give rise to false positives in alternative methods.

Some works have been reported with the aim of showing the feasibility of bacteria culture directly performed in microfluidic channels. This is achieved by flowing a nutrient-rich medium and controlling the camber temperature usually set at the optimal growth temperature (typically 37°C). However, one of the main challenges of microfluidic cell culture is the need for mixing. Mixing is essential in batch-based culture procedures, for example with mechanical stirring or shaking. The quality of mixing has a direct influence in cell growth since mixing keeps the organisms in suspension and ensures the homogeneous availability of nutrients and oxygen, simultaneously avoiding the built up of cellular waste products.

Therefore, heating, mixing and valve control (for multiplex culture) are needed in order to obtain efficient culture. To overtake these problematics, (Gan et al. 2011) proposed a multilayer microfabrication solution in which PDMS valves (see Chapter 1) were used to create a loop movement of nutritious medium containing the bacteria of interest (first inserted through a single entrance, Fig. 4.8). The authors compare the growth of bacteria in this system with conventional batch culture, showing similar results, and the same system without mixing, with much poorer results. With this kind of system, the multiplexed culture of different bacterial strains should then be possible with high efficacy.

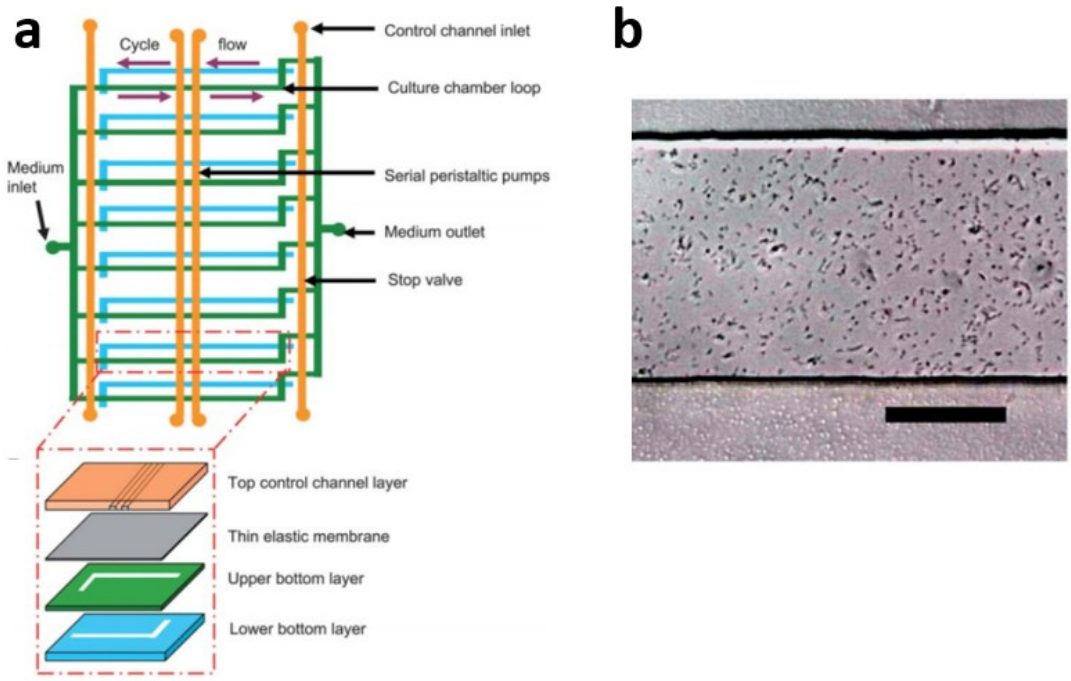

Figure 4.8. (a) Diagram of microfluidic chip for multichannel culture of bacteria based on 4 PDMS layers and (b) optical micrograph of E.Coli suspension culture (scaler bar: 50µm) (Gan et al. 2011).

In a recent publication, (Bouguelia et al. 2013) reported a culture-capture-measure approach in which a first *in situ* culture step is performed in the presence of surface grafted antibodies, with refraction index changes monitored in real time through surface plasmon resonance (SPR) (Fig. 4.9). This allows the overtaking of the limiting LOD obtained with SPR systems by increasing the initial bacteria population in a single-chamber fluidic-free system. Measured LODs were as low as 3 CFU/mL for three different bacterial strains (*Salmonella enterica*, *Streptococcus pneumoniae* and *Escherichia coli O157:H7*) in food samples. The relatively large chamber volume (500 µL) permits to partially overcome the need for mixing seen in truly microfluidic channels, in this case sacrificing culture efficiency for simplicity gains. This work represents a step forward in terms of meeting the requirements of microtechnology for industrial needs. However, it is still partly limited by the complexity and cost of SPR technology.

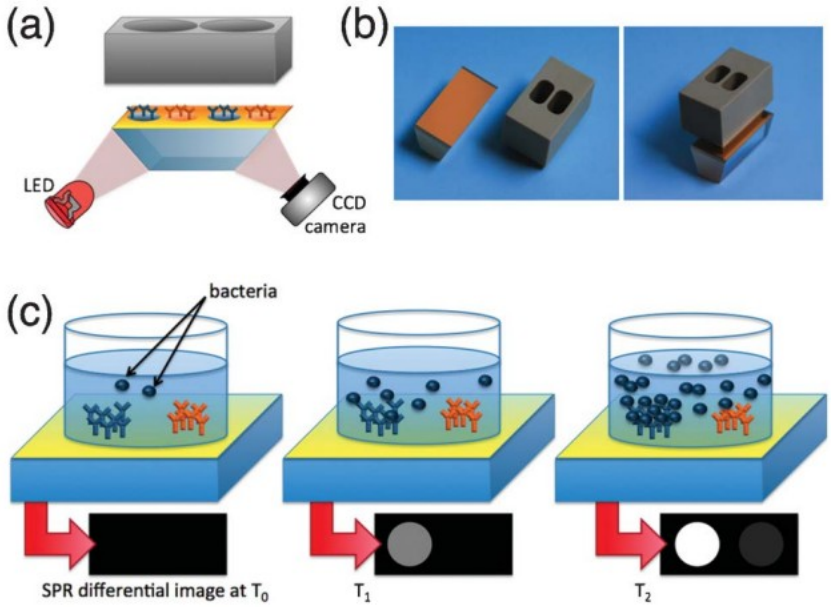

Figure 4.9. Schematic view of microchip for culture-SPR pathogen detection (a), double culture chamber device (b) and SPR signal monitoring during cell multiplication on specific and non-specific antibody spots (c).

4.5. Microfluidic magnetic fluidized bed for bacteria detection

In the previous section, a brief review of the large existing literature on microfluidic pathogen detection methods has revealed the challenges of this objective in terms of sample preparation, need for high-throughput analysis and required sensitivity. To put it into perspective, some organisms require the total absence of Salmonella in 25 g of dairy products (FDA 2001). This means that around 25 mL samples must be treated through some enrichment method (usually culture or filtration) before the actual identification procedures (even in the case of conventional plating protocols). High throughput devices capable of treating large sample volumes in short testing times are then particularly needed. Although this represents too ambitious throughput capabilities, the ability of the

fluidized bed to extract/preconcentrate target from complex media at constant flowrates can represent a step in this direction. This idea was hence proposed to solve sample preparation issues in multi-modular pathogen detecting devices, in collaboration with European partner laboratories integrated in the EU-FP7 project LOVE-FOOD.

LOVE-FOOD is a project with the aim of developing a fully integrated lab-on-chip platform for bacteria detection in dairy liquid samples. The system was envisioned to include all necessary steps, from sample pre-treatment, bacteria lysis and nucleic acid purification to amplification and final detection. DNA amplification was conceived with a micro-PCR module with isothermal regions, while the detection is based on an array of Love wave acoustic sensors. It is in the sample pre-treatment step with magnetic microbeads where the fluidized bed technology was considered an appealing candidate to preconcentrate bacteria, and eventually include other steps such as cell lysis. In particular, the capacity of the fluidized bed to resist clogging was regarded as a crucial advantage for the analysis of milk samples, which can contain important amounts of lipids and proteins. This capacity was nonetheless not yet proven, as was the possibility for the fluidized bed to capture entities similar in size to the fluidized magnetic beads, and how this would affect the physical properties of the system. This study eventually led to much more development than a simple sample pretreatment, finally integrating in the fluidized bed itself all the necessary steps for bacteria detection from raw samples.

This work has been recently submitted for publication and is therefore included in its original format in the following pages.

One-step capture, amplification and label-free quantitation of bacteria from raw samples in a microfluidic magnetic fluidized bed

Author list

Iago Pereiro, Amel Bendali, Lucile Alexandre, Sanae Tabnaoui, Jana Srbova, Zuzana Bilkova, Jean-Louis Viovy, Bruno Dupuy, Laurent Malaquin, Stéphanie Descroix

Abstract :

A microfluidic method able to specifically capture and detect live bacteria based on surface antigens and proliferative power is presented. It involves a microscale fluidized bed, in which magnetic and drag forces are balanced to retain antibody-functionalized superparamagnetic beads in a chamber during sample perfusion. Captured cells are then cultivated in situ, infusing nutritionally rich medium. Their growth is followed label-free, observing by naked eye or with a low-cost camera the modification of the volume of the bed. The technology was applied to the direct and one-step detection of *Salmonella enterica serovar* Typhimurium and *Enterobacter cloacae* in unskimmed milk, spiked with an excess 500/1 of *Lactoccocus lactis* in order to assess specificity. A quantitative detection with a dynamic range from 100 to 10^7 cfu/ml was achieved in 2 to 8 hours depending on initial concentration, opening the route to fast, low-cost, portable and automated bacteria detection for various applications in food, environment, security and clinics.

The dramatic decrease of mortality rates due to infectious diseases in the 20th century, following progress in hygiene and the discovery of antibiotics, raised the hope that these would become a minor health problem in the future of humanity. However, the rate has been increasing again since the 80's, and infectious diseases have been identified in a recent World Health Organization (WHO) report as a global threat to human health[1]. Considering the slow progress in new antibiotics discovery, the main hopes of control lie in the development of prevention, and of fast, convenient and low-cost technologies for early pathogen identification in clinics, transport security, environmental control and food.

Here, we present a simple and compact microfluidic device allowing sensitive, fast and low cost pathogen detection directly from a complex raw liquid sample. This technology could be applied to all kinds of bacteria detection issues, but for a first application we apply and validate it to food-borne pathogens, and more specifically *Salmonella* species and *Enterobacter cloacae.* Food-borne infectious diseases are a common, distressing and often life-threatening problem for millions of people around the world, *Salmonella* being the most commonly reported pathogen[2]. In industrialized countries, strict testing protocols are enforced by food safety authorities. Due to the long time required by current detection methods, however, products carrying pathogenic bacteria can be already widespread before alert, with risks for consumers and important economic costs. The health threat in developing countries and remote areas is even worse, since no affordable testing method is available. *Salmonella* are gram-negative rod shaped bacteria that can cause serious infections[3,4] and prove fatal in young children, frail or elderly people, and other patients with weakened immune systems, notably patients with AIDS[5]. *Enterobacter cloacae* belongs to Enterobacter spp and have emerged as major pathogen causing nosocomial Gram-negative bloodstream infections[6].

Plating and colony-counting are widely used for bacteria detection, and are still considered the gold standard. This protocol is highly sensitive and specific, but it typically requires from one to

several days, skilled personnel and large volumes of consumables. Hence, a great diversity of alternative analytical methods based either on metabolic properties (biochemical identification techniques, chromogenic agar broth[7]), antibodies targeting (ELISA[8], flow cytometry[9], immune-separation[10]), nucleic acids (hybridization[11], PCR[12], microarrays[13]), or microfluidics[14] have been developed. Various disadvantages or limitations, however, have hindered their widespread certification and/or use in routine practice (see Supplementary information online, SIO). PCR-based methods, for instance, are rapidly developing in diagnosis, but they also detect dead bacteria, which limits their use in food analysis. Most microfluidic-based methods cannot accommodate large complex samples, and require a pre-enrichment and/or pre-purification step.

Here we present a new microfluidic concept allowing direct detection and quantification of bacteria contamination in raw liquid samples, down to a few colony forming units (cfu) in a few hours. The sample is flown across a microfluidic fluidized bed in which superparamagnetic beads bearing antibodies directed to the pathogens of interest recirculate continuously. This ensures a high density of beads, combined with low flow resistance and resistance to clogging. The system was applied to two pathogenic bacteria strands, *Salmonella enterica* serovar Typhimurium and *Enterobacter cloacae,* with capture rates between 70 and 90%. Live bacteria are then amplified in situ by flowing through the fluidized bed a nutrition buffer. The volume occupied by the growing bacteria modifies the physical properties of the magnetic bed, allowing for a direct and highly specific quantitation of the initial number of bacteria with a 5 orders of magnitudes dynamic range from 10^7 to 100 cfu/ml. The device can be mass-produced by injection molding, and detection can be made by a smartphone-type low-cost visible light camera, opening the route to the industrial development of cost-effective instruments and consumables. For applications in low-technology environments, detection with the same sensitivity can also be achieved by naked eye.

RESULTS

Microfluidic fluidized bed operation.

Macroscopic fluidized beds have been used for decades in industry. They typically consist of a cylindrical reservoir in which particles are kept in suspension by a balance between their weight and the drag force exerted by a fluid flowing upward. The drag force is reduced when interparticle distance (i.e. porosity) increases, so that the equilibrium between drag and gravitational forces leads to a stable, steady-state and stirred suspension of particles behaving as a fluid. Some attempts at creating a microscale fluidized bed can be found in the literature[15117], but miniaturization is not favorable to gravitational fluidized beds, since the drag force scales as r^1, whereas gravitational forces scale as r^3, limiting these devices to relatively large beads and chamber sizes, and low flow rates. To overcome this limitation, we propose a new approach replacing gravity by magnetic forces induced by a magnetic field gradient, and using superparamagnetic particles (1-4 μm in size) as the solid phase. At this scale, magnetic field gradients easily achievable with permanent magnets typically exert forces 3 to 4 orders of magnitude larger than gravitational forces. This allows the use of high flow rates combined with low chamber volumes and high area/volume ratios for fast capture kinetics and high capacity. Also, in this range of sizes, a vast amount of well-calibrated superparamagnetic particles bearing various grafting chemistries and/or affinity ligands have been developed in the past 20 years.

The microfluidic fluidized bed involves a microfluidic chamber with an inlet and an outlet, partially filled with micrometric magnetic particles, an external permanent magnet and a fluid flow controller (Fig. 1a). The conical shape of the microfluidic chamber serves two purposes. First, in contrast to gravitational fluidized beds, here the force opposing drag is derived from a gradient, and it cannot be kept constant over large areas. We thus chose a monotonously decreasing magnetic force along the main axis of the chamber, compensated by a decrease of

the drag force along the same axis thanks to a triangular shape of the chamber. The divergence of the field and flow were also optimized to favor a stable recirculation of beads for optimal capture (Fig. 1b & Supplementary video1). In particular, this new geometry avoids the formation of any preferential pathway of the percolating liquid through the magnetic beads bed, or "bed fracture", a phenomenon that usually occurs with magnetic packed beds at high flow rates[18]. Drag decreases with decreasing beads density, so the system has a low flow resistance and is intrinsically stable for a large range of flow rates (Flow rates ranging from 0.5 to 5 µL/min were used here), and the latter can be optimized for each given application, higher flow rates leading to a longer total length of the fluidized bed and consequently to a higher bed porosity (Fig.1c).

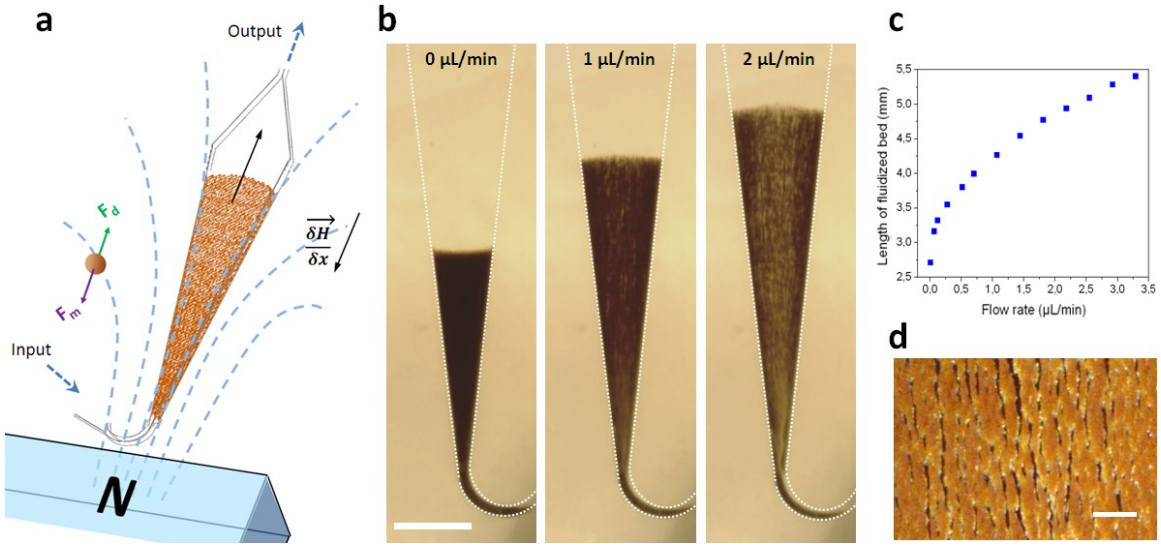

Figure 1. Scheme of microfluidic fluidized bed: an external permanent magnet creates a magnetic gradient inside a triangular shaped chamber, resulting in magnetic forces globally oriented towards the chamber inlet, applied on superparamagnetic beads (a). Fluids are flown into the chamber by the inlet located on the magnet side, by a pressure-based flow controller (MFCS Fluigent). If no pressure is applied, the beads remain in a packed-bed configuration due to magnetic force (scale bar = 1mm); (b) Under flow, the beads also receive drag forces oriented upstream, and above a flow threshold a new, steady-state dynamic equilibrium, called the "open bed" regime, is achieved, favoring high percolation rates and internal recirculation of the beads. The total length of the fluidized bed is directly dependent on the applied flow rate due to a change on the porosity of the bed (c). The bed in the "open" state is shown in the

micrograph (d), the high beads density and the multiple percolation paths leading to efficient and uniform capture (scale bar = 200µm).

Capture of *Salmonella enterica* serovar Typhimurium

The capture efficiency of the device regarding *Salmonella enterica* serovar Typhimurium (*S.* Typhimurium) was investigated, using commercial anti-*salmonella* Dynabeads® to ensure reliable long-term procurement and performance stability[19]. Capture efficiency was first evaluated by flowing at 1µl/mn a sample spiked with *S.* Typhimurium at initial bacteria concentrations ranging from 10^2 to 10^4 cfu/ml (corresponding to 5 and 500 cfu, respectively in 50µL, see Supplementary Methods Online). For bacteria spiked in phosphate buffer pH 7.4 (PBS) a high capture rate of 84 to 93 % (+/- 25% at 10^2 cfu/mL and +/- 3% at 10^4 cfu/ml, respectively) was achieved (see Methods section for details). The extraction rate from raw milk samples was evaluated by spiking various concentrations of *S.* Typhimurium in 50 µL of whole UHT milk, and directly flowing this mix, without pre-filtration or dilution, through the fluidized bed. The capture rate (71% ±8, n = 3), was slightly lower than in PBS. As the presence of lipids and a high concentration of proteins in milk does not result in a dramatic loss of capture efficiency or clogging, we consider these results as a strong validation of our system to extract efficiently bacteria from a complex matrix.

Besides unwanted possible contaminations, dairy products often contain *mesophilic lactic bacteria* at concentrations ranging from 10 to 10^4 cfu/mL depending on milk origin[20]. Thus, such non-pathogenic naturally occurring bacteria could largely outnumber the concentration of *salmonella* and potentially negatively affect their immunocapture. Oppositely, in case of non-specific capture, they could yield false positive results in uncontaminated samples. To mimic such situations, we tested additional samples, in which *Lactococcus lactis* was spiked in the previous UHT milk samples with a ratio of 1/500 of *S.* Typhimurium versus *L. lactic*,. As shown in Fig.2, no significant difference in *S.* Typhimurium capture rate was found between samples with

and without *L. lactis*. The non-specific capture of *L. lactis* was below 0.15% for the three concentrations tested, corresponding to a selectivity of at least 500:1.

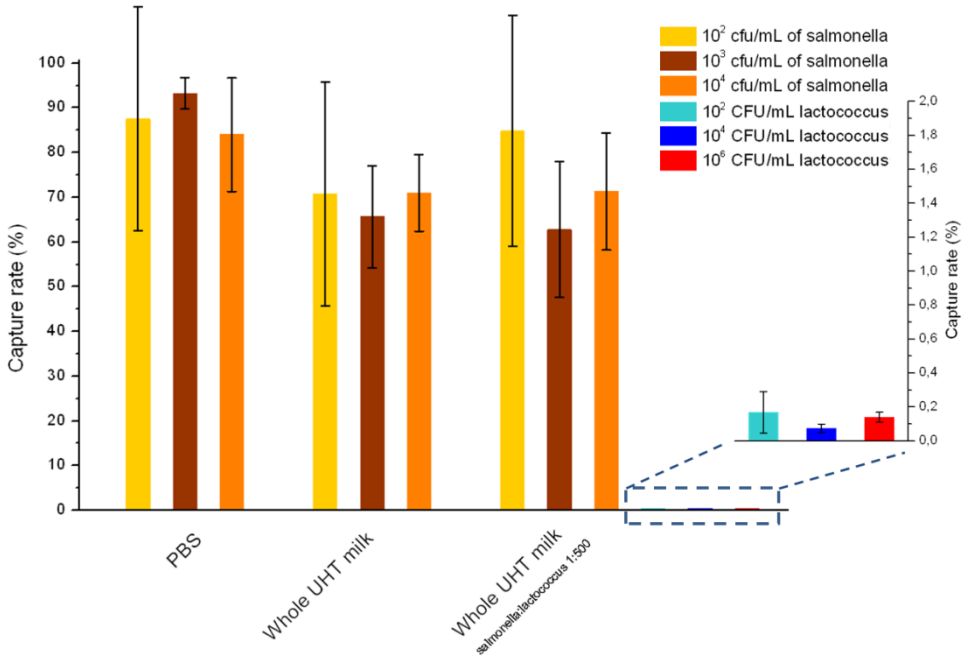

Fig. 2. Capture rates obtained for S. Typhimurium *at three different initial concentrations and for different matrices: PBS, whole UHT milk and whole UHT milk with a proportion of S.* Typhimurium *to* Lactococcus *of 1:500. The non-specific capture of S.* Typhimurium *is given in expanded scale at the right of the histogram.*

Bacteria culture, detection and quantification by bed expansion.

A key innovation to achieve high sensitivity using a full microfluidic process without pre-culture, was the implementation of bacteria culture directly in the fluidized bed.

Immediately after bacteria capture, nutritious medium (LB broth) is perfused trough the magnetic fluidized bed at 0.15 µL/min and the chip temperature is set to 37°C. On-chip bacteria growth was first investigated by monitoring fluorescence of the microfluidic chamber after the capture of GFP-expressing *S.* Typhimurium (Fig. 3 & Methods). As shown in Fig.3, bacteria development is evidenced, from 0 to 120 min, by the appearance of new bacteria or small colonies, leading to a multiplication of bright dots in fluorescence images (Fig 3a). Beyond this

time, fluorescence intensity continues to increase (Fig 3b, green curve), but individual dots become difficult to isolate (Fig 3a). These results evidence the possibility to keep alive bacteria after their capture and to multiply them within the microfluidic device. Interestingly, the distribution of bacteria density is rather homogeneous across the bed, especially at short culture times. This observation has been verified even for initial amounts of bacteria in the single digits, suggesting that “daughter” bacteria distribute across the bed. We associate this with the fluid nature of the bed.

These experiments also revealed a physical change in the fluidized bed during culture, apparent as a progressive increase of area (Fig 3a, 240mn & up, Fig 3b, orange). The area increase roughly follows that of fluorescence, with an initial plateau, an exponential-looking growth, a linear zone and a saturation plateau. This behavior is typical of a non-linear reaction kinetics with reagent saturation.

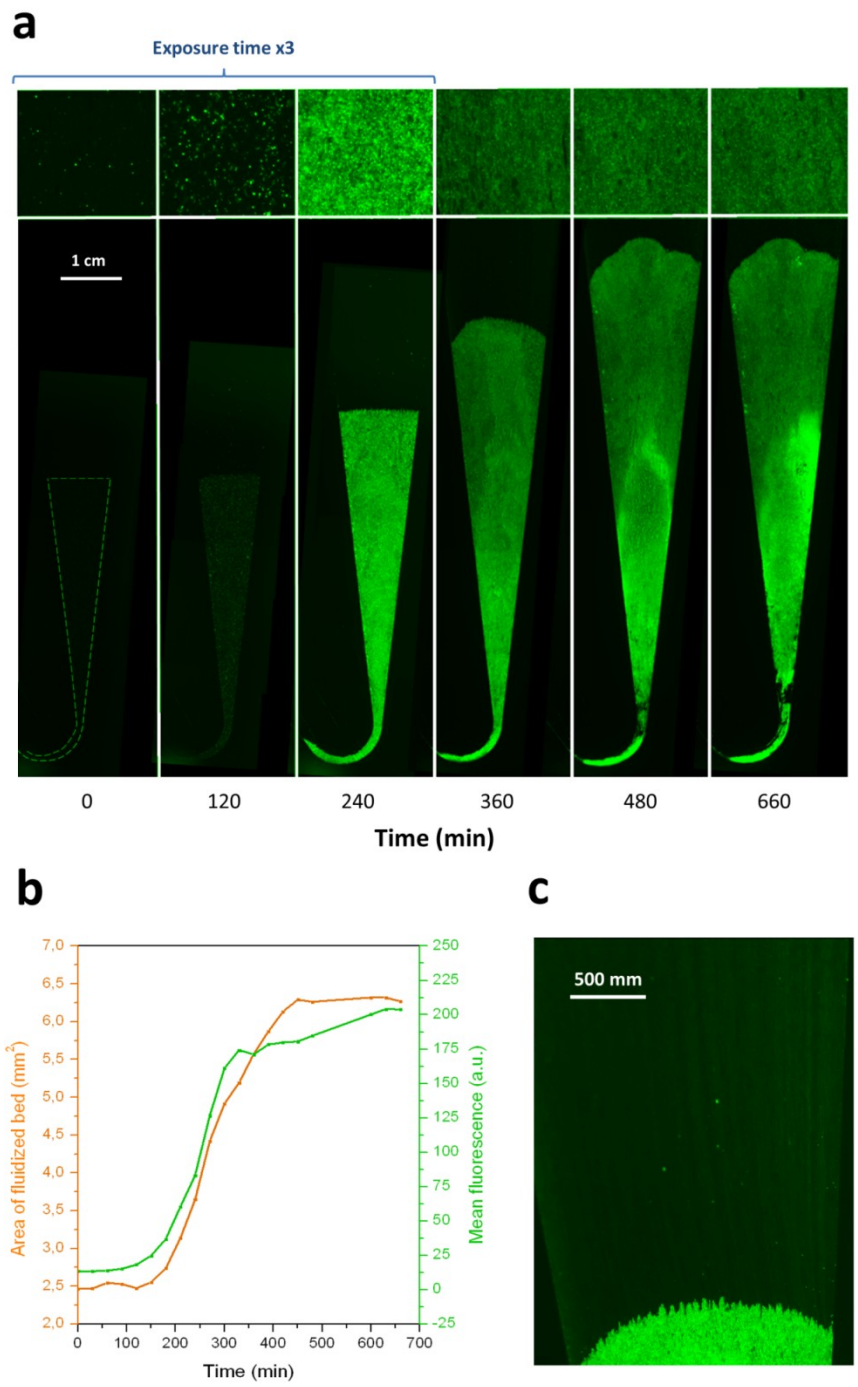

Fig. 3: Fluorescence images were taken every 30 minutes during the culture step of previously immunocaptured GFP-expressing S. Typhimurium*, both the whole bead ensemble and a detail zoom are shown (a). The increase in fluorescence is accompanied by an increase in size of the fluidized bed (b). Towards the end of the bed expansion (300min) a flow of bacteria can be seen leaving the magnetic beads dragged by the flow (c).*

We attribute this fluidized bed expansion to the volume occupancy of the newly grown bacteria (see SIO for quantitative discussion and modeling). Towards the end of the bed expansion an

important flow of bacteria leaves the fluidized bed, dragged by the flow of nutritious medium (Fig 3c). This is a consequence of the saturation in the capacity of the fluidized bed to capture all the newly produced bacteria, a fact that could also explain the observed final plateau in the fluorescence total intensity, and the limited extent of bed expansion (see SIO for details).

The strong release of bacteria at the end of the amplification step demonstrates that the fluidized bed system can be used for direct processing of samples with low concentrations of bacteria, and thus avoid the need of a flask-based pre-culture, and obtain in a few hours amplification factors of typically 10^6. Also, this does not require any bacteria elution additional step, since the escaping bacteria can be collected or directly used downstream. The observed bed expansion however, suggested a more direct detection means for the presence in the initial sample of target bacteria with a proliferative potential (Fig. 4b), since the modification of the chip aspect is large enough to be detected by a simple visible light camera, or even by direct visual inspection (SIO Fig.1). To evaluate the dynamic range, the experiment was reproduced with different starting concentrations of bacteria. This yields a series of similar curves shifted along the horizontal axis, reminiscent of the DNA quantity plots obtained in Polymerase Chain reaction (PCR) (Fig 4c). Taking inspiration from this extremely successful technique, we defined an expansion threshold at 200µm, corresponding to the onset of the quasi-linear expansion phase. The intersection of growth curves with this threshold defines for all initial concentrations an expansion time. When plotted against the logarithm of the initial bacteria number, this expansion time follows a straight line (Fig 4d, blue), providing a calibration curve for the quantitation of the initial bacteria concentration with a wide dynamic range (from 4 cfu/50µl to 10^6 cfu/50µl). The time needed to reach an observable expansion ranges from ~90mn for 60000 cfu/50µl (1.2 10^6 cfu/ml) to 7~8 hours for cfu/50µl (80 cfu/ml).

Finally, to confirm the method specificity, cultures with the same anti-*Salmonella* Dynabeads® were performed after flowing in the cell *Escherichia coli* and *L. lactis (approx. 100 cfu/50 µL in PBS)*. In both cases no expansion of the bed occurred for subsequent cultures of up to 72 hours.

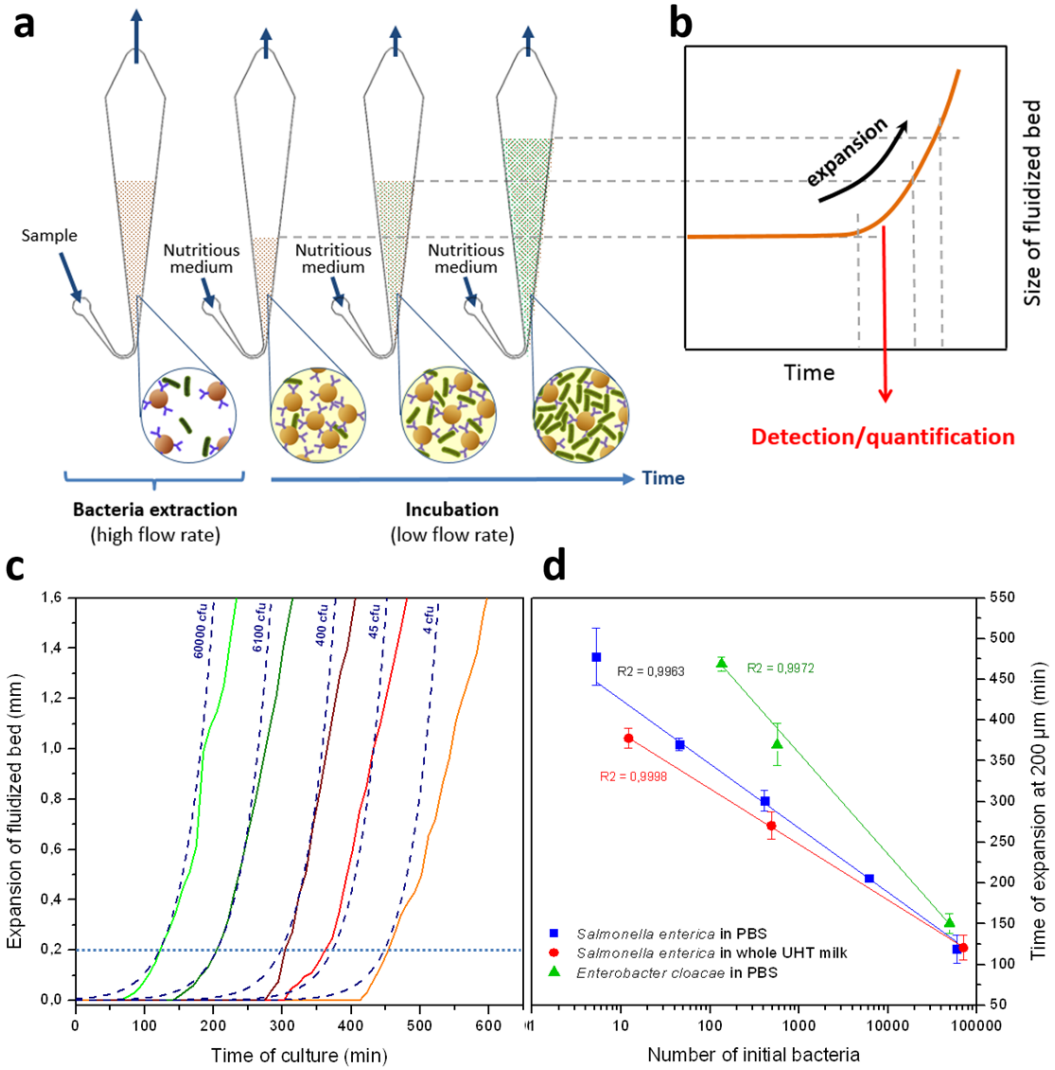

Figure 4: Protocol for direct detection of bacteria by bed expansion. (a): After sample capture and rinsing steps (at 1 and 1.5 µL/min respectively), measurements of the expansion of the fluidized bed (at a constant flow rate of 0.15 µL/min) were made along the chamber axis, with reference to the initial position of the front of the bed before expansion resulting in expansion curves (b). The expansion curves obtained with different initial concentrations of S. *Typhimurium* (indicated in figure as cfu/50 µL of sample) *are shifted with regards to each other (c), and in good agreement with a model of expansion based on the volume of newly-formed bacteria (c, dashed lines, see Supplementary Online Information for description of the model). Defining an expansion threshold at 200 µm (c, dotted line), a time of expansion can be measured for each initial concentration. A logarithmic plot of this expansion time*

versus initial bacterial load is shown in (d) for S. *Typhimurium in PBS (blue squares),* S. *Typhimurium in whole UHT milk (red circles) and E. cloacae in PBS (green triangles).*

Similar series of experiments were performed, starting from whole UHT milk spiked with bacteria. The results (Fig. 4d, red circles) yield very similar results, showing the applicability of the technology to complex, real-life food samples. Indeed, expansion times seem slightly shorter in milk than in PBS, maybe due to the fact that the bacteria were kept in milk for 50 minutes during the capture step, and contrary to PBS, could thus start to grow in this nutritious medium.

Application to *Enterobacter cloacae*

The same approach was applied to *E. cloacae*, in order to explore its generality. Besides its clinical relevance, this assay is also interesting regarding the versatility of the technology, since it uses lectin-functionalized beads for capture. The ligand used here was a lectin specific to *E. cloacae* (GSL-I-B4) grafted on magnetic beads presenting surface tosyl groups (Dynabeads® M-280 Tosylactivated). *E. cloacae* capture efficiency, evaluated as previously described for *S.* Typhimurium, was similarly high (85% ± 4.6%, n = 2). Fig.4d shows that *E. cloacae* can also be cultured and quantitatively detected *in situ* using the same procedure as for *S. Typhimurium*, except for longer expansion times. Expansion times specifically depend on bacteria type and strain, but also on culture conditions, leaving room for speeding up the process[21]. These experiments suggest that the fluidized bed expansion approach to bacteria detection will be applicable to a wide range of problems beyond the question of *Salmonella* in dairy products.

Mechanisms of bed expansion

Bed expansion could be due to a direct steric effect, related to the volume occupied by the new bacteria, or to a modification of the hydrodynamics of the bed, through e.g. changes in adhesion or friction properties of the bacteria-loaded beads, or the formation of biofilms. In order to unravel this question, additional series of experiments were performed, using a wider range of bacteria concentrations in the initial sample, and mutant bacteria with modified adhesion

and/or biofilm formation capabilities. These experiments, in combination with a simple analytical model of bacteria growth (see SIO) demonstrated that bed expansion is mainly due to the direct volume occupancy of “daughter” bacteria recaptured on the beads after cell multiplication by division.

DISCUSSION

This work demonstrates that the fluidized bed concept can be efficiently transposed to the microfluidic world, replacing gravity by magnetic forces. As compared to previous systems based on packed or magnetically stabilized micro-columns, this approach brings in numerous advantages. First, flow-through operations can be performed at low driving pressures, in order to capture bacteria from relatively large volumes (50-100µl, expandable to milliliters in further generations) with a very limited mass of capture particles (typically ~50 µg). With a suitable design of chamber and magnetic field, a constant recirculation of beads with close-to-uniform density can be achieved, maximizing capture efficiency. As compared to the commonly used batch capture on magnetic particles, this flow-through, high beads density mode allows an acceleration of kinetics and a reduction of the number of used beads for a given sample volume, since for rare targets, the kinetics is mostly controlled by target concentration and interbeads average distance during the capture step. The device was applied to the detection of two pathogen bacteria of interest, *S.* Thyphimurium and *E. cloacae.* A capture efficiency better than 70% and a specificity better than 500/1 versus other bacteria (e.g. *L. lactis* or *E. coli*) were achieved.

Then, the possibility to directly cultivate the bacteria in situ in the microfluidic chip was demonstrated. This cultivation yields to a physical expansion of the fluidized bed. This expansion is a consequence of the volume occupied by the developing bacteria. In a first mode, this allows for a very simple method for “yes or no” specific bacteria detection with direct visual readout, and sensitivity of the order of 100 cfu/ml in a few hours, as compared to the typical 1 or 2 days

needed by conventional techniques. In addition, the microfluidic chip design is very simple, and disposable chips can be mass produced, e.g. by injection molding. This, combined with the compactness of the device, can be a breakthrough in non-technical environments, e.g. for on-site investigation of food primary products. The technology is very generic, and we believe it will also find a wide range of applications in early diagnosis.

With a minor increase in complexity, i.e. addition of a low-cost visible light camera, the technique can be made quantitative, by measuring the time needed to reach a threshold of bead expansion. In this mode, quantitative detection with a dynamic range of four to five orders of magnitude can be achieved in a total time from raw sample to result of 2 to 8 hours, depending on initial concentration, the longest time corresponding to a sensitivity of 100 cfu/ml. The image analysis and data processing is simple, so to reduce development costs and allow widespread development including wireless communication of results, the whole imaging and analysis process can be embarked on a smartphone, as suggested e.g. in [22],

Both modes were demonstrated to accommodate direct infusion of complex samples such as unskimmed milk. This robustness to clogging or matrix effects, a definite advantage with regards to microcolums or filter-based devices, is a consequence of the fluidized nature of the capture bed, which can be perfused by liquids containing debris or particles much bigger than the capture beads or targets, as long as these contaminating objects do not present at their surface antigens targeted by the beads.

In comparison with methods based on PCR and molecular biology, this new approach is much simpler and thus less expensive to implement, and it detects only bacteria with a proliferative potential, whereas PCR-based methods will yield false-positive results in the presence of dead bacteria.

Finally, the flow-through nature of this family of devices provides an important flexibility regarding sample volumes, combining in a single seamless process the advantages of

preconcentration, purification and amplification: for instance, the internal volume of the chamber used in the present study is smaller than 1 µl, so it can accommodate sample volumes from typically 1 to 100 µl, varying the duration of the capture step from 1 mn to 1 hour. The geometry could be easily upscaled to accommodate sample volumes in the ml range, if needed.

A detailed cost per analysis evaluation is difficult to achieve accurately at this stage, since this involves many non-technical aspects, but the technology carries several features favoring very low costs: the design of the chips itself is simple, it does not involve active sensors, electrodes, actuators or high resolution features, so the disposable part of the device can be mass produced in thermoplastics for a few cents per chip, by e.g. injection molding. The cost of biochemicals is also considerably reduced as compared to other techniques: the biological specificity and selectivity is carried onto the magnetic beads, avoiding the need to functionalize in-situ the chip. The latter process is a strong hindrance to industrialization, since it involves fluidic connection and processing of each individual chip during production, and it also implies a high consumption of antibodies. In contrast, magnetic beads can be functionalized in large quantities in batch processes, reducing costs and facilitating quality control. Functionalized magnetic carriers can be rather expensive, but the consumption of the fluidized bed device is reduced by a factor of about 10 as compared to methods using beads-based capture in conventional batch format or as a pre-processing step. Finally, the method is also very cost-effective on the detection side, since it does not involve high-tech optics, expensive sensors or cameras, or micro-nano electrodes.

Overall, the magnetic microfluidic fluidized bed approach offers the possibility to perform direct sample-to-result analyses all-in-chip, with a high flexibility regarding initial sample size and nature. It also combines a small footprint and low reagents consumption, with low-cost chip production and detection technologies. We thus believe that it will find applications in numerous bioanalytical and point-of-care applications. The mode of operation presented here, combining

the capture of bacteria with high specificity and efficiency, with their online culture, allows for low-cost, quantitative and specific detection of bacteria with a proliferative potential, on a 5 orders or magnitude from 100 to 10^7 cfu/ml, in a time ranging from 2 to 8 hours. This sensitivity could rather easily be improved to reach the 1 cfu/ml range, or the detection made multiplex, by parallelization of the design. This technology thus opens new potential for many applications involving bacteria detection, e.g. environment control, bio-security, food industry and medicine.

SUPPLEMENTARY DISCUSSION AND DATA

1 Supplementary review of state of the art in bacteria detection

Plating and colony-counting are widely used for bacteria detection, and are still considered the gold standard. The protocol starts with an enrichment phase conducted overnight in liquid broth in agitated flasks. Then, cultures are plated on petri dishes containing agar-based growth medium and incubated for durations that may range from 12 hours to several days before counting. Finally, additional molecular or immunological typing methods may be needed, for specific strain identification. This protocol is highly sensitive and specific, but it typically requires several days, skilled personnel and large volumes of consumables. Hence, a great diversity of alternative analytical methods based either on metabolic properties (biochemical identification techniques, chromogenic agar broth[1]), antibodies targeting (ELISA[2], flow cytometry[3], immune-separation[4]) or nucleic acids (hybridization[5], PCR[6], microarrays[7]) have been developed. However, various disadvantages regarding e.g. specificity, sensitivity or cost, have hindered their widespread certification and/or use in routine practice.

Microfluidic-based technologies can offer platforms for faster and more automated detection systems, while reducing testing costs. A variety of microfluidic separation methods for bacteria can be found in the literature, based e.g. on size sorting [8], electrophoresis [9] or antibody capture[10]. For bacterial identification these methods are often coupled with nucleic acid amplification techniques such as PCR or further immuno-recognition protocols, increasing the complexity of the system. In addition, these methods, require a preliminary enrichment cultivation step to reach a concentration of cells sufficient for reaching the sensitivity level required for most food pathogen detection standards. This is usually performed by conventional, non-microfluidic protocols, limiting the gain as compared to conventional methods. Recently, an interesting article reported a single-step detection of bacteria, using an integrated on-chip culture on antibody capture arrays and label-free detection[11]. This study is certainly an

important step towards global assay acceleration, achieving a sensitivity around 140 cfu/ml in 10 hours for Salmonella spiked in raw milk, but it retains some limitations, such as baseline drift in the presence of real samples, a need for sample pre-treatment, and the need for an expensive surface plasmon resonance technology for detection. Also, specificity versus other commensal bacteria in excess was not assessed.

2. Detection of bacteria by direct visual inspection

Due to the size of the microfluidic chip, and the high absorption of the magnetic beads, the bed expansion can be directly observed by eye (SIO Fig 1). This can be done at regular intervals in order to detect contamination as fast as possible in the process, and have a rough estimate of the level of contamination, or as an “endpoint” “yes or no” detection.

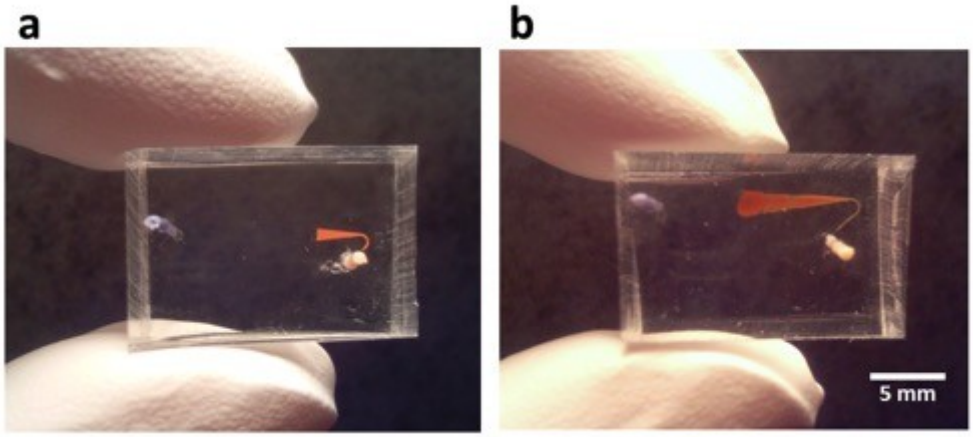

Supplementary Figure 1. Image of a chip before experiment, showing the beads bed in the absence of flow and without bacteria (left) and a second chip, also in the absence of flow but after bed expansion due to the positive detection of *salmonella* (right). Scale bar = 1 cm.

3. Deciphering the mechanisms of bed expansion during culture

Bed expansion could be due to a direct steric effect, related to the volume occupied by the new bacteria, or to a modification of the hydrodynamics of the bed, through e.g. changes in adhesion or friction properties. The first assumption was checked by injecting in the fluidized bed a highly concentrated solution of *S.* Typhimurium 10^8 cfu/mL. In this case, the bed expansion starts

immediately during the capture phase, without nutritious medium and heating of the chip (SIO Fig 2), with a volume increase proportional to the total number of injected bacteria, indicating that the volume occupied by the bacteria has a direct effect on bed expansion. Finally, when bacteria are cultivated on-chip from this pre-expanded state, by flowing culture medium and heating at 37°C, bed expansion continues readily (SIO Fig2b), confirming the absence of lag phase for culture already suggested by direct counting of fluorescent bacteria in the diluted regime.

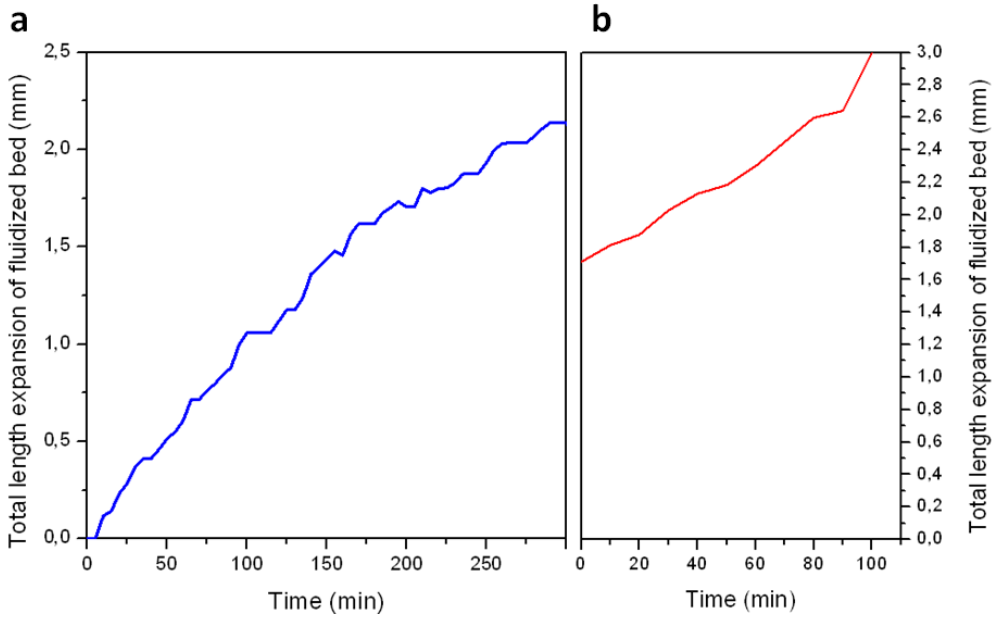

Supplementary Figure 2. (a) Results of experiment showing expansion of the fluidized bed during the capture step from a solution of *S*. Typhimurium at high concentration (10^8 cfu/ml). In this case, the flow rate during capture was 0.15 µL/min, as for the culture step to allow direct comparison of bed lengths. Note that the figure reports the length of the bed. The volume increase, deduced by taking into account the triangular shape of the chamber is, within experimental error, linear in time within the number of injected bacteria (not shown). (b) Expansion curve obtained during culture step, for a very high concentration of initial salmonella (6.10^6 captured bacteria). In both figures the zero length reference corresponds to the size of the bed prior to any cell capture, at a flow rate of 0.15 µL/min.

The above experiments demonstrate a direct steric effect of the captured bacteria to bed expansion. This, however, does not preclude other possible contributions. In particular, numerous studies have shown that *Salmonella spp.* are capable of forming biofilms under

certain conditions dependent on substrate, pH, temperature or salinity[12-13]. Biofilm formation could affect the fluidized bed properties through different mechanisms, such as volume occupancy of the extracellular matrix, crosslinking, or screening of ligands. To investigate this question, we used a biofilm-defective mutant strain of *S.* Typhimurium i.e. a knock-out mutant of the *csgD* gene involved in expression of both curli fimbriae (known to aid in biofilm formation, cell aggregation and cell adhesion[14]) and of cellulose (a main constituent of *Salmonella*-produced biofilms[15]). The doubling time of the mutant was measured in batch (see Methods Online), and shown to be close to that of the wild type (SIO Fig 3).

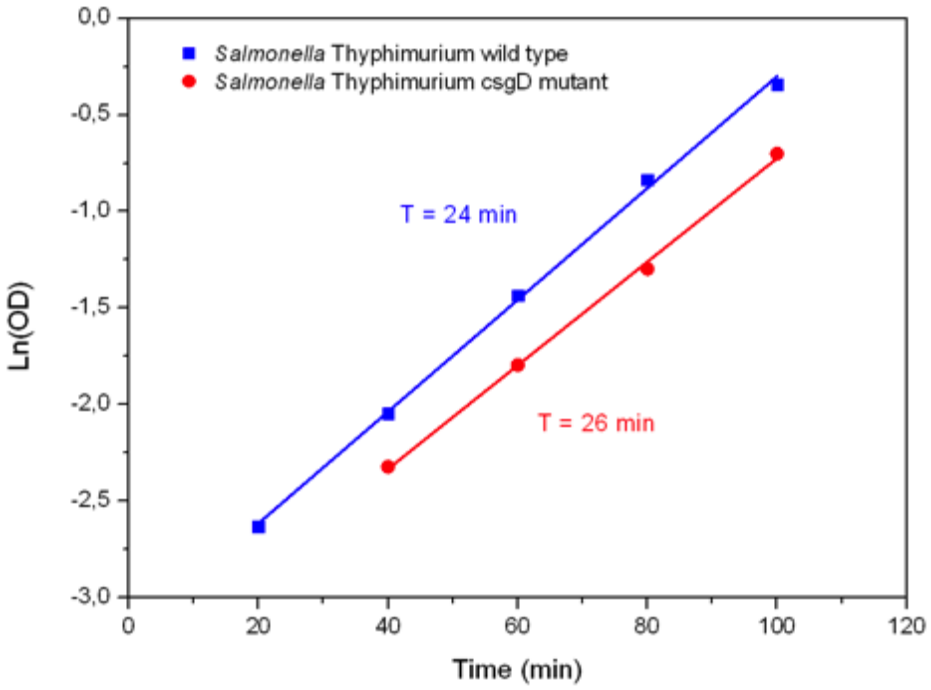

Supplementary Fig 3. Exponential phase of growth curves obtained for the batch culture of *S.* Typhimurium and the *csgD* mutant. Medium was LB Broth and temperature 37°C. The calculated generation times are indicated for both strains. (See Methods Online)

The capture efficiency of the fluidized bed regarding this mutant was then tested, since the mutation could have affected the expression or availability of the surface antigens used for capture. It was found similar to that of the wild type (data not shown).

Expansion times during culture in the chip were finally evaluated for a broad range of initial mutant bacteria loads, and found statistically equivalent to those of the wild type strain (SIO Fig 4).

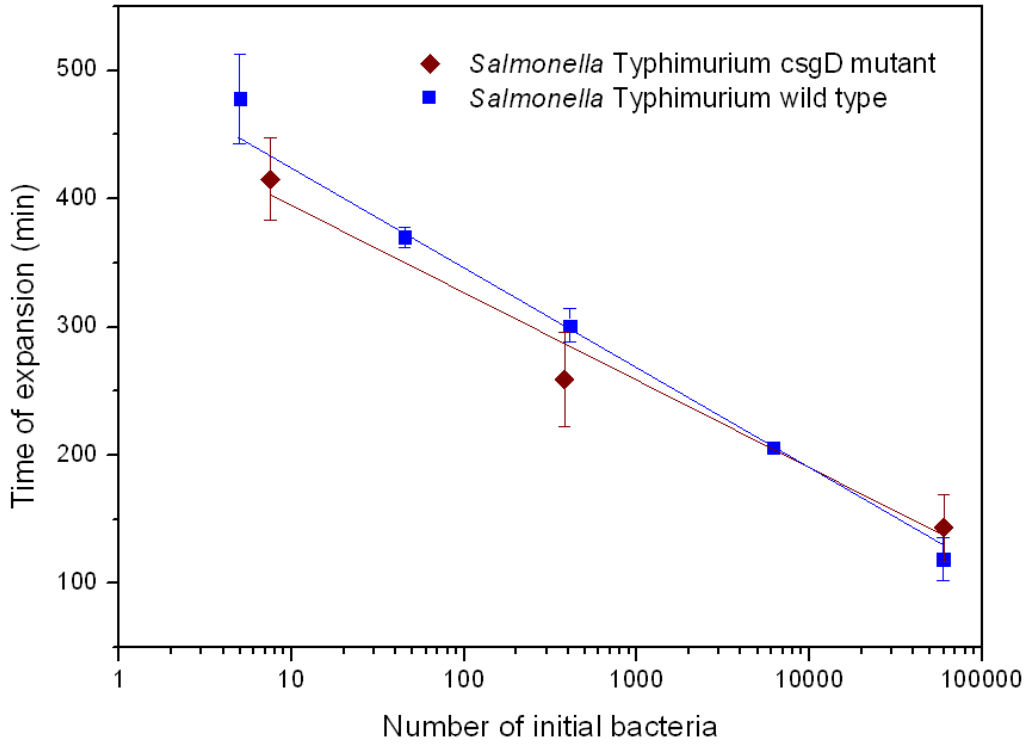

Supplementary Fig 4. Expansion times (for threshold expansion of 200 µm, see article main text) obtained with the *csgD* mutant of *S*. Typhimurium affected in biofilm formation. No significant differences were found with expansion times obtained with wild type *S*. Typhimurium.

This series of experiments suggests that the formation of biofilms does not play a significant role in the expansion phenomenon. Interestingly, it also suggests that adhesion and aggregation of bacteria have a marginal impact on bed expansion. Overall, this suggests that the method is very generic, since it does not depend on some specific collective properties of cells, but merely on their intrinsic volume and proliferation power.

4. Analytical model for growth.

Assuming that all bacteria produced during culture remain confined inside the fluidized bed, a very simple expression can be proposed for the volume expansion as a function of time, based on an exponential cell division:

$$V_{exp} = V_{bac} n_0 2^{\frac{t}{t_d}} \quad (1)$$

Where n_0 t_d and V_{bac} are the initial number of captured bacteria, the mean division time , and the effective volume occupied by a single bacterium, respectively. Injecting in this equation the previously measured capture efficiency, and leaving division time and effective volume as free parameters (taking the same value for all initial concentrations of bacteria) yields a series of curves (dashed curves in Fig 4c, main text), which fit the data within experimental uncertainty on 4 orders of magnitude of concentration. The best fit doubling time, t_d = 23.7min, is very close to 24 mn, the value measured in batch with identical medium and temperature. Considering that the effective volume must take into account steric effects due to the bacteria orientation and of the flagella, the natural variation of volume of each bacteria during its growth, and genotypic and phenotypic differences between different strains in different conditions, it is difficult to provide an accurate “a priori” evaluation of a single bacterium steric exclusion volume. However, the effective volume providing the best fit to the data, V_{bac} = 4.8e-9 µL, is within the expected range (typically between 1.4 and 7.5 e^{-9} µL[1617].

5. Release of bacteria during culture

Finally, to explore the causes of the saturation of bed expansion observed at long times, the release of bacteria from the fluidized bed during on-chip culture was evaluated, by collecting the fluid exiting the chamber and bacteria counting by serial dilution and plating (SIO Fig. 5).

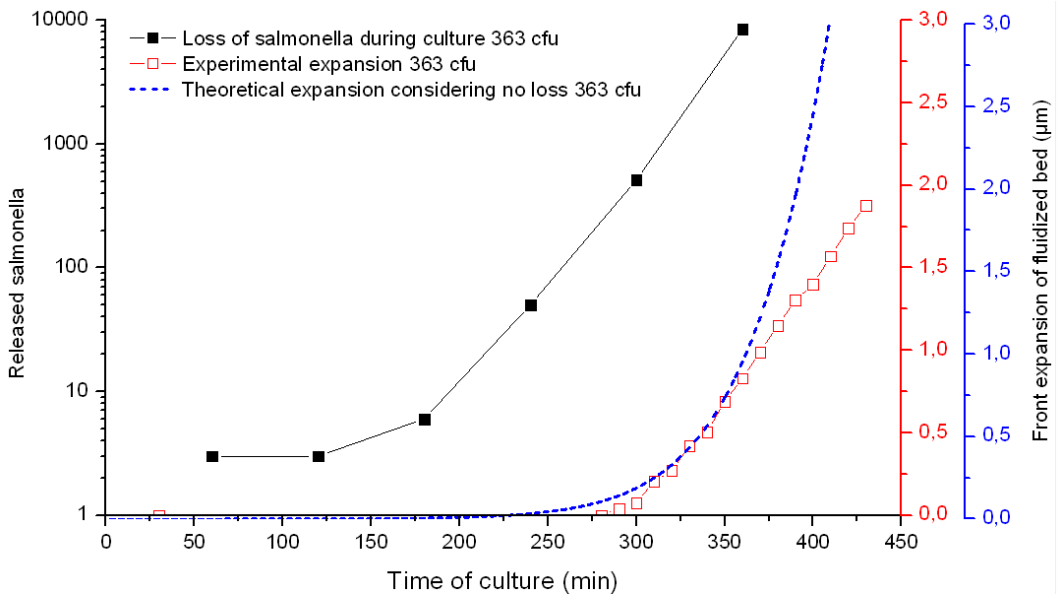

Supplementary Fig 5. Number of Released *S*. Typhimurium cells from the fluidized bed during the culture step, after capture from a 50 µl sample containing 350+/-50 cfu (measured by colony plating). Each square represents the released bacteria in the previous hour. The bed expansion is plotted as red squares (red vertical scale), the model's prediction as blue dashed line (blue vertical line).

During the early stages of growth medium perfusion, essentially no bacterium leaves the bed. This suggests that all bacteria produced during the initial phase are recaptured on the beads. Bacteria start to be released in significant amounts after typically two hours (the indirect mode of measurement by colony plating of the effluent introduces an experimental lag time, since a sufficient volume of effluent must be accumulated before the plating can be performed), and continuously increases afterwards. The experimental bed expansion deviates from the theory around 370 mn, corresponding to a bed expansion of about 1mm representing 60% of the initial bed volume. It is not surprising that such occupancy starts to have a significant screening effect on the recapture of newly produced cells. This, combined with the fact that the release rate of cells continues to grow beyond this time point, suggests that bed growth saturation and deviation of the effective growth from the model are due to a saturation of the capture sites, and not to a loss of viability of the cells in the bed.

METHODS

Microfluidic chips. The general design of the PDMS chips used for capture is presented in Fig. 1 of the main article and in Methods Supplementary Fig.1 below: The main chamber is an asymmetrical triangular shape 13 mm in length and 2.6 mm at its maximum width, with an aperture angle of 13°. A bent channel (100µm width) connects the inlet of the main chamber to 3 fluid inlets. This geometry is necessary to avoid beads escape in no-flow conditions. The outlet is placed on the opposite side of the chamber. The height of all structures was 50 µm. The chips were fabricated by standard casting of PDMS on a prefabricated mold prepared by micromilling and plasma treatment for binding to a second flat PDMS film. A surface treatment with poly-dimethyl-acrylamide bearing epoxy function (E-PDMA)[1] was immediately applied by incubation for one hour in the channel of an aqueous solution of this polymer at a concentration of 0.25% (w/v), followed by rinsing with deionized water.

Pressure and flow control. The three inputs were connected through PEEK tubes (50 µm internal diameter) to their respective sample and reagents reservoirs, and the source of fluid at each time was selected by flipper solenoid valves (Bürkert, 6604). Flow control was achieved thanks to a pressure controller (MFCS™, Fluigent) applying to the sample and reagents reservoirs pressurized regulated thanks to a feedback given by a flowmeter (Flowell, Fluigent) connected to the output of the chip, under control of the dedicated software (FRCM, Fluigent). A PEEK tube, ID 250 µm connected this flowmeter and a waste reservoir.

Capture efficiency. The protocol for evaluation of the capture efficiency (summarized in Supplementary Methods Fig 2, below) was as follows : 1. The whole system was filled with phosphate buffer saline (PBS) with 1% bovine serum albumin (BSA); 2. 50 µg of anti-S*almonella* Dynabeads® were injected inside the chamber thanks to a pipette tip at the chamber outlet. A small magnet below the chip was used to guide the beads to the chamber during this loading step; 3. A NdFeB12 1.47 T permanent magnet (N50, Chen yang Technologies) was placed at a distance of 2 mm from the bent channel, symmetrically aligned with the axis of the main chamber; 4. A sample volume of 50 µL was injected through inlet 1 at a flow-rate of 1

µL/min; 5. The beads were washed inside the chip after capture with 40 µL of PBS 1% BSA through inlet 2 at 1.5 µL/min; 6. Triplicate cell culture plating was performed with 50 µL aliquots of each of: i:the initial sample reservoir; ii; the total eluted volume collected in a tubing at the output of the chip during the capture step (Tygon© 500 µm ID, 60 cm long, instead of the PEEK tube previously described between the output of the chip and the flowmeter); iii) and finally the beads flushed from the chip after the capture step; Colonies were counted the following day and the capture rate was estimated as the ratio between captured bacteria (from plating of beads) and the addition of both capture and non-captured bacteria (non-captured meaning sample collected in Tygon© tube). This procedure was selected, rather than a reference to the initial number of bacteria spiked in the sample. The latter approach led to similar values in average, but with a higher dispersion, probably due to difficulties in evaluating accurately the absolute number of spiked bacteria, especially at low numbers.

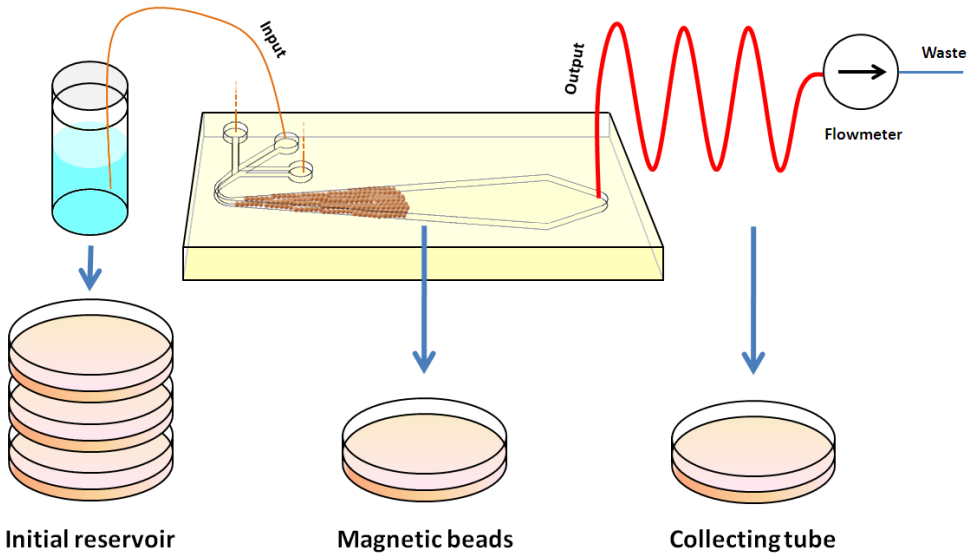

Supplementary Methods Figure 2. Protocol followed for the determination of the capture rate of the immunoextraction step : 50 µL of the initial sample were plated three times for average counting; magnetic beads were extracted from the chip after the washing step by high pressure flushing and immediately culture plated; a Tygon© reservoir was placed at the outlet and just before the flowmeter to collect 120 µL of output volume containing non-captured bacteria, the total volume also plated once.

On-chip bacterial culture and amplification. The protocol for the on-chip culture started as that previously described for capture efficiency evaluation, but diverged from step 6: culture was started by injecting lysogeny broth through inlet 3 at 0.15 µL/min. The temperature was set at 37°C with the use of a

glass slide coated with indium tin oxide connected to a voltage controller (Eurotherm 3508) and feedback -regulated with the input from a thermocouple placed between the glass slide and the chip. For fluorescence measurements, time-Lapse images were taken every 15 minutes with a Nikon Ti microscope and a CoolSNAP HQ2 camera.

For direct detection by bed expansion, images were obtained by real-time recording of the bed by a low-cost camera (AM4013MZTL, Dino-Lite). The bed expansion was quantified from images stacks with a home-made software written in Image-J, taking as reference the position of the front of the initial immobile bed and as a positive measurement any displacement towards the output along the axis of the chamber.

Bacteria strains and viable cell count. *Salmonella enterica* serovar Thyphimurium ATCC14028 and the isogenic csgD mutant strain affected in biofilm formation were obtained from Françoise Norel's collection (Institut Pasteur). Enterobactero cloacae subsp. cloacae ATCC13047 was obtained from Aquila Bioscience. To monitor bed expansion the ATCC14024 strain was transformed by the pFPV25.1 (Ap^R) plasmid, to express green fluorescent protein (GFP)[31]. Quantification of bacteria was achieved by counting the total number of colony-forming units (CFUs) grown onto Brain heart infusion (BHI) agar from serial dilutions of the original sample and expressed as CFU/mL.

Batch determination of population doubling time

The population doubling time of wild type and mutant bacteria strains was determined by measuring as a function of time the optical density (OD) of bacteria suspension in agitated flasks of LB kept at 37°C. OD was measured with a spectrophotometer Hitachi U-1900. The doubling time T is deduced from the slope of the ln(OD) versus time. The result obtained this way is independent of the initial density of bacteria, and of the volume and intrinsic OD of the bacteria strain[23].

4.7 References

1. Organization, W. H. *Antimicrobial resistance: global report on surveillance*. (World Health Organization, 2014).

2. European Food Safety Authority (EFSA). The European Union summary report on trends and sources of zoonoses, zoonotic agents and food-borne outbreaks in 2013. *EFSA J.* **13,** 3991 (2015).

3. Hohmann, E. L. Nontyphoidal salmonellosis. *Clin Infect Dis* **32,** 263–269 (2001).

4. Benenson, S. *et al.* The risk of vascular infection in adult patients with nontyphi Salmonella bacteremia. *Am. J. Med.* **110,** 60–63 (2001).

5. Feasey, N. A., Dougan, G., Kingsley, R. A., Heyderman, R. S. & Gordon, M. A. Invasive non-typhoidal salmonella disease: An emerging and neglected tropical disease in Africa. *The Lancet* **379,** 2489–2499 (2012).

6. Eugene Sanders, W. E. & Sanders, C. C. Enterobacter spp.: Pathogens poised to flourish at the turn of the century. *Clinical Microbiology Reviews* **10,** 220–241 (1997).

7. Cassar, R. & Cuschieri, P. Comparison of Salmonella chromogenic medium with DCLS agar for isolation of Salmonella species from stool specimens. *J. Clin. Microbiol.* **41,** 3229–3232 (2003).

8. Gutiérrez, R. *et al.* Monoclonal antibodies and an indirect ELISA for detection of psychrotrophic bacteria in refrigerated milk. *J. Food Prot.* **60,** 23–27 (1997).

9. Karo, O. *et al.* Bacteria detection by flow cytometry. *Clin. Chem. Lab. Med.* **46,** 947–953 (2008).

10. Wen, C. Y. *et al.* One-step sensitive detection of salmonella typhimurium by coupling magnetic capture and fluorescence identification with functional nanospheres. *Anal. Chem.* **85,** 1223–1230 (2013).

11. Kang, C. H. *et al.* Relationship between genome similarity and DNA-DNA hybridization among closely related bacteria. *J. Microbiol. Biotechnol.* **17,** 945–951 (2007).

12. Pathmanathan, S. G. *et al.* Simple and rapid detection of Salmonella strains by direct PCR amplification of the hilA gene. *J. Med. Microbiol.* **52,** 773–776 (2003).

13. Mitterer, G. *et al.* Microarray-Based Identification of Bacteria in Clinical Samples by Solid-Phase PCR Amplification of 23S Ribosomal DNA Sequences. *J. Clin. Microbiol.* **42,** 1048–1057 (2004).

14. Wu, Z., Willing, B., Bjerketorp, J., Jansson, J. K. & Hjort, K. Soft inertial microfluidics for high throughput separation of bacteria from human blood cells. *Lab Chip* **9,** 1193–1199 (2009).

15. Vilkner, T., Shivji, A. & Manz, A. Dry powder injection on chip. *Lab Chip* **5,** 140–145 (2005).

16. Doroodchi, E., Peng, Z., Sathe, M., Abbasi-Shavazi, E. & Evans, G. M. Fluidisation and packed bed behaviour in capillary tubes. *Powder Technol.* **223,** 131–136 (2012).

17. Zivkovic, V. & Biggs, M. J. On importance of surface forces in a microfluidic fluidized bed. *Chem. Eng. Sci.* **126,** 143–149 (2015).

18. Le Nel, A. *et al.* Controlled proteolysis of normal and pathological prion protein in a microfluidic chip. *Lab Chip* **8,** 294–301 (2008).

19. Shaw, S. J., Blais, B. W. & Nundy, D. C. Performance of the Dynabeads anti-Salmonella system in the detection of Salmonella species in foods, animal feeds, and environmental samples. *J. Food Prot.* **61,** 1507–1510 (1998).

20. Montel, M. C. *et al.* Traditional cheeses: Rich and diverse microbiota with associated benefits. *International Journal of Food Microbiology* **177,** 136–154 (2014).

21. Bevilacqua, A., Cannarsi, M., Gallo, M., Sinigaglia, M. & Corbo, M. R. Characterization and implications of Enterobacter cloacae strains, Isolated from Italian table olives 'bella di cerignola'. *J. Food Sci.* **75,** (2010).

22. Park, T. S., Li, W., McCracken, K. E. K. & Yoon, J. J.-Y. Smartphone quantifies Salmonella from paper microfluidics. *Lab Chip* **22,** 256–258 (2013).

Agrawal, S. et al., 2012. Multiplexed detection of waterborne pathogens in circular microfluidics. *Applied Biochemistry and Biotechnology*, 167, pp.1668–1677.

Bacconi, A. et al., 2014. Improved sensitivity for molecular detection of bacterial and Candida infections in blood. *Journal of clinical microbiology*, 52(9), pp.3164–74.

Barletta, F. et al., 2013. Multiplex real-time PCR for detection of Campylobacter, Salmonella, and Shigella. *Journal of clinical microbiology*, 51(9), pp.2822–9.

Boehme, C.C. et al., 2011. Feasibility, diagnostic accuracy, and effectiveness of decentralised use of the Xpert MTB/RIF test for diagnosis of tuberculosis and multidrug resistance: a multicentre implementation study. *Lancet (London, England)*, 377(9776), pp.1495–1505.

Bouguelia, S. et al., 2013. On-chip microbial culture for the specific detection of very low levels of bacteria. *Lab on a chip*, 13(20), pp.4024–32.

Byrnes, J.J. et al., 1975. Mechanism of hemin inhibition of erythroid cytoplasmic DNA polymerase. *Biochemistry*, 14(4), pp.796–799.

Campbell, G. a & Mutharasan, R., 2005. Escherichia coli O157:H7 detection limit of millimeter-sized PZT cantilever sensors is 700 cells/mL. *Analytical sciences : the international journal of the Japan Society for Analytical Chemistry*, 21(4), pp.355–7.

Cheong, K.H. et al., 2008. Gold nanoparticles for one step DNA extraction and real-time PCR of pathogens in a single chamber. *Lab on a chip*, 8(5), pp.810–3.

Food US, D. administration, 2001. FDA Bacteriological Analytical Manual 8th edition.

Gan, M. et al., 2011. A scalable microfluidic chip for bacterial suspension culture. *Lab on a Chip*, 11(23), p.4087.

Garibyan, L. & Avashia, N., 2013. Polymerase Chain Reaction. *Journal of Investigative Dermatology*, 133(3), p.e6.

Goldman, E. & Green, L.H., 2015. *Practical handbook of microbiology*, CRC Press.

Jenkins, D.M. et al., 2011. Handheld device for real-time, quantitative, LAMP-based detection of Salmonella enterica using assimilating probes. *Biosensors & bioelectronics*, 30(1), pp.255–60.

Jiang, X. et al., 2014. A continuous-flow high-throughput microfluidic device for airborne bacteria PCR detection. *Lab on a chip*, 14(4), pp.671–6.

Kim, S. et al., 2006. Multiplex PCR-based method for identification of common clinical serotypes of Salmonella enterica subsp. enterica. *Journal of Clinical Microbiology*, 44(10), pp.3608–3615.

Lee, J.-G. et al., 2006. Microchip-based one step DNA extraction and real-time PCR in one chamber for rapid pathogen identification. *Lab on a chip*, 6(7), pp.886–895.

Lee, K.M. et al., 2015. Review of Salmonella detection and identification methods: Aspects of rapid emergency response and food safety. *Food Control*, 47, pp.264–276.

LI, Y. & SU, X.-L., 2006. MICROFLUIDICS-BASED OPTICAL BIOSENSING METHOD FOR RAPID DETECTION OF ESCHERICHIA COLI O157:H7. *Journal of Rapid Methods and Automation in Microbiology*, 14(1), pp.96–109.

Lien, K.-Y. et al., 2007. Purification and enrichment of virus samples utilizing magnetic beads on a microfluidic system. *Lab on a chip*, 7(7), pp.868–875.

Lin, F.Y.H. et al., 2005. Development of a nanoparticle-labeled microfluidic immunoassay for detection of pathogenic microorganisms. *Clinical and diagnostic laboratory immunology*, 12(3), pp.418–25.

Liu, R.H. et al., 2004. Self-Contained, Fully Integrated Biochip for Sample Preparation, Polymerase Chain Reaction Amplification, and DNA Microarray Detection. *Analytical Chemistry*, 76(7), pp.1824–1831.

Longo, M.C., Berninger, M.S. & Hartley, J.L., 1990. Use of uracil DNA glycosylase to control carry-over contamination in polymerase chain reactions. *Gene*, 93(1), pp.125–128.

Mahalanabis, M. et al., 2011. Erratum to: An integrated disposable device for DNA extraction and helicase dependent amplification. *Biomedical microdevices*, 13(3), pp.599–602.

Mahmoudian, L. et al., 2008. Rolling circle amplification and circle-to-circle amplification of a specific gene integrated with electrophoretic analysis on a single chip. *Analytical chemistry*, 80(7), pp.2483–90.

McKendry, R. a. & Kappeler, N., 2013. Sensors: Good vibrations for bad bacteria. *Nature Nanotechnology*, 8(7), pp.483–484.

Notomi, T. et al., 2000. Loop-mediated isothermal amplification of DNA. *Nucleic acids research*, 28(12), p.E63.

Oblath, E. a et al., 2013. A microfluidic chip integrating DNA extraction and real-time PCR for the detection of bacteria in saliva. *Lab on a chip*, 13(7), pp.1325–32.

Ottesen, E. a et al., 2006. Microfluidic digital PCR enables multigene analysis of individual environmental bacteria. *Science (New York, N.Y.)*, 314(5804), pp.1464–7.

Radhika, M. et al., 2014. A novel multiplex PCR for the simultaneous detection of Salmonella enterica and Shigella species. *Brazilian journal of microbiology : [publication of the Brazilian Society for Microbiology]*, 45(2), pp.667–76.

Raja, S. et al., 2005. Technology for automated, rapid, and quantitative PCR or reverse transcription-PCR clinical testing. *Clinical Chemistry*, 51(5), pp.882–890.

Sontakke, S. et al., 2009. Use of broad range16S rDNA PCR in clinical microbiology. *Journal of microbiological methods*, 76(3), pp.217–25.

Sun, K. et al., 2002. A heater-integrated transparent microchannel chip for continuous-flow PCR. *Sensors and Actuators, B: Chemical*, 84(2-3), pp.283–289.

Theron, G. et al., 2013. Feasibility, accuracy, and clinical eff ect of point-of-care Xpert MTB/RIF testing for tuberculosis in primary-care settings in Africa: a multicentre, randomised, controlled trial. *Lancet*, 13(9915), pp.424–435.

Tokel, O. et al., 2015. Portable microfluidic integrated plasmonic platform for pathogen detection. *Scientific reports*, 5, p.9152.

Varshney, M. et al., 2007. A label-free, microfluidics and interdigitated array microelectrode-based impedance biosensor in combination with nanoparticles immunoseparation for detection of Escherichia coli O157:H7 in food samples. *Sensors and Actuators, B: Chemical*, 128(1), pp.99–107.

Wang, D. et al., 2011. Rapid detection of Listeria monocytogenes in raw milk with loop-mediated isothermal amplification and chemosensor. *Journal of food science*, 76(9), pp.M611–5.

Yoon, J.Y. & Kim, B., 2012. Lab-on-a-chip pathogen sensors for food safety. *Sensors (Switzerland)*, 12(8), pp.10713–10741.

Zanoli, L.M. & Spoto, G., 2013. Isothermal amplification methods for the detection of nucleic acids in microfluidic devices. *Biosensors*, 3(1), pp.18–43.

Zhang, C. & Xing, D., 2010. Microfluidic gradient PCR (MG-PCR): A new method for microfluidic DNA amplification. *Biomedical Microdevices*, 12(1), pp.1–12.

Zhao, X. et al., 2012. Compatible immuno-NASBA LOC device for quantitative detection of waterborne pathogens: design and validation. *Lab on a Chip*, 12, p.602.

Chapter 5

Microfluidic rolling circle amplification for cancer diagnostics

5.0 Summary

The handling of reagents in magnetic bead protocols is a particular limitation in the applicability of some otherwise very powerful DNA molecular tools. This is the case for padlock-based systems such as rolling circle amplification (RCA), that allow a very accurate single nucleotide recognition for mutation identifiation coupled to precise quantification results, but have so far not reached the clinical diagnosis stage because of the need for multi-step protocols. The microfluidic magnetic fluidized bed presents, as so far shown, very good characteristiscs for bead protocol automation, but is also an efficient preconcentration system, and this is a particularly atractive characteristic for "liquid biopsy" applications such as the detection of circulating tumor DNA in blood samples. In this chapter, the development of a system that combines the fluidized bed for DNA detection and amplification and a microarray for further ampliciation and fluorescent detection, is presented for the KRAS mutation, associated to several types of cancer. The work is still ongoing, and the detection of concentrations as low as those needed for ctDNA detection remains to be proven, but preliminary results show the succesful integration of the full molecular protocol in a single microfluidic chamber, with a simple "samples-in -> results-out" format and high multiplexing potential.

5.1 Introduction

Cancer is caused by alterations in the genome that can be very different from patient to patient, making the disease difficult to treat. A trend then exists towards a more personalized medicine, in which diagnostic testing is employed in order to select the appropriate therapies based, in particular, on genetic information. Further, the disease can evolve over time and as a response to treatment. For cancer monitoring, current methods

rely on tumor imaging, analysis of protein biomarkers in serum and tumor biopsies. While the first two provide information on disease progress, they are blind to the actual genomic characteristic and/or changes experienced by the tumor. Biopsies on the other hand allow the assessment of this information, but are both invasive and risky, if at all possible due to a difficult accessibility or insufficient sample recovery. They are also highly localized, offering little information on tumor heterogeneity.

In recent years, a research impulse has been given to non-invasive cancer diagnostic methods. In particular, plasma-present circulating biomarkers such as circulating tumor cells (CTCs)(Danila et al. 2014), exosomes (Tickner et al. 2014) and circulating tumor DNA (ctDNA)(Bettegowda et al. 2014) have received much attention as means for minimally-invasive diagnosis and prognosis. CTCs are cancer cells that have shed from a primary tumor into the bloodstream, responsible for the formation of metastases in distant organs. The analysis of CTC in patient blood has revealed their reflection of tumor heterogeneity and their frequency correlation with disease progression, making them interesting biomarkers for clinical prognosis (Consoli et al. 2011). This research has been particularly fruitful in the field of microfluidics, with a wide range of proposed CTC separation and analysis methods proposed (Dong et al. 2013)(Autebert et al. 2012), and has led to the appearance of diagnostic devices on the market (notably the FDA approved CellSearch® system)

On the other hand, genomic DNA is known to freely circulate in blood (cell-free DNA, cfDNA) due to cell apoptosis/necrosis and active secretion mechanisms from healthy and cancer cells (Ilie et al. 2014). High levels of cfDNA have been correlated with poor outcome for some cancers (Sozzi et al. 2009), but it is the inherent genetic content of this DNA that offers invaluable information for the study of highly apoptotic elements such as tumors (cfDNA from with tumoral origin referred as ctDNA). The identification of mutations acquired as a result of treatment resistance could provide a particularly useful complement to more conventional biopsies for personalized therapies. Furthermore, the analysis of ctDNA from patient blood samples has been shown to indicate the presence of not yet metastasized tumors, offering an advantage with CTC detection methods (Bettegowda et al. 2014). The release of DNA in blood from heterogeneous tumors may also yield tumor's genetic makeup, without the need for invasive biopsies.

Among the many already identified clinically relevant mutations, those associated with the KRAS gene have become a priority in the cases of lung, pancreatic and colorectal cancers. The KRAS (Kirsten rat sarcoma viral oncogene homolog) gene contains instructions for the production of a protein called K-Ras mainly involved in cell division regulation. This protein is part of a signaling pathway known as RAS/MAPK that relays signals from outside the cell to the cell's nucleus, instructing the cell to grow, divide or differentiate.

The KRAS gene belongs to the Ras family of oncogenes that includes the genes HRAS and NRAS. All of these genes produce GTPase proteins that convert GTP molecules into

GDP for pathway signaling. Mutations in these genes lead to amino acid changes in the produced proteins, what sometimes results in overactivated GTP to GDP conversion, this in turn giving rise to uncontrolled cell division and tumor formation (a slightly overactivated protein can also lead to non-cancerous pathologies such as cardiofaciocutaneous and Noonan syndromes).

KRAS mutations are particularly present in lung cancers, found in 15 to 25% of all cases, and particularly prevalent for populations of European origin (25 to 50% of cases). Three main mutations can been associated with lung cancer (amino acid glycin at positions 12 or 13 and glutamine at position 61 in the K-Ras protein) all of them being somatic, that is, not inherited but acquired during the person's lifetime. Other somatic mutations have been associated with other types of cancer, in particular pancreatic and colorectal cancer.

Mutations present in KRAS have been shown to be predictors of cancer response to treatment (Knickelbein & Zhang 2015). KRAS mutations in colorectal cancer are associated with poor response to common drug therapies such as cetuximab (Lièvre et al. 2006). Similarly, KRAS mutations result in low response to lung cancer treatments such as erlotinib or gefitinib (Suda et al. 2010). These mutations can also appear as a response to drug treatment, resulting in subsequent illness progression.

For certain drug treatments, it has thus become necessary to know in advance the presence of KRAS mutations, something that has been enforced by the FDA and the European Medicines Agency in the labeling of drugs such as *panitumumab* and *cetuximab*.

KRAS mutation detection is conventionally obtained from tissue samples from a tumor biopsy, with methods based on sequencing, such as automated dideoxy sequencing or pyrosequencing, or binary result methods, such as single strand conformation polymorphism (SSCP) analysis and high resolution melt (HRM) analysis. Especially in the latter cases, PCR amplification (see Chapter 4) is a required step to amplify the DNA region in which the mutation of interest lies.

On the other hand, the detection of ctDNA is challenging, as it usually represents a very small fraction of all cfDNA (<1.0%), and is present at very low concentrations (normal cfDNA levels ~0.7-7 ng/mL (Szpechcinski et al. 2015)). Standard sequencing approaches can only be used for patients at advanced cancer stages presenting high levels of ctDNA (Diaz & Bardelli 2014). However, novel genomic methodologies based on PCR-based assays, and in particular digital PCR, have recently made the multiplexed detection and quantification of low levels of ctDNA possible (Huggett & Whale 2013). In digital PCR (dPCR), the sample is separated into a large number of partitions to carry the reaction in each partition individually. This results in more sensitive quantifications of nucleic acids and allows the study of variations in gene sequences. The microfluidic compartimentalization in picodroplets for multiplex dPCR is a particularly rapidly developing field for efficient ctDNA analysis (Taly et al. 2013).

PCR techniques are nowadays highly developed and have become the standard for many clinically relevant diagnostic assays. Nonetheless, some drawbacks of this cycling technique, such as the use of sophisticated and expensive instruments, might open the applicability of alternative amplification methods for certain applications, for example when a higher portability is required. Padlock probe-based methods, such as rolling circle amplification, might additionally offer a relatively simpler robust detection of single nucleotide mutations with quantification capabilities that ideally allow the determination of single molecule events.

5.1.1 Rolling circle amplification and Circle to circle amplification

In Chapter 4, the advantage of alternative isothermal amplification methods for DNA was put forward, and several of the most commonly encountered techniques were cited. Due to its robustness and simplicity, rolling circle amplification (RCA) holds a distinct position as a choice for DNA diagnosis.

In RCA, a circular DNA template is continuously amplified by a strand displacement DNA polymerase. Since for most applications the target DNA of interest is linear (Fig. 5.1 green), an oligonucleotide (called padlock probe) containing extremities specific for two adjacent target sequences, is used to circularly hybridize to the target strand (Fig. 5.1 blue). The gap is then completed through polymerase enzymatic activity or, if no base pair gap is left, directly ligated with a ligase enzyme. In this latter case, a perfect match between padlock probe and target is required, the ligation being sensitive to single nucleotide alterations. Since no amplification takes place if the padlock probe is not fully circularized, this property has been used for highly sensitive detection systems of single nucleotide mutations. After ligation, a polymerase enzyme (ex. Phi29 polymerase) is introduced for double strand synthesis using the target as a starting primer. Once the circle is complete, the polymerase displaces the previously created double strand, continuing its synthesis at a constant rate and forming a long single stranded DNA product. The reaction is fed with deoxynucleotide triphosphates (dNTPs), monomers/building blocks of the RCA process, present in the surrounding medium. The resulting rolling circle product (RCP) is a concatemer containing hundreds of copies of the original padlock. The self-collapsing properties of these long single stranded DNA results in ~500 nm spherical DNA coils (Jarvius et al. 2006) that allow microscopy detection of RCPs by fluorescence labeling and glass slide spreading. Each RCP indicates the amplification of a single original target sequence.

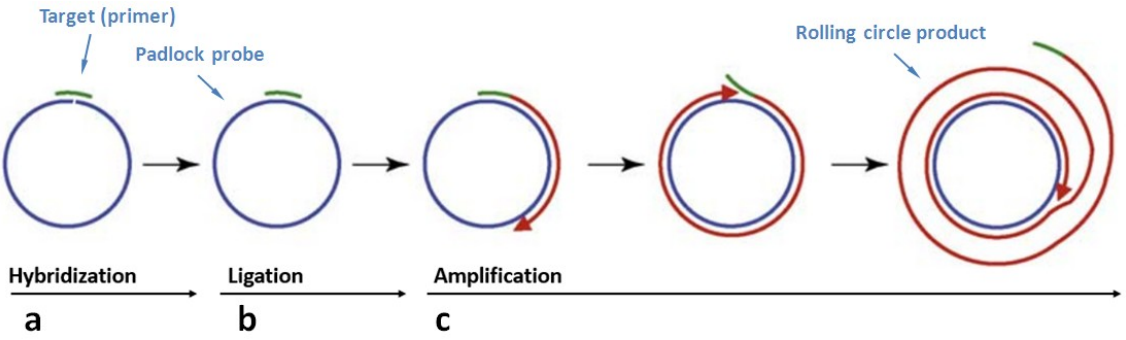

Figure 5.1 Padlock probe and RCA principle: (a) a single stranded DNA probe hybridizes in a circular configuration to the DNA target. (b) The padlock gap is completed through polymerase and/or ligase enzymatic activity and (c) the target is used as a primer for polymerase double strand synthesis, that continues after circle completion by strand displacement. Adapted from (Johne et al. 2009)

The analysis of genomic DNA requires a digestion step with restriction enzymes in order to obtain targets in the form of shorter double-stranded DNA sequences followed by a denaturation step for single-stranded products. In the case of ctDNA, this digestion might be unnecessary, as cfDNA fragment length distribution has been shown to have a mode at 166 bp (Jiang et al. 2015). The amplification of RNA is also possible by an initial reverse-transcription process.

Compared with PCR, the RCA amplification process is linear, resulting in less DNA product for the same amount of time. Modifications of the conventional RCA allow exponential amplifications, for example by the hybridization of multiple primers at the same time on the circularized probe, or with a hyperbranched RCA (HRCA) in which the RCP is used as a template for additional sets of primers, obtaining a ramified amplification (Ali et al. 2014). The amplification techniques of these methods are nonetheless difficult to control, resulting in difficult target quantification and multiplexing.

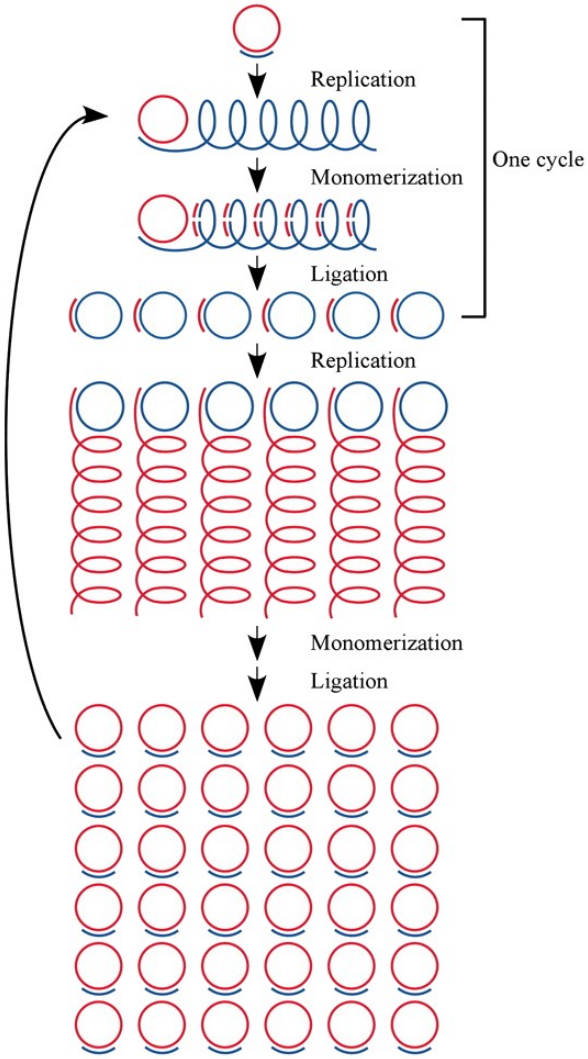

Figure 5.2. The C2CA mechanism. (Dahl et al. 2004)

Another solution to the limited amplification of the RCA process was proposed by Nilsson and co-workers (Dahl et al. 2004) using a serial RCA of monomerized RCPs called circle to circle amplification (C2CA). The process is described in Fig. 5.2. A first RCA results in an amplification product (blue) that can be monomerized by the use of a restriction enzyme and short ssDNA strands (restriction oligos, RO) specific for the repeated sequence of the RCP (restriction enzymes require dsDNA substrate recognition). Heating for restriction enzyme inactivation results in the dissociation of the RO fragment. When the temperature is lowered, the non-digested ROs still present in the solution hybridize with monomers resulting in a padlock probe configuration. After a ligation step, the RO can act as a primer for a new RCA. These amplification cycles can be repeated in series, resulting in billion-fold highly controlled amplifications.

Besides the obvious advantage of isothermal amplification, the C2CA procedure has been shown to yield higher amounts of individual amplicons than PCR and different amplicons have also been shown to be amplified more evenly with C2CA (their proportion is better maintained)(Dahl et al. 2004). This offers the potentiality of higher multiplexing levels

and dynamic ranges (Dahl et al. 2004). Furthermore, fewer polymerase errors should be induced in the amplified sequences (Dahl et al. 2005).

Since the repeated steps result in accumulated unreacted oligonucleotides and sample, this can lead to amplification inhibition. Therefore, the efficiency and sensitivity of the C2CA process can be enhanced with the use of solid supports, in particular magnetic beads (Ke et al. 2011)(Göransson et al. 2012). However, despite the high performance of this system, the multiple steps and manual handling required are a disadvantage for diagnostic applications. Microfluidic integration is then desired for protocol automation.

5.1.2. Rolling circle amplification in microfluidics

A few attempts at RCA and C2CA integration in a microfluidic platform have already been reported. As compared with PCR, these isothermal methods make integration easier by avoiding regular fast temperature cycling, although temperature steps are usually required for enzyme inactivation. (Mahmoudian et al. 2008) demonstrated the integration of the C2CA protocol in a poly(methyl methacrylate) (PMMA) chip, in which the amplification took place in a reservoir and the products were separated and detected by downstream electrophoresis (Fig. 5.3). An additional step was added to the molecular protocol to convert ssDNA into dsDNA. A mix of low and high molecular weight polymers was used to fill all channels, reducing diffusion from reservoir and enhancing electrophoretic separation.This platform was successfully used to detect bacterial genomic DNA, but full integration has not been achieved, and the lack of purification steps and reduced reservoir volume limited detection sensitivity.

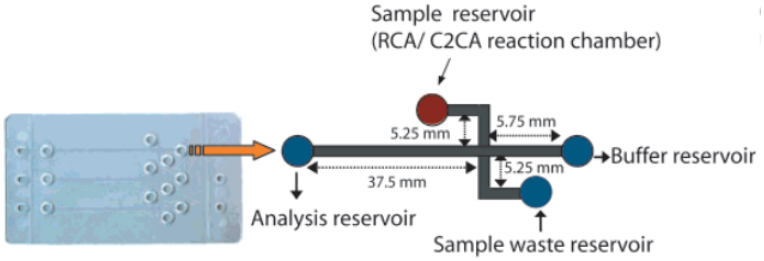

Figure 5.3. Microfluidic chip integrating RCA/C2CA a µ-CE (Mahmoudian et al. 2008).

(Sato et al. 2010a) demonstrated the integration of all RCA processes in a microfluidic chip using a dam structure for bead retention and a Peltier element for temperature control (Fig. 5.4). The use of a solid phase allows the easy change of media and constant flow to avoid reagent exhaustion. In this case, the primer was grafted to the polymer beads and a hybridized padlock probe served as the capture oligonucleotide of genomic bacterial DNA. After a surface amplification step, the resulting RCPs were labeled with fluorophore and imaged for in situ detection. However, since this detection is performed on the surface of the beads, an accurate counting of RCP products is difficult.

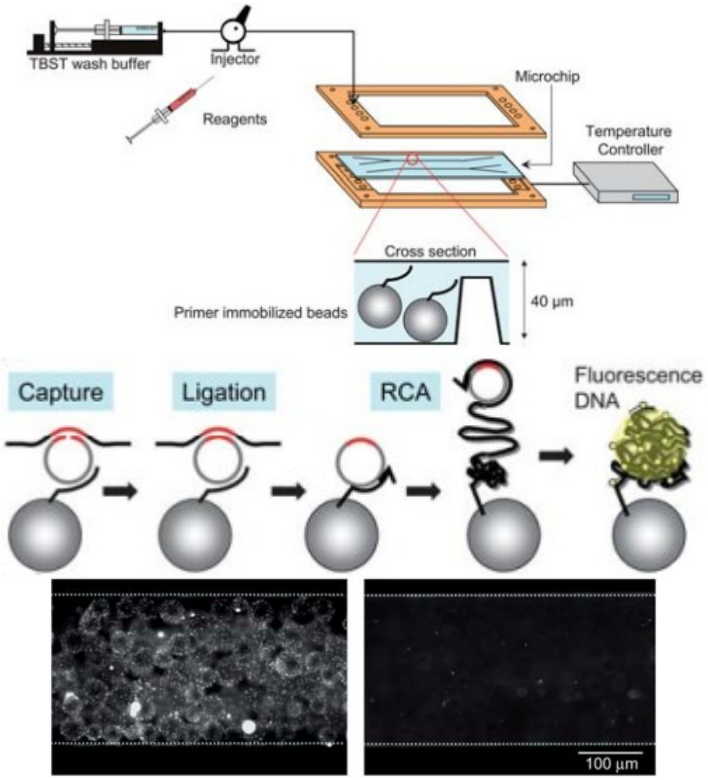

Figure 5.4. Glass microchip containing a dam structure for bead retention (a). Capture and RCA steps are performed in the surface of the beads (b) and the resulting RCPs observed by direct microscopy imaging (c). (Sato et al. 2010b).

The full integration of C2CA on chip was recently reported by (Kühnemund et al. 2014). In this case, reagent mixing (liquid handling) was obtained with digital microfluidic manipulation of droplets acting as reaction chambers. Droplets are transported on a surface through electrowetting-on-dielectric (EWOD), in which the change of surface wetting by the application of an electric field is used for droplet displacement between isolated substrates. The transfer of magnetic particles between droplets through the displacement of a permanent magnet also allowed efficient reagent exchange. A flow-chart in Fig. 5.5b illustrates all the merging and separation steps, the resulting RCPs quantified by fluorescence on a glass slide (Fig. 5.5c). The target DNA is directly captured by a padlock probe previously hybridized to a bead-grafted capture oligonucleotide. The first RCA is then performed on the surface of the beads, while the second RCA is obtained in a different droplet after bead removal. This work demonstrates a high sensitivity, presenting elegant solutions for reagent handling and bead separation. The sample volume is however largely limited to a few µL, the pipetting of all the reagent droplets is still necessary during the procedure, and the detection step is still performed manually by droplet aspiration and glass slide spreading. An accurately controlled surfactant content of the droplets also hinders versatility, of the initial sample in particular.

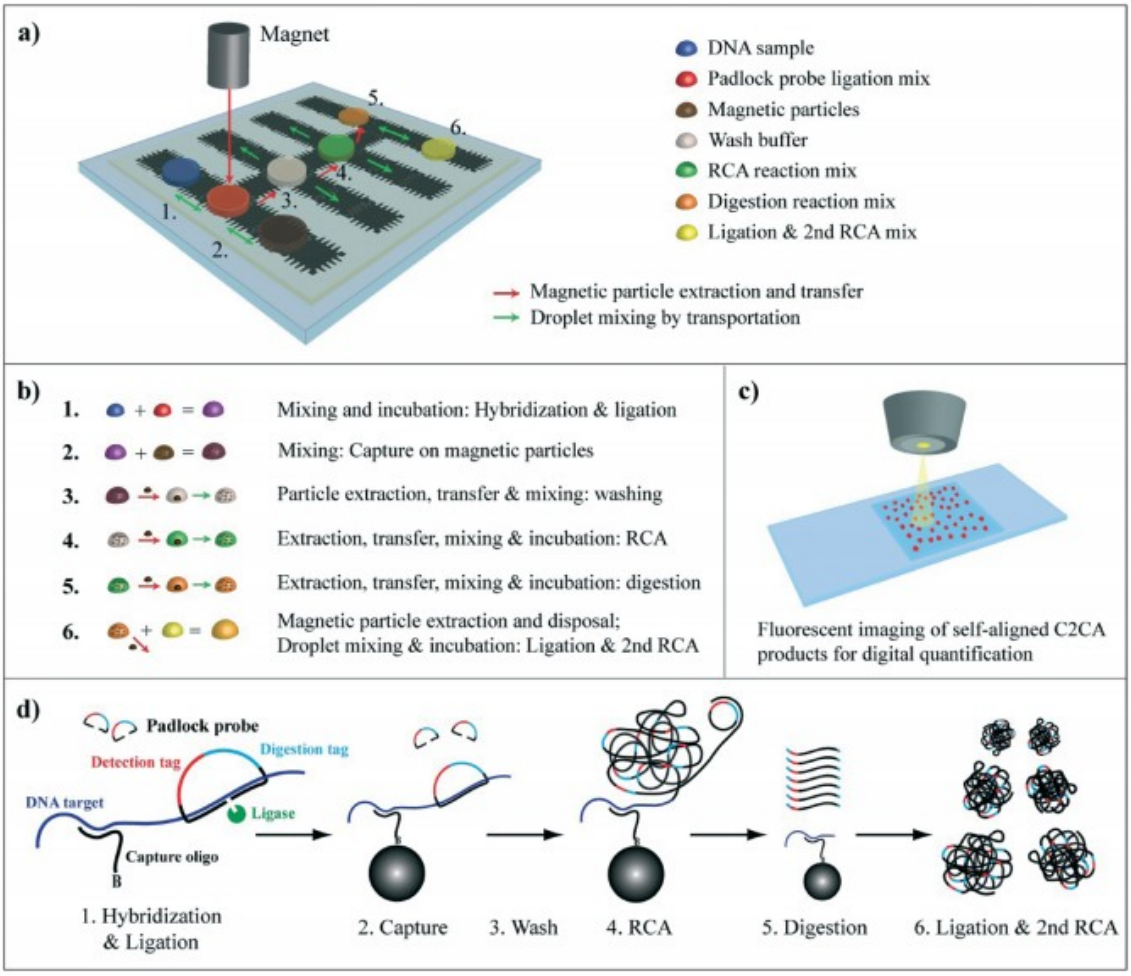

Figure 5.5. C2CA by digital microfluidic manipulation (a). (b) Flow-chart of all the reaction, separation and mixing steps and (c) fluorescence detection. (c) Target capture on magnetic beads and double amplification.

In this chapter, the microfluidic integration of the C2CA protocol is proposed with the use of the fluidized bed as preconcentration module for target DNA, and a two-times surface RCA, first on the surface of the fluidized beads, and a second time on a downstream microarray. The whole procedure is performed in a single microfluidic chamber and allows the in situ detection of labeled RCPs. Further, multiplexing is proposed for a variety of mutations of the KRAS oncogene, with the objective of rapid and accurate diagnosis of ctDNA in cancer patients.

Since this work is still ongoing, preliminary results are presented.

5.2. Initial proof of concept of fluidized bed as an RCA platform

The group of Mats Nilsson in the SciLife Lab of Stockholm University is a pioneer in the development of novel molecular assays, in particular for infectious and cancer diagnosis. While the nucleic acid tools they have created present enormous potential for genotyping and sequencing, the multiple steps usually involved has resulted in a recent focus on lab-on-a-chip integration development. As members the EU FP7 project Diatools, and in view of their development of microbead assays for easier reagent separation steps, a

collaboration was initiated in order to explore the feasibility of a microbead-based assay microfluidic integration with the fluidized bed technology developed at Curie.

In an initial phase, a proof of concept of C2CA assay integration was conceived before moving to more quantitative development. A molecular protocol especially designed for on-chip integration was designed, in which all the steps take place on a solid surface. This allows the molecular reactions to be obtained with a sequential single passing of reagents in contact with the surface (Fig. 5.6), and avoids the need for any mixing of solutions, something non-trivial in microfluidic devices.

Briefly, the target ssDNA is specifically captured by the complementary hybridization of a capture oligonucleotide grafted on the surface of the beads (1-2). This capture is obtained for a non-mutant specific part of the gene sequence, in order to in a first step separate KRAS genes from an eventual pool of very diverse DNA. A padlock probe is then passed through the bed for circularization and ligation, specific for the mutation of interest (3). Different padlock probes are then needed to analyze different mutations. After padlock ligation a Phi29 DNA polymerase then proceeds to amplification directly on beads (4) (since this amplification is a concatemer replication of the padlock probe, the amplification product contains information specific for the mutant analyzed). Complementary restriction oligonucleotides are then used to hybridize to every monomer of the rolling circle product, and two enzymes (AluI and HpyCH4V) cut the resulting double strands in two parts, allowing the dehybridization of the small resulting double stranded fragments on each extremity of the monomers. The use of two enzymes is needed to cut away part of the monomer, in order to create a new sequence that can only be captured to the surfaces oligonucleotides in the next step and not to the still remaining restriction oligonucleotides in solution (5). The solution of monomers is then sent to a chip whose bottom part has been grafted with oligonucleotides designed for the circular hybridization of these restricted monomers (6). This hybridization is non-mutant specific, so that a single sequence is sued for all surface oligonucleotides. After a second ligation and RCA, the protocol ended with the mutant-specific labelling of the RCPs for fluorescence microscopy observation.

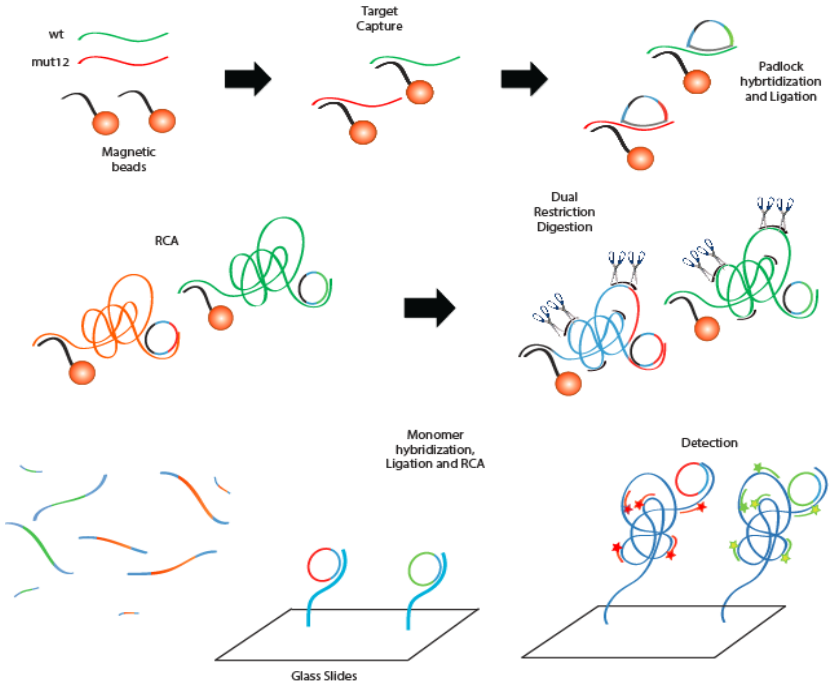

Figure 5.6. Initial molecular protocol for on-chip C2CA.

The efficiency of this complex molecular protocol was first evaluated by in tube testing of the bead-based first RCA, followed by the incubation of monomers and reagents in a commercial chip (ChipShop) for the second RCA and detection step (Fig. 5.7). This chip consisted of a thermoplastic compartment containing a single microfluidic chamber (50 µL) that was adhesive-bound to a glass slide homogeneously grafted with streptavidin. The capture oligo of step (6) was homogeneously grafted on the glass slide through a biotin functionalization and biotin-streptavidin interaction. To directly investigate the protocol multiplexing ability, two KRAS sequences were tested, one for the wild type gene and a second one with a mutation for codon 12. The results, shown in Fig. 5.7, were obtained with the quantification of labeled RCPs on the surface of the chip, each mutation product labeled with a different fluorescent marker (based on the sequence-specific hybridization of a fluorescently labeled short ssDNA strand). Negative controls were performed in the absence of the initial target, while the concentration of positive targets was the same in all cases (100 fM, 10 µL). These results indicate that the assay is highly sensitive and specific, even when several target sequences are analyzed simultaneously. The difference in the total amount of RCPs obtained for wildtype and mutant might be due to variations in the concentration of synthetic DNA provided by the manufacturer. Padlock efficiency might also be at play, as two padlock probes are competing for the same ligation site, influencing kinetics.

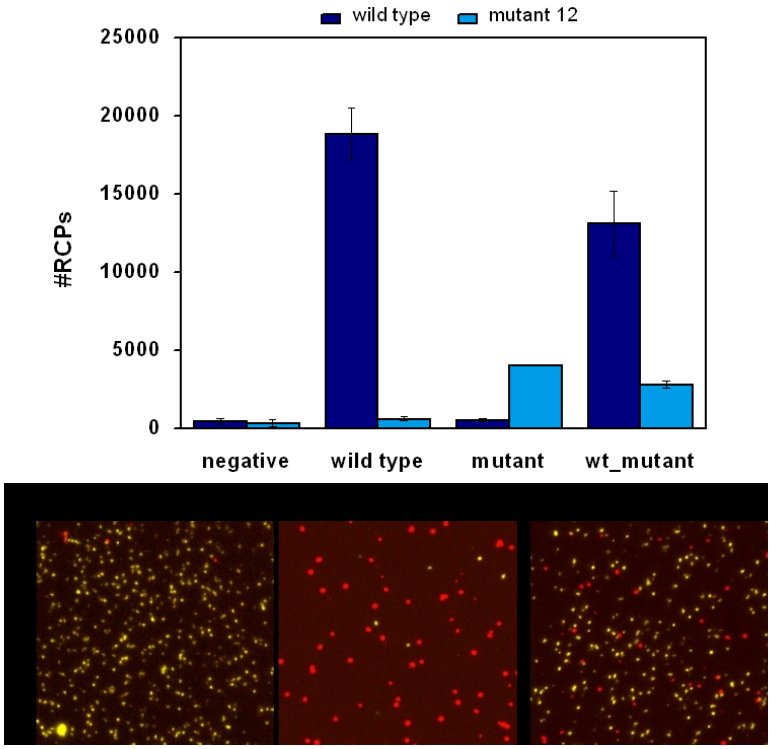

Figure 5.7. Tests in tube/on commercial chip indicate multiplexing ability high assay specificity.

Once the feasibility of the beads base protocol established, the same protocol was then applied to the fluidized bed in a constant fluidization mode to allow the continuous renewal of reagents. The protocol details are described in Appendix B. Before the full protocol integration, the different steps were tested sequentially in a Cyclic Olefin Copolymer (COC) chip and the beads removed from the chip to continue the assay in tube. In this way, the ligation, RCA and digestion steps were first verified and parameters (temperature, flowrate, concentration of reagents) adjusted, while the initial capture rate was seen to be superior to 90%. Briefly, the conditions for the different steps were set as: target capture at 1 µL/min 10 µL 65°C, ligation at 1 µL/min 10 µL 65 °C, RCA at 0.3 µL/min 20 µL 37°C and digestion at 0.5 µL/min 5 µL and 37°C. All the steps were intercalated with a washing step with 5 µL of buffer at 1.5 µL/min. Temperatures beyond 65 °C were avoided to avoid observed bead aggregation and bubble formation. At the end of the RCA procedure the recirculation of beads was drastically reduced, probably due to inter-bead interactions as a result of the presence of long DNA products on the bead surface. Once the feasibility of bead-based part of the assay was demonstrated, we have proposed a semi-integrated version of the C2CA approach: the outlet of the fluidized bed chip was connected to the commercial chip previously described (Fig. 5.8a), grafted with a homogeneous distribution of monomer-complementary oligonucleotides. The connection was obtained through a PEEK tube (ID 250 µm, interval volume 4 µL). In this case, after the initial steps as initially described, during the digestion step the monomers were pushed towards the second chip (0.5 µL/min) for hybridization in padlock mode and the subsequent reagents needed for RCA and labeling were injected from the inlet of the first chip (second ligation 1 µL/min 15 µL 37 °C, second RCA 1 µL/min 40 µL 37 °C and labeling 1 µL/min 40 µL 37 °C). This configuration led to the

successful detection of RCPs in the second chip for an initial target of wildtype KRAS at 10 nM (Fig. 5.8b). While in the protocol evaluation phase the second part of the assay was performed by statically incubating the different solutions at 37 °C in the commercial chip, these results show that the same protocol can be applied with a flow-through configuration. This facilitates the microfluidic integration, since steps such as monomer digestion/hybridization must be performed at the same time on both modules.

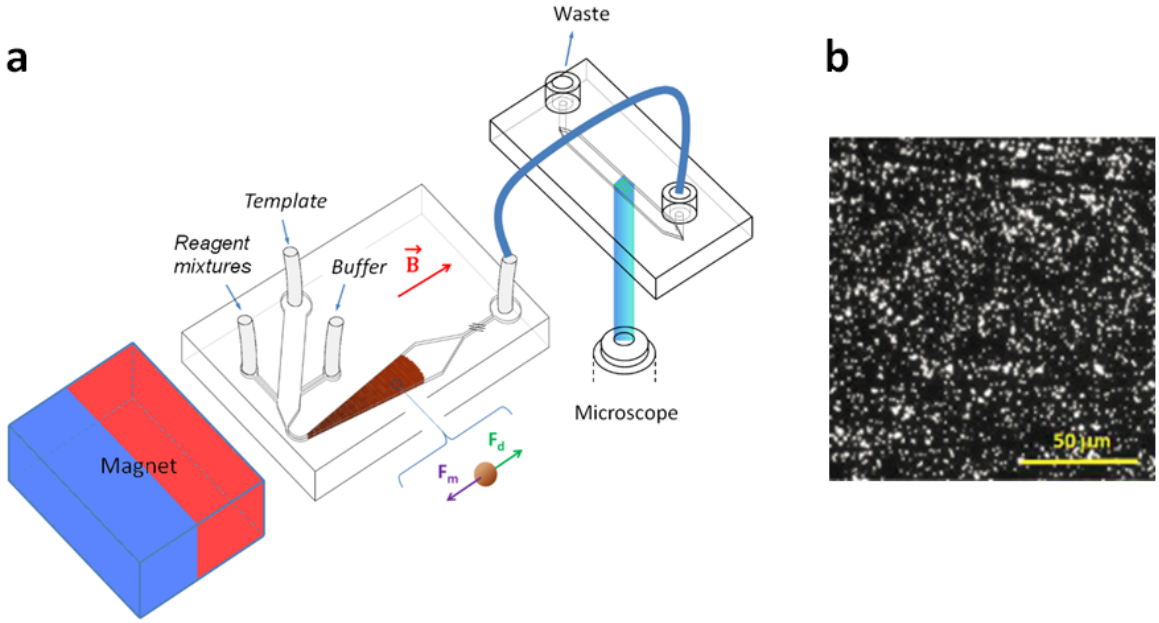

Figure 5.8. (a) Semi-integrated system composed of: fluidized bed for extraction and first RCA and commercial chip for second RCA and detection. (b) Epifluoresence microscope photograph showing immobilized and fluorescently labeled micron-sized RCPs which are counted as single digital objects on the glass surface in the detection module.

5.3. Optimized molecular protocol and microfluidic platform

This two-chips protocol served as a proof of concept of microfluidic integration, but the adopted configuration presented several limitations and drawbacks such as high dead volume of the connecting tube (with the subsequent loss of enzymatic activity and difficult fluidic control) and a difficult quantification, as the second chamber was particularly large and RCPs distributed heterogeneously. Furthermore, multiplexing was severely limited by the fact that RCPs from different mutations could only be discriminated based on fluorescent labeling. Since fluorescent emission at different wavelengths can easily overlap, this constituted a severe limitation to the number of mutations that the system could analyze.

An alternative C2CA protocol, specially adapted to the needs of the microfluidic platform and allowing high multiplexing was then designed (Fig. 5.9). As before, magnetic beads conjugated with a capture oligonucleotide specific for the KRAS gene (1) are used for fluidized bed filling and KRAS-specific sample target capture. Different padlock probes are then added for single nucleotide discrimination of different gene mutations. In contrast with the previous system, in this case the padlock sequence is designed to obtain

the self-hybridization of part of the oligonucleotide, creating a double-stranded loop structure (3). The rolling circle product obtained with Phi29 polymerase replicates this loop for every sequential monomer (4). This double-stranded structure can then be directly cut with a restriction enzyme (SapI) avoiding the need for restriction oligos and subsequent heating for oligo disassociation (5). More importantly, and in contrast with the previous protocol, this system allows the release of monomers with base sequences on both extremities independent for each padlock. This is because SapI is a Type IIs restriction enzyme that cleaves DNA outside of their recognition sequence on one side, and this sequence has been designed in the non-monomer side of the loop structure and is independent of the initial mutation. The monomers resulting from this restrictions step are then freed and sent downstream, where they mutant-specifically hybridize in a circular conformation with a surface-grafted capture oligonucleotide. In this case, different oligonucleotide are used for each KRAS mutation analyzed. A second RCA is then performed after ligation of the circularized probe, and fluorescent labeling takes place for in situ RCP detection (6). Since the surface oligonucleotides are now mutant-specific, the RCPs obtained from different mutations can be spatially separated (in our case in an array of spots, as described further below) avoiding the need to use different fluorophores for discrimination.

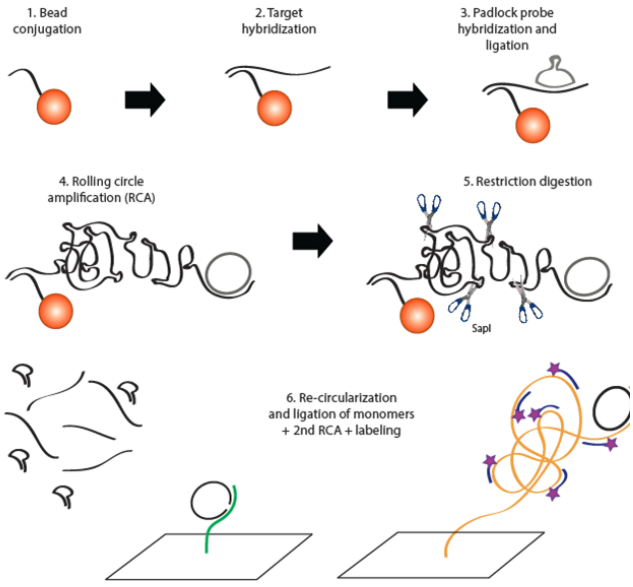

Figure 5.9. Molecular protocol for on-chip C2CA.

For full C2CA integration, a new chip was designed in which the fluidized bed and the RCP detection surface were integrated in a single chamber (Fig. 5.10). This modified principle improves the sensitivity and readability of the assay, since digital quantifiable objects are immobilized, amplified and located in the same focal plane. The whole chip is fabricated in cyclic olefin copolymer (COC) for transparent visualization and resistance to thermal heating. The magnetic beads conjugated with the capture oligo are introduced in a v-shaped chamber entrance for fluidized bed establishment and a larger consecutive area (6 mm wide and 12 mm long) consisting in an array of 6x10 spots (500 nm in

diameter), each spot grafted with capture oligos specific for monomers originating from a given mutation. The array is designed to contain a given mutation recognition per row of 6 spots, allowing the total analysis of 10 different initial target sequences. The large chamber width results in reduced local flow velocities, with the aim of increasing the residence time of monomers and reagents in contact with the surface of the spots.

Concerning chip fabrication, the chip design was hot-embossed in COC and the resulting piece bonded to a 1 mm thick COC film (Fig. 5.10b). Temperature is controlled through an Indium Tin Oxyde (ITO) thin film deposited on a glass slide enabling full transparency (see Materials and Methods for details).

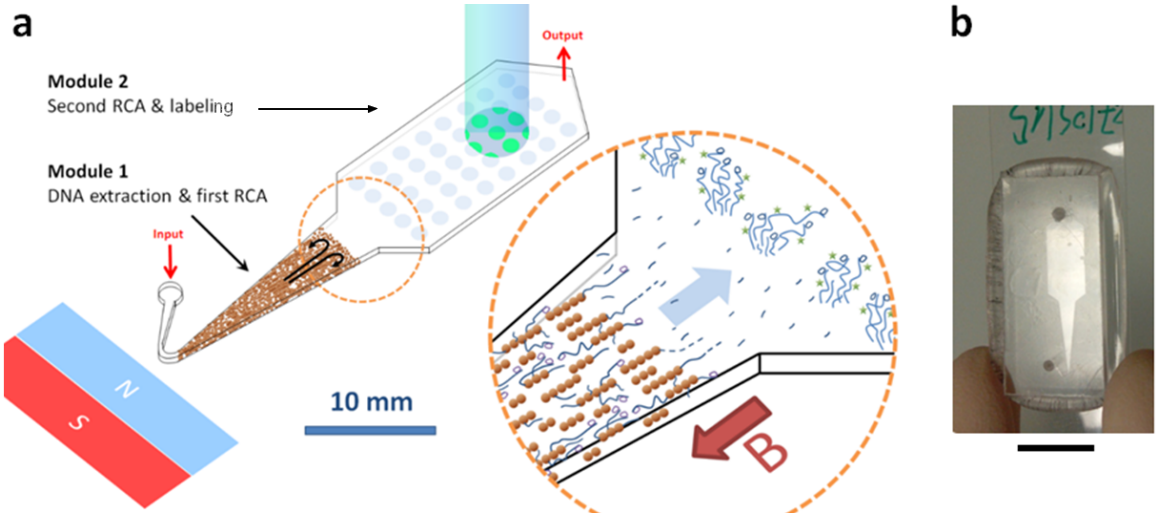

Figure 5.10. (a) Scheme of microfluidic chip showing the two-modules for C2CA in a single chamber; the zoom shows the molecular protocol as adapted on-chip. (b) Final COC chip (scale bar = 1cm).

This time, each module was first optimized and its efficiency evaluated before integration of the whole protocol. In the next sections, the optimization experiments and results are first described for each module, followed by the results of the full integration.

5.3.1 Module 1: magnetic fluidized bed for DNA extraction and first amplification

The fluidized bed, constituting module 1, is used for target extraction and a first amplification step. This allows the analysis of larger sample volumes (from 20 to 200 µL) than what was possible in previously reported microfluidic RCA assays (section 5.1.2). This target preconcentration step in the smaller volume of the fluidized bed (~0.1 µL) also represents a first preconcentration step for increased sensitivity of detection. Therefore, the efficiency of the extraction step was first evaluated. This was obtained in a similar way to the capture efficiency evaluation of proteins (Chapter 3), by the use of labeled DNA (Alexa Fluor 488 nm) and the measurement of fluorescence at the outlet, in the absence of beads or when the fluidized bed is in place and an active capture takes place (Fig. 5.11a). By doing this, the capture efficiency was evaluated at 93% for target concentrations of 100 nM or below in PBS at 1µL/min and 65°C. Admittedly, no capture

saturation studies were performed, as the system is conceived for low target concentration detection.

The remaining padlock probe ligation, RCA and digestion steps are performed in a constant flow configuration under permanent fluidization. The evaluation of the efficiency of the whole module was evaluated by performing all of these operations until RCA with a starting target concentration of 10 nM in 10 µL. The beads were then released from the chip and the RCPs on the surface of the beads enzymatically cut at its base (restriction of initial target template) and counted with an RCP counting unit (Aquila 400, Q-linea). The results, shown in Fig. 5.11b, were compared with the same protocol adapted for tube testing, indicating an enhanced performance on-chip. This might be due to either a more efficient capture step and/or a better access of reagents to the bead surface during the ligation and amplification steps due to the intimate liquid/particle contact in the fluidized bed and constant recirculation, in contrast with the in tube tests in which beads tend to sediment (in tube tests are usually performed in a PCR thermocycler, as was our case).

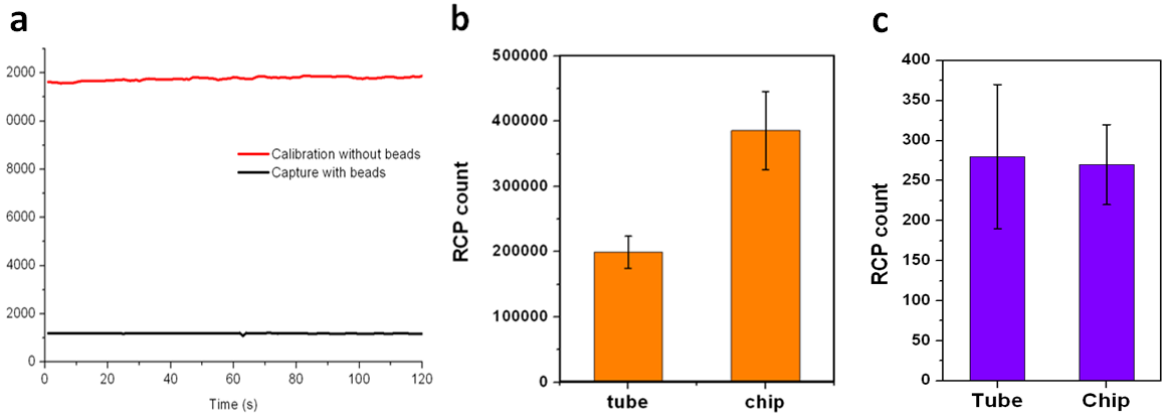

Figure 5.11. (a) Evaluation of capture efficiency through fluorescence measurements. (b) RCPs in 20 µL obtained with in tube/on-chip protocols until first RCA and off-chip RCP restriction release (initial solution of 5 µL and 10 nM). (c) RCPs obtained with whole off-chip protocol and tube/on-chip enzymatic digestion (initial solution of 10 µL and 1 nM)(arbitrary units).

Finally, the digestion step was evaluated independently with full C2CA protocol in tube except for digestion: beads were inserted in the chip after RCA and subsequently fluidized in the presence of digestion enzymes, followed by outlet collection and in tube assay completion. The results were compared with tube digestion, resulting in equivalent efficiency in both cases (Fig. 5.11c). In this case the RCP count was done on a glass slide on a same region of interest and the initial sample concentration was 1 nM.

In summary, the performance of the fluidized bed proved to be equivalent if not higher than conventional tube handling. The need for multiplexing and high sensitivity required however an additional round of RCA and a platform for independent mutant detection. A microarray of spots was thus developed and is described next.

5.3.2 Module 2: microarray for second amplification and detection

The microarray module has been designed to allow target quantification based on the presence of RCPs on spots specific for a given mutation. In this way, all the RCPs of the whole array can be labeled with the same fluorophore, their recognition being solely based on their array position. This is in contrast with the commercial chip previously used, in which the RCPs from different mutations randomly distributed on the bottom of the chamber and could only be discriminated with different fluorescence probes. Furthermore, the chamber volume has been reduced from 50 to 5 µL, in order to reduce monomer dilution after digestion and enhance their residence time on the surface of the spot.

An easy and low-cost capture oligo grafting on the chip surface was envisioned to maintain the complexity of the device as low as possible. A direct grafting of the capture oligonucleotides on the COC surface of the chip was hence desired. Our grafting procedure was based on the work of (Sun et al. 2012) in which the authors demonstrate the possibility of direct DNA immobilization on COC surfaces with poly(T)poly(C)-tagged oligonucleotides and UV irradiation in surfactant-containing buffer (0.004% Triton X, sodium phosphate buffer). The grafting mechanism is not clearly understood, although the combination of both T and C in the tag are known to be essential. Our capture oligos were hence designed to contain a 10 TC tag sequence on their 5' end. The spots were obtained by robot deposition of 50 nL sodium phosphate buffer solutions (containing 10 nM of oligonucleotides) on the film before bonding. After droplet drying, the area was UV irradiated at 254 nM for 30 seconds. Since our spot size greatly differs from the reported work (diameter of 500 µm instead of < 100) parameters such as irradiation time, surfactant content and surface roughness had to be first optimized (these two last parameters directly affecting the surface angle of the droplets), in order to obtain a relatively uniform drying leading to more homogeneous distribution of DNA on the surface of the spot.

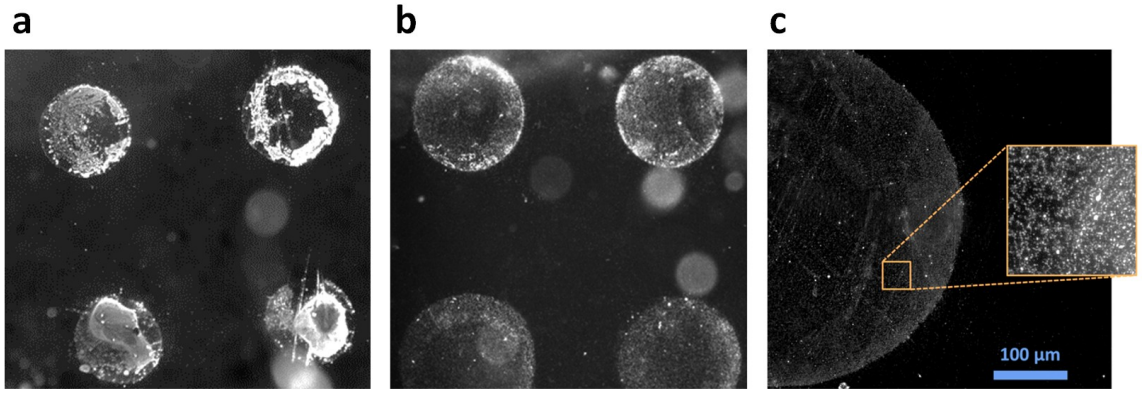

Figure 5.12. Partial view of the array of spots, showing homogeneous spots obtained for wild type synthetic monomers (a) and detailed view of a spot with zoom on RCPs (b).

To evaluate the ability of this microarray device to be used as amplification and detection module, synthetic monomers (equivalent to those obtained after first RCA and digestion)

were directly injected in the chip to skip all the bead-based part of the protocol and start with on-chip capture/ligation. Fig. 5.12 shows spots obtained this way for wild type KRAS after monomer capture, ligation, RCA and labeling. After the spotting optimization previously described, the obtained spots were homogeneous enough to allow RCP counting at high magnification (Fig. 5.12a before optimization, Fig. 5.12b after). Similar results were obtained for codon 12 mutation sequences (in both cases 10 nM of monomer in 50 µL of the initial capture/ligation solution).

This shows that the proposed conditions for this array-based second part of the protocol are functional. No sensitivity or reproducibility studies have been performed in this preliminary phase, but these will be evaluated for the whole integrated protocol.

5.3.3 Full C2CA integration

The system was finally successfully implemented for the detection of KRAS mutant codon 12, with the preliminary results of a calibration curve shown in Fig. 5.13. A linear tendency for RCPs measured in the spots of the array as a function of initial target concentration seems to indicate that quantification measurements are indeed possible. Micrographs in this image show the aspect of spots for three different concentrations of initial mutant target. More experiments are needed to confirm these results as well as to optimize the C2CA integrated protocols for increased sensitivity.

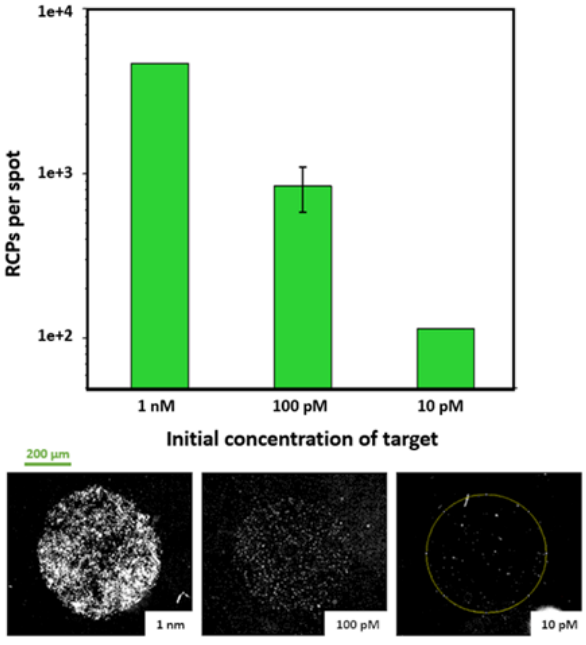

Figure 5.13. Preliminary calibration curve for RCPs counted for single spots at three initial concentrations of mutant codon 12 target, and images of example spots obtained for each concentration.

Although in principle straightforward, in view of the preceding encouraging results, the full on-chip integration proved a bit difficult. Several factors not considered before integration were in play, notably the fact that all the reagents necessary for module 1 also passed through the microarray before reaching the chip outlet. In particular, enzymes like

Phi29 Polymerase, necessary for the first RCA, also present some exonuclease activity (nucleotide cleavage from the end of polynucleotide chains) that was seen to degrade the array of capture oligos grafted on the COC surface. The time for first RCA was subsequently reduced but this plays unfavorably in the final sensitivity of the system. Research is still ongoing to either protect these oligonucleotides with functionalization or modify the chip design to deviate flow path. Furthermore, the molecular protocol for wildtype proved frail, with very variable results (even in tube tests). A redesign of probe sequences for increased robustness is thus necessary.

Nonetheless, the obtained results confirm the possibility of integration of the C2CA protocol in our microfluidic device. The limit of detection (~10 pM) is, however, superior to what would be expected from a double amplification system, in which femtomolar target concentrations are usually detectable in tube. Since the first module, based on the fluidized bed, was verified to be at least as efficient as in tube protocols, the loss of sensitivity should in principle be a result of microarray problems. The optimization of parameters such as spot oligo content, array distribution or reagent flow handling (static/dynamic modes, flow rates) should enable better results.

5.4. Conclusions

The microfluidic integration of a C2CA molecular assay was demonstrated for the analysis of the oncogene KRAS in a platform that combines different microfluidic and molecular principles achieving a simple "sample-in->results-out" format. The system should be able to analyze larger volumes of liquid samples than previously reported RCA based methods integrated on-chip. Due to the padlock probe-based amplification method used, the on-chip results should allow high detection specificity with single nucleotide resolution and a high multiplex capacity. This, combined with isothermal amplifications, could provide an alternative to more conventional PCR-based methods, more difficult to integrate in a simple portable platform. The optimization of the device is now ongoing for lower target concentrations in view of a validation with clinical samples.

5.5. Materials and methods

Microarrays were prepared by pipetting 50 nL of 150 mM sodium phosphate buffer solutions with 0.004% Triton X 100 containing ligation template oligo at a concentration of 10 μM. Oligos were ordered from IDT-DNA Technologies, containing a poly(T)10-poly(C)10 tag. Pipetting was automatized with a Rotaxis (Cetoni) positioning system, controlled by the Qmix Element software. The interspot distance was 1 mm, distributed in an array of 6x10 spots on 1 mm thick COC (Topas®) slides. After droplet drying, the arrays were exposed to UV irradiation at 254 nm with a power of 10 mW/cm^2 for 30 s. Subsequently, the COC slides were washed in a solution of 0.1x standard saline citrate (SSC) with 0.1% (w/v) sodium dodecyl sulfate (SDS) for 10 minutes under wheel rotating, and rinsed with deionized water.

Chip microfabrication. The chip design consisted of a single inlet and outlet, the inlet connected to an elbow channel followed by a 13°C tapered chamber, 12 mm long, followed by a squared area of 1.2x0.6 cm. Chips were fabricated in COC by hot embossing of brass micro-milled masters at 120°C for 10 minutes under 5 bar of pressure. After inlet and outlet drilling the embossed piece was bonded to the microarray COC slides with a solvent bonding by applying 15% Hexadecane 75% isopropanol in the interface and pressing at 5 bar 70 °C for 10 minutes. Tygon© 2 mm tubings were inserted the inlet and outlets and PEEK tubes (50 nm ID at inlet, 250 nm ID outlet) plugged inside, ensuring sealing.

Fluidics control was performed as described in previous chapters. **Heating** was obtaining with a transparent indium tin oxide coated glass slides (Sigma-Aldrich) with two 0.5x4 cm copper films cold soldered parallel to each other acting as electrodes. These electrodes were connected to an Eurotherm 3508 thermocontroller that received a feedback from a thermocouple placed between the slide and chip. Chip channels were filled by **buffer** containing Tris-HCl pH 7.5 at 10 mM, EDTA pH 7 at 5mM, NaCl at 0.1 M and Tween-20 at 0.1%.

Enzymes. T4 DNA Ligase (1U/µL , Sigma-Aldrich) was used for padlock ligation, Phi29 DNA polymerase (100mU/µL, New England Biolabs(NEB)) for amplification, AluI (10 U/µL, NEB) and HpyCH4V (5 U/µL, NEB) for enzymatic restriction of initial protocol, and SapI (10U/µL, NEB) for loop protocol restriction.

DNA sequences were as follows:
Capture oligo: TCATTTTCAGCAGGCCTTATAATAAAAATAATGAAAATGT
Wildtype target:
ACATTTTCATTATTTTTATTATAAGGCCTGCTGAAAATGACTGAATATAAACT
TGTGGTAGTTGGAGCTGGTGGCGTAGGCAAGAGTGCCTTGACGATA
Mutant 12 target:
ACATTTTCATTATTTTTATTATAAGGCCTGCTGAAAATGACTGAATATAAACT
TGTGGTAGTTGGAGCTAGTGGCGTAGGCAAGAGTGCCTTGACGATA
Initial system:
Padlock wildtype: AGCTCCAACTACCACAA AGTCGATAGTCACGGCTACT
ATAGATAAAG CTCTCTTG CAGGACGACG CTTGCCTACGCCACC
Padlock mutant 12: AGCTCCAACTACCACAA AGCCAAACATGTGCATTGAG
ATAGATAAAG CTCTCTTG CAGGACGACG TCTTGCCTACGCCACT
Restriction oligo: ATAAAG CTCTCTTG CAGGAC
Ligation template : CTCTCTCTCTCTCTCTCT ATAGATAAAGCATTACGACG
Detection oligo wt : AGTAGCCGTGACTATCGACT
Detection oligo mut12 : CCTCAATGCACATGTTTGGCTCC
Loop-based system:
Padlock wildtype: AGCTCCAACTACCACAA AGTCGATAGTCACGGCTACT
CAGACGTAAC G GAAGAGCTTTTGCTCTTC C GTT CAGTGATGCC
CTTGCCTACGCCACC

Padlock mutant 12: AGCTCCAACTACCACAA AGCCAAACATGTGCATTGAG GCGCTACATC G GAAGAGCTTTTGCTCTTC C GAT AACTGACATA TCTTGCCTACGCCACT
Ligation template wt: CTCTCTCTCTCTCTCTCTCT CAGACGTAACCAGTGATGCC
Ligation template mut12: CTCTCTCTCTCTCTCTCTCT GCGCTACATCAACTGACATA
Detection oligo wt: AGTAGCCGTGACTATCGACT
Detection oligo mut12: CCTCAATGCACATGTTTGGCTCC

5.6 References

Ali, M.M. et al., 2014. Rolling circle amplification: a versatile tool for chemical biology, materials science and medicine. *Chemical Society reviews*, 43(10), pp.3324–41.

Autebert, J. et al., 2012. Microfluidic: An innovative tool for efficient cell sorting. *Methods*, 57(3), pp.297–307.

Bettegowda, C. et al., 2014. Detection of circulating tumor DNA in early- and late-stage human malignancies. *Science translational medicine*, 6(224), p.224ra24.

Consoli, F. et al., 2011. Circulating tumor cells as predictors of prognosis in metastatic breast cancer: clinical application outside a clinical trial. *Tumori*, 97(6), pp.737–42.

Dahl, F. et al., 2004. Circle-to-circle amplification for precise and sensitive DNA analysis. *Proceedings of the National Academy of Sciences of the United States of America*, 101(13), pp.4548–4553.

Dahl, F. et al., 2005. Multiplex amplification enabled by selective circularization of large sets of genomic DNA fragments. *Nucleic Acids Research*, 33(8), pp.1–7.

Danila, D.C. et al., 2014. Circulating tumors cells as biomarkers: progress toward biomarker qualification. *Cancer journal (Sudbury, Mass.)*, 17(6), pp.438–50.

Diaz, L. a. & Bardelli, A., 2014. Liquid biopsies: Genotyping circulating tumor DNA. *Journal of Clinical Oncology*, 32(6), pp.579–586.

Dong, Y. et al., 2013. Microfluidics and circulating tumor cells. *The Journal of molecular diagnostics : JMD*, 15(2), pp.149–57.

Göransson, J. et al., 2012. Rapid identification of bio-molecules applied for detection of biosecurity agents using rolling circle amplification. *PloS one*, 7(2), p.e31068.

Huggett, J.F. & Whale, A., 2013. Digital PCR as a novel technology and its potential implications for molecular diagnostics. *Clinical chemistry*, 59(12), pp.1691–1693.

Ilie, M. et al., 2014. Current challenges for detection of circulating tumor cells and cell-free circulating nucleic acids, and their characterization in non-small cell lung carcinoma patients. What is the best blood substrate for personalized medicine? *Annals of Translational Medicine*, 2(11), p.107.

Jarvius, J. et al., 2006. Digital quantification using amplified single-molecule detection. *Nature methods*, 3(9), pp.725–727.

Jiang, P. et al., 2015. Lengthening and shortening of plasma DNA in hepatocellular carcinoma patients. *Proceedings of the National Academy of Sciences of the United States of America*, 112(11), pp.E1317–25.

Johne, R. et al., 2009. Rolling-circle amplification of viral DNA genomes using phi29 polymerase. *Trends in Microbiology*, 17(5), pp.205–211.

Ke, R. et al., 2011. Colorimetric nucleic acid testing assay for RNA virus detection based on circle-to-circle amplification of padlock probes. *Journal of clinical microbiology*, 49(12), pp.4279–85.

Knickelbein, K. & Zhang, L., 2015. Mutant KRAS as a critical determinant of the therapeutic response of colorectal cancer. *Genes & Diseases*, 2(1), pp.4–12.

Kühnemund, M. et al., 2014. Circle-to-circle amplification on a digital microfluidic chip for amplified single molecule detection. *Lab on a chip*, pp.2983–2992.

Lièvre, A. et al., 2006. KRAS mutation status is predictive of response to cetuximab therapy in colorectal cancer. *Cancer Research*, 66(8), pp.3992–3995.

Mahmoudian, L. et al., 2008. Rolling circle amplification and circle-to-circle amplification of a specific gene integrated with electrophoretic analysis on a single chip. *Analytical chemistry*, 80(7), pp.2483–90.

Sato, K. et al., 2010a. Microbead-based rolling circle amplification in a microchip for sensitive DNA detection. *Lab on a chip*, 10(10), pp.1262–6.

Sato, K. et al., 2010b. Microbead-based rolling circle amplification in a microchip for sensitive DNA detection. *Lab on a chip*, 10(10), pp.1262–6.

Sozzi, G. et al., 2009. Plasma DNA quantification in lung cancer computed tomography screening: Five-year results of a prospective study. *American Journal of Respiratory and Critical Care Medicine*, 179(1), pp.69–74.

Suda, K., Tomizawa, K. & Mitsudomi, T., 2010. Biological and clinical significance of KRAS mutations in lung cancer: an oncogenic driver that contrasts with EGFR mutation. *Cancer metastasis reviews*, 29(1), pp.49–60.

Sun, Y. et al., 2012. Direct immobilization of DNA probes on non-modified plastics by UV irradiation and integration in microfluidic devices for rapid bioassay. *Analytical and Bioanalytical Chemistry*, 402(2), pp.741–748.

Szpechcinski, A. et al., 2015. Cell-free DNA levels in plasma of patients with non-small-cell lung cancer and inflammatory lung disease. *British journal of cancer*, 113(3), pp.476–483.

Taly, V. et al., 2013. Multiplex picodroplet digital PCR to detect KRAS mutations in circulating DNA from the plasma of colorectal cancer patients. *Clinical Chemistry*, 59(12), pp.1722–1731.

Tickner, J. a et al., 2014. Functions and therapeutic roles of exosomes in cancer. *Frontiers in oncology*, 4(May), p.127.

Conclusions

The potential of the magnetic fluidized bed as a versatile platform for the integration of very different bioanalytical applications has been demonstrated. Its enhanced surface to volume ratio, a consequence of a very dense and highly percolated bead density, results in high capture efficiencies for species as diverse as DNA, proteins or bacterial cells, with the added versatility of the binding process (e.g. complementary oligonucleotide hybridization, antibody immunocapture, lectin-based binding). Furthermore, because of the resistance to clogging of the system, complex sample matrixes such as whole fat milk or fetal bovine serum have been successfully tested without a significant detriment to the capture process. In this way, and by collecting enough sample volume in a flow-through configuration, preconcentration factors of up to 800 times have been found in the case of immunocaptures.

Perhaps more salient is the fact that in this work we have demonstrated the potential uses of the magnetic fluidized bed beyond simple capture and preconcentration steps. Applications such as the in situ fluorescent labeling of bead-captured proteins, the detection of bacteria through expansion phenomena or the use of complex enzymatic DNA protocols (ligation, amplification, digestion), have all of them been performed during the fluidization regime. These are successful examples of just how many applications could be envisioned by combining the possibilities of bead-based assays with the physical characteristics of the fluidized bed.

Furthermore, the system is simple to integrate in a microfluidic device, and this integration alone presents many advantages compared to batch-based protocols, such as possibility of automation, reduced reagent and bead consumption and higher reproducibility. The use of thermoplastics has also been demonstrated, important for an eventual industrial transfer.

While the system holds great potential, two main limiting factors still need to be overcome: (i) a relatively low throughput and (ii) a so far manual insertion of beads. Nonetheless, these should not represent unsurmountable problems and some progress towards these aims (larger microfluidic channels, 3D bed configurations, channel filling by in-flow of beads) has already been accomplished but left outside this manuscript for simplicity reasons.

Overall, this technology opens new potential for many applications involving trace level detection, e.g. environment control, bio-security, food industry and medicine.

Appendix A

Publication

Magneto-immunocapture with on-bead fluorescent labeling of amyloid-β peptides: towards a microfluidized-bed-based operation

Analyst

PAPER

View Article Online
View Journal | View Issue

Cite this: *Analyst*, 2015, **140**, 5891

Magneto-immunocapture with on-bead fluorescent labeling of amyloid-β peptides: towards a microfluidized-bed-based operation

Thanh Duc Mai,[a,b] Iago Pereiro,[c] Mohamed Hiraoui,[a,b] Jean-Louis Viovy,[c] Stéphanie Descroix,[c] Myriam Taverna[a,b] and Claire Smadja*[a,b]

A new sample treatment approach for sensitive determination of three amyloid-β peptides (Aβ 1-42, Aβ 1-40 and Aβ 1-38) with capillary electrophoresis coupled with laser induced fluorescent detection is reported herein. These Aβ peptides are considered an important family of biomarkers in the cerebrospinal fluid (CSF) for early diagnosis of Alzheimer's disease (AD). Due to their extremely low abundance in CSF (down to sub nM ranges), batch-wise preconcentration *via* magneto-immunocapture with enrichment factors up to 100 was implemented. The Aβ peptides were first captured onto magnetic micro-beads. Then, on-beads fluorescent labeling of the captured Aβ peptides were carried out to avoid the unwanted presence of extra fluorescent dye in the eluent as in the case of in-solution labeling. Finally thermal elution was performed and eluted labeled peptides were analyzed off line with CE-LIF. The Aβ-capturing efficiencies of different commercially available antibodies grafted onto magnetic beads were tested. Aβ peptides in CSF samples collected from AD's patients and healthy persons (used as controls) were measured and evaluated. As a proof of concept, the developed strategy was adapted into a miniaturized fluidized bed configuration that has the potential for coupling with a microchip separation system.

Received 12th June 2015,
Accepted 17th July 2015

DOI: 10.1039/c5an01179e

www.rsc.org/analyst

1. Introduction

Amyloid β (Aβ) peptides having from 37 to 43 amino acids (AA) are naturally produced in our body fluids, mainly cerebrospinal fluid (CSF), *via* proteolysis of a larger protein known as the amyloid precursor protein (APP).[1] Among these Aβ isoforms, Aβ 1-42 and Aβ 1-40 are considered well-established and internationally validated biomarkers for early diagnosis of Alzheimer's disease (AD).[2] CSF is a relevant biological fluid for the monitoring of AD evolution as it reflects molecular events occurring in the brain thanks to its direct contact with the extracellular brain space.[3] In AD patients, the CSF levels of Aβ 1-42 (<500 pg mL^{-1}) are lower than those in normal people (about 800 pg mL^{-1}) due to its aggregation in the brain's senile plaques.[2] On the other hand, low levels of Aβ 1-42 in CSF may be also associated with other neurodegenerative diseases (NDs), notably dementia with Lewy body (DLB), Parkinson's disease (PDD) or Creutzfeld–Jacob disease (CJD).[4] The determination of Aβ 1-42 together with other biomarkers has therefore been implemented for more precise discrimination of AD from other NDs. Different proposed biomarker combinations for AD include Aβ 1-42 and Tau/p-Tau protein,[5,6] Aβ 1-42/Aβ 1-40 ratio,[6,7] Aβ 1-42, Aβ 1-40 and Aβ 1-38,[8,9] the ratio of Aβ 1-42/(Aβ 1-42 + Aβ 1-40 + Aβ 1-38),[10] the ratio Aβ 1-40/42 and those between Aβ 1-37, Aβ 1-38 and Aβ 1-39[11,12] and Aβ 1-42 together with Aβ 2-42.[13] Esselmann *et al.* described in their patent the use of quantitative ratio of Aβ 1-42, Aβ 2-40 and Aβ 2-42 for early diagnosis of AD.[14]

In the context of determination/quantification of different AD's biomarkers in general and Aβ peptides in particular in CSF, the most frequently employed analytical approaches are immunoassays,[15–19] mass spectrometry[16,20–23] and Western blot.[11,24–26] Like the two other techniques, the immunoassay based ones (MSD, xMAP, ELISA) can now detect different AD's biomarkers at the same time as they can employ simultaneously different antibodies specific for each biomarker.[15,27] However, all these methods, albeit being well established and having been used as reference techniques, are hardly convertible into miniaturized formats and therefore have little or no potential for production of point-of-care devices for early AD diagnosis purpose.

One alternative to the aforementioned techniques which has a high potential for miniaturization, automation and

[a]*Université Paris-Sud, Institut Galien Paris-Sud, 5 rue JB Clément, 92296 Châtenay-Malabry, France. E-mail: claire.smadja@u-psud.fr; Fax: +33 1-46-83-54-62*
[b]*CNRS, UMR 8612, 5 rue JB Clément, 92296 Châtenay-Malabry Cedex, France*
[c]*Macromolecules and Microsystems in Biology and Medicine, Institut Curie, Centre National de Recherche Scientifique, Université Pierre et Marie Curie, UMR 168, 75005 Paris, France*

integration while offering also peptide separation capabilities is electrokinetic separation. Capillary zone electrophoresis (CZE), being the simplest mode of this technique, was applied successfully for separation and quantification of a mixture of different Aβ peptides down to 300–500 nM with UV detection[28] and 35 nM with laser-induced fluorescent detection (LIF),[10] respectively. Downscaling of this approach to microchip platforms has also been reported by our group with detectable levels of Aβ peptides close to 200 nM.[9,29] These detection limits however were not sufficient for analyses of CSF samples where concentrations of Aβ peptides are only at sub nM ranges. Recently Wiltfang's group presented a novel method based on capillary isoelectric focusing (CIEF) immunoassay which was capable of detecting total Aβ in CSF after desalting/buffer exchange.[26] This method nevertheless is not applicable to C-truncated peptides possessing the same isoelectric point such as Aβ 1-38, Aβ 1-40 and Aβ 1-42. To compensate for the insufficient sensitivity of Aβ peptides determination *via* electrokinetic techniques, inclusion of a forefront sample treatment module based on magnetic immuno-capture, so-called immuno-precipitation (IP) has been proposed.[10,26,29,30] This technique belongs to the sample treatment strategies that are based on bio-functionalized magnetic nanoparticles. They are particularly suitable for peptides pre-concentration due to their large surface area, biocompatibility and ease in manipulation.[31] To further enhance the detection sensitivity, one option is to combine the magnetic pre-concentration step with fluorescent chemical labeling to allow then LIF detection. Fluorescent derivatization of Aβ peptides was already carried out off-line prior to the magnetic pre-treatment step.[29,30] However this labeling–capture–elution sequence was hardly adaptable to the microchip platform due to at least two following limitations: (1) the requirement of one additional microchamber containing no microbeads for fluorescent labeling of Aβ peptides prior to their magneto-immunocapture and (2) the difficulty in well mixing the laminar flows of sample and fluorophore solutions in microchannels. In addition, the previous studies employed magnetic micro-beads that were kept stationary in the form of tiny columns inside the micro-chip. This may not offer optimal contact between Aβ peptides and the beads' surface which is needed for higher capture efficiency.

Herein we reported for the first time an integrated capture–label–elution strategy that allows Aβ peptides enrichment *via* magnetic-bead-based immunocapture followed by their *in situ* fluorescent-labeling directly on beads prior to CE-LIF operation. One of the advantages of this novel sample treatment strategy is that the unwanted presence of extra fluorescent dye and fluorescent side products[9,10] are avoided in the electrophoresis profile. In an effort to enhance IP efficiency, different antibodies with varying specificities toward several Aβ peptides were investigated. The optimized whole sample treatment process developed in batchwise mode, including magnetic-bead-based capturing, on-bead fluorescent labeling and thermal elution offered enrichment factors up to 100. The batch-wise mode was then downscaled into a micro-fluidized bed for perspective coupling with microchip electrophoresis operation. The magnetic beads in this case were made circulated inside the microchannel rather than kept stationary during the passage of the sample flow for improvement of contact between Aβ peptides and magnetic beads and to increase the analysis throughput.

2. Experimental

2.1. Chemicals, reagents and samples

Amyloid peptides Aβ 1-38 and Aβ 1-40 were purchased from Anaspec (Fremont, CA, USA) whereas Aβ 1-42 was obtained from American peptide (Sunnyvale, CA, USA). Boric acid, formic acid, phosphate buffered saline (PBS 10×), bovine serum albumin (BSA), ammonium hydroxide 28.1% (m V^{-1}), sodium hydroxide, dimethyl sulfoxide (DMSO, 99.9% purity), triethanolamine (TEA), IgG from murine serum (reagent grade, ≥95%) and diaminobutane chloride (DAB) were provided by Sigma (St. Louis, MO, United States). The Fluoprobe 488 NHS (FP-488) was purchased from Interchim (Montluçon, France) and was dissolved in DMSO to obtain aliquots of 10 mg mL^{-1} which were then stored at −20 °C in the darkness. Dimethyl pimelimidate dihydrochloride (DMP) was purchased from Thermo Scientific (Rockford, USA). All buffers were prepared with deionized water purified with a Direct-Q3 UV purification system (Millipore, Milford, MA, USA).

Magnetic micro-particles (diameter of 2.8 μm) surface-bound with sheep anti-mouse IgG (Dynabeads M-280, 10 mg mL^{-1}) and different monoclonal anti-Aβ antibodies (6E10, 12F4 and 4G8) were purchased from Covance, Emeryville, CA. The magnetic microbeads employed in our work were the same as those reported in ref 10. All CSF samples were taken by the department of Neurology, university of Ulm (Ulm, Germany), aliquoted and stored at −20 °C until use. The sampling procedure was detailed elsewhere.[9,10] Our CSF samples were provided by the University of Ulm. Their collection and analysis were approved by the Ethics Committee at the University of Ulm.

2.2. Materials and apparatus

All CE-LIF analyses were implemented with a Beckman Coulter PA 800 ProteomLab coupled with a LIF detection system (a 3.5 mW argon-ion laser having an excitation wavelength of 488 nm and a 520 nm band-pass filter for collection of the emitting beam light). Data acquisition and instrument control were realized with the Karat 7.0 software. Bare fused silica capillaries of 375 μm o.d. and 50 μm i.d. were purchased from Phymep (Paris, France). pH values of solutions were controlled with an inoLab WTW series pH 730 meter. Amicon ultra 0.5 centrifugal filters (3 kDa) were purchased from Millipore Ireland (Cork, Ireland). Thermal operation was carried out with a GC oven (GC 5890, series II from Hewlett Packard, USA).

The micro-fluidized bed employed in this work was adapted from the design reported recently.[32,33] The chips were fabricated from cyclic olefin copolymer (COC) material to withstand temperature increase during the elution step.[34] Before the

loading of magnetic beads, the COC channel was coated with BSA 1% to prevent/minimize any possible accumulation of the beads onto the channel wall. More details on the setup and operation of this micro-fluidized bed can be referred to ref. 32 and 33.

2.3. Methods

2.3.1 Peptides preparation and storage. Stock Aβ 1-42 was prepared in ammonium hydroxide 0.16% (m V^{-1}) whereas other amyloid peptides were dissolved in ammonium hydroxide 0.10% (m V^{-1}). Aliquot solutions (10 μL) of individual peptides were prepared at a concentration of 2 mg mL^{-1} and subsequently lyophilized to remove all traces of ammonia. These lyophilized aliquots were then stored at −20 °C until use. For preparation of standard solutions (STDs), the lyophilized Aβ peptides were diluted with borate buffer (pH 10.5, ionic strength IS 40 mM) to obtain desired concentrations. These solutions were freshly prepared and stored at 4 °C for use within one day.

2.3.2 CE-LIF conditions. The procedure for in-solution labeling of Aβ peptides with FP-488, as well as details on CE-LIF conditions for analyses of the fluorescence-labeled Aβ peptides can be found in our previous publication.[10] To minimize the adverse effect of CE-inherent migration time fluctuation on peak identification and quantification, the migration-time-based electropherograms of Aβ peptides after the capture–label–elution process were converted into electrophoretic-mobility-based ones. The peak of FP-488 nonspecifically adsorbed on the beads surface during the labeling process, which always appeared before those of Aβ peptides in the electropherograms, was employed as a reference for this profile correlation.

2.3.3 Magneto-immunoprecipitation with fluorescent labeling. Magnetic micro-particles (Dynabeads M-280, 10 mg in 1 mL) were separately coated with 40 μg of different monoclonal anti-Aβ antibodies (*i.e.* 6E10, 12F4, 4G8 and IgG) according to the manufacturer protocol. Briefly, the Dynabeads M-280 (10 mg) and the antibodies (40 μg) of selected type were suspended in 1 mL of PBS 1× solution containing 0.1% (m V^{-1}) BSA, and were incubated over night on an orbital shaker (VXR basic Vibrax, Ika, Staufen, Germany) at 4 °C. The mixture was then allowed to react with DMP for 1 h at room temperature under a basic condition (0.2 M TEA, pH 10.8) to crosslink the bound antibodies to the surface of magnetic microbeads *via* the covalent binding between this noncleavable imidoester and primary amines in the antibodies. The antibodies-bound magnetic beads were subsequently washed with PBS 1× containing BSA 0.1% and then re-suspended in PBS 1× containing BSA 0.1% and NaN_3 0.02% for storage at 4 °C. These beads (10 mg mL^{-1}) did not aggregate and performed well even after several months of storage. Addition of any unnecessary compound other than the reaction medium, including the manufacturer-recommended washing buffers citrate and EDTA, in any step of the capture–label–elution procedure (even for the beads-washing purpose) was avoided to prevent any possible triggering of aggregation of the easily-aggregable amyloid peptides, especially Aβ 1-42 and also to keep the same buffer composition for labeling, elution and separation. A neodymium magnet (Adem-Mag MSV from Ademtech, Pessac, France) was employed to retain the magnetic beads during removal or addition of a suspension solution.

For magnetic immunocapture in batch, the suspension of antibodies-coated magnetic beads (10 mg mL^{-1}) was vortexed for 3 min for homogenization before withdrawal of 50 μL aliquots. The solution was removed from the aliquot and a volume of 800 μL of either an STD solution (prepared in PBS 1× and BSA 0.1%) or CSF sample was incubated with this 500 μg of magnetic beads coated with the desired antibodies on a shaker at 4 °C for 15 hours. The beads were then washed once with PBS 1×/BSA 0.1% and twice with borate buffer (pH 10.5, IS 40 mM). Subsequently, 50 μL of borate buffer containing FP-488 (0.2–1 mg mL^{-1}) was poured into the washed beads and the suspension was vigorously orbitally shaken for 5–60 min at room temperature. This optimization was implemented based on our previous work on in-solution fluorescent labeling of Aβ peptides.[10] Several parameters were changed upon optimization for on-beads fluorescent labeling, including the shaking time (from 5 to 60 min) and the concentration of FP-488 (from 0.2 to 1 mg mL^{-1}). The optimized on-beads labeling conditions (FP-488 at 0.6 mg mL^{-1}, shaking time of 30 min, see section 3.1.2) were employed throughout all capture and elution experiments. The beads were then washed twice with borate buffer to remove all un-reacted FP-488, followed by elution of the labeled Aβ peptides bound on beads. Different elution approaches were tested, including chemical elution with borate buffer (pH 10.5) or 0.1 M formic acid (pH 2.2) at ambient temperature and thermal elution at 95 °C. The eluents were subsequently subjected to CE-LIF analyses without further dilution. Note that the eluent volumes were dependent on the desired enrichment factors. For the tested enrichment factors of 40 and 100, the used eluent volumes were 20 μL and 8 μL respectively.

For immunocapture with the fluidized bed platform, 50–100 μg of magnetic beads were injected in the microchip. The cross diameters of its input and output channels were 110 μm and 100 μm, respectively. The microbeads – containing chamber had a conic form that reached a diameter of 1800 μm at its widest width. The total volume of the chamber was 0.46 μL whereas that occupied by the microbeads was 0.085 μL. 100 μL of an STD solution of Aβ peptides (60 nM) was injected in the chamber with a flow-rate of 1 μL min^{-1}. The beads were then washed with 20 μL of borate buffer at a flow-rate of 1.5 μL min^{-1}, followed by passage of 15 μL of borate buffer containing FP-488 at 0.5 μL min^{-1}. After this labeling step, the extra and unreacted fluorescent dye was washed out of the chamber with a flow of borate buffer (2 μL min^{-1} for 20 min). For thermal elution, the chip was heated to 70 °C once the flow inside the chamber was completely stopped. The neodymium magnet was always positioned at the bottom of the fluidized bed to prevent the magnetic beads from escaping out of the system. Upon conclusion of the elution step, the solution inside the fluidic chamber was pushed into a PEEK tubing

(length of 30 cm, internal diameter of 250 μm) connected at the output of the micro-fluidic chip. The solution inside this reservoir tubing was then collected for subsequent CE-LIF analyses.

3. Results and discussion

3.1. Magnetic-beads-based sample treatment optimization

The sample treatment operation can be divided into three steps: (1) capture of the Aβ peptides onto the antibody-grafted magnetic beads, (2) chemical fluorescent labeling of the Aβ peptides by the fluoprobe FP488 and (3) elution of the peptides from the immunosupport into a small and defined eluent volume for analyte preconcentration and further electrokinetic separation. These steps can in principle be carried out with different orders. We selected the capture–labeling–elution sequence as it was expected to simultaneously satisfy efficient Aβ peptides enrichment, removal of extra fluorophore and possible translation from batchwise into micro-fluidized bed format. Compared to the method of static interaction where the antibodies are immobilized onto a planar surface, the circulation of the magnetic beads in our approach is expected to facilitate the dynamic interaction between the antibodies and the Aβ peptides, which in turn should improve the immune-capture efficiency. This also is the case for subsequent on-beads fluorescent labeling. In addition, the surface area provided by a microbead of diameter D (Area = πD^2) is much larger than that of a square planar surface having the same length D (Area = D^2). As a result, for the same antibody immobilization efficiency, a higher density of antibodies is expected for micro-beads, allowing better immuno-capture and higher enrichment gains.

3.1.1. Capture of Aβ peptides onto magnetic beads. The capture of Aβ peptides onto the magnetic beads is based on specific interaction between Aβ peptides with the antibodies grafted onto the surface of the beads.[29,30,35,36] The binding yields of the antibodies to the magnetic microbeads and their specificity towards the targeted peptide epitope play a crucial role in determining efficiency of the immune-capture process. Accordingly, three commercial monoclonal mouse antibodies from Covance, namely 6E10, 4G8 and 12F4, which are reactive to amino acid residues 1–16 (N-terminus), amino acid residues 17–24 and the C-terminus of beta amyloid, respectively were tested. 12F4 is specific for the peptide isoform's ending at the 42nd amino acid and was already used in a silicon-platform-based high-sensitivity immunoassay for Aβ 1-42.[17] Non specific IgG from murine serum was employed to check for non specific capture. Magnetic beads grafted with the different antibodies were subjected to the same sample treatment process, *i.e.* capture–labeling–elution. Eluted fractions with the enrichment factor of 40 were directly analyzed with CE-LIF (Fig. 1). With the antibodies 6E10 and 4G8, Aβ 1-42 and Aβ 1-40 peaks could be detected whereas only that of Aβ 1-42 appeared in the case of 12F4. In the case of 6E10, the area ratio of Aβ 1-40/Aβ 1-42 was 0.44, which means that the original concentration ratio of Aβ 1-42 (8 nM)/Aβ 1-40 (15 nM) was preserved after the immunocapture process. The peaks obtained with 6E10 and 12F4 are much higher (approximately 4 times) than those with 4G8. Clearly, 6E10 and 12F4 exhibit the best performance in terms of capture of Aβ 1-40 and Aβ 1-42 for the former and Aβ 1-42 for the latter respectively under the tested conditions. To our opinion, the poorer result with 4G8 is possibly associated with: (1) low binding yields of antibodies to the beads surface, leading to an unsatisfactory on-bead antibody density and (2) less or no accessibility of primary and/or Lysine's amino groups which are needed for subsequent fluorescent labeling once the Aβ peptides are on-bead-immobilized. The efficient binding of 4G8 immobilized onto a silicon microarray platform to underivatized Aβ 1-42 and Aβ 1-39, as reported by Gagni *et al.* (see ref. 17), excludes the possibility that the immobilized 4G8 antibody shows low affinity for the concerned peptides.

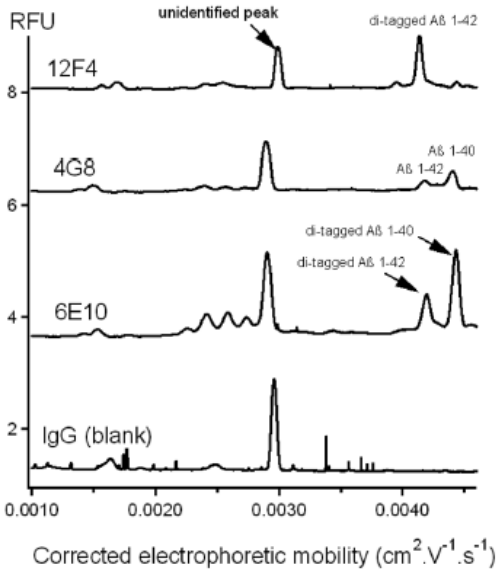

Fig. 1 CE-LIF electropherograms of a mixture of Aβ 1-42 (8 nM) and Aβ 1-40 (15 nM) after magnetic-beads-based sample treatment (capture–label–elution) obtained with different anti-Aβ antibodies. The batch-based capture and label conditions were detailed in the 'Experimental' section. For elution, the magnetic beads were heated up to 95 °C for 5 min in the presence of borate buffer (pH 10.5, IS 40 mM). Enrichment factor of 40. CE-LIF conditions: fused silica capillary with effective length (l_{eff}) of 38.4 cm and total length (L) of 48.2 cm; BGE: borate buffer (pH 9.25, IS 40 mM) added with DAB 3.25 mM; LIF detection with excitation wavelength (λ) of 488 nm.

3.1.2. On-bead fluorescent labeling of Aβ peptides. Considering the aforementioned preliminary results, the optimization of on-bead fluorescent labeling with FP488 was then performed with 6E10 as the capture antibody. Borate buffer (pH 10.5) was employed to provide a basic medium needed to produce mainly ditagged species formation. Ditagged species

display indeed higher fluorescent intensities and are better resolved by CE-LIF than monotagged species.[10] The alkaline pH required for achievement of desirable di-tagged peptides still belongs to the pH range for pH-independent fluorescence emission of FP-488 which is 4–10 according to the manufacturer. In our previous work reporting in-solution fluorescent labeling, it was found that a 5 min static incubation of Aβ peptides with 0.2 mg mL^{-1} FP-488 (molar ratio of FP-488 to Aβ peptides more than 4) was sufficient for complete in-solution peptide labeling with Aβ concentrations ranging from some dozen up to at least a thousand nM.[9,10] The direct application of this in-solution labeling conditions however led to unsatisfactory fluorescent tagging of Aβ peptides when they were bound on biofunctionalized beads. FP-488 is a fluorescent dye that binds covalently to amino groups of the peptides. Each intact beta amyloid possesses three conjugable amino groups, *i.e.* one primary and two on Lysine's residues. Nevertheless, they can become less accessible after the binding of Aβ peptides on beads. In the case of 6E10, the primary amine of Aβ peptides might partially lose its availability once 6E10 binds to their 1–16 amino acid residues. Another obstacle to efficient on-bead Aβ labeling came from the employment of a basic medium (pH 10.5). While this medium is expected to facilitate ditagged labeling,[10] it can also accelerate hydrolysis of the FP-488, which in turn could degrade the labeling efficiency over time. To overcome these problems, two optimizations were performed. Firstly, a prolongation of incubation time to 30 min in combination with vigorous agitation was carried out to favor the contact between FP-488 and on-beads bound Aβ peptides. Secondly, an increase in FP-488 concentration was implemented to compensate for the amount of FP-488 lost due to hydrolysis in the basic medium and to maintain the reaction towards stable conjugate formation over the prolonged period. Accordingly, it was found that a shaking incubation with an elevated FP-488 concentration of 0.6 mg mL^{-1} in borate buffer at room temperature for 30 min offered the best on-bead fluorescent labeling of Aβ peptides. The labeling reaction occurred under the presence of DMSO at small amounts (2–6% v/v) when FP-488 prepared in DMSO was added into the mixture. Nevertheless, the effect of DMSO on the established binding equilibrium between Aβ peptides and on-beads-immobilized antibodies (if any) was considered insignificant due to its small volumetric percentage. An efficient on-beads capture of Aβ peptides under such presence of DMSO was already reported in the label–capture–elution approach developed by Svobodova *et al.*[30]

3.1.3. Elution of the bound and labeled Aβ peptides. Different approaches for elution of the captured Aβ right after magnetic-immunoprecipitations were already reported, including chemical elution with a large volume of ammonium hydroxide,[10,30] formic acid[35,36] or thermal elution in the presence of a neutral buffer.[26] While these methods exhibited satisfactory performance in a two-step capture–elution procedure, the inclusion of an on-bead fluorescent labeling process in between may render the Aβ peptides elution more difficult due to the hindrance of FP-488 dyes non-specifically adsorbed onto the beads during this labeling step. Furthermore, the elution medium had to be optimized taking into consideration the subsequent CE-LIF analysis as it would significantly influence the analytical performance in terms of Aβ peak shape and sensitivity. This situation is reflected in Fig. 2 with electropherograms of fluorescently labeled Aβ 1-40 prepared in different media. The Aβ 1-40 peptide was labeled by a 5 min static incubation of Aβ 1-40 with 0.2 mg mL^{-1} FP-488 prepared in DMSO according to the procedure reported in our previous publication.[10] High and sharp peaks were obtained with alkaline media while an evident decrease in peak height was observed with a shift of pH towards acidic conditions. Based on these considerations, different elution options were then investigated and their capacities of desorbing labeled Aβ out of the magnetic beads were compared (Fig. 3). Regardless of the medium used and its pH, the chemical elution at room temperature did not lead to appearance of Aβ peaks in the electropherograms. Elution with ammonium hydroxide 0.16–1% or citric acid 100 mM was tested as well, but led to no detectable peaks with CE-LIF. This confirms that the on-beads bound Aβ were not eluted by the basic medium (pH 10.5) employed during the fluorescent labeling process. Only thermal elution at 95 °C for 5 min allowed detecting Aβ peptides with CE-LIF. The heating is therefore critical in breaking the interaction between Aβ peptides and the antibodies. No observable thermally induced modification of labeled Aβ peptides conformation was found, as no electrophoretic mobilities shift was

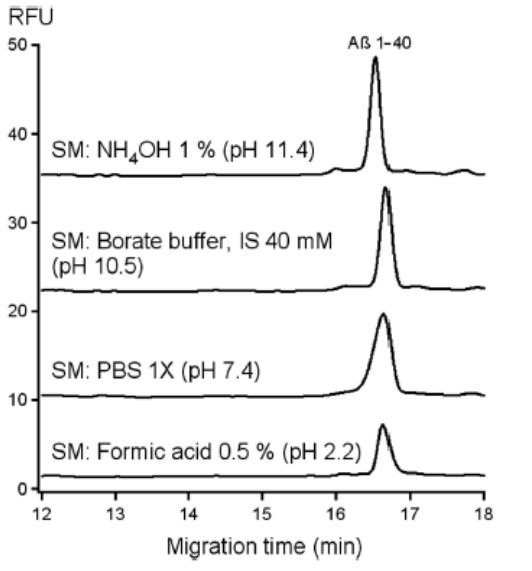

Fig. 2 CE-LIF electropherograms of fluorescently labeled Aβ 1-40 (1000 nM) prepared in different media. The Aβ 1-40 peptide was labeled by 5 min static incubation of Aβ 1-40 with 0.2 mg mL^{-1} FP-488 prepared in DMSO according to the procedure reported in our previous publication.[10] SM: sample medium. CE conditions as in Fig. 1.

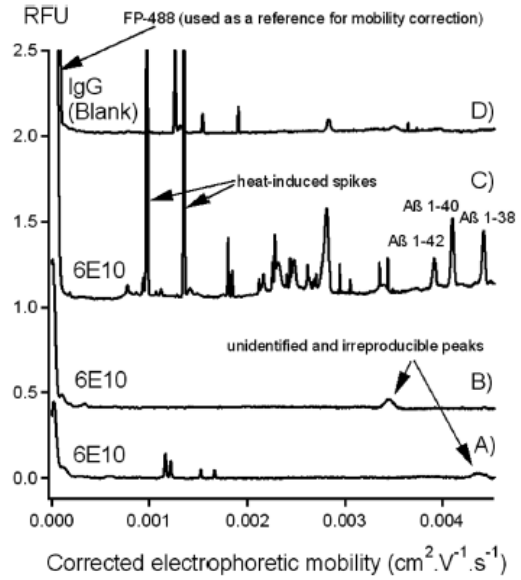

Fig. 3 CE-LIF electropherograms of the captured and labeled Aβ 1-42 (8 nM), Aβ 1-40 (15 nM) and Aβ 1-38 (15 nM) after chemical and thermal elutions. Capture was done with magnetic micro-beads coated with either 6E10 or IgG (for blank control). CE conditions as in Fig. 1. (A) Capture with 6E10 and elution with formic acid 0.5% at room temperature for 15 min; (B) capture with 6E10 and elution with borate buffer (pH 10.5, IS 40 mM) at room temperature for 15 min; (C) capture with 6E10 and elution with borate buffer (pH 10.5, IS 40 mM) at 95 °C for 5 min and (D) capture with IgG and elution with borate buffer (pH 10.5, IS 40 mM) at 95 °C for 5 min (blank).

observed for the thermally eluted peptides compared to the in-solution labeled ones. With this thermal elution approach, the antibodies-coated magnetic beads could be used only once because the antibodies could be denatured by such high temperature. Due to its favorable properties in terms of sharp peak shapes (Fig. 2) and high compatibility with the subsequent CE analysis, borate buffer (pH 10, IS 40 mM) was selected as the elution medium in this thermal approach. In addition the use of the same buffer compositions for thermal elution and for the fluorescent labeling is expected to facilitate the subsequent translation of this batchwise operation into micro-fluidic fluidized bed format. By employing the borate buffer, three consecutive steps, including fluorescent labeling, beads washing and elution can share the same medium.

3.2. Separation and sensitive detection of Aβ peptides in CSF samples

Excluding all washing steps, the optimized batchwise procedure of magnetic-bead-based sample treatment prior to CE-LIF comprised 15 hours of magneto-immunocapture at 4 °C, 30 min of on-bead fluorescent labeling at room temperature and 5 min of thermal elution at 95 °C. With this protocol using 6E10 antibody, the salient performance data were presented in Table 1. Calibration curves were acquired with satisfactory linearity (correlation coefficients more than 0.96) for the concentration ranges of 40–400 nM for Aβ 1-42 and 40–800 nM for Aβ 1-38 and Aβ 1-40 respectively. Over these ranges no further increase in peak heights was observed. The reproducibility of the inter-batch measurements of corrected peak areas and migration times was found to be about 12% and 1%, respectively. They deemed acceptable considering that these RSD values are due to the accumulation of errors of all operations, *i.e.* sample preconcentration, labeling, elution, injection and separation. In the case of repeated CE-LIF measurements of the same batch, the intra-batch RSD values for peak areas were improved to around 6%. An enrichment factor of 100 (calculated from the sample to eluent volumes ratio) for the Aβ 1-38, Aβ 1-40 and Aβ 1-42 peptides could be obtained (Table 1). The calculation of preconcentration gains based on a referenced peak area was not possible due to the unavailability of the (commercial) standard fluorescently ditagged Aβ peptides containing no extra FP-488. Deduction of the concentrations of fluorescently labeled peptides from those of the standard peptides was not done neither because the precise yield of Aβ peptides fluorescent di-tagging could not be determined. For this reason, while the relative ratios of different peptides captured on micro-beads could be provided (see section 3.1.1), information on the absolute recovery was

Table 1 Linearity of the response, detection limits (LODs) and reproducibility for the determination of preconcentrated Aβ peptides by CE-LIF. CE-LIF conditions as in Fig. 1

Analyte	Range (nM)	Correlation coefficient	LOD[a] (nM)	LOD-P[b] (nM)	RSD % T_m[c] (n = 4)	RSD % A_{inter}[d] (n = 4)	RSD % A_{intra}[e] (n = 3)
Aβ 1-42	40–400	0.9675	10	0.1	1.31	14.03	7.39
Aβ 1-40	40–800	0.9712	8	0.08	1.63	11.79	5.29
Aβ 1-38	40–800	0.9882	10	0.1	1.03	11.95	6.34

[a] Based on peak heights corresponding to 3 times the baseline noise. [b] LOD-P: detectable concentrations with the calculated enrichment factor F = 100. [c] Migration time, corrected to the reference peak of FP-488. RSD was measured with standard concentration of 15 nM. [d] RSD % A_{inter}: Inter-batch RSD values for peak areas (comparison of 4 different batches). The peak areas were calculated from the mobility-based electropherograms that were converted based on the migration times of FP-488 that was used as the referenced peak. [e] RSD % A_{intra}: RSD values for peak areas obtained with the same batch. The batch was measured three times with CE-LIF. The peak areas were calculated from the mobility-based electropherograms that were converted based on the migration times of FP-488 that was used as the referenced peak.

not obtainable. The smallest Aβ concentrations that were detectable by LIF detection, in other words the detection limits without preconcentration, where 8–10 nM, which are almost 4 times lower than that reported in the precedent work on CE-LIF.[10] This is mainly due to the absence of exceeding fluorescent dye in the final sample solution, which is only made possible with on-bead labeling approach. Further improvement in LODs could be achievable just by increasing the amount of magnetic beads in the batchwise capture process. This however was not envisaged as diminution of beads amount would be needed for a prospective adaptation towards a micro-fluidized bed platform. The detectable levels of Aβ peptides by LIF after our developed immune-capture–on-beads labeling–thermal elution procedure with an enrichment factor of 100 were 0.08–0.1 nM which are compatible with the Aβ peptides level in the CSF. In terms of sensitivity, our method has not reached yet the ELISA performance whose quantifiable level of Aβ 1-42 is 0.03 nM.[15] On the other hand, our method offers some advantages over ELISA, including (1) concurrent separation and determination of different structurally close Aβ peptides without recourse to simultaneous employment of different antibodies of high specificity towards each Aβ peptide of interest[9,10] and (2) distinguishing of monomeric and oligomeric forms of Aβ 1-42.[37]

The concentrations of Aβ 1-38, Aβ 1-40 and Aβ 1-42 in CSF samples were determined using the aforementioned sample treatment method followed by CE-LIF analyses. Electropherograms of CSF samples obtained from cognitive normal (controls) or AD patients are shown in Fig. 4. Both the standards and the CSF samples were subjected to the same enrichment – fluorescent derivatization for appropriate comparison. The filtration through 3 kDa filters was employed to remove all small unwanted species from the sample matrix while retaining the concerned Aβ. Much better baseline with no signal drifting was achieved with sample pre-filtering. Among the three Aβ peptides, Aβ 1-40 in CSF samples was present at the highest concentrations of 6–8 nM. Aβ 1-38 in these CSF samples was found to be at the order of 1–2 nM. The most challenging was the determination of Aβ 1-42 due to its extremely low abundance in CSF samples, as well as the presence of some unknown peaks adjacent to that of Aβ 1-42 (see Fig. 4). However, identification of these other compounds was not envisaged in the scope of this work. Recourse to immunocapture with 12F4 was then realized for selective determination of Aβ 1-42, as demonstrated in Fig. 5. The employment of this antibody specific for the C-terminus of Aβ 1-42 led to a clear visualization of Aβ 1-42 peak only. A decrease in Aβ 1-42 concentration could be observed in the CSF sample from an AD patient compared to that of a control one. The relative concentrations ratios of Aβ peptides in CSF samples obtained with our approach were in agreement with those reported by Svobodova *et al.*[30] who used the same antibodies and CSF samples provided from the same source (Ulm hospital) but not from the same patient. Pre-filtering of CSF samples would probably increase the performance of our system. Nevertheless, our main goal was to conceive a microsystem that integrates all

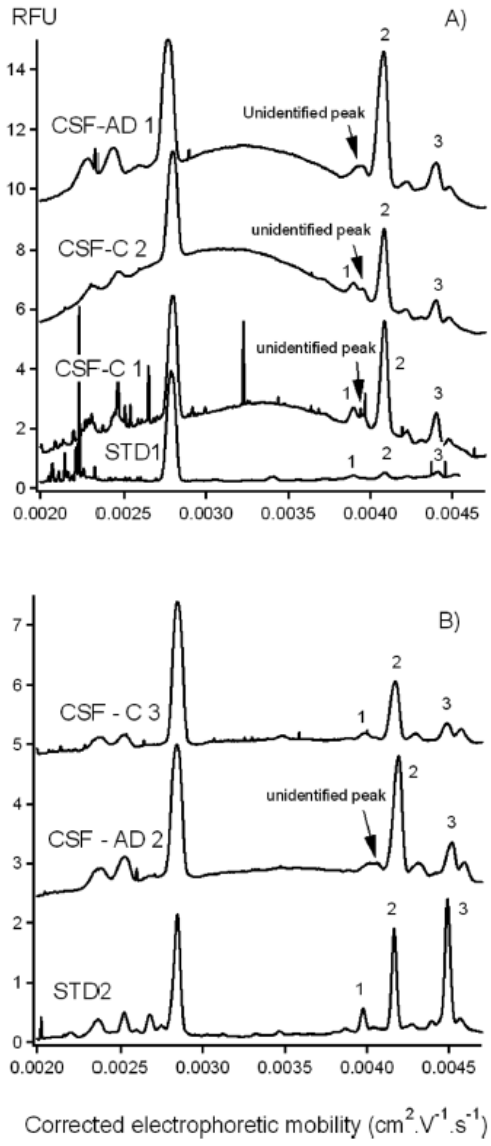

Fig. 4 CE-LIF electropherograms of CSF samples after magnetic immune-precipitation using the antibody 6E10 (enrichment factor of 100) and on-beads fluorescent labeling. Thermal elution conditions: 95 °C for 5 min in the presence of borate buffer (pH 10.5, IS 40 mM). CE conditions as in Fig. 1. (A) Sample treatment without pre-filtering of CSF samples; (B) sample treatment with pre-filtering of CSF samples using 3 K Dalton filters. Peak identification: (1) Aβ 1-42, (2) Aβ 1-40, (3) Aβ 1-38. CSF – AD stands for CSF samples from AD patients; CSF – C stands for CSF samples from cognitive normal people used as controls; STD 1: standard solution of Aβ 1-42 (0.2 nM), Aβ 1-40 (0.2 nM) and Aβ 1-38 (0.2 nM); STD 2: standard solution of Aβ 1-42 (2 nM), Aβ 1-40 (8 nM) and Aβ 1-38 (8 nM). The indicated concentrations in the brackets were those of the standards before immune-enrichment. Both standards and CSF samples were subjected to the same immunocapture–label–elution procedure.

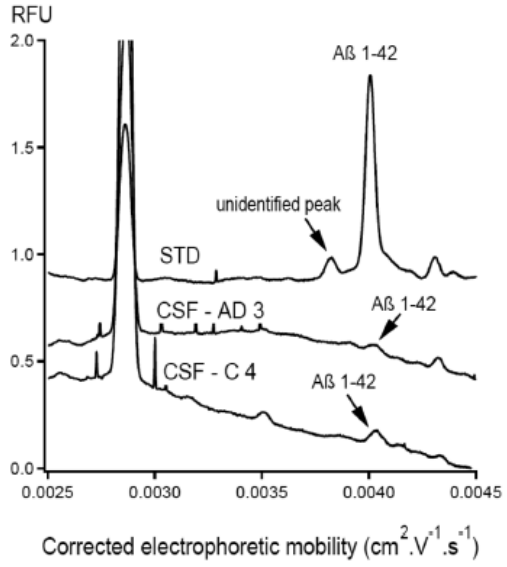

Fig. 5 CE-LIF electropherograms of CSF samples after magnetic immune-precipitation using the antibody 12F4 (enrichment factor of 100) and on-beads fluorescent labeling. Thermal elution conditions: 95 °C for 5 min in the presence of borate buffer (pH 10.5, IS 40 mM). CE conditions as in Fig. 1. Sample treatment was carried out without pre-filtering of CSF samples. CSF-AD: CSF sample collected from an AD patient; CSF-C: CSF sample from a cognitive normal person (used as control); STD: standard Aβ solution (8 nM). The indicated concentration in the brackets was that of the standard before immune-enrichment. Both the standard and CSF samples were subjected to the same immuno-capture–label–elution procedure.

pre- and analytical steps. As filtering in microsystems is not trivial, this additional sample treatment step was not further considered in this work.

3.3. Operation in a microfluidic fluidized bed: a proof of concept

While the batchwise mode of the developed magnetic immunocapture exhibited satisfactory performance for the determination of Aβ peptide mixture in CSF samples, its long operation time with manual solution switching may pose some inconvenience to the operator. Our prospective objective is therefore to integrate all capture, label, elution and MCE-LIF separation steps into an automated procedure in a microfluidic platform. The preliminary stage towards this objective relies on the implementation of the capture–label–elution protocol inside a microfluidic fluidized bed whose configuration was reported recently.[32,33] Inside its chamber, magnetic microparticles continuously re-circulate thanks to two counter driving forces, *i.e.* pressure-driven hydrodynamic and magnetic attraction forces. The contact of magnetic beads with Aβ peptides (during the capturing step) and with FP-488 (during the on-bead labeling process) is therefore expected to be much improved in this case compared to the previous microchip design where magnetic microbeads were kept stationary inside the microchannel.[29,30] Indeed, with the previous microchip design, fracture in the magnetic plug could occur over a certain flowrate. In case of fracture the liquid could preferentially flow through this fracture of lower hydrodynamic resistance and thus reduces drastically the bed surface in contact with the sample. With our device we obtained a homogeneous contact of the liquid with all the beads and we could thus expect a better efficiency. Compared to batch experiment, this micro-fluidized bed configuration allows an efficient stirring and should enhance the mass transfer between the solid and the liquid phase. Accordingly, better capture efficiency and labeling interaction are expected to be achievable within shorter operation duration. The capture–label–thermal elution procedure was then carried out in the micro-fluidized bed and the fluorescent signal obtained at its output microchannel after thermal elution is shown in Fig. 6A. This fluorescent fraction was subsequently collected and subjected to CE-LIF separation for visualization of Aβ 1-42, Aβ 1-40 and Aβ 1-38 as shown in Fig. 6B. The fluorescent signal shown in Fig. 6A was indeed the total signals of the released FP-488 and labeled Aβ peptides that were well separated with CE-LIF as displayed in Fig. 6B. The operation time was shortened from more than 15 hours in the batch-based mode into only around 3 hours with the fluidized bed configuration. To avoid saturation of the microchannel, the amount of magnetic beads was tenfold reduced. Even under this condition, successful capture–label–elution operation in this micro-fluidized bed was still achieved with an enrichment factor of 20. Higher preconcentration gains are expected if dilution of the eluent at the output of the microfluidized bed (at the nL range) into a collectable volume (some μL) for subsequent CE-LIF operation could be avoided. This would be the case when integrating the preconcentration step to the microchip electrophoresis operation will be realized. We demonstrated therefore that this novel approach which integrated for the first time Aβ capturing and fluorescent labeling on the same immunosupport could be downscaled. In the case of offline labeling followed by immunocapture,[29,30] manual batchwise in-solution labeling in the absence of magnetic beads can hardly be downscaled into the micro-fluidized bed platform. Operation integration and automation in the magnetic-beads based microfluidic system for perspective point-of-care device production are therefore more achievable with the developed capture–label–elution strategy where the sample capture and labeling can be both implemented on-chip in the same microchamber. Furthermore, the undesirable preferential capture of fluorescently labeled Aβ 1-42 over the other Aβ peptides encountered in the offline labeling–immunocapture technique reported by Svobodova *et al.*[30] was not observed with our capture–label–elution approach. For successful perspective development of a point-of-care device that can quantitatively reach the extremely low level of Aβ 1-42 in CSF samples, three processes have been envisaged, including: (1) improvement of LIF detection limit from 35 nM to 8 nM without the preconcentration step by the

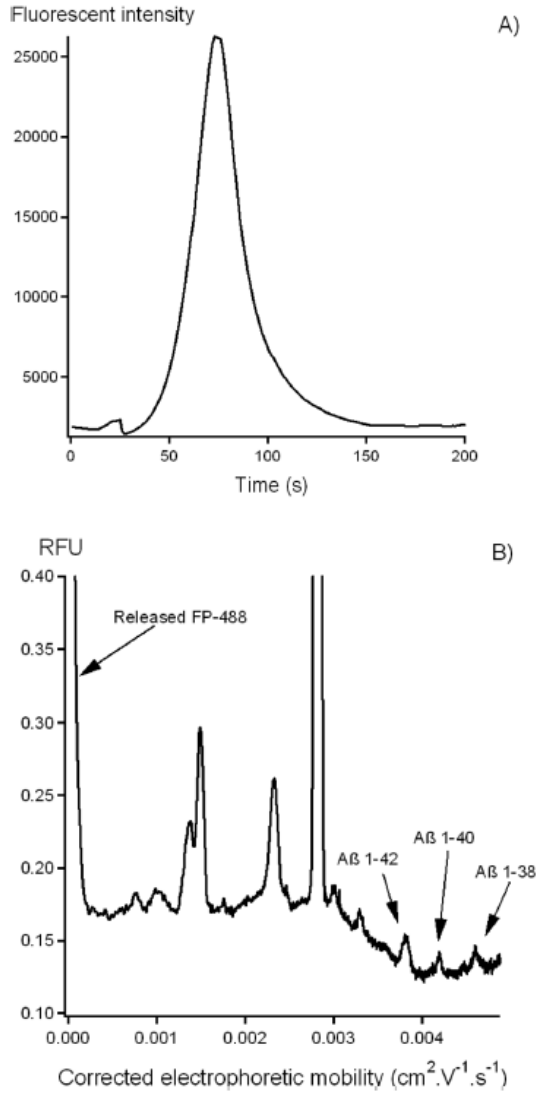

Fig. 6 (A) Fluorescent observation at the output channel of the micro-fluidized bed during the passage of the eluent after thermal elution. The sample is 100 µL of 60 nM standard peptides. The capture–label–elution procedure can be found in section 2.3. (B) CE-LIF electropherogram obtained for the eluent collected at the output channel of the micro-fluidized bed after thermal elution. CE conditions as in Fig. 1.

removal of the exceeding fluorophores in the sample matrix after the labeling, by using microbeads (2) pre-concentration of Aβ peptides with microbeads-based immunocapture and (3) integration of all steps, *i.e.* preconcentration–labeling–elution–separation on a microfluidized bed coupled with a separation microchip to eliminate the volume loss and variation at each step and to significantly reduce the elution volume for better enrichment gain. At the present stage, the presence of Aβ 1-42 in CSF samples was detected with the first two aforementioned approaches.

4. Conclusions

This work contributed significantly to three achievements. Firstly, an MCE/CE-LIF compatible technique of Aβ peptides enrichment was successfully developed based on magneto-immunocapture operation. Secondly, the successful fluorescent labeling of Aβ peptides was for the first time done on-beads, leading to the removal of all unwanted extra fluorescent dyes. These pre-concentration and fluorescent labeling steps which act as a forefront sample treatment process prior to CE-LIF render the separation and sensitive detection of Aβ 1-42, Aβ 1-40 and Aβ 1-38 in CSF samples possible. The FP-488 that was non-specifically adsorbed onto microbeads during the labeling process and then released into the eluent during the elution step was profited as the internal standard for calculation of relative migration times of Aβ peptides in CE-LIF profiles. Finally, a proof of concept of micro-fluidized bed based operation for enrichment and fluorescent-labeling of Aβ was successfully demonstrated. This opens the door for production of hand-held devices for facile and high-throughput probing of Aβ peptides in CSF samples based on lab-on-chip electrokinetic separation. Perspective work on coupling the fluidized bed with microchip electrophoresis will be soon envisaged.

Acknowledgements

This work and the post-doctoral fellowship for Dr Thanh Duc Mai have been financially supported by the European Community's Seventh Framework Programme (NaDiNe FP7/2010-2015) under the grant agreement no 246513. The post-doctoral fellowship for Dr Mohamed Hiraoui was supported by DIM Analytics program (http://www.dim-analytics.fr/). We would like to thank Dr Romain Verpillot for valuable discussion. We are also grateful to Dr Ute Haussmann and Dr Hans Klafki (University of Duisburg-Essen, Germany) for their useful advices concerning bead grafting, as well as to Prof. Dr Markus Otto at the department of Neurology, university of Ulm (Ulm, Germany) for CSF sampling operation.

References

1 J. Kang, H. G. Lemaire, A. Unterbeck, J. M. Salbaum, C. L. Masters, K. H. Grzeschik, G. Multhaup, K. Beyreuther and B. Mullerhill, *Nature*, 1987, 325, 733–736.
2 C. Humpel, *Trends Biotechnol.*, 2011, **29**, 26–32.
3 E. R. Peskind, R. Riekse, J. F. Quinn, J. Kaye, C. M. Clark, M. R. Farlow, C. DeCarli, C. Chabal, D. Vavrek, M. A. Raskind and D. Galasko, *Alzheimer Dis. Assoc. Disord.*, 2005, **19**, 220–225.

4 B. Mollenhauer, H. Esselmann, S. Roeber, W. Schulz-Schaeffer, C. Trenkwalder, M. Bibl, P. Steinacker, H. Kretzschmar, J. Wiltfang and M. Otto, *J. Neural Transm.*, 2011, **118**, 1261–1262.
5 K. Blennow and H. Hampel, *Lancet Neurol.*, 2003, **2**, 605–613.
6 P. Lewczuk, H. Esselmann, M. Otto, J. M. Maler, A. W. Henkel, M. K. Henkel, O. Eikenberg, C. Antz, W.-R. Krause, U. Reulbach, J. Kornhuber and J. Wiltfang, *Neurobiol. Aging*, 2004, **25**, 273–281.
7 N. R. Graff-Radford, J. E. Crook, J. Lucas, *et al.*, *Arch. Neurol.*, 2007, **64**, 354–362.
8 V. Welge, O. Fiege, P. Lewczuk, B. Mollenhauer, H. Esselmann, H.-W. Klafki, S. Wolf, C. Trenkwalder, M. Otto, J. Kornhuber, J. Wiltfang and M. Bibl, *J. Neural Transm.*, 2009, **116**, 203–212.
9 K. Mesbah, R. Verpillot, M. Chiari, A. Pallandre and M. Taverna, *Analyst*, 2014, **139**, 6547–6555.
10 R. Verpillot, H. Esselmann, M. R. Mohamadi, H. Klafki, F. Poirier, S. Lehnert, M. Otto, J. Wiltfang, J. L. Viovy and M. Taverna, *Anal. Chem.*, 2011, **83**, 1696–1703.
11 J. Wiltfang, H. Esselmann, M. Bibl, A. Smirnov, M. Otto, S. Paul, B. Schmidt, H. W. Klafki, M. Maler, T. Dyrks, M. Bienert, M. Beyermann, E. Rüther and J. Kornhuber, *J. Neurochem.*, 2002, **81**, 481–496.
12 J. Wiltfang, H. Esselmann, A. Smirnov, M. Bibl, L. Cepek, P. Steinacker, B. Mollenhauer, K. Buerger, H. Hampel, S. Paul, M. Neumann, M. Maler, I. Zerr, J. Kornhuber, H. A. Kretzschmar, S. Poser and M. Otto, *Ann. Neurol.*, 2003, **54**, 263–267.
13 M. Bibl, M. Gallus, V. Welge, H. Esselmann, S. Wolf, E. Rüther and J. Wiltfang, *J. Neural Transm.*, 2012, **119**, 805–813.
14 H. Esselmann, T. W. Groemer, J. Kornhuber, P. Lewczuk, J. M. Maler and J. Wiltfang, Patent WO2011124376A1, Application No. PCT/EP2011/001724, February 21, 2013.
15 J.-H. Kang, M. Korecka, J. B. Toledo, J. Q. Trojanowski and L. M. Shaw, *Clin. Chem.*, 2013, **59**, 903–916.
16 S. Lista, H. Zetterberg, B. Dubois, K. Blennow and H. Hampel, *J. Neurol.*, 2014, **261**, 1234–1243.
17 P. Gagni, L. Sola, M. Cretich and M. Chiari, *Biosens. Bioelectron.*, 2013, **47**, 490–495.
18 N. Xia, L. Liu, M. G. Harrington, J. Wang and F. Zhou, *Anal. Chem.*, 2010, **82**, 10151–10157.
19 M. Ammar, C. Smadja, L. G. T. Phuong, M. Azzouz, J. Vignerond, A. Etcheberry, M. Taverna and E. Dufour-Gergam, *Biosens. Bioelectron.*, 2013, **40**, 329–335.
20 G. Grasso, *Mass Spectrom. Rev.*, 2011, **30**, 347–365.
21 Y. Liu, H. Qing and Y. Deng, *Int. J. Mol. Sci.*, 2014, **15**, 7865–7882.
22 J. Pannee, E. Portelius, M. Oppermann, A. Atkins, M. Hornshaw, I. Zegers, P. Hojrup, L. Minthon, O. Hansson, H. Zetterberg, K. Blennow and J. Gobom, *J. Alzheimer's Dis.*, 2013, **33**, 1021–1032.
23 M. E. Lame, E. E. Chambers and M. Blatnik, *Anal. Biochem.*, 2011, **419**, 133–139.
24 N. Ida, T. Hartmann, J. Pantel, J. Schröder, R. Zerfass, H. Förstl, R. Sandbrink, C. L. Masters and K. Beyreuther, *J. Biol. Chem.*, 1996, **271**, 22908–22914.
25 M. Bibl, B. Mollenhauer, H. Esselmann, P. Lewczuk, H.-W. Klafki, K. Sparbier, A. Smirnov, L. Cepek, C. Trenkwalder, E. Rüther, J. Kornhuber, M. Otto and J. Wiltfang, *J. Brain*, 2006, **129**, 1177–1187.
26 U. Haussmann, O. Jahn, P. Linning, C. Janssen, T. Liepold, E. Portelius, H. Zetterberg, C. Bauer, J. Schuchhardt, H.-J. Knoelker, H. Klafki and J. Wiltfang, *Anal. Chem.*, 2013, **85**, 8142–8149.
27 J.-H. Kang, H. Vanderstichele, J. Q. Trojanowski and L. M. Shaw, *Methods*, 2012, **56**, 484–493.
28 R. Verpillot, M. Otto, H. Klafki and M. Taverna, *J. Chromatogr., A*, 2008, **1214**, 157–164.
29 M. R. Mohamadi, Z. Svobodova, R. Verpillot, H. Esselmann, J. Wiltfang, M. Otto, M. Taverna, Z. Bilkova and J.-L. Viovy, *Anal. Chem.*, 2010, **82**, 7611–7617.
30 Z. Svobodova, M. R. Mohamadi, B. Jankovicova, H. Esselmann, R. Verpillot, M. Otto, M. Taverna, J. Wiltfang, J.-L. Viovy and Z. Bilkova, *Biomicrofluidics*, 2012, **6**, 024126.
31 J. He, M. Huang, D. Wang, Z. Zhang and G. Li, *J. Pharm. Biomed. Anal.*, 2014, **101**, 84–101.
32 S. Tabnaoui, I. Pereiro, M. Fermigier, S. Descroix, J.-L. Viovy and L. Malaquin, 17th International Conference on Miniaturized Systems for Chemistry and Life Sciences, Freiburg, Germany, 2013, http://www.rsc.org/images/loc/2013/PDFs/Papers/467_0838.pdf.
33 S. Tabnaoui, PhD Thesis, Curie Institute, Université Pierre et Marie Curie - Paris VI, 2013, https://tel.archives-ouvertes.fr/tel-00839133/document.
34 K. Perez-Toralla, J. Champ, M. R. Mohamadi, O. Braun, L. Malaquin, J.-L. Viovy and S. Descroix, *Lab Chip*, 2013, **13**, 4409–4418.
35 E. Portelius, A. J. Tran, U. Andreasson, R. Persson, G. Brinkmalm, H. Zetterberg, K. Blennow and A. Westman-Brinkmalm, *J. Proteome Res.*, 2007, **6**, 4433–4439.
36 E. Portelius, A. Westman-Brinkmalm, H. Zetterberg and K. Blennow, *J. Proteome Res.*, 2006, **5**, 1010–1016.
37 D. Brinet, J. Kaffy, F. Oukacine, S. Glumm, S. Ongeri and M. Taverna, *Electrophoresis*, 2014, **35**, 3302–3309.

Appendix B

Integrated C2CA protocol

Reagents

Buffers

	B&Wtw	Wtw
Tris-HCl pH 7,5	10 mM	10 mM
EDTA 0.5 M	5 mM	5 mM
NaCl	1 M	0.1 M
Tween-20	0.10%	0.10%

Labeling mix

Tris-HCl pH 8	20 mM
EDTA 0.5 M	20 mM
Tween-20	0,10%
Detection oligo	5 nM
NaCl	1 M

Preparation

I – Template dilution

Dilute synthetic template to 1 nM (10 µL) in 1xB&Wtw buffer

II – Bead preparation

Wash streptavidin-coupled Dynabeads 3 times in 1x Wtw buffer in a tube (use magnetic rack, gently vortex in between washes), use 5 µL of beads per sample

Add 1 equal volume 2x Wtw and use the mix in step I in protocol below

Procedure

Note : prepared volumes are always in excess to prevent air from entering the device

I - Coupling (bead conjugation)

	Stock conc.	Final conc.	vol per sample (µl)
beads	2 × Wtw-buffer	~1 × Wtw-buffer	5
CO (capture oligo with biotin)	1 µM	50 nM	1
dH_2O	-	-	4
		mix volume	10
		total volume	10

Incubate in tube at room temperature for 5 min; rotation

Wash with 1 × Wtw twice

II - Plug formation

	vol per sample
Form a plug from 5µl bead mix	5

III - Template hybridization

	Stock conc.	Final conc.	Vol (µL)
Synthetic Target/s wt	1 nM		5
Synthetic Target/s mut12	1 nM		5
2xB&Wtw			10
			20
Incubate at 60°C	10 µL 1 µL/min		
Wash with 1xWtw	10 µL 2 µL/min		

IV - Padlock hybridization + ligation

	Stock conc.	Final conc.	Vol (µL)
Padlock mut	1 µM	50 nM	1
Padlock wt	1 µM	75 nM	1,5
BSA	2 µg/µl, stf	0.2 µg/µl	2
Ampl Buffer	10 ×	1 ×	2
Ampligase	5 U/µl	0.5 U/µl	2
H_2O			11,5
			20
Incubate at 60°C	10 µL 1 µL/min		
Wash with 1xWtw	10 µL 2 µL/min		

V - 1st RCA

	Stock conc.	Final conc.	Vol (µL)
BSA	2 µg/µl, stf	0,2 µg/µl	2
dNTPs	2,5 mM	125 µM	1
phi29 buffer	10 ×	1 ×	2
phi29 polymerase	10 U/µl	200 mU/µl	0,2
MQ H_2O			14,8
			20
Incubate at 37°C	20 µL 0,3 µL/min		
Wash with 1xWtw	10 µL 2 µL/min		

VI - Digestion SapI

	Stock conc.	Final conc.	Vol (µL)
BSA sterile filt.	2 µg/µl	0.2 µg/µl	2,5
phi29 buffer	10 x	1x	2,5
Sap I	10 U/µl	120 mU/µl	0,3
dH_2O	-		19,7
			25

Incubate at 37°C	20 µL 0,5 µL/min
Wash with 1xWtw	10 µL 2 µL/min

VII - Ligation

	Stock conc.	Final conc.	Vol (µL)
BSA sterile filt.	2 µg/µl	0,2 µg/µl	2
T4 buffer	5x	1x	4
T4 DNA ligase	1 U/ul	20 mU/µl	0,4
MQ H_2O	-	-	13,6
			20
Incubate at 37°C	10 µL 0,5 µL/min		
Wash with 1xWtw	15 µL 2 µL/min		

VIII - RCA (COC surface)

	Stock conc.	Final conc.	Vol (µL)
BSA sterile filt.	2 µg/µl	0,2 µg/µl	2,5
phi29 buffer	10 x	1x	2,5
dNTP	2,5mM	125 µM	1,5
phi29pol	10 U/µl	0,2 U/µl	0,5
MQ H_2O	-	-	18
			25
Incubate at 37°C	20 µL 0,3 µL/min		
Wash with 1xWtw	15 µL 2 µL/min		

IX - Labeling (slide)

	Stock conc.	Final conc.	Vol (µL)
Labelling mix	2x	1x	12,5
DO Cy3 KRAS	10 µM	100 nM	0,25
MQ H_2O			12,25
		mix volume	25
		total volume	
Incubate at 55°C	15 µL 1 µL/min		
Wash with 1xWtw	15 µL 2 µL/min		